UV RESONANCE RAMAN STUDIES OF PEPTIDE FOLDING, PEPTIDE FIBRILLIZATION AND $Cl^- \rightarrow H_2O$ CHARGE TRANSFER TRANSITION

by

Kan Xiong

B.Sc. in Chemistry, The University of Science and Technology of China, 2006

Submitted to the Graduate Faculty of

The DIETRICH School of Arts & Sciences in partial fulfillment

of the requirements for the degree of

Doctor of Philosophy

University of Pittsburgh

2012

UNIVERSITY OF PITTSBURGH

The Kenneth P. DIETRICH School of Arts & Sciences

This dissertation was presented

by

Kan Xiong

It was defended on

Feburary 13, 2012

and approved by

Prof. Lillian Chong, Assistant Professor, Chemistry

Prof. Michael A. Trakselis, Assistant Professor, Chemistry

Prof. Ronald Wetzel, Departmental of Structural Biology

Committee Chair: Prof. Sanford A. Asher, Distinguished Professor, Chemistry

UV RESONANCE RAMAN STUDIES OF PEPTIDE FOLDING, PEPTIDE FIBRILLIZATION AND $Cl^- \rightarrow H_2O$ CHARGE TRANSFER TRANSITION

Kan Xiong, PhD

University of Pittsburgh, 2012

Protein folding problem is one of the most important unsolved problems in biology. Many diseases such as Alzheimer disease and Parkinson disease are caused by protein unfolding, protein misfolding and protein aggregation. Understanding molecular mechanism(s) of these diseases could facilitate drug design to treat diseases.

UV resonance Raman spectroscopy (UVRR) is a powerful method to quickly determine protein conformational ensembles and the dynamics of conformational transitions. UVRR enables monitoring of the protein conformational distributions and Gibbs free energy landscapes along the Ramachandran Ψ coordinate.

We utilized UVRR to examine the dependence of Gibbs free energy landscapes of an α-helical peptide on solution environment such as salt species (Chapter 3) and alcohol species (Chapter 4). We also examined poly-L-glutamate (PGA) conformation dependence on salt concentrations, and surprisingly found that high concentrations of NaCl and KCl do not alter the unfolded PPII and 2.5_1-helix conformations of PGA (Chapter 5).

In Chapter 6, we reported the first time experimental measurements of Ramachandran Ψ-angle distributions for intrinsically disordered peptides: the N-terminal peptide fragment (Residues 17-29) of tumor suppressor p53 and its P27S mutant form. We also measured UVRR spectra of Leu26 deuterated peptides to determine conformational distributions of Leu26 in the p53 peptides.

In Chapter 7, we reported the first experimental measurements of the impact of ion binding on poly-L-lysine (PLL) (un)folding kinetics. We also examined PLL (un)folding coordinate(s) to obtain insight into PLL (un)folding mechanism(s).

In Chapter 8, we developed a method and for the first time directly monitored the backbone and side chain hydrogen bonding of a polyGLN peptide whose solution structure can be controlled to either fibrillize or not fibrillize.

In Chapter 9, we utilized UVRR to probe the lowest energy allowed electronic transitions of aqueous solutions containing Cl^- salts. We showed that the waters hydrating the Cl^- are involved in charge transfer transitions that transfer electron density from Cl^- to the water molecules. These charge transfer transitions cause significant change in the H-O-H bond angle in the excited states, which results in a strong enhancement of the preresonance Raman intensity of the water bending modes.

TABLE OF CONTENTS

PREFACE ..... **XXIV**

1.0 PROTEIN FOLDING **1**

1.1 PROTEIN STRUCTURE **1**

1.1.1 Dihedral angles **2**

1.1.2 Ramachandran plot **3**

1.1.3 Common helix structures **4**

1.2 PROTEIN STABILITY **6**

1.2.1 Conformational entropy **7**

1.2.2 Hydrophobic interaction **7**

1.2.3 Hydrogen bonding **8**

1.2.4 Electrostatic interactions **9**

1.3 PROTEIN FOLDING MECHANISM **9**

1.3.1 Classical protein folding mechanism **9**

1.3.2 Energy landscape theory **10**

1.4 TECHNIQUES TO STUDY PROTEIN FOLDING **12**

1.4.1 X-Ray crystallography **12**

1.4.2 NMR **12**

1.4.3 Circular Dichroism (CD) spectroscopy **12**

1.4.4 Infrared spectroscopy (IR) 13

1.4.5 Molecular dynamics (MD) simulation 13

1.4.6 UV Resonance Raman spectroscopy (UVRR) 14

1.5 REFERENCES 15

2.0 RAMAN EFFECT 20

2.1 RAMAN THEORY 20

2.1.1 Classical oscillator model 20

2.1.2 Quantum mechanical treatment 23

2.2 VIBRATIONAL RESONANCE RAMAN SCATTERING 26

2.3 PROTEINS/PEPTIDES UV RESONANCE RAMAN SPECTRA 28

2.3.1 Electronic transitions of peptide bond 28

2.3.2 Amide vibration modes 29

2.4 RERERENCE 32

3.0 SALT DEPENDENCE OF AN α-HELICAL PEPTIDE FOLDING ENERGY LANDSCAPES 35

3.1 INTRODUCTION 35

3.2 EXPERIMENTAL 36

3.3 RESULTS 37

3.3.1 CD results 37

3.3.2 UV Resonance Raman Measurements: 41

3.3.3 Molecular Dynamic Simulation Results: 48

3.4 DISCUSSION 50

3.5 CONCLUSIONS 53

3.6 ACKNOWLEDGEMENTS 53

3.7 REFERENCES 54

4.0 CIRCULAR DICHROSIM AND UV RESONANCE RAMAN STUDY OF THE IMPACT OF ALCOHOLS ON THE GIBBS FREE ENERGY LANDSCAPE OF AN α-HELICAL PEPTIDE 59

4.1 INTRODUCTION 59

4.2 EXPERIMENTAL 60

4.3 RESULTS 61

4.3.1 CD measurements 61

4.3.2 UVRR measurements 62

4.4 DISCUSSION 68

4.5 CONCLUSIONS 70

4.6 ACKNOWLEDGEMENTS 70

4.7 REFERENCES 70

5.0 CONFORMATION OF POLY-L-GLUTAMATE IS INDEPENDENT OF IONIC STRENGTH 75

5.1 INTRODUCTION 75

5.2. EXPERIMENTAL 76

5.3 RESULTS AND DISCUSSION 77

5.3.1 CD results 77

5.3.2 UVRR results 79

5.4. CONCLUSIONS 84

5.5 ACKNOWLEDGEMENTS 84

5.6 REFERENCES 84

6.0 DIRECT OBSERVATIONS OF CONFORMATIONAL DISTRIBUTIONS OF INTRINSICALLY DISORDERED P53 PEPTIDES USING UV RAMAN AND EXPLICIT SOLVENT SIMULATIONS 88

6.1 INTRODUCTION 89

6.2 EXPERIMENTAL AND COMPUTATIONAL METHODS 90

6.2.1 Experimental Methods 90

6.2.2 Computational Methods 91

6.3 RESULTS AND DISCUSSION 95

6.3.1 Temperature dependence of peptide conformations 95

6.3.2 Conformational diversity of peptides 98

6.3.3 Does binding occur by conformational selection? 101

6.3.4 Conformational diversity of a selected peptide residue: Leu26 102

6.3.5 Solvent exposure of the Trp residue 106

6.4 CONCLUSIONS 107

6.5 ACKNOWLEDGMENTS 108

6.6 REFERENCES 108

7.0 IMPACT OF ION BINDING ON POLY-L-LYSINE (UN)FOLDING ENERGY LANDSCAPE AND KINETICS 113

7.1 INTRODUCTION 113

7.2 EXPERIMENTAL 115

7.3 RESULTS 116

7.3.1 Static UVRR 116

7.3.2 Kinetic UVRR of PLL in $NaClO_4$ 117

7.3.3 Kinetic UVRR of PLL in pure water 124

7.4 DISCUSSION 129

7.5 CONCLUSIONS 140

7.6 ACKNOWLEDGEMENTS 140

7.7 REFERENCES 141

8.0 UV RESONANCE RAMAN MONITORS POLYGLUTAMINE BACKBONE AND SIDE CHAIN HYDROGEN BONDING AND FIBRILLIZATOIN 145

8.1 INTRODUCTION 146

8.2 EXPERIMENTAL 147

8.3 RESULTS 149

8.4 DISCUSSION 162

8.5 CONCLUSIONS 163

8.6 ACKNOWLEDGEMENTS 164

8.7 REFERNCES 164

9.0 LOWEST ENERGY ELELECTRONIC TRANSITION IN AQUEOUS Cl^- SALTS: $Cl^- \rightarrow (H_2O)_6$ CHARGE TRANSFER TRANSITION 169

9.1 INTRODUCTION 169

9.2 EXPERIMENTAL 170

9.3 RESULTS 171

9.4 DISCUSSION 178

9.5 CONCLUSIONS 179

9.6 ACKNOWLEDGEMENTS 180

9.7 REFERENCES 180

APPENDIX A 182

APPENDIX B 184

APPENDIX C 188

APPENDIX D 190

APPENDIX E 200

APPENDIX F 204

10.0 CONCLUSIONS 209

11.0 FUTURE WORK 213

LIST OF TABLES

Table 3.1: Thermodynamic parameters calculated from CD data. 39

Table 3.2: Impact of ions on AP α-helix stability; "+" helix stabilizing; "-" helix destabilizing; "0" no impact. 52

Table 6.1.Calculated amide II´p frequencies and potential energy distributions for Acetyl-L-P-NH_2 and its perdeuterated lecucine isotopomer; Acetyl-A-P-NH_2 and its perdeuterated alanine isotopomer.....104

Table 7.1: Kinetic parameters for the 0.5 M $NaClO_4$ (pH 10.66) PLL α-helix-like conformations, the pure α-helix, and the π-helix (bulge) (un)folding.....123

Table 7.2: Kinetic parameters for the pure water (pH 10.66) PLL α-helix-like conformations, the pure α-helix, and the π-helix(bulge) (un)folding. 128

Table 7.3: The pure α-helix and the π-helix(bulge) unfolding and folding time for an alanine peptide and PLL at different final temperatures. 131

Table 7.4: The PLL pure α-helix folding and unfolding time. 131

Table 7.5: The PLL (un)folding activation energies..... 132

Table 8.1: The measured total differential Raman cross sections for valeramide (mbarn•molecule^{-1}•sr $^{-1}$) at 22 ^{o}C 153

Table 8.2: The measured AmI, AmII, rNH_2^1 and rNH_2^2 frequencies of valeramide. 154

Table 9.1: Total differential Raman cross sections of $\delta_{H\text{-}O\text{-}H}$ Raman band, σ_A; $\delta_{H\text{-}O\text{-}H}$ of first hydration shell water about the Cl^-, $\sigma_{A\ hyd}$ (numbers underlined) and the ν_e, K_1, and K_2 parameters.....177

Table 9.2: Total differential Raman cross sections of $\nu_{O\text{-}H}$ Raman band, σ_B and the ν_e, K_1, and K_2 parameters. 178

Table D1. Comparison of theoretical and experimental[2] chemical shifts for the wild-type p53 peptide.....197

Table D2. Comparison of theoretical and experimental[2] chemical shifts for the P27S mutant p53 peptide. 198

Table D3. Comparison of theoretical and experimental[2] $^3J_{\alpha N}$ coupling constants for the wild-type p53 peptide. 198

Table D4. Comparison of theoretical and experimental[2] $^3J_{\alpha N}$ coupling constants for the P27S mutant p53 peptide..... 198

LIST OF FIGURES

Figure 1.1: Definition of dihedral angles - Φ and Ψ. 2

Figure 1.2 Ramachandran Plot. 3

Figure 1.3: Common helix structures. 4

Figure 1.4: Various types of free energy landscapes. 11

Figure 2.1: Diagram of Stokes Raman scattering, Rayleigh scattering and anti-Stokes Raman scattering. 20

Figure 2.2: Polarizability variations in the neighborhood of the equilibrium position and vibrational Raman activity for a linear ABA molecule. 22

Figure 2.3: Different types of Raman scattering processes. 25

Figure 2.4: Potential energy curves (with the same shape) and Frank-Condon overlaps. 27

Figure 2.5: (A) Electronic energy levels and electronic transitions of a peptide bond. (B) Absorption spectra of α-helix, β-sheet and random coil. 29

Figure 2.6: Temperature dependence of the 204 nm excited UVRR spectra of poly-L-glutamic acid at low pH. Also shown are the vibration modes. 30

Figure 2.7: Relative orientations of N-H and C_α-H bonds in the polyproline II and α-helix conformations. 31

Figure 3.1: Temperature dependence of the CD spectra of AP in pure water at pH 7 38

Figure 3.2: Θ_{222} melting curve of AP in a. $NaClO_4$ at different ionic strengths. b. in NaCl at different ionic strengths. c. in Na_2SO_4 at various ionic strength. 38

Figure 3.3: Calculated T_m of AP α-helix melting in different salts. 41

Figure 3.4: Temperature dependence of 204 nm excited UVRR spectra of AP in pure water..... 42

Figure 3.5: Non-PPII (primarily α-+3_{10}+π-helix) fractions of AP in different salt solutions..... 42

Figure 3.6: Temperature dependence of calculated α-helix-like spectra in 0.2 M $NaClO_4$, and difference spectra between different salt solutions: Red, 0.2 M NaCl minus 0.2 M $NaClO_4$; Green, 0.0667 M Na_2SO_4 minus 0.2 M $NaClO_4$; Blue, pure water minus 0.2 M $NaClO_4$. All displayed calculated α-helix-like spectra were normalized to the intensity of the $AmIII_1$ band of the 2.4 ^oC α-helix-like spectrum in $NaClO_4$. The difference spectra between salts were calculated from these normalized spectra. 43

Figure 3.7: Calculated 2.4 ^oC Gibbs free energy landscape of AP in pure water and in 0.2 M $NaClO_4$. We use the PPII-like conformation as the reference state..... 45

Figure 3.8: Calculated Gibbs free energy landscape of AP along the Ramachandran Ψ angle coordinate. The PPII-like conformation is the reference state..... 46

Figure 3.9: Molecular dynamics calculated AP non-PPII fraction in 0.2 M $NaClO_4$ solution and in pure water by REMD simulations. The molecular dynamics predicted AP α-helical conformation melting temperatures are higher than the experimental values because current force fields overstabilize the α-helical conformation [68]. Also, REMD simulations often predict much higher melting temperatures than standard MD simulations because the dynamical information is distorted by the REMD simulation temperature exchange process [69]. 47

Figure 3.10: ClO_4^- occupancy around AP. The green contour shapes represent a higher than normal probability of finding ClO_4^- in a volume element near AP. **b** results from rotating **a** 180

degrees about the helix axis. **c** looking down the helix axis from the N-terminus to the C-terminus..... 48

Figure 3.11: Average radial distribution functions of ClO_4^- with **a** the average ala residue and the terminal $-NH_3^+$ and **b** the different args. r is the distance between the Cl in ClO_4^- and the beta carbon of ala or the nitrogen of the terminal $-NH_3^+$ or the arg zeta carbon. 49

Figure 4.1: Temperature dependence of the CD spectra of 1 mg/ml AP in pure water.....61

Figure 4.2: θ_{222} of AP **(a)** in 25% (v/v) alcohol and **(b)** in 50% (v/v) alcohol; (c) $\Delta\theta_{222}$ (θ_{222} in 50% alcohol minus θ_{222} in 25% alcohol). 62

Figure 4.3: 204 nm excited UVRS of AP in pure water (solid line) and in 50% methanol (dashed line) at 10 ^{0}C. The UVRS of AP in pure water was scaled to facilitate comparison. 63

Figure 4.4: Temperature dependence of 204 nm excited UVRS of AP in 50% methanol and UVRS of AP in pure water at 2 ^{0}C (dashed line); The methanol contribution was subtracted. The UVRS of AP was scaled to facilitate comparison. 64

Figure 4.5: Raman calculated AP α-helical-like fractions (primarily α- and 3_{10} and π-helix (bulge)) of AP in different solutions. 65

Figure 4.6: Calculated α-helix-like spectra of AP in pure water (solid line) and in 50% (v/v) methanol (dashed line). Calculated α-helix-like difference spectra were normalized to the intensity of the $AmIII_1$ band. 65

Figure 4.7: Calculated Gibbs free energy landscape of AP along the Ramachandran Ψ angle coordinate. The PPII-like conformation is the reference state. 67

Figure 4.8: Calculated θ_{222} of AP in pure water and in 50% (v/v) alcohols. 69

Figure 5.1: CD spectra of 1 mg/ml PGA in pure water and in a) 0.2 M, b) 1.0 M and c) 2 M NaCl and KCl at pH 8.3 at 10 ^{o}C.....79

Figure 5.2: a) Temperature dependence of 204 nm excited UVRS of 1 mg/ml PGA in pure water. UVRS of PGA in pure water and in the presence of 2 M NaCl and KCl and their difference spectra: b) at 10 ^{0}C; c) at 30 ^{0}C; d) at 50 ^{0}C; All spectra were normalized to the 1450 cm^{-1} band which shows little intensity variation. [15] 81

Figure 5.3: 204 nm excited UVRS of sodium acetate (NaAc) and potassium acetate (KAc) and in the presence of 4 M NaCl and 4 M KCl at 10 ^{0}C: a) 0.02 M NaAc + 4 M NaCl; b) 0.02 M KAc + 4 M KCl; c) 0.02 M KAc; d) 0.02 M NaAc. 82

Figure 6.1: Temperature dependence of the CD spectra of a) the p53 wild-type peptide, and b) the mutant peptide. 95

Figure 6.2: Temperature dependence of the 204 nm excited UVRR spectra of the p53 wild-type peptide (top) and the P27S mutant peptide (bottom); contributions from Trp and Phe aromatic rings (Fig. D4) have been removed. 96

Figure 6.3: Ramachandran plots computed from explicit solvent MD simulations for a) the wild-type p53 peptide ensemble and b) the P27S mutant p53 peptide ensemble. A difference plot of b) relative to a) is presented in c). 98

Figure 6.4: Distributions of backbone Ψ angles for the a) wild-type and b) P27S mutant peptides at 30 ^{o}C determined from explicit solvent MD simulations (blue) and UVRR spectroscopy (green). 99

Figure 6.5. 204 nm excited UVRR spectra of Leu26 perdeuterated and non-deuterated p53 a) wild-type peptide, and b) P27S mutant peptide, and their difference spectra (red) at 30 ^{0}C. All spectra were normalized to the intensity of the AmI band. 103

Figure 6.6. 229 nm excited UVRR spectra of the p53 wild-type and P27S mutant peptides. a) 10 °C spectra of the wild-type peptide and difference spectra between the 10 °C spectrum and that

at higher temperature, b) temperature difference spectra of the mutant peptide; c) difference spectra between wild-type and mutant peptides. All spectra were normalized to the peak height of the 932 cm^{-1} ClO_4^- band..... 106

Figure 7.1: a) Temperature dependence of the 204 nm excited UVRR spectra of 1 mg/ml PLL in 0.5 M $NaClO_4$ at pH 10.65. All spectra were normalized to the 932 cm^{-1} ClO_4^- peak height. b) Calculated fractions of α-helix-like conformations of PLL in 0.5 M $NaClO_4$ and in pure water at pH 10.65.....117

Figure 7.2 T-jump difference UVRR spectra of PLL in 0.5 M $NaClO_4$ (pH 10.66) at different delay times between the pump and probe laser pulses. a) Difference spectra for a 10 to 40 ^oC T-jump. b) Difference spectra for a 20 to 48 ^oC T-jump.. 118

Figure 7.3: Ramanchandran Ψ probability distributions for PLL at 10 ^oC and 20 ^oC in 0.5 M $NaClO_4$ (pH 10.66). Delay time dependent difference Ramachandran Ψ probability distributions for PLL in 0.5 M $NaClO_4$ (pH 10.66).. 119

Figure 7.4: Delay time dependent fractions of turn conformations of PLL in 0.5 M $NaClO_4$ at pH 10.66..... 120

Figure 7.5. T-jump relaxation of the 0.5 M $NaClO_4$ (pH 10.66) (a) integrated C_α-H band intensities, (b) the α-helix-like concentrations, (c) the pure α-helix concentrations, and (d) the π-helix (bulge) concentrations of PLL.. 122

Figure 7.6: T-jump difference UVRR spectra of PLL in pure water at pH 10.66 at different delay times between the pump and probe laser pulses. a) Difference spectra for a T-jump from 10 to 44 ^oC. b) Difference spectra for a T-jump from 20 to 54 ^oC. 124

Figure 7.7: Ramanchandran Ψ probability distributions for PLL at 10 ^{o}C and 20 ^{o}C in pure water (pH 10.66). Delay time dependent difference Ramachandran Ψ probability distributions for PLL in pure water (pH 10.66). 126

Figure 7.8: Delay time dependent fractions of T1 and T2 turn conformations of PLL in pure water (pH 10.66). 126

Figure 7.9: T-jump relaxation of the pure water (pH 10.66) (a) integrated C_{α}-H band intensities, (b) the α-helix-like concentrations, (c) the pure α-helix concentrations, and (d) the π-helix(bulge) concentrations of PLL.. 127

Figure 7.10: Two state reaction coordinate for the 0.5 M $NaClO_4$ PLL pure α-helix (un)folding at 40 ^{o}C and 48 ^{o}C (pH 10.66).. 134

Figure 7.11: Two-state reaction coordinate for the PLL π-helix(bulge) (un)folding in 0.5 M $NaClO_4$ at 40 ^{o}C and 48 ^{o}C (pH 10.66)..... 134

Figure 7.12: Two-state reaction coordinate for the PLL π-helix(bulge) (un)folding in pure water at 44 ^{o}C and 54 ^{o}C (pH 10.66).. 135

Figure 7.13: Calculated projection of the Gibbs free energy landscapes for PLL in 0.5 M $NaClO_4$ at pH 10.66, along the Ramachandran Ψ-angle coordinate. PPII is the reference state. 136

Figure 7.14: Calculated projection of the Gibbs free energy landscapes for PLL in pure water at pH 10.66, along the Ramachandran Ψ-angle coordinate. PPII is the reference state. 138

Figure 7.15: Multi-state reaction coordinate for the 0.5 M $NaClO_4$ (pH 10.66) PLL π-helix (bulge) and pure α-helix unfolding and folding at 40 ^{o}C and 48 ^{o}C. 139

Figure 7.16: Multi-state reaction coordinate for the pure water (pH 10.66) PLL π-helix (bulge) and pure α-helix unfolding and folding at 44 ^{o}C and 54 ^{o}C..... 139

Figure 8.1: Temperature dependence of the 204 nm excited UVRR spectra of valeramide in water at 22 ^{o}C (Black) and 65 ^{o}C (Red).....150

Figure 8.2: The 204 nm excited UVRR spectra of valeramide at 22 ^{o}C: Black in water; Red in pure acetonitrile. Solvent contributions were removed. 151

Figure 8.3: The 204 nm excited UVRR spectra of valeramide solid (Red) and in water (Black) at 22 ^{o}C. Water contributions were removed. The intensities were normalized to the AmIII+δCH_2 peak height. 152

Figure 8.4. CD spectra of 1 mg/ml DQ10 (solid line) and NDQ10 (dashed line) in pure water at 22 ^{o}C. Measured by using a 0.02 cm path length cuvette. 155

Figure 8.5. The 204 nm excited UVRR spectra of the DQ10 (black) and NDQ10 (red) in pure water at 22 ^{o}C. 156

Figure 8.6. Calculated Ψ-angle distributions for the NDQ10 and DQ10 in pure water at 22 ^{o}C. 157

Figure 8.7. The 198 (blue) and 204 nm (black) excited UVRR spectra of the NDQ10 in pure water at 22 ^{o}C, and the difference spectrum between them (red). 158

Figure 8.8. The difference spectra between the 198 and 204 nm excited UVRR spectra of the NDQ10 (red) and DQ10 (black) in pure water at 22 ^{o}C. The 204 nm excited UVRR spectrum of glutamine in pure water at pH 1.6 at 22 ^{o}C (blue). 159

Figure 8.9. The 204 nm excited UVRR spectra of the NDQ10 solid (black) and solution (red), DQ10 solid (blue) and solution (green) at 22 ^{o}C.. 161

Figure 8.10. Powder x ray diffraction of NDQ10 solid. The sample was prepared by slowly evaporating NDQ10 solution on a glass slide over ~ 2 days. 161

Figure 8.11: Proposed structures of NDQ10 and DQ10.. 162

Figure 8.12. Electron micrograph of NDQ10 fibrils in pure water after incubation at 60 ^{o} C for ~ 2 days. 163

Figure 9.1: 204 nm excited UVRS of pure water (solid line) and in the presence of 2 M KCl (dashed line) or 2 M KF (dotted line) at 20 ^{o} C; $\delta_{H\text{-}O\text{-}H}$ and $\nu_{O\text{-}H}$ indicate the O-H bending band and O-H stretching band.....172

Figure 9.2: Dependence of the $\delta_{H\text{-}O\text{-}H}$ Raman cross sections (λ_{ex}=204 nm), σ_{exp} (relative to that of pure water, σ_{bulk}) on the ratio of Cl^- to water, $N_{Cl^-/w}$ 174

Figure 9.3: Total differential Raman cross section excitation profile of the 1660 cm^{-1} H_2O $\delta_{H\text{-}O\text{-}H}$ band..... 175

Figure 9.4: Total differential Raman cross section excitation profile of the 3400 cm^{-1} H_2O $\nu_{O\text{-}H}$ band..... 177

Figure B1: $f_{\alpha CD}$ vs. $f_{\alpha Raman}$ of AP.....184

Figure B 2: Linear fit of previously measured θ_{222} and $f_{\alpha Raman}$ of AP in pure water.[9] 186

Figure C1: CD spectra of 1 mg/ml PGA in pure water and in a) 0.2 M, b) 1.0 M and c) 2 M NaCl and KCl at pH 8.3 at 30 ^{o}C.....188

Figure C2: CD spectra of 1 mg/ml PGA in pure water and in a) 0.2 M, b) 1.0 M and c) 2 M NaCl and KCl at pH 8.3 at 50 ^{o}C.. 189

Figure D1: Deconvolution of 204 nm UVRR spectrum of the wild-type peptide at 30 ^{0}C.....191

Figure D2: Deconvolution of the $AmIII_3$ region of the wild-type peptide into the sum of 3 Gaussians. 191

Figure D3. Deconvolution of AmIII region of calculated helical spectra of the mutant peptide into a sum of 5 Gaussian bands..... 194

Figure D4. 204 nm excited UVRR spectra of the p53 wild-type peptide, the mutant peptide, tryptophan and phenylalanine at 30^0C. 194

Figure D5. Convergence of simulation ensembles by Ramachandran analysis. 195

Figure D6. Markovian behavior of the kinetic clustering of wild-type peptide configurations is demonstrated by the invariance of the "implied timescales" (related to the eigenvalues of the transition matrix) beyond a certain timescale (the Markov time of the system). Both the implied timescales of the microstate transition matrix (red circles) and those of the macrostate transition matrix (blue squares) are nearly constant after 50 ns. 196

Figure D7. 204 nm UVRR difference spectra for the PPII (red) and α-helical conformations (blue) between hydrogenated (C_α-H) versus deuterated (C_α-D) of a mainly polyalanine peptide. 197

Figure E1: a) 204 nm excited water stretching bands at 10 ^{o}C and the difference spectra between higher temperatures and 10 ^{o}C. b) T-jump calibration curve which relates the magnitude of water stretching band spectral shift to the temperature change.....200

Figure E2. 204 nm excited water stretching bands of 5 mg/ml PLL in 0.5 M $NaClO_4$ (and 0.015 M NaBr) with (red) and without (black) IR pulses at 10 ^{o}C, and the difference spectrum (blue). The temperature jump is 30 ^{o}C. 200

Figure E3. 204 nm excited water stretching bands of 5 mg/ml PLL in 0.5 M $NaClO_4$ (and 0.015 M NaBr) with (red) and without (black) IR pulses at 20 ^{o}C, and the difference spectrum (blue). The temperature jump is 28 ^{o}C. 201

Figure E4: 204 nm excited water stretching bands of 15 mg/ml PLL in pure water with (red) and without (black) IR pulses at 10 ^{o}C, and the difference spectrum (blue). The temperature jump is 34 ^{o}C..... 201

Figure E5: 204 nm excited water stretching bands of 15 mg/ml PLL in pure water with (red) and without (black) IR pulses at 20 ^{o}C, and the difference spectrum (blue). The temperature jump is 34 ^{o}C..... 202

Figure E6: Molar absorptivity of NaBr in pure water..... 202

Figure E7: Temperature dependence of 204 nm excited UVRR spectra of 1 mg/ml PLL in pure water at pH 10.65. The intensities were normalized to the isosbestic point at 1235cm^{-1}. 203

Figure F1: Deconvolution of 204 nm UVRR spectrum of the NDQ10 in pure water at 22 ^{0}C.....205

Figure F2. Deconvolution of 204 nm UVRR spectrum of the DQ10 at 22 ^{0}C.. 205

Figure F3. CD spectra of 1 mg/ml NDQ10 (black) and DQ10 in pure water at 22 ^{o}C..... 207

PREFACE

I would like to express my sincerest gratitude to my advisor Prof. Sanford Asher. I am exceptionally grateful for his wisdom and patience. Throughout my graduate career, he has provided invaluable guidance and encouragement to overcome the enormous obstacles that occasionally occurred on the path to success. From him, I learned the true value of independent work, critical thinking, and values that have allowed me become a better scientist.

I would like to thank Mrs. Sharon Mansfield for everything she did to make my life at Pitt easier and happier.

I also would like to thank my colleagues, past and present for all their help during these years. Special thanks to Dr. Zeeshan Ahmed and Dr. Sergei V Bykov who provided so much needed assistance with instrumentation and life in general.

I would like to thank Mr. Tom Gasmire and Mr. Jeff Sicher at machine shop for making hardware needed for the experiments, and Mr. Jim Mcnerney at electronics shop for his efforts in repairing YAG lasers.

I would like to thank Prof. Youcheng Liu, Mr. Hongju Gu and Dr. Guifu Zhou at the University of Science and Technology of China for guidance and help through college.

Lastly and most importantly, my family, for their unconditional love and support through all of my days.

1.0 PROTEIN FOLDING

Protein folding is one of the most important unsolved problems in biology.[1-7] Protein folding research has been searching for answers to two important questions: (1) how does a protein's amino acid sequence dictate its 3D structure following Anfinsen's hypothesis [8] (in 1961) that protein folding information is encoded in the amino acid sequence? (2) how does a protein fold from its denatured state to its native state within a reasonable time? The well-known Levinthal Paradox [9] demonstrated that if a protein were to attain its correctly folded configuration by sequentially checking all the possible conformations, it would take longer than the age of our universe. However, most small proteins fold spontaneously on a millisecond or even microsecond time scale.

Despite extensive studies over the past 50 years, the mechanism(s) by which proteins fold into their native states is still poorly understood.[1,2,4,5,10,11] In general, it is still impossible to predict protein 3D structures from the amino acid sequences unless these sequences have been previously observed in proteins with known structures. Understanding protein folding is important as many diseases (e.g. Alzheimer disease, Parkinson disease, etc) are caused by protein unfolding, protein misfolding and protein aggregation.[12,13] Understanding molecular mechanism(s) of these diseases can facilitate drug design to treat diseases.

1.1 PROTEIN STRUCTURE

From bottom-up approach, protein structure can be interpreted from four levels: (1) *Primary structure:* Primary structure is the covalent connection of amino acids in order. (2) *Secondary structure*: Secondary structure refers to the 3D form of local segments, which is defined by

hydrogen bonding patterns of backbone amides. A less formal but quite useful way to define secondary structure is by the dihedral angles - Φ and Ψ. (3) *Tertiary structure:* Tertiary structure is the packing of secondary structures into 3D structure on one polypeptide chain. (4) *Quaternary structure:* Quaternary structure involves the assembly of multiple tertiary structures.

Intrinsically disordered proteins (IDPs): IDPs are proteins which completely or, in part, lack well defined secondary structures[14], comprise at least a third of some eukaryotic genomes.[15] These proteins lack specific tertiary structures, and often involve heterogeneous ensembles of conformations. Many of these IDPs are involved in cell signaling and cell cycle control, such as transcription and translation regulation. [16]

1.1.1 Dihedral angles

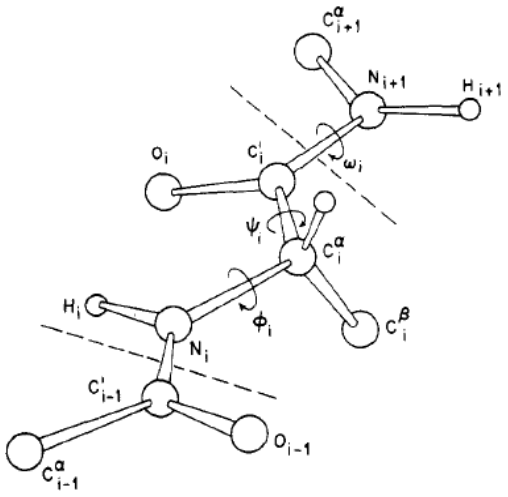

Figure 1.1: Definition of dihedral angles - Φ and Ψ. Reproduced from Rackovsky et al.[17]

The peptide bond (O)C-N has double bond character from its resonance structure, and thus can not rotate freely. The six atoms: C_{α}^{i}, C^{i}, O^{i}, N^{i+1}, H^{i+1} and C_{α}^{i+1} are more or less in the same plane. The peptide chain gains freedom by rotating along N-C_{α} bonds and C_{α}-C bonds. The Φ-angle is defined as the dihedral angle between HNC_{α} plane and $NC_{\alpha}C$ plane while rotating along

N-C_α bond, while the Ψ-angle is the dihedral angle between $NC_\alpha C$ plane and $C_\alpha CO$ plane while rotating along C_α-C bond. The Φ and Ψ angles in Figure 1.1 are both 180°. Protein secondary structure is defined by pairs of Φ and Ψ angles.

1.1.2 Ramachandran plot

The Ramachandran plot maps the sterically allowed regions of Φ and Ψ combinations based on hard sphere model.[18]

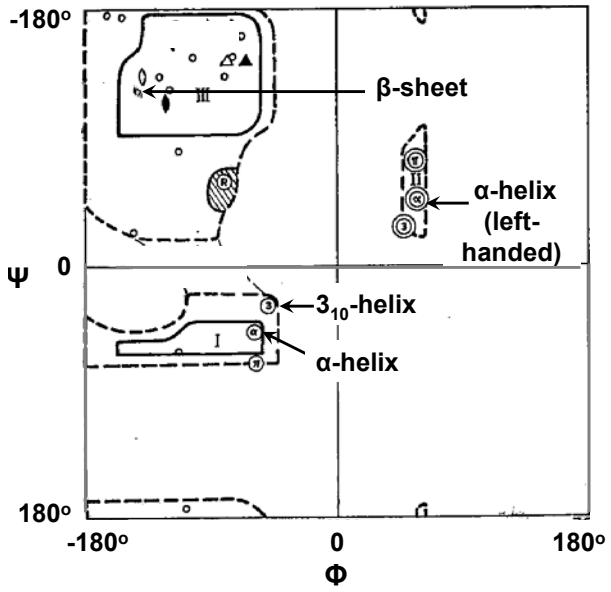

Figure 1.2 Ramachandran Plot. Reproduced from Ramachandran et al. [18]

The solid line regions correspond to allowed conformations, for example: the α-helical conformations and β-sheet conformations where there are no steric clashes. The dashed line areas show the allowed regions if the atoms are allowed to come slightly closer than the sum of their van der Waals radii. This brings out an additional region which corresponds to the left-handed α-helix. Other areas in Fig. 1.2 correspond to conformations where atoms in the polypeptide come

closer than the sum of their van der Waals radii, and thus are sterically disallowed. The Fig. 1.2 Ramachandran plot is right for most amino acids other than glycine which is unique in that it lacks a side chain and thus it can adopt Φ and Ψ angles in all four quadrants of Ramachandran plot, and other than proline whose side chain imposes extra constraints on Φ-angle.[18] For asparagine, aspartate, glutamine, glutamate and arginine whose side chains can hydrogen bond to the backbone, otherwise disallowed conformations in Fig. 1.2 can be stabilized.[18]

1.1.3 Common helix structures

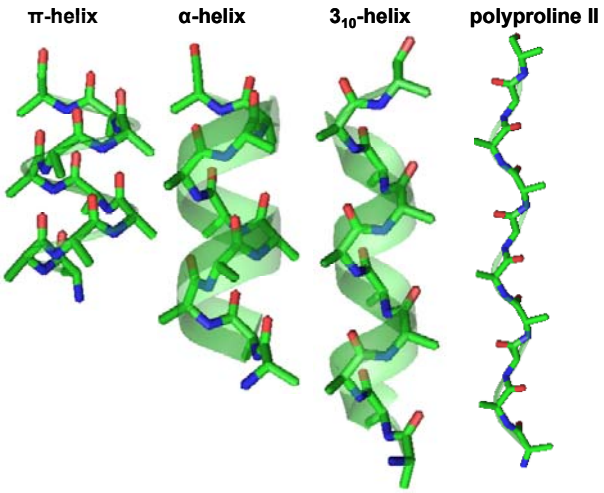

Figure 1.3: Common helix structures.

The α-helix: The α-helix is a right-handed coiled structure, in which every *i* th backbone N –H group donates a hydrogen bond to the *i-4* th backbone C=O group. The Φ and Ψ angles of the α-helix are -57 ^{o} and -47 ^{o}, respectively. One reason why the α-helix is so stable is that the backbone NH and CO groups are naturally pointed toward each other for hydrogen bond formation. There are several other important factors affecting the α-helix stability.

(1). Helix propensity of amino acid: The host-guest experiments indicated [19] that different amino acids have different propensities to form α-helix, for example: alanine is known

to have the highest helix forming propensity due to its small relative entropy loss of the side chain upon helix formation.

(2). Helix dipole moment – charge interaction: Addition of individual dipoles of carbonyls produces a large helix dipole moment along helix axial pointing from the N-terminal to C-terminal. Thus, positive/negative charge at N-terminal destabilizes/stabilizes the α-helix, while positive/negative charge at C-terminal stabilizes/destabilizes the α-helix.[20,21]

(3). Terminal cap: Terminal cap usually stabilizes the α-helix by removing terminal charge, thus removing unfavorable terminal charge-helix dipole moment interaction. N-terminal cap can possibly form an additional hydrogen bond to the backbone, which further stabilizes the α-helix.

(4). Ionic strength: Ions screen electrostatic interactions and thus impact the α-helix stability.

(5). Non-covalent side-chain interactions: Ion pair and salt bridge formation between oppositely charged side chains can stabilize the α-helix, while electrostatic repulsion between like-charged side chains destabilizes the α-helix.

(6). Trifluoroethanol (TFE)/dehydration: TFE dehydrates the peptide backbone, enhancing intramolecular hydrogen bonding and thus stabilizing the α-helix.[22] Recently, it was proposed that long side chains shield the backbone from the solvent, resulting in increased α-helix stability.[23,24]

The 3_{10}-helix: The 3_{10}-helix is a right-handed coiled structure, with the i^{th} backbone N-H group forming a hydrogen bond with the $i-3^{th}$ backbone C = O group. The Φ and Ψ angles of the 3_{10}-helix are -74^{o} and -4^{o}, respectively. The 3_{10}-helix is much less abundant than the α-helix because its hydrogen bonds are tilted and less stable than those of the α-helix. The 3_{10}-helix has

been known to occur at the C-terminal of helical peptides [25] and been proposed as an intermediate during α-helix unfolding. [26,27]

The π-helix: The amino acids in a standard π-helix are arranged in a right-handed helical structure, with the i^{th} backbone N-H group forming a hydrogen bond with the $i\text{-}5^{th}$ backbone C=O group. The Φ and Ψ angles of the π -helix are -57^{o} and -70^{o}, respectively. The π-helix is extremely rare in nature due to three reasons: its dihedral angles are energetically unfavorable relative to the α-helix, its 3D structure has a 1 Å hole down the center that is too narrow for access by a water molecule, resulting in the loss of van der Waals interactions, and a higher number of residues (four) must be correctly oriented before the first *i*, *i+5* hydrogen bond can form. The π-helix also has been proposed as an intermediate during α-helix unfolding.[28,29]

PolyProline II helix (PPII): The left-handed PPII is formed when sequential residues adopt Φ and Ψ angles of ~ -75° and ~150°, respectively. There is no intramolecular hydrogen bond; instead, carbonyls and amines form hydrogen bonds with water. The PPII-like conformation has been proposed as the unfolded conformation of many proteins and peptides. [30-35]

1.2 PROTEIN STABILITY

Under physiological conditions, the folded protein is only marginally more stable than the unfolded forms, with ΔG of folding ranging from -20 to -60 kJ/mol.[36] This small net conformational stability results from stabilizing contributions of hydrophobic effect and hydrogen bonding, and to a much less extent from favorable electrostatic interaction contribution (e.g. ion pairs, etc). The major destabilizing source is the conformational entropy.

1.2.1 Conformational entropy

Each residue in a protein can exist in a number of conformations because of rotation allowed along the Ramachandran Φ and Ψ coordinates, and rotation along the bonds of side chains. Even if a residue could only exist in two conformations, it would mean that a 100-residue protein could adopt over 10^{30} conformations. Thus, it is almost impossible that a protein would adopt a specific conformation due to the huge loss of conformational entropy. Both theory and experiment estimate that at 25 ^{0}C, the contribution of conformational entropy to ΔG is ~7 kJ/mol per residue.[37] Thus, for a 100-residue protein, there will be an unfavorable contribution of 700 kJ/mol that must be overcome by stabilizing contributions when the protein folds.

1.2.2 Hydrophobic interaction

"Hydrophobic interaction", the concept which is elusive by itself describes the phenomenon that apolar side-chain moieties of amino acids prefer to reside in an apolar non-aqueous environment, and therefore they tend to gather together to form a cluster of apolar groups.[38] Hydrophobic interaction is a major driving force for protein folding.

Several models were proposed to explain hydrophobic effect. In 1945, Frank and Evans proposed the "iceberg model" [39] in which water molecules build a microscopic "clathrate" around non-polar molecules and discussed the entropic ramifications of this "freezing", for example: larger non-polar molecules will "freeze" more water molecules and induce larger entropy loss, and therefore are less soluble. Another interesting attempt to explain thermodynamics data of apolar compound solvation in water is the scaled particle theory

(SPT)[40,41]. SPT assumes that the solvation proceeds by two steps. The first step is the creation of a cavity in the solvent which has the appropriate size to accommodate the solute particle. The second step is the introduction of a solute molecule into the cavity. The Gibbs energies of these two processes are generally referred to as G_c and G_i, respectively. An essential feature of SPT is that the creation of a cavity in a liquid to accommodate a solute particle requires exclusion of solvent particles. This process requires a large amount of work in water due to the particularly small size of water molecules. The rather unfavorable G_c in water explains the low solubility of apolar solute in water.

Several major steps toward quantifying the hydrophobic interaction were taken. In 1959, Kauzmann proposed a solvent transfer model[42] suggesting that the free energy change for burying a non-polar side chain inside the interior of a protein can be estimated by experiments in which a model compound is partitioned between water and a non-aqueous solvent: $\Delta G^0 = -RT \ln \chi$, where χ is the solubility (mole fraction) of a non-polar side chain in water. The estimated free energy change for burying non-polar side chain inside proteins ranges from -8 – -25 kJ/mol per side chain.[42] In the early 1970s, it was realized that transfer free energy is likely to be proportional to the water accessible surface area of a nonpolar solute. [43-45] The transfer free energy is given by: $\Delta G = k \cdot [(ASA)_N - (ASA)_U]$, where ASA is defined as the water accessible surface area.

1.2.3 Hydrogen bonding

The carbonyl (C=O) hydrogen bonding to H-N is primarily responsible for stabilizing secondary structures such as the α-helix and β-pleated sheet structures. In water where dielectric constant is

high, ΔG of forming a hydrogen bond is only ~ -4 kJ/mol, while ΔG is ~ -20 kJ/mol in a nonpolar medium. Proteins are stabilized by ~ 4 - 8 kJ/mol by the formation of a buried intramolecular hydrogen bond. [36]

1.2.4 Electrostatic interactions

Electrostatic interactions make little or no contribution to protein stability. The electrostatic interaction on the surface of a protein is weak due to the high dielectric constant of water; in protein interior, electrostatic contribution is little due to the significant cost of desolvating charged groups.[46,47]

1.3 PROTEIN FOLDING MECHANISM

1.3.1 Classical protein folding mechanism

The framework model[48] and related diffusion-collision model[49] propose that local secondary structures form first as a scaffold, followed by docking of the pre-formed secondary structure unites to yield the native, folded protein. The framework model gained support from studies on small, relatively stable, helical peptides.[50,51] In the absence of tertiary contacts, these peptides form stable secondary structures that might represent the starting point for folding.

The hydrophobic collapse model [52] proposes that hydrophobic collapse drives the compaction of the protein so that folding can take place in a confined volume, thereby narrowing the conformational search to the native state. Support for the hydrophobic collapse model came from

early studies showing that hydrophobic driving force from burying nonpolar surfaces is substantial.[53]

The nucleation-condensation model [54] claims certain local structure forms first as nucleus, and then globule structures condense around to form native conformation. It's a unifying version of the framework model and the hydrophobic collapse model. The nucleation-condensation model resulted from two events in the early 1990s: (1) the discovery that protein could fold by simple two-state process [55]; and (2) Φ-values analysis of the transition state, which showed that secondary structure and tertiary structure are formed in parallel as chymotrypsin inhibitor 2 undergoes a general collapse [56]. The former two models can be treated as two extremes. In the framework model, secondary structure is sufficiently stable without tertiary contacts, while in the hydrophobic collapse model the intrinsic preference for secondary structure is weak and the transition state formation requires tertiary contacts.

1.3.2 Energy landscape theory

Traditionally, it has been thought that protein folds from a single unfolded conformation to a single folded conformation by following a single folding pathway. However, the energy landscape theory suggests [4,10,57,58] that the denatured state is an ensemble of many unfolded conformations, where each unfolded conformation folds to the final state by following its own pathway. This new view resulted from advances in both experiment and theory.[57] The main experimental advances have been those that give faster and more detailed structural information, down to the atomic level. Theoretical modeling recognizes that the macroscopic denatured state and transition state or intermediate state are really ensembles of individual chain conformations.

This revolutionary view can be best visualized by free energy funnels as shown below:

Fig. 1.4a shows a "golf-course" like landscape where it is flat everywhere except for a deep well at one point indicating the native state. Thus, each unfolded conformation randomly searches on the "golf-course" for one native state, which can take infinitely long time. The "golf-course" landscape helps visualize the Levinthal paradox.

Fig. 1.4b shows a very smooth landscape where unfolded conformations can ski down the mountainside toward the native state very fast without any barriers, appearing as a "two-state" process by kinetic experiment.

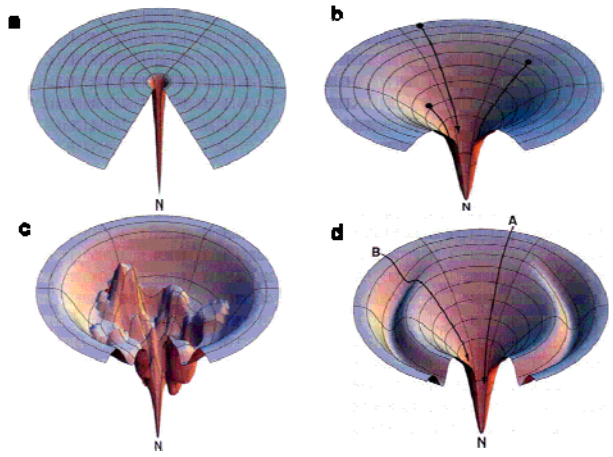

Figure 1.4: Various types of free energy landscapes; Reproduced from Dill et al [57].

Fig. 1.4c shows a rugged landscape where unfolded conformations can be trapped at local minima (transient intermediate) after a fast skiing down the mountainside. The slow process arises from climbing an uphill slope (breaking existing favorable contacts), then reaching a mountain pass, before returning to the next downhill search.

Fig. 1.4d shows a moat landscape where folding can proceed by a two-state A-path or a multi-state B-path.

1.4 TECHNIQUES TO STUDY PROTEIN FOLDING

There are a variety of techniques to study structures and dynamics of proteins during folding events. All these techniques shown below have advantages and limitations, and are complementary to each other. For example: some of these approaches provide ensemble averaged structures, while others provide information on conformational distributions.

1.4.1 X-Ray crystallography

X-Ray crystallography can offer the most detailed information about 3D structures of proteins.[59] Unfortunately, its use requires the preparation of protein crystals. Also, X-Ray crystallography can not obtain the dynamic structural information.

1.4.2 NMR

NMR is another powerful tool to obtain detailed structure information on proteins.[60] However, NMR is only able to probe protein dynamics at relatively long time scales because of its low time resolution.[61] Traditionally, NMR spectroscopy has been limited to relatively small proteins or protein domains. This is in part caused by problems with resolving overlapping peaks in larger proteins.

1.4.3 Circular Dichroism (CD) spectroscopy

CD spectroscopy is one of the most general and basic tools to study protein folding.[62] CD spectroscopy measures the absorption of circularly polarized light. In proteins, structures such as α helicies and β-sheets are chiral, and thus absorb such light. The absorption of this light acts as a

marker of various secondary structures. CD can also be combined with fast-mixing devices, such as stopped flow, to measure protein folding kinetics. The problem of CD is that absorption bands are usually broad, and there is lack of well-defined basis spectra for different secondary structures, making it hard to extract complete information from CD spectra.

1.4.4 Infrared spectroscopy (IR)

The AmI band of IR is most conformational sensitive and widely used to monitor dynamics of secondary structure transitions.[63] While, the AmI region is contaminated by water band which has to be subtracted from the measured spectra. Spectra subtraction will reduce S/N, and decreases the accuracy of quantitative results.

1.4.5 Molecular dynamics (MD) simulation

MD simulation is an important tool for studying protein folding and dynamics in silico.[64] MD simulation can provide microscopic details on protein folding. However, because of high computational cost, MD simulations with explicit water are limited to peptides and very small proteins.[65] MD simulations of larger proteins remain restricted to dynamics of the experimental structure or its high-temperature unfolding. In order to simulate long time folding processes (beyond 1 microsecond), such as folding of small-size proteins (about 50 residues) or larger, approximations or simplifications in protein models need to be introduced. A number of innovative approaches have been applied to generate long MD simulations (approaching the millisecond and beyond),[65,66] such as the use of a specialized computer hard wired for long MD

simulations, called Anton,[67] the use of innovative conformational sampling approaches like Markov state models [68], etc. MD simulation results always need to be compared to experimental results to test the accuracy.

1.4.6 UV Resonance Raman spectroscopy (UVRR)

UVRR is an incisive tool for examining protein folding.[69-75] Protein backbone amide vibrations are very sensitive to the backbone conformations. Amino acid side chain vibrations also report on the side chain conformations (e.g., Trp, Tyr and Phe aromatic ring vibrations monitor the local environments and solvent exposure of the side chains[76,77]; Asn and Gln side chain amide vibrations are sensitive to the hydrogen bonding of side chain amides.) By tuning the excitation wavelength, UVRR allows selective probing of different chromophoric segments of proteins. Isotope labeling also enables monitoring particular peptide bonds.[78] Quantitative methods for the analysis of protein second structure have been developed. Further, recent advances in UVRR allow monitoring of the conformational distributions as well as protein (un)folding energy landscapes along Ψ-coordinate. Dynamic UVRR studies such as T-jump UVRR measurements can probe protein dynamics with nanosecond time resolution. [79-82] The current state-of-the-art UVRR measurements lack sufficient S/N to monitor the conformational changes at the single peptide bond level of a ~ 100 residue protein. [75]

All of these techniques are complementary to each other. UVRR can monitor protein conformational ensembles, while, NMR and X-ray crystallography provide ensemble averaged structures; UVRR can not obtain very detailed structural information as NMR and X-ray crystallography do; NMR and X-ray crystallography lack sufficient temporal resolution; MD

simulations offer a complementary approach, providing extremely high-resolution spatial and temporal data on protein folding processes.

1.5 REFERENCES

(1) Baldwin, R. L.; Rose, G. D. *Trends Biochem Sci* **1999**, *24*, 26-33.

(2) Baldwin, R. L.; Rose, G. D. *Trends Biochem Sci* **1999**, *24*, 77-83.

(3) Dobson, C. M. *Philos. Trans. R. Soc. London Ser. B* **2001**, *356*, 133-145.

(4) Dobson, C. M.; Sali, A.; Karplus, M. *Angew. Chem., Int. Ed.* **1998**, *37*, 868-893.

(5) Jahn, T. R.; Radford, S. E. *Febs Journal* **2005**, *272*, 5962-5970.

(6) Lindberg, M. O.; Oliverberg, M. *Curr. Opin. Struct. Biol.* **2007**, *17*, 21-29.

(7) Daggett, V.; Fersht, A. *Nat. Rev. Mol. Cell Biol.* **2004**, *4*, 497-502.

(8) ANFINSEN CB, H. E., SELA M, WHITE FH Jr. *Proc Natl Acad Sci U S A.* **1961**, *47*, 1309-1314.

(9) C, L. *J Chem Phys* **1968**, *65*, 44-45.

(10) Dill, K. A.; Ozkan, S. B.; Shell, M. S.; Weikl, T. R. *Annu Rev Biophys* **2008**, *37*, 289-316.

(11) Ivarsson, Y.; Travaglini-Allocatelli, C.; Brunori, M.; Gianni, S. *Eur Biophys J Biophys Lett* **2008**, *37*, 721-728.

(12) Dobson, C. M. *Nature* **2002**, *418*, 729-730.

(13) Kelly, J. W. *Nat. Struct. Biol* **2002**, *9*, 323-325.

(14) Fink, A. L. *Curr Op Struct Biol* **2005**, *15*, 35-41.

(15) Dunker, A. K.; Obradovic, Z. *Nat Biotech* **2001**, *19*, 805-806.

(16) Vucetic, S.; Brown, C. J.; Dunker, A. K.; Obradovic, Z. *Proteins: Struct, Func, Genet* **2003**, *52*, 573-584.

(17) Rackovsky, S.; Scheraga, H. A. *Acc Chem Res* **1984**, *17*, 209-214.

(18) Ramachandran, G. N.; Sasisekharan, V. *Conformation of polypeptides and proteins*; Elsevier: New york, 1968; Vol. 23.

(19) Chakrabartty, A.; Kortemme, T.; Baldwin, R. L. *Protein Sci* **1994**, *3*, 843-852.

(20) Hol, W. G. J.; Duijnen, P. T. v.; Berendsen, H. J. C. *Nature* **1978**, *273*, 443-446.

(21) Shoemaker, K. R.; Kim, P. S.; York, E. J.; Stewart, J. M.; Baldwin, R. L. *Nature* **1987**, *326*, 573-567.

(22) Starzyk, A.; Barber-Armstrong, W.; Sridharan, M.; Decatur, S. *Biochemistry* **2005**, *44*, 369-376.

(23) Garcia, A. E.; Sanbonmatsu, K. Y. *PNAS* **2002**, *99*, 2782-2787.

(24) Vila, J. A.; Ripoll, D. R.; Scheraga, H. A. *PNAS* **2000**, *97*, 13075-13079.

(25) Young, W. S.; Brooks, C. L. *J Mol Biol* **1996**, *259*, 560-572.

(26) Millhauser, G. L. *Biochemistry* **1995**, *34*, 3873-3877.

(27) Sheinerman, F. B.; Brooks, C. L. *J Am Chem Soc* **1995**, *117*, 10098-10103.

(28) Chapman, R.; Kulp, J. L.; Patgiri, A.; Kallenbach, N. R.; Bracken, C.; Arora, P. S. *Biochemistry* **2008**, *47*, 4189-4195.

(29) Lee, K. H.; Benson, D. R.; Kuczera, K. *Biochemistry* **2000**, *39*, 13737-13747.

(30) Asher, S. A.; Mikhonin, A. V.; Bykov, S. *J Am Chem Soc* **2004**, *126*, 8433-8440.

(31) Kentsis, A.; Mezei, M.; Gindin, T.; Osman, R. *Proteins: Struct., Funct., Bioinf.* **2004**, *55*, 493-501.

(32) Mezei, M.; Fleming, P.; Srinivasan, R.; Rose, G. *Proteins: Struct., Funct., Bioinf.* **2004**, *55*, 502-507.

(33) Mikhonin, A. V.; Asher, S. A. *J Am Chem Soc* **2006**, *128*, 13789-13795.

(34) Pappu, R.; Rose, G. *Protein Sci* **2002**, *11*, 2437-2455.

(35) Shi, Z.; Olson, C.; Rose, G.; Baldwin, R.; Kallenbach, N. *Proc Natl Acad Sci U S A* **2002**, *99*, 9190-9195.

(36) Pace, C. N.; Grimsley, C. R. In *Handbook of Proteins*; Cox, M. M., George N. Phillips, J., Eds.; John Wiley & Sons Ltd: 2007; Vol. 1, p 162-166.

(37) Pace, C. N.; Grimsley, G. R.; Scholtz, J. M. *eLS* **2009**.

(38) Meyer, E. E.; Rosenberg, K. J.; Israelachvili, J. *Proc. Natl. Acad. Sci. USA* **2006**, *103*, 15739-15746.

(39) Frank, H. S.; Evans, M. W. *J. Chem. Phys.* **1945**, *13*, 507-532.

(40) Blokzijl, W.; Engberts, J. B. F. N. *Angew. Chem., Int. Ed.* **1993**, *32*, 1545-1579.

(41) PIEROTTI, R. A. *Chem Rev* **1976**, *76*, 717-726.

(42) W., K. *Adv Protein Chem.* **1959**, *14*, 1-63.

(43) Chothia, C. *Nature* **1974**, *248*, 339.

(44) Hermann, R. B. *J. Phys. Chem.* **1972**, *76*, 2754-2759.

(45) Jacqueline A. Reynolds, D. B. G., and Charles Tanford *Proc. Natl. Acad. Sci. USA* **1974**, *71*, 2925-2927.

(46) Salari, R.; Chong, L. T. *J Phys Chem Lett* **2010**, *1*, 2844-2848.

(47) Sheinerman, F. B.; Honig, B. *J Mol Biol* **2002**, *318*, 161-177.

(48) Kim, P. S.; Baldwin, R. L. *Annu. Rev. Biochem.* **1982**, *51*, 459-489.

(49) Karplus, M.; Weaver, D. L. *nature* **1976**, *260*, 404-406.

(50) Bierzynski, A.; Kim, P. S.; Baldwin, R. L. *Proc Natl Acad Sci U S A* **1982**, *79*, 2470-2474.

(51) Shoemaker, K. R.; Kim, P. S.; Brems, D. N.; Marqusee, S.; York, E. J.; Chaiken, I. M.; Stewart, J. M.; Baldwin, R. L. *Proc Natl Acad Sci U S A* **1985**, *82*, 2349-2353.

(52) Baldwin, R. L. *Trends Biochem Sci* **1989**, *14*, 291-294.

(53) Kauzmann, W. *Adv Protein Chem* **1959**, *14*, 1-63.

(54) Daggett, V.; Fersht, A. R. *Trends Biochem Sci* **2003**, *28*, 18-25.

(55) Jackson, S. E.; Fersht, A. R. *Biochemistry* **1991**, *30*, 10428-10435.

(56) Otzen, D. E.; Itzhaki, L. S.; Elmasry, N. F.; Jackson, S. E.; Fersht, A. R. *Proc Natl Acad Sci U S A* **1994**, *91*, 10422-10425.

(57) Dill, K. A.; Chan, H. S. *Nat Struct Biol* **1997**, *4*, 10-19.

(58) Dill, K. A. *Protein Sci* **1999**, *8*, 1166-1180.

(59) Dickerson, R. E. *Annu. Rev. Biochem.* **1972**, *41*, 815-842.

(60) Mittermaier, A.; Kay, L. E. *science* **2006**, *312*, 224-228.

(61) Wuthrich, K. *Acta Crystallogr. Sect. D* **1995**, *51*, 249-270.

(62) Sreerama, N.; Woody, R. W. *Circular Dichroism*; 2nd ed., 2000.

(63) Gulotta, M.; Gilmanshin, R.; Buscher, T. C.; Callender, R. H.; Dyer, R. B. *Biochemsitry* **2001**, *40*, 5137-5143.

(64) Hummer, G.; Garcia, A. E.; Grade, S. *Phys. Rev. Lett.* **2000**, *85*, 2637-2640.

(65) Freddolino, P. L.; Harrison, C. B.; Liu, Y.; Schulten, K. *Nat Phys* **2010**, *6*, 751-758.

(66) Schlick, T.; Collepardo-Guevara, R.; Halvorsen, L. A.; Jung, S.; Xiao, X. *Quart Rev Biophys* **2011**, *44*, 191-228.

(67) Shaw, D. E.; Maragakis, P.; Lindorff-Larsen, K.; Piana, S.; Dror, R. O.; Eastwood, M. P.; Bank, J. A.; Jumper, J. M.; Salmon, J. K.; Shan, Y.; Wriggers, W. *Science* **2010**, *330*, 341-6.

(68) Noe, F.; Schutte, C.; Vanden-Eijnden, E.; Reich, L.; Weikl, T. R. *Proc Natl Acad Sci U S A* **2009**, *106*, 19011-6.

(69) Mchale, J. L. *Resonance Raman Spectroscopy*, 2002; Vol. 1.

(70) Asher, S. A. *Annu Rev Phys Chem.* **1988**, *39*, 537-588.

(71) Spiro, T. G.; Grygon, C. A. *J Mole Strut* **1988**, *173*, 79-90.

(72) Tuma, R. *J Raman Spectros* **2005**, *36*, 307-319.

(73) Schweitzer-Stenner, R. *J Raman Spectrosc* **2001**, *32*, 711-732.

(74) Miyazawa, T. *characteristic amide bands and conformations of polypeptides*, 1961.

(75) Asher, S. A.; Oladepo, S. A.; Xiong, K.; Hong, Z. M. *J Phys Chem Lett* **2011**, *2*, 334-344.

(76) Chi, Z. H.; Asher, S. A. *J Phys Chem B* **1998**, *102*, 9595-9602.

(77) Ahmed, Z.; Beta, I. A.; Mikhonin, A. V.; Asher, S. A. *J Am Chem Soc* **2005**, *127*, 10943-10950.

(78) Ianoul, A.; Mikhonin, A.; Lednev, I. K.; Asher, S. A. *J Phys Chem A* **2002**, *106*, 3621-3624.

(79) Lednev, I. K.; Karnoup, A. S.; Sparrow, M. C.; Asher, S. A. *J Am Chem Soc* **1999**, *121*, 8074-8086.

(80) Spiro, T. G.; Huang, C. Y.; Balakrishnan, G. *Biochemistry* **2005**, *44*, 15734-15742.

(81) Spiro, T. G.; Balakrishnan, G.; Hu, Y.; Bender, G. M.; Getahun, Z.; DeGrado, W. F. *J Am Chem Soc* **2007**, *129*, 12801-12808.

(82) Mikhonin, A. V.; Asher, S. A.; Bykov, S. V.; Murza, A. *J Phys Chem B* **2007**, *111*, 3280-3292.

2.0 RAMAN EFFECT

The Raman effect is an inelastic scattering process where the electromagnetic field and the molecule exchange a quantum of energy (Fig. 2.1). The difference in energy between the incident light and scattering light corresponds to the Raman active molecular vibrational energy.

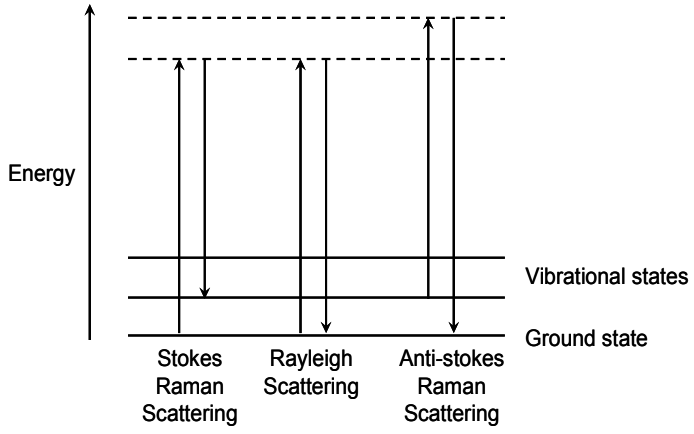

Figure 2.1: Diagram of Stokes Raman scattering, Rayleigh scattering and anti-Stokes Raman scattering.

In contrast, Rayleigh scattering is an elastic scattering process where there is no net energy exchange between the electromagnetic field and the molecule (Fig. 2.1).

2.1 RAMAN THEORY

2.1.1 Classical oscillator model

As light at frequency ν_1 (electromagnetic field) interacts with a molecule, it disturbs the electron cloud distribution of the molecule to induce time dependent dipole moments $P^{(1)}$, $P^{(2)}$, $P^{(3)}$…, and the total time dependent dipole moment P is defined as:

$$P = P^{(1)} + P^{(2)} + P^{(3)} + \ldots \qquad (2.1)$$

$P^{(1)} >> P^{(2)} >> P^{(3)} >> \ldots$. It is often sufficient to just consider the linear induced dipole moment, $P^{(1)}$, thus

$$P = P^{(1)} = \alpha \cdot E \qquad (2.2)$$

α is the polarizability tensor, and E is the incident electric field. Assuming that the molecule is space-fixed in its equilibrium configuration (no rotation) where nuclei may vibrate about the equilibrium positions, α can be expressed with respect to the normal coordinates of vibration, Q_k in a Taylor series:

$$\alpha_{\rho\sigma} = (\alpha_{\rho\sigma})_0 + \sum_k \left(\frac{\partial \alpha_{\rho\sigma}}{\partial Q_k} \right)_0 Q_k + \frac{1}{2} \sum_{k,l} \left(\frac{\partial^2 \alpha_{\rho\sigma}}{\partial Q_k \partial Q_l} \right)_0 Q_k Q_l + \ldots \qquad (2.3)$$

Ignoring terms involving powers of Q higher than the first, we can write:

$$(\alpha_{\rho\sigma})_k = (\alpha_{\rho\sigma})_0 + (\alpha'_{\rho\sigma})_k Q_k \qquad (2.4)$$

$$(\alpha'_{\rho\sigma})_k = \left(\frac{\partial \alpha_{\rho\sigma}}{\partial Q_k} \right)_0 \qquad (2.5)$$

Assuming simple harmonic motion, the time dependence of Q_k is given by

$$Q_k = Q_{k0} \cos(\omega_k t + \delta_k) \qquad (2.6)$$

Substituting eq. 2.6 into eq. 2.4, we obtain:

$$\alpha_k = \alpha_0 + \alpha_k' Q_{k0} \cos(\omega_k t + \delta_k) \qquad (2.7)$$

Introducing the frequency dependence of E,

$$E = E_0 \cdot \cos \omega_1 t \qquad (2.8)$$

Substituting eq. 2.7 and 2.8 into eq. 2.2, we obtain,

$$P^{(1)} = \alpha_0 E_0 \cos \omega_1 t + \frac{1}{2} \alpha_k' E_0 Q_{k0} \cos(\omega_k t + \delta - \omega_1 t) + \frac{1}{2} \alpha_k' E_0 Q_{k0} \cos(\omega_k t + \delta + \omega_1 t) \quad (2.9)$$

Eq. 2.9 can be written as:

$$P^{(1)} = P^{(1)}(\omega_1) + P^{(1)}(\omega_1 - \omega_k) + P^{(1)}(\omega_1 + \omega_k) \quad (2.10)$$

$P^{(1)}(\omega_1)$ indicates Rayleigh scattering, $P^{(1)}(\omega_1-\omega_k)$ indicates Stokes Raman scattering, and $P^{(1)}(\omega_1+\omega_k)$ indicates Anti-stokes Raman scattering.

To be Raman active, at least one component of $(\alpha'_{\rho\sigma})_k$ has to be non-zero, which means that derivatives with respect to Q_k must be non-zero at equilibrium according to eq. 2.5.

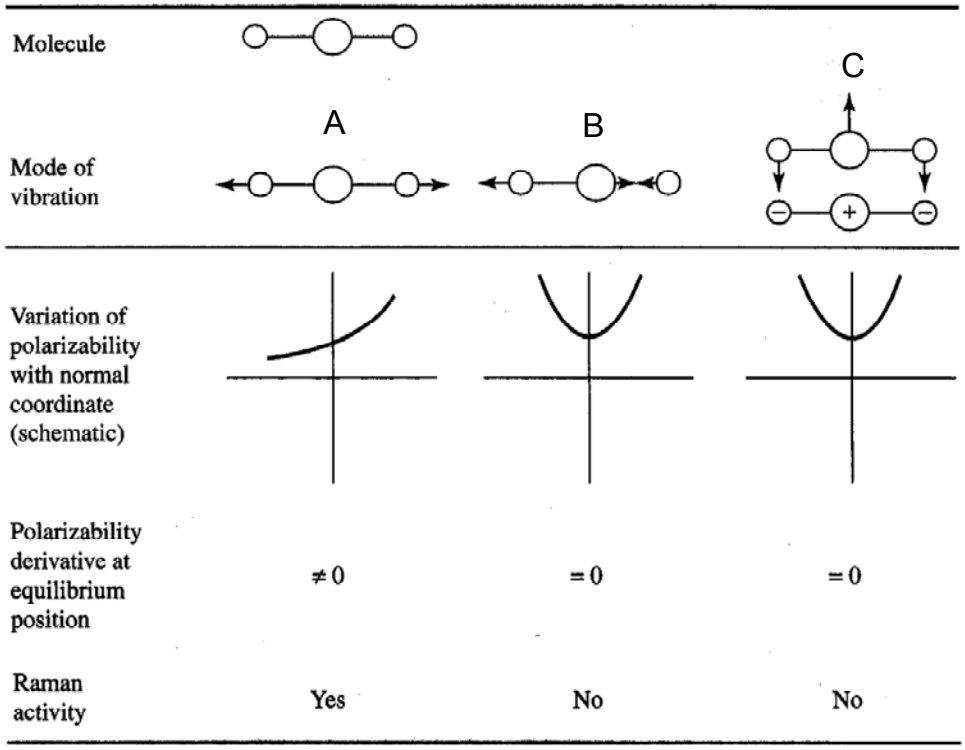

Figure 2.2: Polarizability variations in the neighborhood of the equilibrium position and vibrational Raman activity for a linear ABA molecule. Reproduced from Long [2].

Fig. 2.2 shows polarizability variations of three vibration modes around the equilibrium position. Mode A is Raman active because polarizability derivative at the equilibrium position is non-zero, while modes B and C are not Raman active because polarizability derivatives at equilibrium position are zero.

Limitation of classical model: The classical oscillator model predicts that anti-Stokes Raman scattering occurs at higher frequency $\omega_1+\omega_k$, Rayleigh scattering occurs at frequency ω_1 and stokes Raman scattering occurs at lower frequency $\omega_1-\omega_k$. However, it fails to predict frequency dependence of Raman intensity, for example: Rayleigh scattering is known to be the strongest, stokes Raman scattering is much weaker and anti-stokes scattering further weaker, but the classical model gives the same intensity for all the scatterings. Besides, classical model does not indicate the dependence of Raman intensity on the excitation frequency. These problems can be handled well by quantum mechanical treatment below.

2.1.2 Quantum mechanical treatment

Quantum mechanical treatment treats the interacting molecules in the material system quantum mechanically but continues to treat the electromagnetic radiation classically. The induced electric dipole moment in classical model is replaced by the transition dipole-moment P_{fi} which is associated with a transition from an initial state, i, to a final state, f. P_{fi} is defined as:

$$(P)_{fi} = \left\langle \psi'_f \left| \hat{P} \right| \psi'_i \right\rangle \qquad (2.11)$$

ψ'_f and ψ'_i are the time-dependent perturbed wave functions of the initial and final states, respectively:

$$\psi'_i = \psi_i^{(0)} + \psi_i^{(1)} + \psi_i^{(2)} + \ldots + \psi_i^{(n)} \qquad (2.12)$$

$$\psi'_f = \psi_f^{(0)} + \psi_f^{(1)} + \psi_f^{(2)} + \ldots + \psi_f^{(n)} \qquad (2.13)$$

Substituting eq.2.12 and 2.13 into eq.2.11, and we obtain

$$(P)_{fi} = (P^{(0)})_{fi} + (P^{(1)})_{fi} + (P^{(2)})_{fi} + \ldots \quad (2.14)$$

$$(P^{(0)})_{fi} = \left\langle \psi_f{}^{(0)} \middle| \hat{P} \middle| \psi_i{}^{(0)} \right\rangle \qquad (2.15)$$

$$(P^{(1)})_{fi} = \left\langle \psi_f{}^{(0)} \middle| \hat{P} \middle| \psi_i{}^{(1)} \right\rangle + \left\langle \psi_f{}^{(1)} \middle| \hat{P} \middle| \psi_i{}^{(0)} \right\rangle \qquad (2.16)$$

Ignoring the zero-order (which represents the permanent dipole moment which is independent of incident electric field and does not play a role in light scattering) and higher than 1st order parts, the transition dipole moment is given by:

$$(P)_{fi} = (P^{(1)})_{fi} = \left\langle \psi_f^{(1)} \middle| \hat{P} \middle| \psi_i^{(0)} \right\rangle + \left\langle \psi_f^{(0)} \middle| \hat{P} \middle| \psi_i^{(1)} \right\rangle \quad (2.17)$$

Expanding on the work of Krammers and Heisenberg, Dirac [3] utilized perturbation theory to derive the following expression for the ρ component of the real induced transition electric dipole moment:

$$(p_\rho^{(1)})_{fi} = \frac{1}{2h} \sum_{r \neq i,f} \left\{ \frac{\langle f | \hat{p}_\rho | r \rangle \langle r | \hat{p}_\sigma | i \rangle}{\omega_{ri} - \omega_1 - i\Gamma_r} + \frac{\langle f | \hat{p}_\sigma | r \rangle \langle r | \hat{p}_\rho | i \rangle}{\omega_{ri} + \omega_1 + i\Gamma_r} \right\} \widetilde{E}_{\sigma 0} \exp - i(\omega_1 - \omega_{fi})t$$

+complex conjugate (2.18)

where |r> is the virtual state, which is not an eigen solution of a Schrödinger equation and hence does not correspond to a well-defined energy level of stationary state. Virtual states are described by the time-dependent wavefunctions where the energy and hence the weighted contribution of each state to wavefunctions evolves with time. ω_1 is the excitation energy; ω_{ri} is the difference between the virtual state and the initial state energies; Γ_r is the dampening factor and related to the lifetime τ_r of the virtual state by the uncertainty principle ($\Gamma_r = \hbar/2\tau_r$).

The transition polarizability tensor is defined as:

$$(\alpha_{\rho\sigma})_{fi} = \frac{1}{h} \sum_{r \neq i,f} \left\{ \frac{\langle f | \hat{p}_\rho | r \rangle \langle r | \hat{p}_\sigma | i \rangle}{\omega_{ri} - \omega_1 - i\Gamma_r} + \frac{\langle f | \hat{p}_\sigma | r \rangle \langle r | \hat{p}_\rho | i \rangle}{\omega_{ri} + \omega_1 + i\Gamma_r} \right\} \qquad (2.19)$$

Eq. 2.19 indicates that frequency denominators have huge impact on transition polarizability tensor. Fig. 2.3 shows different types of Raman scattering.

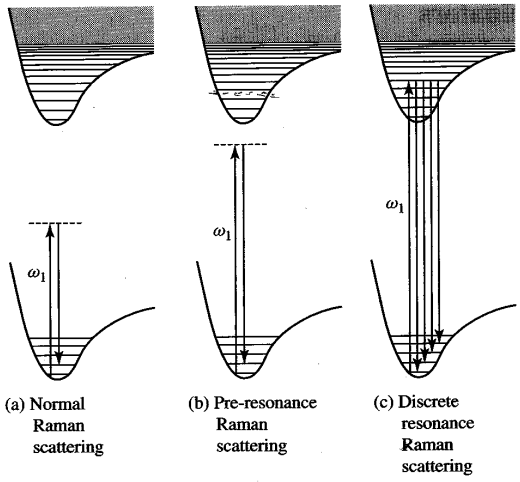

Figure 2.3: Different types of Raman scattering processes. Reproduced from Long [2].

(1) Normal Raman scattering: Normal Raman scattering occurs when $\omega_l << \omega_{ri}$ (excitation wavelength is far away from the first electronic absorption band). $(\alpha_{\rho\sigma})_{fi}$ is determined by a weighted sum over all the states |r>.

(2) Pre-resonance Raman scattering: Pre-resonance Raman scattering occurs when $\omega_l \rightarrow \omega_{ri}$ (excitation wavelength is close to the first electronic absorption band). Virtual states in the first electronic excited state will contribution more to Raman intensities. Thus, $(\alpha_{\rho\sigma})_{fi}$ is determined by a limited number of states.

(3) Resonance Raman scattering: Resonance Raman scattering occurs when $\omega_l \approx \omega_{ri}$ (excitation wavelength is within the first electronic absorption band). The first term of the polarizablity tensor will dominate and virtual states in the first electronic excited state will contribute the most. The Raman intensities will be strong. Resonance Raman scattering can obtain structural information about the excited vibronic and rovibronic states, and their lifetimes.

Selection rules: for $(\alpha_{\rho\sigma})_{fi}$ to be non-zero, the product $\Gamma\psi_f \times \Gamma\rho\sigma \times \Gamma\psi_i$ must belong to a representation which contains the totally symmetric species, i.e., $\Delta v = \pm 1$.

2.2 VIBRATIONAL RESONANCE RAMAN SCATTERING

Vibrational resonance Raman scattering is the scattering process where initial and final states are at the same electronic level but different vibrational levels.

Born-Oppenheimer approximation and perturbation theory are introduced to make the general formula for polarizability tensor more tractable.[2]

After simplification, the polarizability tensor is expressed as:

$$\left(\alpha_{\rho\sigma}\right)_{e^g v^f, e^g v^i} = A + B + C + D \tag{2.20}$$

$$A = \frac{1}{\hbar}(p_\rho)^0_{e^g e^r}(p_\sigma)^0_{e^r e^g}\sum_{v_k^r}\frac{\left\langle v_k^{f(g)}\middle| v_k^{r(r)}\right\rangle\left\langle v_k^{r(r)}\middle| v_k^{i(g)}\right\rangle}{\omega_{e^r v_k^r : e^g v_k^i} - \omega_1 - i\Gamma_{e^r v_k^r}} \tag{2.21}$$

$$\begin{aligned} B = {} & \frac{1}{\hbar^2}(p_\rho)^0_{e^g e^s}\frac{h^k_{e^s e^r}}{\omega_{e^r} - \omega_{e^s}}(p_\rho)^0_{e^r e^g}\sum_{v_k^r}\frac{\left\langle v_k^{f(g)}\middle|Q_k\middle| v_k^{r(r)}\right\rangle\left\langle v_k^{r(r)}\middle| v_k^{i(g)}\right\rangle}{\omega_{e^r v_k^r : e^g v_k^i} - \omega_1 - i\Gamma_{e^r v_k^r}} + \\ & \frac{1}{\hbar^2}(p_\rho)^0_{e^g e^r}\frac{h^k_{e^r e^s}}{\omega_{e^r} - \omega_{e^s}}(p_\sigma)^0_{e^s e^g}\sum_{v_k^r}\frac{\left\langle v_k^{f(g)}\middle| v_k^{r(r)}\right\rangle\left\langle v_k^{r(r)}\middle|Q_k\middle| v_k^{i(g)}\right\rangle}{\omega_{e^r v_k^r : e^g v_k^i} - \omega_1 - i\Gamma_{e^r v_k^r}} \end{aligned} \tag{2.22}$$

$$\begin{aligned} C = {} & \frac{1}{\hbar^2}(p_\rho)^0_{e^t e^r}\frac{h^k_{e^g e^t}}{\omega_{e^g} - \omega_{e^t}}(p_\rho)^0_{e^r e^g}\sum_{v_k^r}\frac{\left\langle v_k^{f(g)}\middle|Q_k\middle| v_k^{r(r)}\right\rangle\left\langle v_k^{r(r)}\middle| v_k^{i(g)}\right\rangle}{\omega_{e^r v_k^r : e^g v_k^i} - \omega_1 - i\Gamma_{e^r v_k^r}} + \\ & \frac{1}{\hbar^2}(p_\rho)^0_{e^g e^r}\frac{h^k_{e^t e^g}}{\omega_{e^g} - \omega_{e^t}}(p_\sigma)^0_{e^s e^g}\sum_{v_k^r}\frac{\left\langle v_k^{f(g)}\middle| v_k^{r(r)}\right\rangle\left\langle v_k^{r(r)}\middle|Q_k\middle| v_k^{i(g)}\right\rangle}{\omega_{e^r v_k^r : e^g v_k^i} - \omega_1 - i\Gamma_{e^r v_k^r}} \end{aligned} \tag{2.23}$$

$$D = \frac{1}{\hbar^2}(p_\rho)^0_{e^g e^s}\frac{h^k_{e^s e^r}h^k_{e^r e^{s'}}}{(\omega_{e^r} - \omega_{e^s})(\omega_{e^r} - \omega_{e^{s'}})}(p_\sigma)^0_{e^{s'} e^g}\sum_{v_k^r, v_{k'}^r}\frac{\left\langle v_k^{f(g)}\middle|Q_k\middle| v_k^{r(r)}\right\rangle\left\langle v_{k'}^{r(r)}\middle|Q_{k'}\middle| v_{k'}^{i(g)}\right\rangle}{\omega_{e^r v_k^r : e^g v_k^i} - \omega_1 - i\Gamma_{e^r v_k^r}} \tag{2.24}$$

A-term is defined by electronic transition moment and Frank-Condon overlaps; B-term involves vibronic coupling of the resonant excited state $|e^r\rangle$ to another excited state $|e^s\rangle$; C-term

involves coupling of the ground electronic state $|e^g\rangle$ to an excited electronic state $|e^t\rangle$; D-term involves coupling of the excited electronic state $|e^r\rangle$ to two other excited electronic states $|e^s\rangle$ and $|e^{s'}\rangle$.

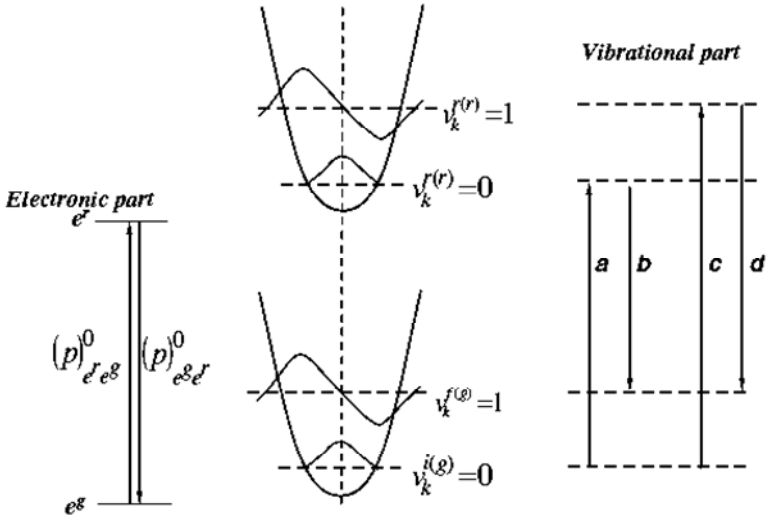

$$(a)\ \left\langle v_k^{r(r)}=0 \middle| v_k^{i(g)}=0 \right\rangle \neq 0 \qquad (b)\ \left\langle v_k^{f(g)}=1 \middle| v_k^{r(r)}=0 \right\rangle = 0$$

$$(c)\ \left\langle v_k^{r(r)}=1 \middle| v_k^{i(g)}=0 \right\rangle = 0 \qquad (d)\ \left\langle v_k^{f(g)}=1 \middle| v_k^{r(r)}=1 \right\rangle \neq 0$$

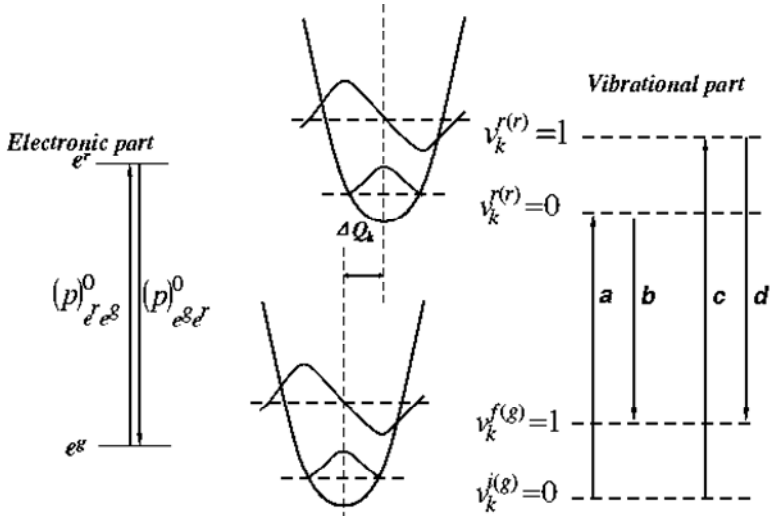

$$(a)\ \left\langle v_k^{r(r)}=0 \middle| v_k^{i(g)}=0 \right\rangle \neq 0 \qquad (b)\ \left\langle v_k^{f(g)}=1 \middle| v_k^{r(r)}=0 \right\rangle \neq 0$$

$$(c)\ \left\langle v_k^{r(r)}=1 \middle| v_k^{i(g)}=0 \right\rangle \neq 0 \qquad (d)\ \left\langle v_k^{f(g)}=1 \middle| v_k^{r(r)}=1 \right\rangle \neq 0$$

Figure 2.4: Potential energy curves (with the same shape) and Frank-Condon overlaps. Reproduced from Long [2]

For strongly electronic dipole allowed transition, for example, $\pi \rightarrow \pi^*$ transition, the A-term is most important.

For A-term Raman activity, two requirements must be met:

1. Electronic transition $|e^r> \rightarrow |e^g>$ must be electric-dipole allowed, e.g. the $\pi \rightarrow \pi^*$ transition of backbone amide is allowed, while the $n \rightarrow \pi^*$ transition is forbidden.
2. The Frank-Condon overlaps are non-zero. Two conditions can occur:
    1) The potential function has different shapes in the ground and excited electronic state.
    2) There is a coordinate displacement in the excited state relative to the ground state (See Fig. 2.4).

Fig. 2.4 shows potential energy curves and Frank-Condon overlaps. In the upper diagram, the potential energy shapes are the same for the ground and excited electronic states, and there is no coordinate displacement. Thus, Frank-Condon overlaps are zero due to orthogonality of the vibrational wavefunctions, and the vibration is not Raman active. While in the lower case, there is coordinate displacement, Frank-Condon overlaps are non-zero, and the vibration is Raman active.

2.3 PROTEINS/PEPTIDES UV RESONANCE RAMAN SPECTRA

2.3.1 Electronic transitions of peptide bond

Fig. 2.5 A shows electronic orbital energy levels and four electronic transitions of a peptide bond in the UV range. $\sigma \rightarrow \pi^*$ (at 165 nm) and $n \rightarrow \sigma^*$ (at 160 nm) transitions both occur in the

vacuum UV range. $\pi \rightarrow \pi^*$ transition (at 190 nm) is strong and easily monitored by experiments, and $n \rightarrow \pi^*$ transition (at 210 nm) is dipole forbidden and weak. Fig. 2.5 B shows UV absorption spectra of the α-helix, the β-sheet and random coil. All secondary structures have strong $\pi \rightarrow \pi^*$ absorption bands between 190 nm and 200 nm, and α-helix has weaker absorptivity due to the hypochromism of the α-helix [5].

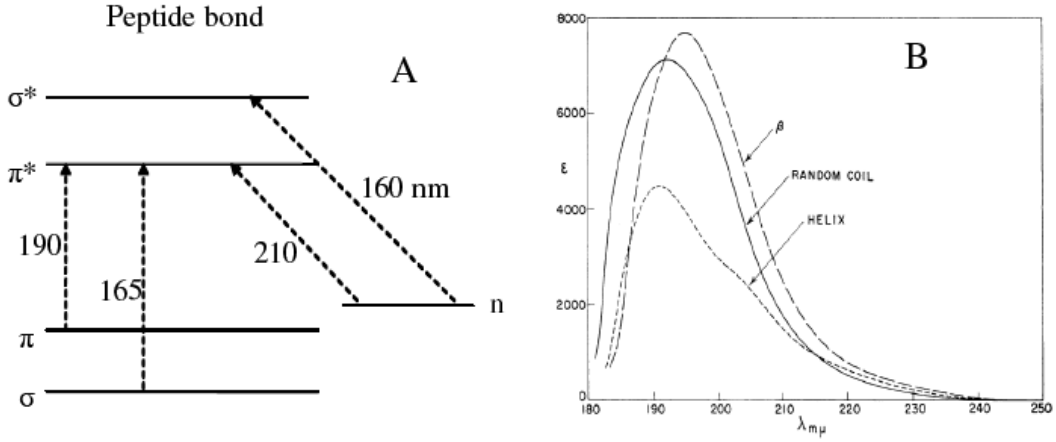

Figure 2.5: (A) Electronic energy levels and electronic transitions of a peptide bond. (B) Absorption spectra of α-helix, β-sheet and random coil. Reproduced from Rosenheck et al [4].

2.3.2 Amide vibration modes

~ 200 nm resonance Raman excitation occurs within the $\pi \rightarrow \pi^*$ electronic transition of the backbone amides. Thus, the amide vibrations are enhanced. For example, Fig. 2.6 shows the 204 nm excited UV resonance Raman (UVRR) spectra of poly-L-glutamic acid (PGA) at low pH. PGA is α-helical at low temperatures, but melts to PPII-like conformations at high temperatures. The low temperature α-helix UVRR spectrum shows an AmI band (mainly CO stretching) at ~1647 cm^{-1}, an AmII band (mainly out of phase combination of C-N stretching and N-H bending) at ~1560 cm^{-1}, a (C)C_α-H bending band at ~1390 cm^{-1}, and an $AmIII_3$ band (mainly in

phase combination of C-N stretching and N-H bending) at ~ 1260 cm^{-1}. As the temperature increases, the AmI band upshifts, while the AmII band downshifts. Previous studies indicate that hydrogen bonding to the carbonyls downshifts the AmI band, while hydrogen bonding to –NH groups upshifts the AmII band.[7] The C_α-H band intensity increases with increasing temperature, indicating α-helix melting.[8] As the temperature increases, the melted PPII-like conformation increases in concentration and the corresponding unfolded PPII $AmIII_3$ band (~1247 cm^{-1}) in PGA becomes more prominent, overshadowing the lower temperature α-helical $AmIII_3$ band.

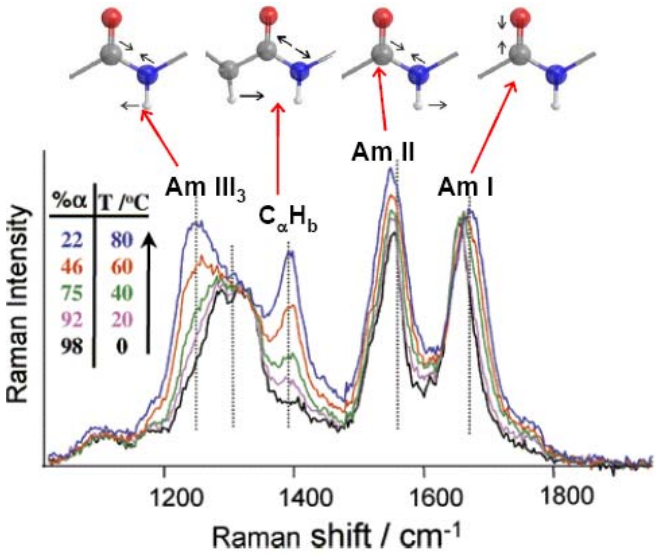

Figure 2.6: Temperature dependence of the 204 nm excited UVRR spectra of poly-L-glutamic acid at low pH. Also shown are the vibration modes. Reproduced from Asher et al [6].

The large $AmIII_3$ band frequency conformational dependence derives from the fact that coupling between C_α-H bending and N-H bending motions depends sensitively on the peptide bond Ramachandran Ψ dihedral angle that, in part, defines the peptide bond secondary structure conformation.[6]

The Asher group discovered a sinusoidal dependence of the $AmIII_3$ frequency on the Ramachandran Ψ angle.[6,9] Conveniently, they also found little dependence of the $AmIII_3$

frequency on the other dihedral angle, the Ramachandran Φ angle (for sterically allowed Ψ angles).[10] The origin of this Ψ angle frequency difference between the α-helix and extended conformations results from the fact that the α-helix peptide bond conformations have *trans* N-H and C_α-H bonds that prevent coupling (see Fig. 2.7). Thus, the α-helix $AmIII_3$ frequency occurs at 1258 cm^{-1} and the C_α-H bending band contains negligible C-N and N-H bending motion, and is, thus, not resonance enhanced.

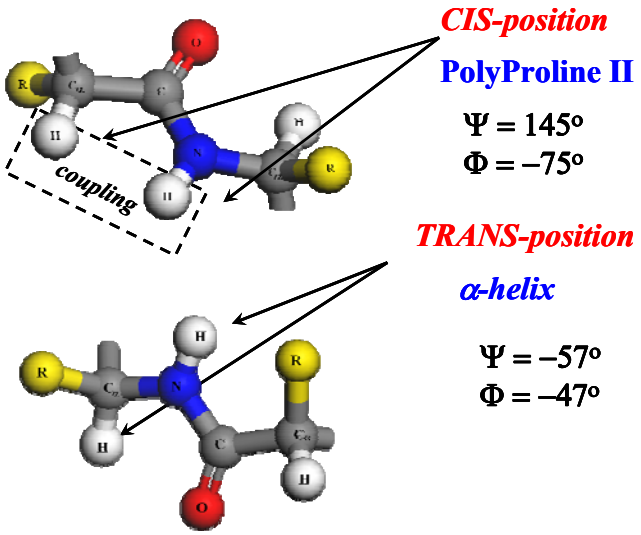

Figure 2.7: Relative orientations of N-H and C_α-H bonds in the polyproline II and α-helix conformations.

In contrast, peptide bonds adopting an extended PPII-like conformation have *cis* N-H and C_α-H bonds whose motions couple well. The $AmIII_3$ band frequency downshifts to 1245 cm^{-1} and the C_α-H bending vibration contains C-N stretching and N-H bending motion, resulting in resonance enhancement. Quantitative relations were determined that relate the $AmIII_3$ band frequencies to Ramachandran Ψ angles for different peptide bond HB states.[9]

For example, for peptide bonds fully hydrogen bonded to water such as in PPII, 2.5_1-helix, and extended β-strand conformations:

$$\nu_{AmIII_3}(\Psi,t) = 1256 \ \ cm^{-1} - 54 \ \ cm^{-1} \cdot \sin(\Psi + 26^o) - 0.11 \frac{cm^{-1}}{^oC} t \quad (2.25)$$

The family of quantitative relationships determining the $AmIII_3$ frequencies ignore the more modest Ramachandran Φ angle dependencies.[10] This family of equations allow estimation of the Ψ angle for the different possible peptide bond HB states. The estimated error of this determination was suggested to be $\leq \pm 14°$.[9] Correlating the inhomogeneously broadened $AmIII_3$ bandshape to the underlying Ramachandran Ψ angle distribution enables the determination of the peptide bond conformational distributions in peptides and proteins.[11] Most importantly, these conformational distributions can be used to calculate the Gibbs free energy landscapes along the Ψ angle coordinate, which is the most important (un)folding reaction coordinate.[9,12]

2.4 RERERENCE

(1) Asher, S. A. *Anal Chem* **1993**, *65*, A59-A66.

(2) Long, D. A. *THE RAMAN EFFECT: a unified treatment of the theory of raman scattering by molecules* West Sussex, England, 2002.

(3) Dirac, P. A. M. *Proceedings of the Royal Society of London. Series A, Containing Papers of a Mathmatical and Physical Character* **1927**, *114*, 710-728.

(4) Rosenheck, K.; Doty, P. *PNAS* **1961**, *47*, 1775-1785.

(5) Sharma, B.; Bykov, S. V.; Asher, S. A. *J Phys Chem B* **2008**, *112*, 11762-11769.

(6) Asher, S. A.; Ianoul, A.; Mix, G.; Boyden, M. N.; Karnoup, A.; Diem, M.; Schweitzer-Stenner, R. *J Am Chem Soc* **2001**, *123*, 11775-11781.

(7) Myshakina, N. S.; Ahmed, Z.; Asher, S. A. *J Phys Chem B* **2008**, *112*, 11873-11877.

(8) Wang, Y.; Purrello, R.; Jordan, T.; Spiro, T. G. *J Am Chem Soc* **1991**, *113*, 6359-6368.

(9) Mikhonin, A. V.; Asher, S. A. *J Am Chem Soc* **2006**, *128*, 13789-13795.

(10) Ianoul, A.; Boyden, M. N.; Asher, S. A. *J Am Chem Soc* **2001**, *123*, 7433-7434.

(11) Asher, S. A.; Mikhonin, A. V.; Bykov, S. *J Am Chem Soc* **2004**, *126*, 8433-8440.

(12) Thomas, A. S.; Elcock, A. H. *J Am Chem Soc* **2007**, *129*, 14887-14898.

CHAPTER 3

Salt Dependence of an α-helical Peptide Folding Energy Landscapes

This Chapter was published in *Biochemistry,* **2009**, 48, 10818-10826. The co-authors are Kan Xiong, Eliana K. Asciutto, Jeffry D. Madura and Sanford A Asher.

3.0 SALT DEPENDENCE OF AN α-HELICAL PEPTIDE FOLDING ENERGY LANDSCAPES

We used CD, UV resonance Raman spectroscopy and molecular dynamics simulation to examine the impact of salts on the conformational equilibria and the Ramachandran Ψ angle (un)folding Gibbs free energy landscape coordinate of a mainly polyala α-helical peptide, AP of sequence AAAAA(AAARA)$_3$A. $NaClO_4$ stabilizes α-helical-like conformations more than does NaCl, which stabilizes more than Na_2SO_4 at identical ionic strengths. This α-helix stabilization ordering is the reverse of the Hofmeister series of anions in their ability to disorder water hydrogen bonding. Much of the $NaClO_4$ α-helix stabilization results from ClO_4^- association with the AP terminal -NH_3^+ groups and arg side chains. ClO_4^- stabilizes 3_{10}-helix conformations but destabilizes turn conformations. The decreased Cl^- and SO_4^{2-} AP α-helix stabilization probably result from a decreased association with the arg and terminal -NH_3^+ groups. Cl^- is expected to have a smaller binding affinity and thus stabilizes α helical conformations intermediately between $NaClO_4$ and Na_2SO_4. Electrostatic screening stabilizes π-bulge conformations.

3.1 INTRODUCTION

The mechanism(s) whereby peptides and proteins fold into their native states are poorly understand[1-6]. The well-known Levinthal Paradox [7] clearly demonstrates that proteins do not fold through a random search of their conformational space since this would take longer than the age of our universe. Recent energy landscape models[1, 3, 8, 9] propose that funnel-shaped folding energy landscapes occur, where the native state is accessed via a strategically sloped energy landscape that funnels unfolded conformations towards the native folded state.[3, 10, 11]

In the work here we use CD, UV resonance Raman spectroscopy (UVRR) and molecular dynamics simulations to examine the Gibbs free energy landscape along the Ψ Ramachandran angle folding coordinate of a mainly polyala peptide, AP of sequence $AAAAA(AAARA)_3A$ in pure water and in the presence of $NaClO_4$, NaCl and Na_2SO_4. AP-like peptides have been the subject of intensive experimental [12-30] and theoretical[31-42] studies which have probed the mechanism(s) of α-helix folding and unfolding. The AP peptide is ~50% α-helical-like at 0 ^{0}C and melts to PPII-like conformations at higher temperatures[43-47]. We previously found that AP (un)folding is not a simple two-state process because it involves other secondary structure conformations such as π-bulge and 3_{10}-helix and turn structures [22, 31, 32, 41, 42, 48, 49]. We examined the dependence of the AP conformational equilibrium and melting on the presence of different salts and find that ion-binding and electrostatic screening significantly modulate the Gibbs free energy landscape and stabilize α-helix conformations. We also find that the ordering of salt stabilization of the α-helical content can be explained by Collins et al. "Law of Matching Water Affinities" [50-52].

3.2 EXPERIMENTAL

The 21-residue peptide AP of sequence $AAAAA(AAARA)_3A$ was purchased from AnaSpec Inc. (> 95% purity). Anhydrous NaCl, $NaClO_4$ and Na_2SO_4 were purchased from J. T. Baker (> 99% purity). All AP samples were prepared at 1.0 mg/ml concentrations at pH 7.

The CD spectra were measured by using a Jasco-715 spectropolarimeter, using a 200 μm path length cuvette. We co-added ten individual spectra.

The UVRR spectrometer was described in detail by Bykov et al[53]. Briefly, 204 nm UV light was obtained by generating the fifth anti-Stokes Raman harmonic of the third harmonic of a Nd:YAG laser (Coherent, Infinity). We used a spectral accumulation time of 5 min for each measurement and co-added 4 accumulations.

Molecular Dynamics Simulation: We performed Replica Exchange Molecular Dynamics (REMD) studies of AP immersed in pure water and in a 0.2 M $NaClO_4$ aqueous solution. The temperatures studied range from 270 K to 505 K. The simulation details are given in the Supplemental Material. To investigate the mechanisms which govern helix stabilization we used Chimera[54] to calculate the average ion occupancy surrounding the AP peptide (See Appendix A for molecular dynamic simulation details).

3.3 RESULTS

3.3.1 CD results

Fig. 3.1 shows the temperature dependence of the CD spectra of AP in pure water. The lower temperature CD spectra show two troughs at 222 and 206 nm that are characteristic of α-helix conformations[55]. As the temperature increases the ellipticity at 222 nm, Θ_{222} becomes less negative indicating α-helix melting. The isosbestic point at 202 nm indicates that this melting appears spectroscopically as a "two-state" process. Previous work by our group demonstrated that the AP α-helix conformation melts to a dominantly PPII-like conformation[56].

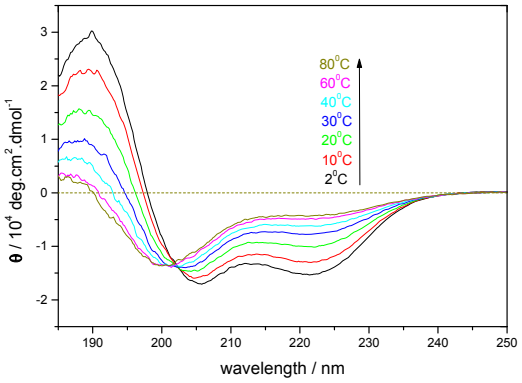

Figure 3.1: Temperature dependence of the CD spectra of AP in pure water at pH 7.

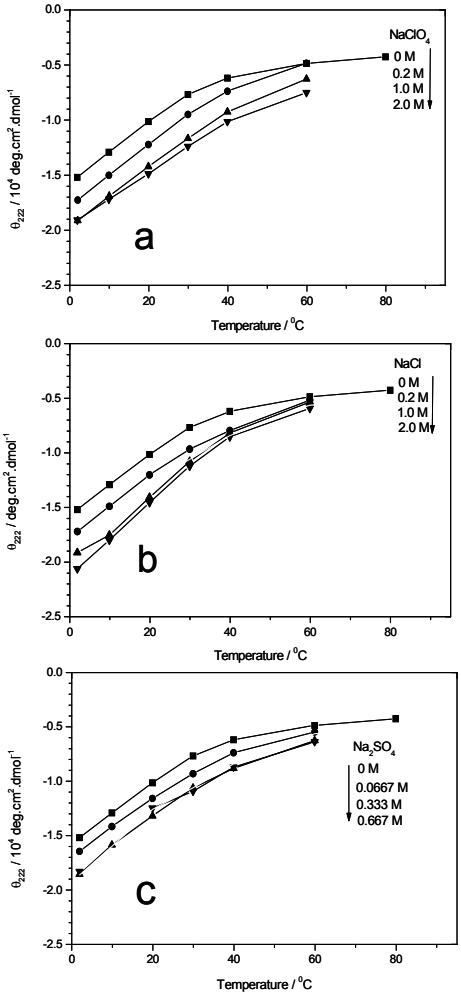

Figure 3.2: Θ_{222} melting curve of AP in a. $NaClO_4$ at different ionic strengths: ■ Pure water; ● 0.2 M $NaClO_4$; ▲1.0 M $NaClO_4$; ▼2.0 M $NaClO_4$. b. in NaCl at different ionic strengths: ■ Pure water; ● 0.2 M NaCl; ▲1.0 M NaCl; ▼2.0 M NaCl. c. in Na_2SO_4 at various ionic strength: ■ Pure water; ● 0.0667 M Na_2SO_4; ▲0.333 M Na_2SO_4; ▼0.667 M Na_2SO_4.

Addition of $NaClO_4$ (Fig. 3.2a) increases the AP α-helical content at all temperatures, as evident from the more negative values of Θ_{222}; however, the CD changes are relatively small between 1 and 2 M $NaClO_4$ concentrations. As discussed below, T_m also increases as the $NaClO_4$ concentration increases.

Figs. 3.2b and c show similar AP melting curves for NaCl and Na_2SO_4. Again the α-helix fractions increase as evident from the more negative Θ_{222} values as the salt concentrations increase. Again, little increase occurs between 1 and 2 M salt concentrations.

Table 3.1: **Thermodynamic parameters calculated from CD data.**

Solution	Δ H / KJ. mol^{-1}	Δ S / J. mol^{-1}.K^{-1}	T_m / K[a]	R^2
Pure water	-33.4±1.4	-121±5	276	0.995
0.2 M NaCl	-36.4±1.1	-128±4	284	0.998
1.0 M NaCl	-41.8±1.4	-144±5	290	0.998
2.0 M NaCl	-42.1±1.0	-144±3	292	0.999
0.2 M $NaClO_4$	-39.7±1.5	-140±5	284	0.997
1.0 M $NaClO_4$	-35.5±0.5	-122±2	291	0.999
2.0 M $NaClO_4$	-30.4±0.5	-104±2	292	0.999
0.0667 M Na_2SO_4	-33.5±0.5	-119±2	281	0.999
0.333 M Na_2SO_4	-33.7±0.6	-117±2	288	0.999
0.667 M Na_2SO_4	-32.4±1.5	-113±5	287	0.997

[a]We do not calculate the T_m standard error because it is likely that its error is not dominated by random processes, but instead is dominated by bias due to the ignored temperature dependencies of ΔH and ΔS.

To quantitatively model α-helix melting, we calculated the α-helical conformational fraction, f_α, using a two-state model (eq. 3.1) by utilizing the reported Θ_{222} values for the pure α-

helix ($[\theta]_\alpha$= -26000 deg.cm^2.dmol^{-1}), and the "pure melted" conformations ($[\theta]_r$= -3500 deg.cm^2.dmol^{-1}) [57].

$$f_\alpha = \frac{[\theta]-[\theta_r]}{[\theta_\alpha]-[\theta_r]} \qquad (3.1)$$

As shown below, the structure is actually more complex than a two-state transition, but significant useful thermodynamics information associated with the resulting quasi-two state transition can be extracted from the CD data.

We also calculated the melting thermodynamic parameters by fitting the calculated equilibrium α-helix fraction, f_α to:

$$\ln K = \ln \frac{f_\alpha}{1-f_\alpha} = \frac{-\Delta H}{R} \cdot \frac{1}{T} + \frac{\Delta S}{R} \qquad (3.2)$$

The fits to eq. 3.2 versus T^{-1} are highly linear with R^2 values of >0.995. Table 3.1 lists the calculated values for ΔH, ΔS and the resulting estimated T_m values. Fig. 3.3 shows that T_m increases for all salts as their concentrations increase (except at the highest Na_2SO_4 concentration). $NaClO_4$ and NaCl stabilize α-helices more than does Na_2SO_4. T_m increases as the Na_2SO_4 concentration increases to 0.333 M (ionic strength of 1.0 M) but then begins to decrease at a concentration of ~0.667 M (ionic strength of 2.0 M).

ΔH becomes more negative as the $NaClO_4$ concentration increases to 0.2 M, but then becomes less negative at higher $NaClO_4$ concentrations. A similar trend occurs for ΔS. Thus, the α-helix becomes more (less) favored enthalpically (entropically) as the salt concentration increases. ΔG, the difference between ΔH and TΔS, for α-helix formation becomes more negative as the $NaClO_4$ concentration increases.

In contrast, ΔH and ΔS both become more negative as the NaCl concentration increases to 1.0 M, but the values saturate upon concentration increases to 2.0 M.

Na_2SO_4 also stabilizes the α-helix giving rise to an increasingly negative ΔG. However, ΔH and ΔS only show a modest dependence on the Na_2SO_4 concentration. They both change together to make ΔG increasingly negative as evident from the Fig. 3.2c melting data for the lower concentrations.

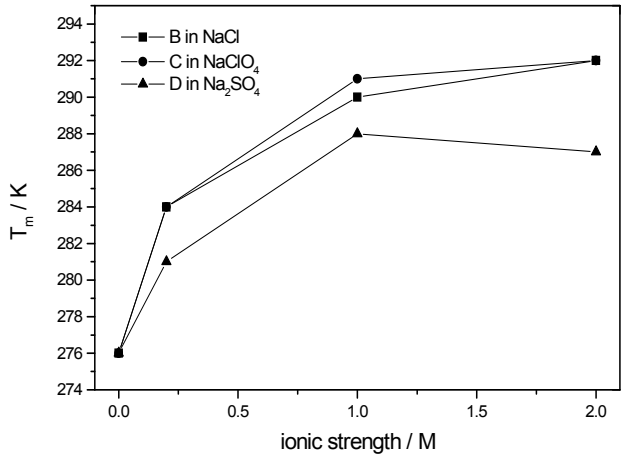

Figure 3.3: Calculated T_m of AP α-helix melting in different salts.

3.3.2 UV Resonance Raman Measurements:

Fig. 3.4 shows the temperature dependence of the AP 204 nm UVRR spectra. The AmI band (~1660 cm^{-1}) results from a mainly C=O stretching vibration. The AmII band (~1550 cm^{-1}) derives from out-of-phase motion of C-N stretching and N-H bending. The C_α-H doublet (~1372 cm^{-1} and ~1393 cm^{-1}) derives from a C_α-H bending vibration which is resonance enhanced because of coupling of C_α-H bending to N-H bending. The intensities of the C_α-H bending bands increase as the concentration of non-helical conformations increases[58]. The AmIII bands arise from vibrations which involve in-phase contributions of C-N stretching and N-H bending, The AmIII region contains three sub-bands: the $AmIII_1$ band (~1336 cm^{-1}), the $AmIII_2$ band (~1306 cm^{-1}) and the $AmIII_3$ band (~1250 cm^{-1}).

The $AmIII_3$ band is the most conformationally sensitive because it involves ψ-angle dependent coupling between N-H bending and the C_α-H bending motions[59]. For example, the $AmIII_3$ band of the α-helix appears at 1258 cm^{-1} and contains little C_α-H bending. However, it shifts to 1247 cm^{-1} in the PPII conformation[60] and contains significant C_α-H bending. The α-helix $AmIII_3$ band cross section is roughly half that of the PPII-like conformation because of the α-helix conformation electronic transition hypochromism[61]. As the temperature increases the intensities of the C_α-H bands increase, indicating α-helix melting. Also, the $AmIII_3$ band frequency shifts from ~1258 cm^{-1} at 2 ^{0}C to ~1247 cm^{-1} at 80 ^{0}C.

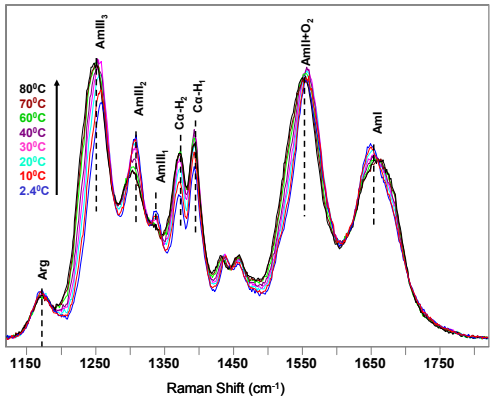

Figure 3.4: Temperature dependence of 204 nm excited UVRR spectra of AP in pure water.

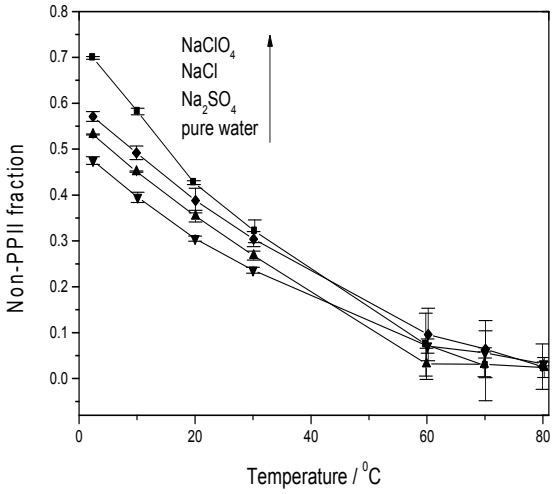

Figure 3.5: Non-PPII (primarily α-+3_{10}+π-helix) fractions of AP in different salt solutions: ■ in 0.2 M $NaClO_4$; ♦ in 0.2 M NaCl; ▲ in 0.0667 M Na_2SO_4; ▼ in pure water.

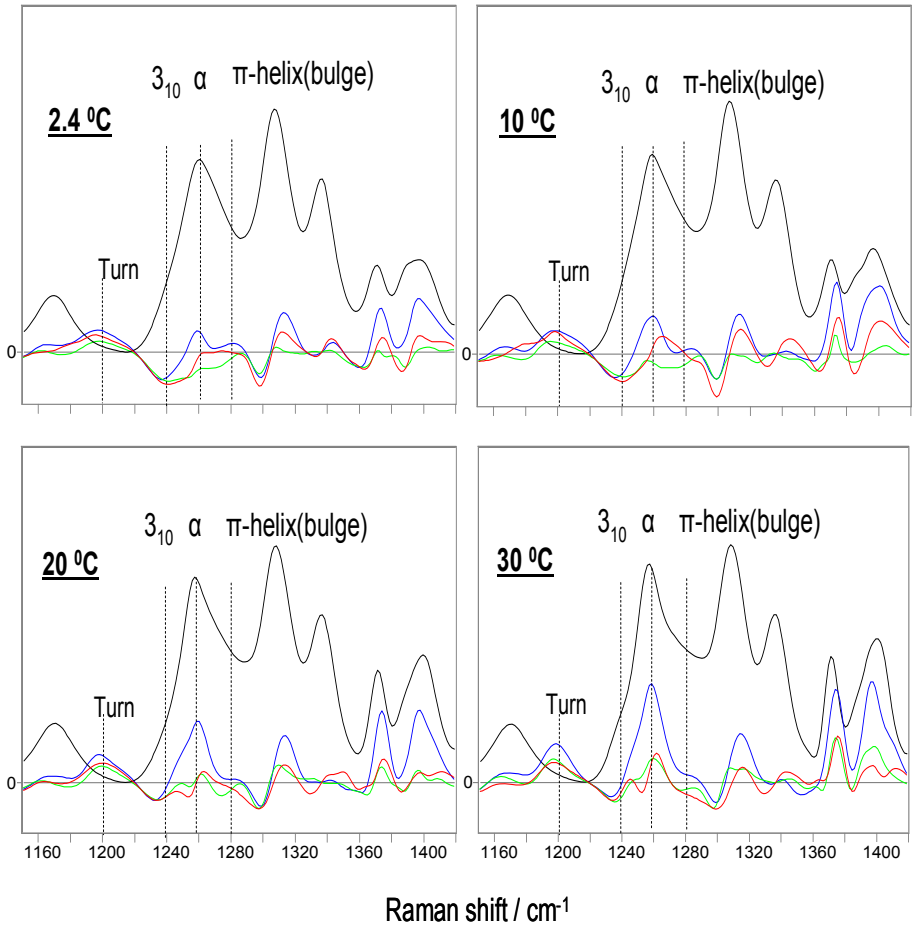

Figure 3.6: Temperature dependence of calculated α-helix-like spectra in 0.2 M $NaClO_4$, and difference spectra between different salt solutions: Red, 0.2 M NaCl minus 0.2 M $NaClO_4$; Green, 0.0667 M Na_2SO_4 minus 0.2 M $NaClO_4$; Blue, pure water minus 0.2 M $NaClO_4$. All displayed calculated α-helix-like spectra were normalized to the intensity of the $AmIII_1$ band of the 2.4 °C α-helix-like spectrum in $NaClO_4$. The difference spectra between salts were calculated from these normalized spectra.

The UVRR spectra of AP in 0.2 M NaCl, 0.2 M $NaClO_4$ and 0.0667 M Na_2SO_4 solutions all indicate α-helix melting as the temperature increases (spectra not shown). The spectra of samples without ClO_4^- or SO_4^{2-} were normalized to the AmI band integrated intensity, which shows little variation upon peptide conformational changes [62].

To calculate the α-helical fractions we calculated the temperature dependent basis spectra of the PPII-like conformation by using the method of Lednev et al[57]. We then digitally smoothed and then subtracted the appropriate amount of the PPII-like conformation basis spectra from the measured and smoothed UVRR spectra of AP.

The relative amount of the PPII conformation subtracted is the maximum amount of the PPII basis spectrum which minimized the C_α-H region intensity, with the constraint that no negative features occur in the difference spectrum. The basis spectral intensities subtracted are directly proportional to the concentration of the PPII conformation at each temperature [57]. The resulting difference spectra should result only from non PPII conformations, and appear to be mainly α-helix-like.

Fig. 3.5, which shows the temperature dependence of the non-PPII fraction, indicates that $NaClO_4$ is the most "helix" stabilizing salt, followed by NaCl, Na_2SO_4 and then pure water. These results agree with the CD results above, and with the salt ordering previously observed by others[63].

Fig. 3.6 shows the temperature dependence of the calculated non PPII, α-helix-like spectra of AP in $NaClO_4$, NaCl and Na_2SO_4 and the difference spectra between the different salt solution spectra. At all temperatures we observe a triplet of bands which are the hallmark of α-helix-like UVRR spectra. The 30° C spectrum shows a change in the $AmIII_3$ bandshape as earlier noted by Mikhonin et al[48]. The 30 °C $AmIII_3$ band slightly narrows, while the maximum becomes more sharply peaked. This bandshape change, which appeared as a more simple band narrowing in our previous poorer S/N spectra, was ascribed to a decrease in the concentrations of 3_{10}-helix and π-bulge conformations relative to the α-helix concentration as the temperature increases.

The most prominent difference between the different salt spectra is that a ~1200 cm^{-1} band that occurs in pure water, in NaCl and in Na_2SO_4 disappears in $NaClO_4$ as indicated by the ~1200 cm^{-1} troughs in the difference spectra. A new band occurs at ~1240 cm^{-1} in $NaClO_4$ solution, as evident by the trough in the difference spectra between the $NaClO_4$ solution and the other salts and pure water (most clearly at temperatures below 20 °C). Previous work[48, 62] indicated that an $AmIII_3$ band at ~1200 cm^{-1} derives from turn structures, while the $AmIII_3$ band at ~1240 cm^{-1} derives from 3_{10}-helix conformations. Therefore, we conclude that $NaClO_4$ selectively stabilizes 3_{10}-helix conformations which are replaced in pure water, in NaCl and Na_2SO_4 by turn conformations.

We calculated the Gibbs free energy landscapes of AP along the Ψ-folding coordinate from the UVRR spectra (Fig. 3.7 and Fig. 3.8) by using the methodology of Mikhonin et al[48, 53, 60, 64]. We calculate the Ψ angle probability distribution from the $AmIII_3$ bandshape and utilize the Boltzmann relationship to calculate the Gibbs free energy landscape.

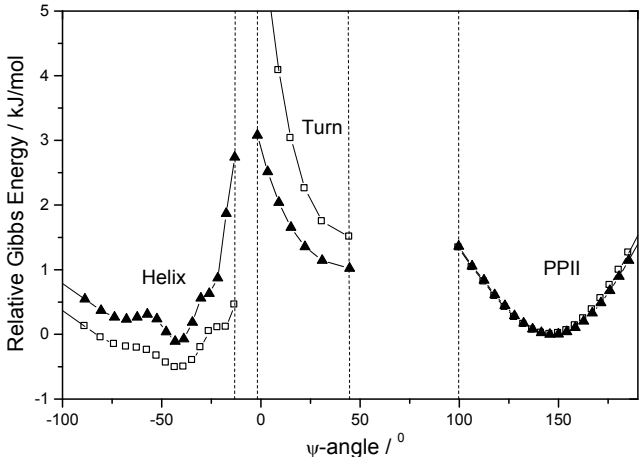

Figure 3.7: Calculated 2.4 °C Gibbs free energy landscape of AP in pure water, ▲ and in 0.2 M $NaClO_4$, □. We use the PPII-like conformation as the reference state.

The calculated AP Gibbs free energy landscapes in pure water and in 0.2 M $NaClO_4$ at 2.4 ^{0}C (Fig. 3.7) show a broad α-helix-like conformational region which includes Ψ angles corresponding to 3_{10} helices, α helices, and π bulges and the broad PPII region. The presence of 0.2 M $NaClO_4$ selectively decreases the Gibbs free energies of the 3_{10}-helix conformations, but increases the free energy of the turn conformations.

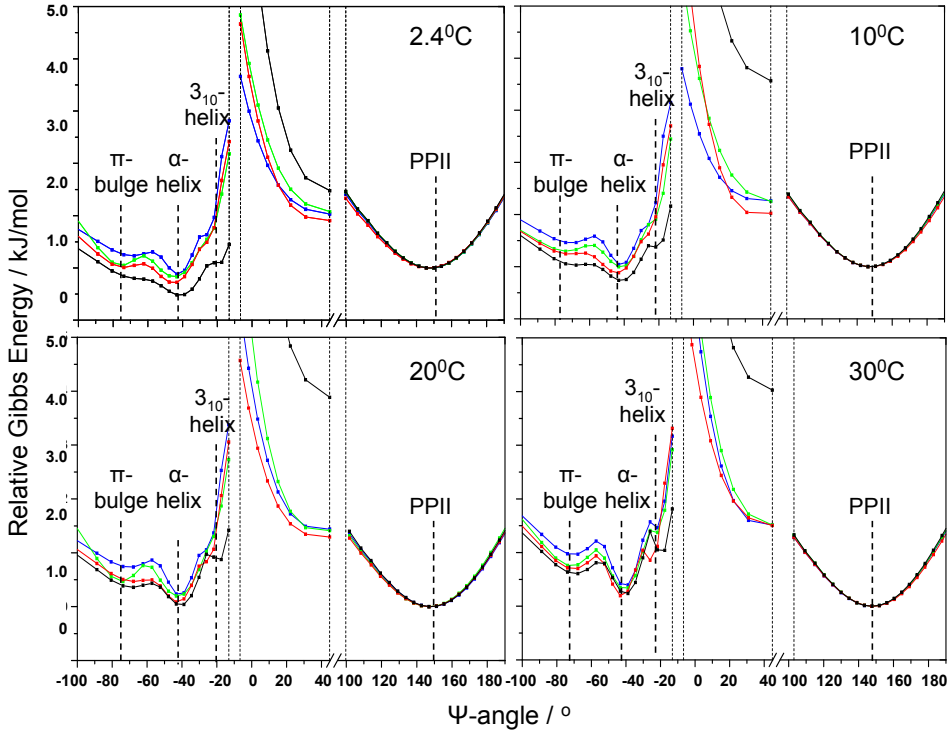

Figure 3.8: Calculated Gibbs free energy landscape of AP along the Ramachandran Ψ angle coordinate. — in pure water; — in 0.0667 M Na_2SO_4; — in 0.2 M NaCl ; — in 0.2 M $NaClO_4$. The PPII-like conformation is the reference state.

The α-helix-like region, the turn region and the PPII region are separated by high activation barriers due to steric clashes. These results are consistent with the calculated Φ and Ψ dependence of the Gibbs free energies of peptide conformations[65]. High activation energies are expected between α-helix and turn conformations and PPII conformations. Our ability to monitor

turn conformations is important for insight into the mechanisms of α-helix melting since these turn conformations are likely to serve as intermediates along the reaction coordinate that links α-helix-like to the melted PPII-like conformations[66, 67]

The energy landscape (Fig. 3.8) is bumpy within the α-helix-like basin. Within this basin the pure α-helix conformation (Ψ ~ -45º) is always lowest in energy, followed by the π-bulge conformation (Ψ ~ -70º). The 3_{10}-helix conformation (Ψ ~ -20º) lies at a slightly higher energy. Both the π-bulge and 3_{10}-helix conformations appear to show activation barriers between their minima and that of the α-helix conformation. The relative energy of the π-bulge conformation compared to the α-helix conformation is highest in pure water. As the temperature increases the α-helix basin Gibbs free energy increases indicating that the α-helix is destabilized relative to the PPII conformation. We have drawn the energy landscape as a projection onto the Ψ angle coordinate.

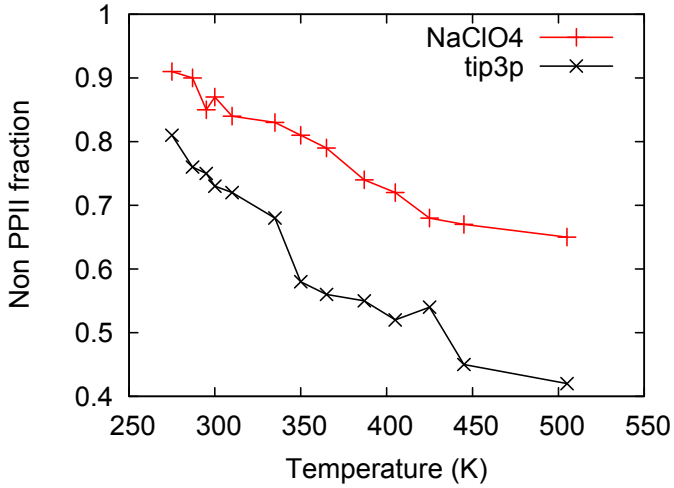

Figure 3.9: Molecular dynamics calculated AP non-PPII fraction in 0.2 M $NaClO_4$ solution and in pure water by REMD simulations. The molecular dynamics predicted AP α-helical conformation melting temperatures are higher than the experimental values because current force fields overstabilize the α-helical conformation [68]. Also, REMD simulations often predict much higher melting temperatures than standard MD simulations because the dynamical information is distorted by the REMD simulation temperature exchange process [69].

Traversing the energy landscape from one conformation to another could involve complex dynamics and involve significant dynamics involving Φ angle excursions and excursions in other coordinates.

Fig. 3.8 also shows the dependence of the conformational energies as a function of the salts dissolved in the AP solution at 0.2 M ionic strengths. For all temperatures, the lowest α-helix Gibbs free energies occur in the presence of $NaClO_4$, followed by NaCl, Na_2SO_4 and pure water. The 3_{10}-helix conformation is selectively stabilized by $NaClO_4$.

3.3.3 Molecular Dynamic Simulation Results:

The $NaClO_4$ α-helix stabilization was qualitatively reproduced by REMD simulations. Fig. 3.9 shows the theoretically calculated AP non-PPII fraction as a function of temperature in 0.2 M $NaClO_4$ solution and in pure water (All conformations with dihedral angles $\psi < +50°$ are counted as non-PPII conformations). The AP α-helical-like conformations (non-PPII conformations) concentrations in $NaClO_4$ are greater than in pure water at all temperatures.

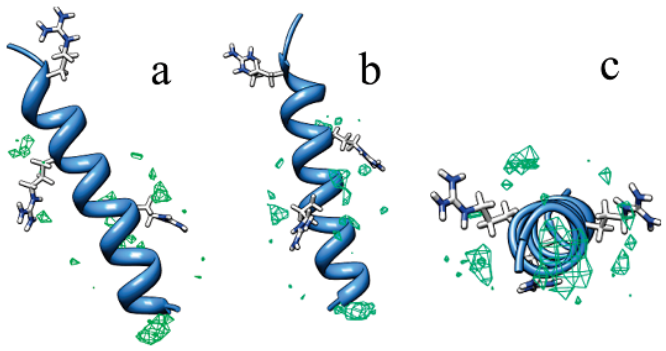

Figure 3.10: ClO_4^- occupancy around AP. The green contour shapes represent a higher than normal probability of finding ClO_4^- in a volume element near AP. b results from rotating a 180 degrees about the helix axis. c looking down the helix axis from the N-terminus to the C-terminus.

To investigate the mechanisms governing the helical stabilization we studied the equilibrium ClO_4^- distribution around AP. The average ClO_4^- concentrations around AP were calculated by using Chimera[54], where we calculated the average occupancy of ClO_4^- within a 3D grid over the trajectory frames. Fig. 3.10 shows the concentration distribution where a green volume indicates a region of increased ClO_4^- occupancy.

The largest increased ClO_4^- occupancy occurs around the N-terminus. Figs. 3.10 **a** and 10 **b** also show increased ClO_4^- occupancies around arg 9 and arg 14, with no increased ClO_4^- occupancy around arg 19, presumably due to the neutralization of arg 19 charge by the carboxylate. Fig. 3.10 **c** shows that the ClO_4^- occupancy increases in the region between the arg side chain and the peptide backbone.

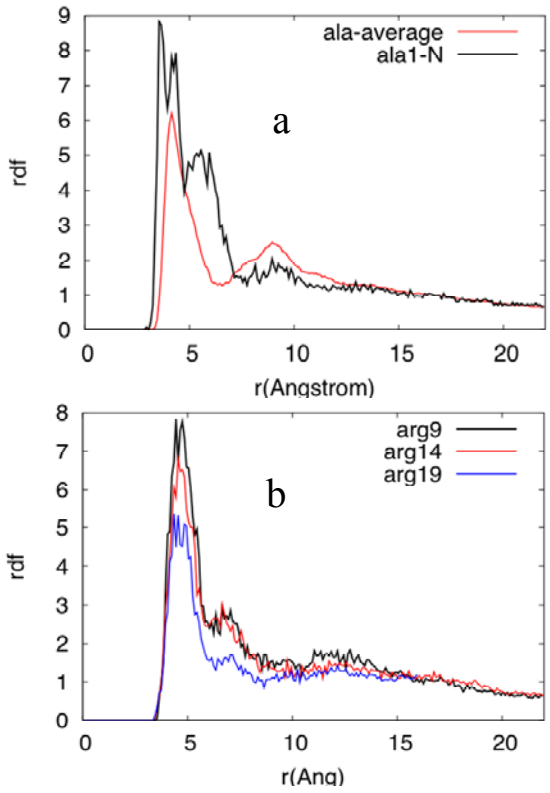

Figure 3.11: Average radial distribution functions of ClO_4^- with a the average ala residue and the terminal -NH_3^+ and b the different args. r is the distance between the Cl in ClO_4^- and the beta carbon of ala or the nitrogen of the terminal -NH_3^+ or the arg zeta carbon.

Figs. 3.11 a and b, which show the radial distribution functions for ClO_4^-, for the average β-carbon of ala, the terminal $-NH_3^+$ and the three different args ζ-carbon, indicate that ClO_4^- is located on the average 4.5 Å from the ala beta carbon and ~4 Å from the terminal $-NH_3^+$ nitrogen, while it is on the average ~5 Å from the arg zeta carbon. The distribution of ClO_4^- around the terminal $-NH_3^+$ is highest, indicating that the largest association of ClO_4^- with AP occurs around the terminal $-NH_3^+$. Arg9 has the highest affinity for ClO_4^-, followed by arg14 and then arg19.

ClO_4^- binding to the terminal $-NH_3^+$ and to arg is expected from Collion's matching water affinity model [50-52] where ion pair formation occurs preferentially between oppositely charged ions of similar charge densities. In this model small ions of high charge density tend to preferentially form ion pairs. Large ions of low charge density also preferentially form ion pairs. Ion pairing between oppositely charged ions of high and low charge density is less favorable. Thus, for AP we expect that the weakly hydrated (with low charge density) N-terminal and arg side chains [50-52] will most strongly bind to the weakly hydrated, low charge density ClO_4^- which will promote neutralization of the electrostatic interactions within AP which will significantly stabilize the α-helix conformation.

3.4 DISCUSSION

Both the CD and UVRR results show that salts stabilize α-helical like conformations of AP, with efficiencies: $NaClO_4$ > NaCl ~Na_2SO_4. Numerous previous studies[68, 69] have proposed that these salts affect the protein/peptide stability through three main effects.

[1]. The Hofmeister effect[70] phenomenon proposes that salts differentially "salt-in" or "salt-out" proteins/peptides by differentially interacting with water molecules, leaving more water or less water available for protein/peptide hydration. The Hofmeister series orders ions in their decreasing ability to perturb water structure. For example, SO_4^{2-} preceeds Cl^- in the Hofmeister series, and thus will more efficiently "salt-out" proteins/peptides. SO_4^{2-} will preferentially dehydrate the AP backbone and should stabilize α-helix-like conformations [14, 71-73]. ClO_4^- follows Cl^- and will "salt-in" proteins/peptides by interacting weakly with water, which leaves more water available for protein/peptide hydration. This predicts that ClO_4^- should better stabilize melted, water-hydrogen bonded PPII-like conformations. Cl^- should have an intermediate dehydration impact compared to SO_4^2 and ClO_4^-.

[2] Ionic screening decreases electrostatic interactions between protein and peptide charges[74]. Higher ionic strengths increasingly screen electrostatic interactions between charges, as well as between charges and the helix dipole which can impact α-helix stability. For AP at pH 7, interactions between the α helix dipole and the N-terminal positive charge, as well as the anionic carboxylate C-terminal charge, destabilizes the α-helical conformation[75-77]. In addition, electrostatic repulsions between the three arg side-chains should destabilize the α-helix. Electrostatic screening by high ionic strength solutions will decrease these unfavorable interactions and will thus stabilize α-helical-like conformations.

[3] Specific ion binding between solution ions and peptide and protein sidechains can impact the α-helix stability according to Collins et al [50-52] model of matching water affinities where ion pair formation is predicted on the basis of preferential formation between oppositely charged ions of similar charge densities. Small ions of high charge density (kosmotropes) tend to preferentially to form ion pairs. In contrast, large ions of low charge density (chaotropes)

forming ion pairs between themselves. Hydrated ion pairing between kosmotropes and chaotropes is less favorable.

Thus, for AP we expect that the weakly hydrated N-terminal and arg side chains[50-52] most strongly bind to the weakly hydrated chaotrope ClO_4^-. The resulting charge neutralization will decrease electrostatic interactions within AP which should significantly stabilize the α-helix conformation. Our Molecular Dynamic simulations directly observe association of ClO_4^- with the terminal NH_3^+ group and the arg. SO_4^{2-} is expected to show the least ion pairing with NH_3^+ and arg, while Cl^- should show intermediate ion pairing. These ion pairing propensities predict that $NaClO_4$ should be the most helix stabilizing, followed by NaCl, and then Na_2SO_4.

Table 3.2: Impact of ions on AP α-helix stability; "+" helix stabilizing; "-" helix destabilizing; "0" no impact.

Solution	Ionic screening	Hofmeister effect	Specific ion-binding
Pure water	**0**	**0**	**0**
NaCl	+	**0**	+
$NaClO_4$	+	-	+
Na_2SO_4	+	+	0

Table 3.2 summarizes the expected impact of ions on AP α-helix stability from different effects. Our observations show that at identical ionic strengths α-helical like conformations are most stabilized by $NaClO_4$, followed by NaCl, Na_2SO_4 and then pure water. For $NaClO_4$ to exhibit the most stabilization, the positive impact from specific ion-binding effect must override the negative impact of the Hofmeister effect. The fact that NaCl stabilizes α-helical like conformations less than does $NaClO_4$ but more than Na_2SO_4 suggests that the Hofmeister effect (water structure modification) has little impact.

The fact that π-helix (bulge) is disfavored in pure water, but is stabilized in the presence of these three salts demonstrates that importance of electrostatic screening, where formation of the π bulge must overcome repulsion between arg side chains spaced at i, i+5 positions. In

contrast, the arg side chains are spaced further apart for the α-helix and the 3_{10}-helix. We are continuing to study why $NaClO_4$ stabilizes the 3_{10}-helix but destabilizes the turn structure.

3.5 CONCLUSIONS

We used CD and UV resonance Raman spectroscopy and Molecular Dyamcis to study the solution conformation of a mainly polyala peptide containing arg groups for solubility. We calculated the Gibbs free energy landscape along the Ramachandran Ψ angle folding coordinate. We observe that at identical ionic strengths α-helical like conformations are stabilized most by $NaClO_4$ due to preferential ion-binding of ClO_4^- to the terminal NH_3^+ and arg side chains. ClO_4^- stabilizes 3_{10} helices but destabilizes turn conformations. Cl^- has a smaller binding affinity and thus stabilizes α helical conformations intermediate between $NaClO_4$ and Na_2SO_4. Electrostatic screening stabilizes π-bulge conformations. We find that we can understand ion association to the peptide through the Collins "Laws of Matching Water Affinities Model".

3.6 ACKNOWLEDGEMENTS

We thank Aleksandr V. Mikhonin, Zeeshan Ahmed, Bhavya Sharma, Lu Ma and Zhenmin Hong for useful discussions.

3.7 REFERENCES

(1) Dill, K. A.; Ozkan, S. B.; Shell, M. S.; Weikl, T. R. *Annu. Rev. Biophys.* **2008,** 37, 289-316.

(2) Ivarsson, Y.; Travaglini-Allocatelli, C.; Brunori, M.; Gianni, S. *Biophys. J. Biophys. Lett.* **2008,** 37, (6), 721-728.

(3) Dobson, C. M.; Sali, A.; Karplus, M. *Angew. Chem. Int. Ed.* **1998,** 37, (7), 868-893.

(4) Baldwin, R. L.; Rose, G. D. *Trends Biochem. Sci.* **1999,** 24, (2), 77-83.

(5) Baldwin, R. L.; Rose, G. D. **1999,** 24, (1), 26-33.

(6) Jahn, T. R.; Radford, S. E. *FEBS J.* **2005,** 272, (23), 5962-5970.

(7) C, L. *J Chem. Phys.* **1968,** 65, 44-45.

(8) Dill, K. A.; Chan, H. S. *Nat. Struct. Biol.* **1997,** 4, (1), 10-19.

(9) Dill, K. A. *Protein Sci.* **1999,** 8, (6), 1166-1180.

(10) Mello, C. C.; Barrick, D. *Proc. Natl. Acad. Sci. USA* **2004,** 101, (39), 14102-14107.

(11) Levy, Y.; Jortner, J.; Becker, O. M. *Proc. Natl. Acad. Sci. USA* **2001,** 98, (5), 2188-2193.

(12) Ihalainen, J.; Bredenbeck, J.; Pfister, R.; Helbing, J.; Chi, L.; van Stokkum, I.; Woolley, G.; Hamm, P. *Proc. Natl. Acad. Sci. USA* **2007,** 104, (13), 5383-5388.

(13) Balakrishnan, G.; Hu, Y.; Bender, G.; Getahun, Z.; DeGrado, W.; Spiro, T. *J. Am. Chem. Soc.* **2007,** 129, (42), 12801-12808.

(14) Starzyk, A.; Barber-Armstrong, W.; Sridharan, M.; Decatur, S. *Biochemistry* **2005,** 44, (1), 369-376.

(15) Wang, T.; Zhu, Y.; Getahun, Z.; Du, D.; Huang, C.; DeGrado, W.; Gai, F. *J. Phys. Chem. B* **2004,** 108, (39), 15301-15310.

(16) Huang, C.; Getahun, Z.; Zhu, Y.; Klemke, J.; DeGrado, W.; Gai, F. *Proc. Natl. Acad. Sci. USA* **2002,** 99, (5), 2788-2793.

(17) Huang, C.; Klemke, J.; Getahun, Z.; DeGrado, W.; Gai, F. *J. Am. Chem. Soc.* **2001,** 123, (38), 9235-9238.

(18) Thompson, P.; Munoz, V.; Jas, G.; Henry, E.; Eaton, W.; Hofrichter, J. *J. Phys. Chem. B* **2000,** 104, (2), 378-389.

(19) Yoder, G.; Pancoska, P.; Keiderling, T. *Biochemistry* **1997,** 36, (49), 15123-15133.

(20) Thompson, P.; Eaton, W.; Hofrichter, J. *Biochemistry* **1997,** 36, (30), 9200-9210.

(21) Thompson, P.; Eaton, A.; Hofrichter, J. *Biophys. J.* **1997,** 72, (2), WP377-WP377.

(22) Millhauser, G.; Stenland, C.; Hanson, P.; Bolin, K.; vandeVen, F. *J. Mol. Biol.* **1997,** 267, (4), 963-974.

(23) Williams, S.; Causgrove, T.; Gilmanshin, R.; Fang, K.; Callender, R.; Woodruff, W.; Dyer, R. *Biochemistry* **1996,** 35, (3), 691-697.

(24) Shalongo, W.; Dugad, L.; Stellwagen, E., Distribution of helicity within the model peptide Actyl(AAQAA)$_3$Amide. *J. Am. Chem. Soc.* **1994,** 116, (18), 8288-8293.

(25) Fiori, W.; Miick, S.; Millhauser, G. *Biochemistry* **1993,** 32, (45), 11957-11962.

(26) Scholtz, J. M.; York, E. J.; Stewart, J. M.; Baldwin, R. L. *J. Am. Chem. Soc.* **1991,** 113, 5102-5104.

(27) Marqusee, S.; Robbins, V. H.; Baldwin, R. L. *Proc. Natl. Acad. Sci. USA* **1989,** 86, 5286-5290.

(28) Ramajo, A. P.; Petty, S. A.; Volk, M. *Chem. Phys.* **2006,** 323, (1), 11-20.

(29) Silva, R. A. G. D.; Kubelka, J.; Bour, P.; Decatur, S. M.; Keiderling, T. A. *Proc. Natl. Acad. Sci. USA* **2000,** 97, (15), 8318-8323.

(30) Long, H. W.; Tycko, R. *J. Am. Chem. Soc.* **1998,** 120, (28), 7039-7048.

(31) Wang, W.; Lin, T.; Sun, Y. *J. Phys. Chem. B* **2007,** 111, (13), 3508-3514.

(32) Sorin, E.; Rhee, Y.; Shirts, M.; Pande, V. *J. Mol. Biol.* **2006,** 356, (1), 248-256.

(33) Morozov, A.; Lin, S. *J. Phys. Chem. B* **2006,** 110, (41), 20555-20561.

(34) Sorin, E.; Pande, V. *Biophys. J.* **2005,** 88, (4), 2472-2493.

(35) Jas, G.; Kuczera, K. *Biophys. J.* **2004,** 87, (6), 3786-3798.

(36) Gnanakaran, S.; Hochstrasser, R.; Garcia, A. *Proc. Natl. Acad. Sci. USA* **2004,** 101, (25), 9229-9234.

(37) Gnanakaran, S.; Hochstrasser, R.; Garcia, A. *Abstr. Paper Am. Chem. Soc.* **2003,** 226, U335-U335.

(38) Ghosh, T.; Garde, S.; Garcia, A. *Biophys. J.* **2003,** 85, (5), 3187-3193.

(39) Armen, R.; Alonso, D.; Daggett, V. *Protein Sci.* **2003,** 12, (6), 1145-1157.

(40) Vila, J.; Ripoll, D.; Scheraga, H. *Biopolymers* **2001,** 58, (3), 235-246.

(41) Shirley, W.; Brooks, C. *Proteins: Struct., Funct. Genet.* **1997,** 28, (1), 59-71.

(42) Zhang, W.; Lei, H. X.; Chowdhury, S.; Duan, Y. *J. Phys. Chem. B* **2004,** 108, (22), 7479-7489.

(43) Asher, S.; Mikhonin, A.; Bykov, S. *J. Am. Chem. Soc.* **2004,** 126, (27), 8433-8440.

(44) Kentsis, A.; Mezei, M.; Gindin, T.; Osman, R. *Proteins: Struct. Funct. Bioinf.* **2004,** 55, (3), 493-501.

(45) Mezei, M.; Fleming, P.; Srinivasan, R.; Rose, G. *Proteins: Struct., Funct. Genet.* **2004,** 55, (3), 502-507.

(46) Pappu, R.; Rose, G. *Protein Sci.* **2002,** 11, (10), 2437-2455.

(47) Shi, Z.; Olson, C.; Rose, G.; Baldwin, R.; Kallenbach, N. *Proc. Natl. Acad. Sci. USA* **2002,** 99, (14), 9190-9195.

(48) Mikhonin, A. V.; Asher, S. A. *J. Am. Chem. Soc.* **2006,** 128, (42), 13789-13795.

(49) Mikhonin, A.; Asher, S.; Bykov, S.; Murza, A. *J. Phys. Chem. B* **2007,** 111, (12), 3280-3292.

(50) Collins, K. D. *Biophys. J.* **1997,** 72, (1), 65-76.

(51) Collins, K. D. *Methods* **2004,** 34, (3), 300-311.

(52) Collins, K. D.; Neilson, G. W.; Enderby, J. E. *Biophys. Chem.* **2007,** 128, (2-3), 95-104.

(53) Bykov, S.; Lednev, I.; Ianoul, A.; Mikhonin, A.; Munro, C.; Asher, S. A. *Appl. Spectrosc.* **2005,** 59, (12), 1541-1552.

(54) Pettersen, E. F.; Goddard, T. D.; Huang, C. C.; Couch, G. S.; Greenblatt, D. M.; Meng, E. C.; Ferrin, T. E. *J. Compt. Chem.* **2004,** 25, 1605-1612.

(55) Manning, M. C.; Woody, R. W. *Biopolymers* **1991,** 31, 569-586.

(56) Asher, S. A.; Mikhonin, A. V.; Bykov, S. *J. Am. Chem. Soc.* **2004,** 126, (27), 8433-8440.

(57) Lednev, I.; Karnoup, A.; Sparrow, M.; Asher, S. *J. Am. Chem. Soc.* **1999,** 121, (35), 8074-8086.

(58) Wang, Y.; Purrello, R.; jordan, T.; Spiro, T. G *J. Am. Chem. Soc.* **1991,** 113, 6359-6368.

(59) Asher, S. A.; Ianoul, A.; Mix, G.; Boyden, M. N.; Karnoup, A.; Diem, M.; Schweitzer-Stenner, R. *J. Am. Chem. Soc.* **2001,** 123, (47), 11775-11781.

(60) Mikhonin, A. V.; Bykov, S. V.; Myshakina, N. S.; Asher, S. A. *J. Phys. Chem. B* **2006,** 110, (4), 1928-1943.

(61) Sharma, B.; Bykov, S. V.; Asher, S. A. *J. Phys. Chem. B* **2008,** 112, (37), 11762-11769.

(62) Ma, L.; Ahmed, Z.; Mikhonin, A. V.; Asher, S. A. *J. Phys. Chem. B* **2007,** 111, (26), 7675-7680.

(63) Damodaran, S. *Int. J. Biol. Macromol.* **1988,** 11.

(64) Ma, L.; Ahmed, Z.; Mikhonin, A.; Asher, S. *J. Phys. Chem. B* **2007,** 111, (26), 7675-7680.

(65) Ramachandran, G. N.; Sasisekharan, V., *Conformation of Polypeptides and Proteins*. Academic Press: New York, 1968; Vol. 23, p 283-437.

(66) Sundarlingam, M.; Sekharudu, Y. C. *Science* **1989,** 244, 1333-1337.

(67) Millhauser, G. L. *Biochemistry* **1995,** 34, (32), 10318-10318.

(68) Beck, D. A. C.; White, G. W. N.; Daggett, V. *J. Struct. Biol.* **2007,** 157, (3), 514-523.

(69) Hornak, V.; Abel, R.; Okur, A.; Strockbine, B.; Roitberg, A.; Simmerling, C. *Proteins: Struct. Funct. Bioinf.* **2006,** 65, (3), 712-725.

(70) Goto, Y.; Takahashi, N.; Fink, A. L. *Biochemistry* **1990,** 29, 3480-3488.

(71) Thomas, A. S.; Elcock, A. H. *J. Am. Chem. Soc.* **2007,** 129, (48), 14887-14898.

(72) Collins, K. D.; Washabaugh, M. W. *Quart. Rev. Biophys.* **1985,** 18, 323-422.

(73) Vila, J. A.; Ripoll, D. R.; Scheraga, H. A. *Proc. Natl. Acad. Sci. USA* **2000,** 97, 13075-13079.

(74) Garcia, A. E.; Sanbonmatsu, K. Y. *Proc. Natl. Acad. Sci. USA* **2002,** 99, 2782-2787.

(75) Mukherjee, S.; Chowdhury, P.; Gai, F. *J. Phys. Chem. B* **2006,** 110, 11615-11619.

(76) Debye, P.; Huckel, E., *Phys. Z* **1923,** 24, 185-206.

(77) Hol, W. G. J. *Prog. Biophys. molec. Biol* **1985,** 45, 149-195.

(78) Hol, W. G. J.; Duijnen, P. T. v.; Berendsen, H. J. C. *Nature* **1978,** 273, 443-446.

(79) Shoemaker, K. R.; Kim, P. S.; York, E. J.; Stewart, J. M.; Baldwin, R. L. *Nature* **1987,** 326, 573-567.

Chapter 4

Circular Dichroism and UV Resonance Raman Study of the Impact of Alcohols on the Gibbs Free Energy Landscape of an α-helical Peptide

This Chapter was published in *Biochemistry,* **2010**, 49, 3336-3342. The co-authors are Kan Xiong and Sanford A Asher.

4.0 CIRCULAR DICHROSIM AND UV RESONANCE RAMAN STUDY OF THE IMPACT OF ALCOHOLS ON THE GIBBS FREE ENERGY LANDSCAPE OF AN α-HELICAL PEPTIDE

We used CD and UV resonance Raman spectroscopy to study the impact of alcohols on the conformational equilibria and relative Gibbs free energy landscapes along the Ramanchandran Ψ-coordinate of a mainly poly-ala peptide, AP of sequence $AAAAA(AAARA)_3A$. 2,2,2-trifluroethanol (TFE) most stabilizes the α-helical-like conformations, followed by ethanol, methanol and pure water. The π-bulge conformation is stabilized more than the α-helix, while the 3_{10}-helix is destabilized due to the alcohol increased hydrophobicity. Turns are also stabilized by alcohols. We also found that while TFE induces more α-helices, it favors multiple, shorter helix segments.

4.1 INTRODUCTION

Protein folding depends both on its primary sequence and its solvent environment. Addition of alcohol to aqueous solution changes the hydration of protein. The resulting conformational changes can be used as a valuable tool for probing protein – water interactions.[1-7] It is important to realize that despite intensive investigations over the years, the mechanism(s) by which alcohols perturb protein conformation is still poorly understood. [8-18]

In this work, we used CD and UV resonance Raman (UVRR) spectroscopy to study the impact of alcohols on the conformational equilibria and relative Gibbs free energy landscapes along the Ramanchandran Ψ-coordinate of a mainly poly-ala peptide, AP of sequence $AAAAA(AAARA)_3A$. We find that the α-helix and π-bulge conformations are most stabilized by 2,2,2-trifluroethanol (TFE), followed by ethanol, methanol and pure water. Turn conformations

are also stabilized. However, 3_{10}-helices are destabilized. We also find that TFE induces an increased abundance of α-helices. However, the average α-helix length is decreased.

4.2 EXPERIMENTAL

The 21-residue peptide AP of sequence $AAAAA(AAARA)_3A$ was purchased from AnaSpec Inc. (> 95% purity). Absolute methanol was purchased from J. T. Baker. Absolute ethanol was purchased from Pharmco. 2,2,2-trifluroethanol (TFE, 99.8% purity) was purchased from Acros. The pH 7 solution samples contain 1 mg/ml concentration of AP and 0.05 M $NaClO_4$.

The CD spectra were measured by using a Jasco-715 spectropolarimeter, by using a 0.02 cm path length cuvette. We co-added five individual CD spectra.

The UV resonance Raman (UVRR) apparatus was described in detail by Bykov et al. [19] Briefly, 204 nm UV light (1 mW average power, 100 μm diameter spot) was obtained by mixing the 3rd harmonic with the fundamental (816 nm wavelength, 1 kHz repetition rate, 0.6 W average power, 25-40 ns pulse width) of a tunable Ti:Sapphire laser system from Photonics Industries. The sample was circulated in a free surface, temperature-controlled stream. A 180 ^{o} sampling backscattering geometry was used. The collected light was dispersed by a double monochromator onto a back thinned CCD camera (Princeton Instruments Spec 10 System, 1.5 cm^{-1} resolution with 100 μm slit width). We used 5 min accumulation times, and four accumulations were co-added. The 732 cm^{-1} and 1379.5 cm^{-1} bands of Teflon were utilized to calibrate the frequencies. The frequencies are reproducible to less than 1 cm^{-1}. Raman spectra were normalized to the peak height of the 932 cm^{-1} ClO_4^- band. No Raman saturation occurs at these low excitation powers

4.3 RESULTS

4.3.1 CD measurements

Fig. 4.1 shows the temperature dependence of the CD spectra of AP in pure water. The low temperature

CD spectra show two troughs at 222 nm and 206 nm which are characteristic of α-helix conformation.[20] As the temperature increases the ellipticity at 222 nm, Θ_{222} becomes less negative indicating α-helix melting. The isosbestic point at 202 nm indicates that the melting behavior appears spectroscopically as a "two-state" process. Previous work by our group demonstrated that the AP α-helix conformation melts to a dominantly PPII-like conformation. [21]

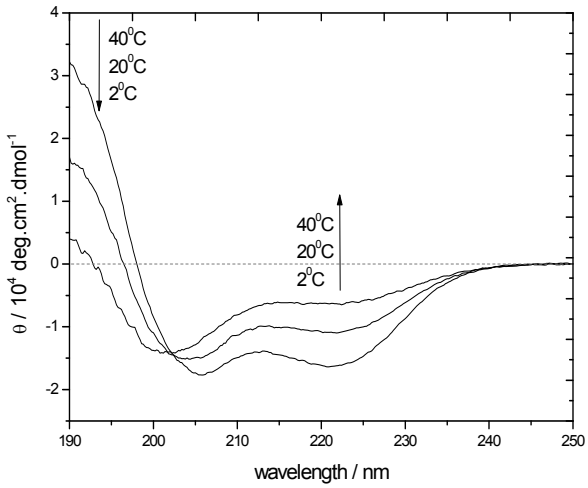

Figure 4.1: **Temperature dependence of the CD spectra of 1 mg/ml AP in pure water.**

Fig. 4.2a and 2b show the temperature dependence of the mean residue ellipticity at 222 nm, θ_{222} of AP in pure water and in the presence of different alcohols. Alcohols increase the α-helix content. At 20 ^{0}C and 25% alcohol (by volume), TFE most stabilizes the α-helix, followed closely by ethanol and then methanol, consistent with previous studies [8,12,18]. At 50% (v/v) alcohol, ethanol is the most α-helix stabilizing, followed by TFE and then methanol. As the

alcohol concentration increases from 25% to 50%, θ_{222} decreases in methanol and ethanol but changes little in TFE (Fig. 4.2c). Previous studies also showed that TFE does not appear in CD measurements to induce additional α-helix concentrations above 25% (v/v). [11]

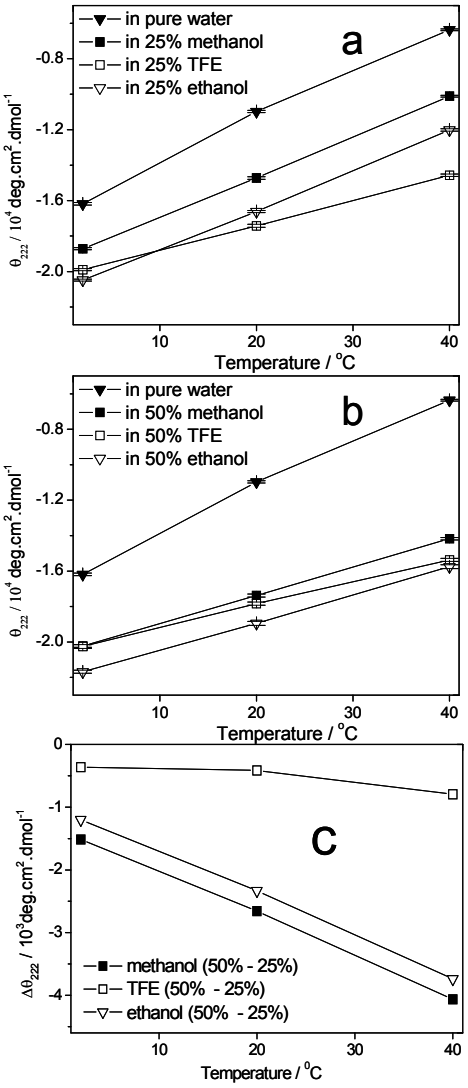

Figure 4.2: θ_{222} of AP (a) in 25% (v/v) alcohol and (b) in 50% (v/v) alcohol; (c) $\Delta\theta_{222}$ (θ_{222} in 50% alcohol minus θ_{222} in 25% alcohol).

4.3.2 UVRR measurements

204 nm UV Raman spectra (UVRS) of AP in pure water (Fig. 4.3) show mainly the amide RR bands. In contrast, 204 nm UVRS of AP in 50% methanol (Fig. 4.3) show methanol Raman

bands which we numerically removed in the Fig. 4.4 UVRS. The resulting spectra show the temperature dependence of the 204 nm UVRS of AP in 50% methanol. As the temperature increases, the AmI band upshifts from 1652 cm^{-1} to 1658 cm^{-1} while the AmII band downshifts from 1556 cm^{-1} to 1552 cm^{-1}. [22] Previous work [23] indicates that water hydrogen bonding to the peptide bond (PB) C=O site increases the C=O bond length and, thus, downshifts the AmI band, while water hydrogen bonding to the PB N-H upshifts the AmII band. The AmI (AmII) band in pure water (Fig. 4.4) is upshifted (downshifted) relative to that in 50% methanol, indicating less C=O (N-H) hydrogen bonding in alcohol solution. [23] The C_α-H doublet (~1372 cm^{-1} and ~1393 cm^{-1}) frequency does not shift as the temperature increases but its intensity increases.

The C_α-H doublet intensity only slightly increases from 2 ^{0}C to 20 ^{0}C, indicating little α-helix melting. [24] Significant intensity changes observed from 20 ^{0}C to 40 ^{0}C indicates extensive α-helix melting. The $AmIII_3$ band downshifts from ~1264 cm^{-1} at 2 ^{0}C to ~1259 cm^{-1} at 40 ^{0}C while its intensity increases. [22] UVRS of AP in other alcohols (not shown) show very similar α-helix melting behaviors.

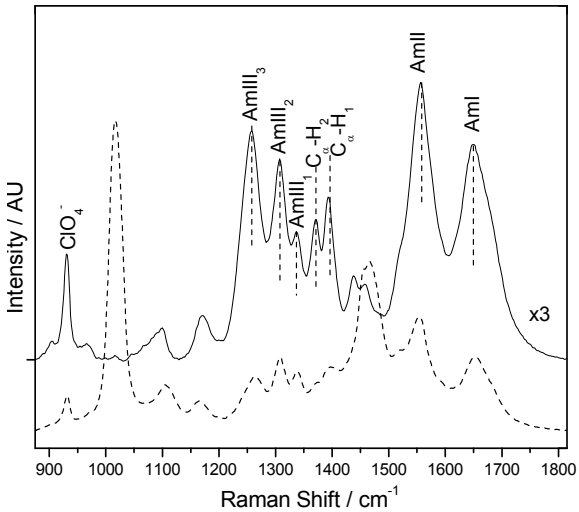

Figure 4.3: **204 nm excited UVRS of AP in pure water (solid line); AP in 50% methanol (dashed line) at 10 ^{0}C. The UVRS of AP in pure water was scaled to facilitate comparison.**

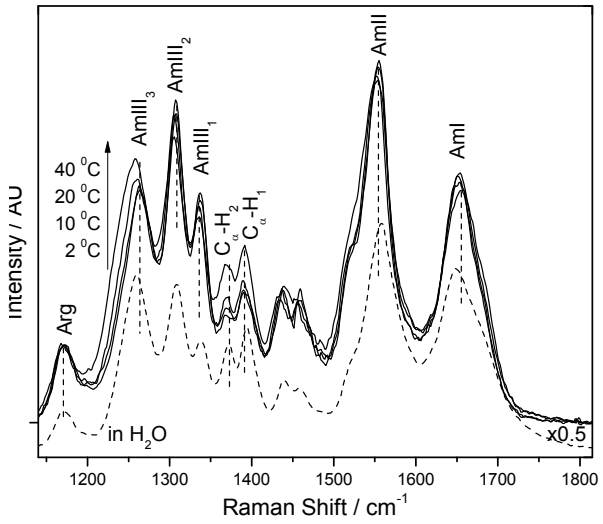

Figure 4.4: **Temperature dependence of 204 nm excited UVRS of AP in 50% methanol and UVRS of AP in pure water at 2 ^{0}C (dashed line); The methanol contribution was subtracted. The UVRS of AP was scaled to facilitate comparison.**

To calculate the α-helical fractions, we subtracted appropriate amounts of the temperature dependent PPII-like conformation basis spectra [22] from the measured and digitally smoothed UVRS of AP to minimize the C_α-H region intensity in the difference spectra. The basis spectra intensities subtracted are directly proportional to the concentrations of the PPII-like conformation at each temperature. The resulting difference spectra appear to be mainly α-helix-like. Fig.4.5 shows UVRR calculated fractions of α-helix-like conformation of AP in pure water and in 50% (v/v) alcohol. The α-helix-like conformations are dramatically stabilized in alcohol, and melt little as the temperature increases. TFE stabilizes the α-helical-like conformations the most, followed by ethanol, and then methanol, as previously observed. [8,12,18] The α-helix-like conformation melting curves in ethanol and in methanol are essentially identical. These conclusions obviously differ from the CD conclusions.

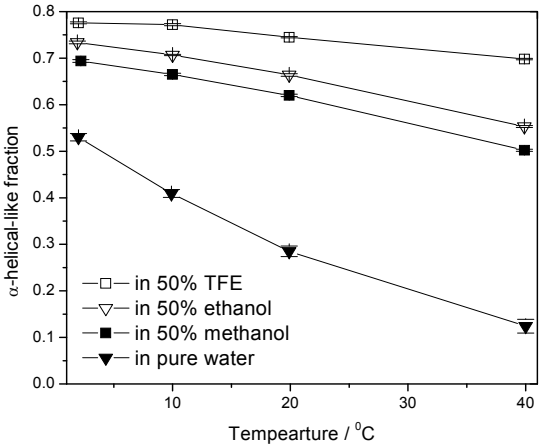

Figure 4.5: Raman calculated AP α-helical-like fractions (primarily α- and 3_{10} and π-helix (bulge)) of AP in different solutions.

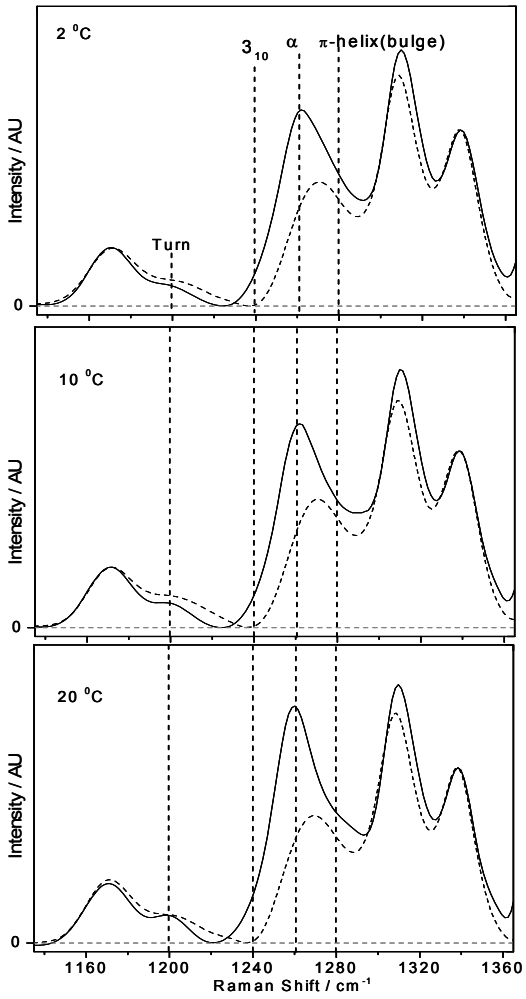

Figure 4.6: Calculated α-helix-like spectra of AP in pure water (solid line) and in 50% (v/v) methanol (dashed line). Calculated α-helix-like difference spectra were normalized to the intensity of the $AmIII_1$ band.

Fig. 4.6 shows the calculated α-helix-like spectra of AP in pure water and in 50% (v/v) methanol. The $AmIII_3$ band in pure water shows a peak at ~1258 cm^{-1} with a shoulder at ~1280 cm^{-1} and another shoulder at ~1240 cm^{-1}. Previous work showed that an $AmIII_3$ band at ~1258 cm^{-1} indicates the pure α-helical conformations, while a band at ~1280 cm^{-1} indicates a π-helix (bulge) while a band at ~1240 cm^{-1} indicates a 3_{10}-helix. [25] The $AmIII_3$ band in pure water narrows at higher temperature as previously observed,[26,27] indicating decreased concentrations of 3_{10}-helix and π-bulge conformations relative to the pure α-helix concentration as the temperature increases. The $AmIII_3$ band in 50% methanol shows a shoulder at ~1258 cm^{-1} and another shoulder at ~1280 cm^{-1} while the ~1240 cm^{-1} component is missing, indicating a lack of 3_{10}-helices. All helical spectra show an $AmIII_3$ band at ~1200 cm^{-1}, indicating turn structures. [26] Calculated α-helix-like spectra in other alcohols (not shown) are essentially identical to those in methanol, indicating similar ensembles of helical conformations.

We calculated the Gibbs free energy landscapes of AP (Fig. 4.7) along the Ψ-folding coordinate from the UVRR by using the methodology of Mikhonin et al. [19,26,28] The energy landscape (Fig. 4.7) is bumpy within the α-helix-like basin. Within this basin the pure α-helix conformation (Ψ ~ -45 º) is always lowest in energy, followed by the π-bulge conformation. The 3_{10}-helix conformation (Ψ ~ -20 º) lies at a slightly higher relative energy in pure water, but at much higher energies in alcohols. As the temperature increases the α-helix basin Gibbs free energy in pure water increases indicating that the α-helix is destabilized relative to the PPII-like conformation. The relative α-helix basin energies change very little with temperature in 50% alcohols. For all temperatures, the lowest α-helix Gibbs free energies occur in 50% TFE, followed by ethanol, methanol and finally pure water. The same trend is seen with the π-bulge energies. The alcohol induced π-bulge energy decrease is larger than that of the α-helix. Turn

conformations are stabilized by alcohols, consistent with previous observations that alcohols stabilize turns over PPII-like conformations.[29] In contrast, 3_{10}-helix conformations are dramatically destabilized by alcohols.

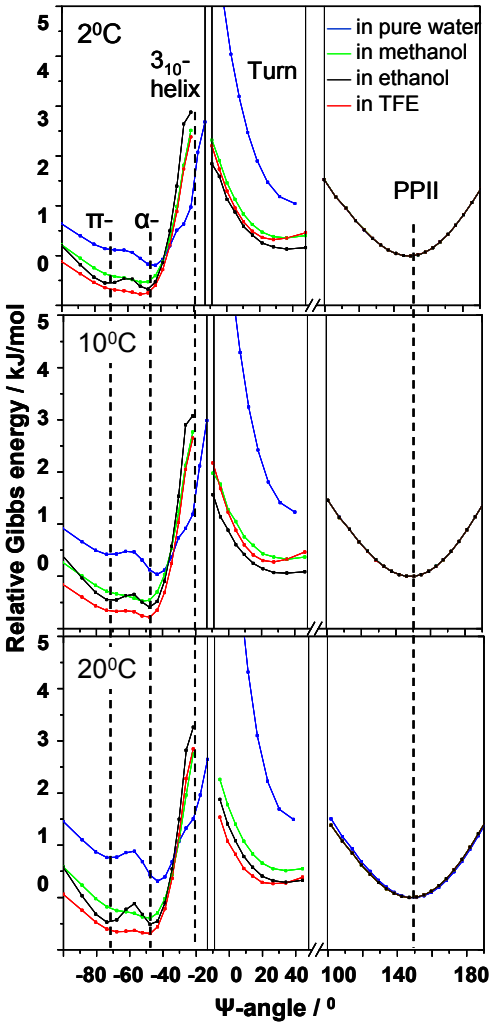

Figure 4.7: **Calculated Gibbs free energy landscape of AP along the Ramachandran Ψ angle coordinate. — in pure water; — in 50% methanol; — in 50% ethanol; — in 50% TFE;. The PPII-like conformation is the reference state.**

4.4 DISCUSSION

Impact of alcohols on the Gibbs free energies of helices. Numerous studies indicate that alcohols induce α-helix formation in proportion to the bulkiness of their alcohol hydrocarbon group. [8,12,18,30] This is confirmed by our UVRR results that the α-helix has the lowest Gibbs free energy in 50% TFE, followed by ethanol and methanol.

Alcohol molecules displace water in the peptide hydration shell which increases the hydrophobicity of the peptide-solvent interface, which should enhance intramolecular hydrogen bonding which should increase the α-helical content [31,32]. Previous studies [33] indicate that 3_{10}-helices allow greater solvent access to the peptide bonds and thus are favored as the solvent hydrophilicity increases. In contrast, the α-helix and π-helix are more favored as the solvent hydrophobicity increases. It is also known that the 3_{10}-helix is favored in the peptide terminal regions where solvent exposure is greatest. [34]

TFE induce multi helix segments. Our UVRR measurements that indicate that 50% TFE most stabilizes α-helical-like conformations, appears to conflict with the CD measurements that 50% TFE does not significantly stabilize α-helical conformations more than 25% TFE. Previous studies[22,35-37] showed that UVRR calculated α-helical conformation concentrations are higher than those calculated from CD [36] because the magnitude of the molar ellipticity per peptide bond (PB) decreases dramatically as the number of PB within an α-helix decreases. [11,38,39] In contrast, Raman is more linear; each peptide bond independently contributes to the Raman intensity [36,40] (except for the AmI band of the α-helical conformation where strong coupling between AmI vibrations exist [41]). Thus, we can explain the spectroscopic results by proposing that TFE induces the most α-helical PBs but also breaks long helices into short helices (See Appendix B1). Recent

studies have showed that TFE binds strongly to peptides, [42,43] while ethanol does not directly bind. [10]

To quantify the dependence of the CD molar ellipticity per PB of an α-helix, θ_n on the number of PBs within the helix, n, we fitted our experimental data to the empirical equation proposed by Chen et al, [39] (See Appendix B2);

$$\theta_n = -34530 \cdot (1 - \frac{1.6}{n}) \ \ \deg \cdot cm^2 \cdot dmol^{-1} \quad (4.1)$$

This allows us to relate the observed θ_{222} values to the UV Raman calculated helical fractions (See Appendix B3). The Fig. 4.8 calculated θ_{222} in 50% TFE is modeled to be less negative than that in 50% ethanol at low temperatures. (Calculated θ_{222} are slightly more negative than those measured in Fig. 4.2b because the $NaClO_4$ used as an internal standard in the UVRR measurements as an internal intensity standard but not included in the CD measurements stabilizes the α-helix conformation.[27])

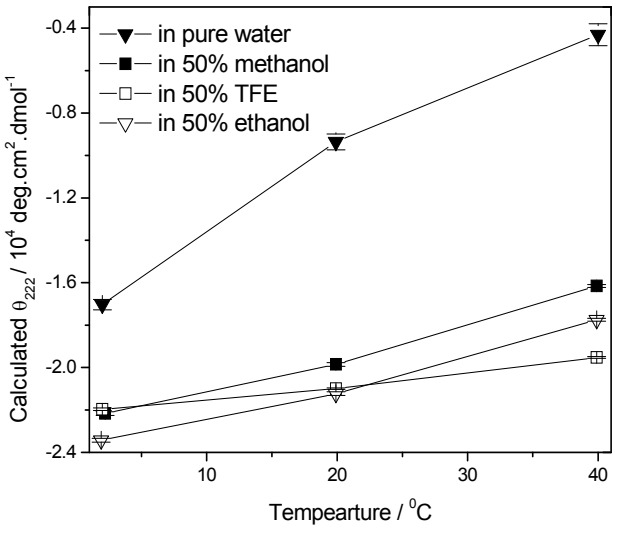

Figure 4.8: Calculated θ_{222} of AP in pure water and in 50% (v/v) alcohols.

4.5 CONCLUSIONS

CD and UVRR measurements indicate that TFE most stabilizes the α-helix, followed by ethanol, methanol and pure water. We determined the Gibbs free energy landscape from the UVRR spectra and found that the alcohol induced π-bulge energy decrease is larger than that of the α-helix, while the 3_{10}-helix energy increases due to the alcohol increased hydrophobicity. Turns are stabilized by alcohols as well. We also found that while TFE induces more α helices, it favors multiple, shorter helical segments.

4.6 ACKNOWLEDGEMENTS

We thank Bhavya Sharma, Lu Ma, Zhenmin Hong and David Punihaole for useful discussions.

4.7 REFERENCES

(1) Klibanov, A. M. *Nature* **2001,** 409, (6817), 241-246.

(2) Carrea, G.; Riva, S. *Angew Chem Int Ed* **2000,** 39, (13), 2226-2254.

(3) Scharnagl, C.; Reif, M.; Friedrich, J. *Biochimica Et Biophysica Acta-Proteins and Proteomics* **2005,** 1749, (2), 187-213.

(4) Kony, D. B.; Hunenberger, P. H.; van Gunsteren, W. F. *Protein Sci* **2007,** 16, (6), 1101-1118.

(5) Waterhous, D. V.; Johnson, W. C. *Biochemistry* **1994,** 33, (8), 2121-2128.

(6) Roccatano, D. *Curr Protein Pep Sci* **2008,** 9, (4), 407-426.

(7) Pace, C. N.; Trevino, S.; Prabhakaran, E.; Scholtz, J. M. *Phil Tran Royl Soc London Ser B-Biol Sci* **2004,** 359, (1448), 1225-1234.

(8) Hirota, N.; Mizuno, K.; Goto, Y. *J Mol Biol* **1998,** 275, (2), 365-378.

(9) Buck, M. *Quart Rev Biophys* **1998,** 31, (3), 297-355.

(10) Fioroni, M.; Diaz, M. D.; Burger, K.; Berger, S. *J Am Chem Soc* **2002,** 124, (26), 7737-7744.

(11) Luo, P. Z.; Baldwin, R. L. *Biochemistry* **1997,** 36, (27), 8413-8421.

(12) Kinoshita, M.; Okamoto, Y.; Hirata, F. *J Am Chem Soc* **2000,** 122, 2773-2779.

(13) Roccatano, D.; Colombo, G.; Fioroni, M.; Mark, A. E. *Proc Natl Acad Sci USA* **2002,** 99, (19), 12179-12184.

(14) Walgers, R.; Lee, T. C.; Cammers-Goodwin, A. *J Am Chem Soc* **1998,** 120, 5073-5079.

(15) Reiersen, H.; Rees, A. R. *Protein Eng* **2000,** 13, (11), 739-743.

(16) Roccatano, D.; Fioroni, M.; Zacharias, M.; Colombo, G. *Protein Sci* **2005,** 14, (10), 2582-2589.

(17) Olivella, M.; Deupi, X.; Govaerts, C.; Pardo, L. *Biophys J* **2002,** 82, (6), 3207-3213.

(18) Liu, H. L.; Hsu, C. M. *Chem Phys Lett* **2003,** 375, (1-2), 119-125.

(19) Bykov, S.; Lednev, I.; Ianoul, A.; Mikhonin, A.; Munro, C.; Asher, S. A. *Appl Spectrosc* **2005,** 59, (12), 1541-1552.

(20) Manning, M. C.; Woody, R. W. *Biopolymers* **1991,** 31, 569-586.

(21) Asher, S.; Mikhonin, A.; Bykov, S. *J Am Chem Soc* **2004,** 126, (27), 8433-8440.

(22) Lednev, I. K.; Karnoup, A. S.; Sparrow, M. C.; Asher, S. A. *J Am Chem Soc* **1999,** 121, (35), 8074-8086.

(23) Myshakina, N. S.; Ahmed, Z.; Asher, S. A. *J Phys Chem B* **2008,** 112, (38), 11873-11877.

(24) Wang, Y.; Purrello, R.; jordan, T.; Spiro, T. G. *J. Am. Chem. Soc.* **1991,** 113, 6359-6368.

(25) Mikhonin, A. V.; Bykov, S. V.; Myshakina, N. S.; Asher, S. A. *J Phys Chem B* **2006,** 110, (4), 1928-1943.

(26) Mikhonin, A. V.; Asher, S. A. *J. Am. Chem. Soc.* **2006,** 128, (42), 13789-13795.

(27) Xiong, K.; Asciutto, E. K.; Madura, J. D.; Asher, S. A. *Biochemistry* **2009**, 10818-10826.

(28) Ma, L.; Ahmed, Z.; Mikhonin, A. V.; Asher, S. A. *J Phys Chem B* **2007,** 111, (26), 7675-7680.

(29) Liu, Z. G.; Chen, K.; Ng, A.; Shi, Z. S.; Woody, R. W.; Kallenbach, N. R. *J. Am. Chem. Soc.* **2004,** 126, (46), 15141-15150.

(30) Dwyer, D. S. *Biopolymers* **1999,** 49, (7), 635-645.

(31) Deshpande, A.; Nimsadkar, S.; Mande, S. C. *Acta Cryst Sec D-Biol Cryst* **2005,** 61, 1005-1008.

(32) Starzyk, A.; Barber-Armstrong, W.; Sridharan, M.; Decatur, S. M. *Biochemistry* **2005,** 44, (1), 369-376.

(33) Sorin, E. J.; Rhee, Y. M.; Shirts, M. R.; Pande, V. S. *J Mol Biol* **2006,** 356, (1), 248-256.

(34) Millhauser, G. L.; Stenland, C. J.; Hanson, P.; Bolin, K. A.; vandeVen, F. J. M. *J Mol Biol* **1997,** 267, (4), 963-974.

(35) Balakrishnan, G.; Hu, Y.; Bender, G. M.; Getahun, Z.; DeGrado, W. F.; Spiro, T. G. *J. Am. Chem. Soc.* **2007,** 129, (42), 12801-12808.

(36) Ozdemir, A.; Lednev, I. K.; Asher, S. A. *Biochemistry* **2002,** 41, (6), 1893-1896.

(37) Ianoul, A.; Mikhonin, A.; Lednev, I. K.; Asher, S. A. *J Phys Chem A* **2002,** 106, (14), 3621-3624.

(38) Woddy, R. W., *Circular Dichroism and the Conformational Analysis of Biomolecules*. Plenum Press: New York, 1996; p 25-68.

(39). Chen, Y.-H.; Yang, J. T.; Chau, K. H. *Biochemistry* **1974,** 13, 3350-3359.

(40) Mikhonin, A. V.; Asher, S. A. *J Phys Chem B* **2005,** 109, (7), 3047-3052.

(41) Myshakina, N. S.; Asher, S. A. *J Phys Chem B* **2007,** 111, (16), 4271-4279.

(42) Gerig, J. T. *Biophys J* **2004,** 86, (5), 3166-3175.

(43) Diaz, M. D.; Berger, S. *Mag Res Chem* **2001,** 39, (7), 369-373.

(44) Hong, Q.; Schellman, J. A. *J Phys Chem* **1992,** 96, (10), 3987-3994.

(45) Doig, A. J. *Biophys Chem* **2002,** 101, 281-293.

(46) Yang, J. X.; Zhao, K.; Gong, Y. X.; Vologodskii, A.; Kallenbach, N. R. *J. Am. Chem. Soc.* **1998,** 120, (41), 10646-10652.

(47) Scholtz, J. M.; Qian, H.; York, E. J.; Stewart, J. M.; Baldwin, R. L. *Biopolymers* **1991,** 31, 1463-1470.

CHAPTER 5

Conformation of Poly-L-Glutamate is Independent of Ionic Strength

This Chapter was published in *Biophysical Chemistry*, **2012**, 162, 1-5. The co-authors are Kan Xiong, Lu Ma and Sanford A Asher.

5.0 CONFORMATION OF POLY-L-GLUTAMATE IS INDEPENDENT OF IONIC STRENGTH

CD and UV resonance Raman measurements surprisingly find that the charge screening of even 2 M concentrations of NaCl and KCl do not alter the unfolded PPII and 2.5_1-helix conformations of poly-L-glutamate. These salts appear to be excluded from the region between the side chain charges and the peptide backbone. Furthermore, no direct ion pairing occurs between these salts and the side chain carboxylates.

5.1 INTRODUCTION

The conformations of peptides and proteins depend upon their solution compositions, especially upon the presence of species that specifically interact with the peptides or proteins, or the water solvent.[1-3] In the work here we investigate the dependence of peptide conformation on the presence of salts.

Previous studies have demonstrated that ions can interact with peptides and proteins by binding, for example, to form ion pairs. [4, 5] Collins et al's model of matching water affinities predicts that preferential ion pair formation occurs between oppositely charged ions of similar charge densities.[4-6] Alternatively the impact of ions can be less specific, as when they passively screen sidechain electrostatic interactions.[7] Higher ionic strengths more effectively screen electrostatic interactions between charges as well as between charges and fields associated with, for example, helix dipoles.[8-10] Another potential mechanism that could impact conformation could occur by the impact of ions on the water solvent properties that control protein/peptide hydration.[11] The Hofmeister series orders ions in their decreasing ability to perturb the water

structure.[12] Kosmotropic ions interact strongly with water, leaving less water available for protein hydration. This phenomenon is proposed to "salt out" proteins. In contrast, chaotropic ions interact weakly with water, leaving water more available for protein hydration. These ions "salt in" proteins.

In this work, we used circular dichroism (CD) and UV resonance Raman spectroscopy (UVRR) to investigate the impact of Na^+ and K^+ on the conformation of poly-L-glutamate (PGA). Previous studies indicate that PGA in pure water at pH 9 adopts predominantly unfolded PPII and 2.5_1-helix conformations.[13] The 2.5_1-helix conformation (with ~2.5 residues per helical turn) is more extended than the PPII conformation (with ~3 residues per helical turn). It was proposed that electrostatic repulsion between GLU side chains is responsible for the formation of the 2.5_1-helix conformation because it minimizes the repulsion between its splayed side chains.[13, 14] Surprisingly, we observe a lack of pertubation by high concentrations of Na^+ and K^+ on the conformation of poly-L-glutamate at pH 8.3. We find that PGA is not converted to the α-helix conformation at high NaCl and KCl concentrations, and further that the equilibrium between PPII and 2.5_1-helix conformations of PGA is not altered by the presence of 2 M salts.

5.2. EXPERIMENTAL

Samples: PGA (MW_{vis}=11600, MW_{mALLS}=6649. DP_{vis} and DP_{MALLS} refer to the degree of polymerization measured by viscosity and multi-angle laser light scattering, respectively.) was purchased from Sigma Chemical. Peptide samples were prepared at 1 mg/ml concentrations by dissolving PGA in pure water or 2 M salt, and adjusted to pH 8.3. Sodium acetate (>99% purity) was purchased from EM Science; potassium acetate (>99% purity) was purchased from Sigma.

CD Spectra: CD spectra were measured for poly-L-glutamate by using a Jasco-715 spectropolarimeter with a 0.02 cm path length cuvette. We collected CD spectra from 250 - 190 nm. We utilized 3-min accumulation times and five accumulations were averaged.

UVRR Spectra: The UVRR apparatus has been described in detail by Bykov et al.[33] Briefly, 204 nm UV light (2 mW average power, 100 μm diameter spot, 25-40 ns pulse width) was obtained by mixing the 3rd harmonic with the 816 nm fundamental of a 1 kHz repetition rate tunable Ti:Sapphire laser system (DM20-527 TU-L-FHG) from Photonics Industries. The sample was circulated in a free surface, temperature-controlled stream. A 165° sampling backscattering geometry was used. The collected light was dispersed by a double monochromator onto a back thinned CCD camera with a Lumogen E coating (Princeton Instruments-Spec 10 System). We utilized 5-min accumulation times, and four accumulations were averaged.

5.3 RESULTS AND DISCUSSION

5.3.1 CD results

The PGA conformations depend on the solution pH which defines the GLU side chain electrostatic interactions.[15] We performed all measurements at pH 8.3 where all GLU side chains are charged. The CD spectrum of PGA in pure water at 10 °C at pH 8.3 (black, Fig. 5.1) shows a positive band at ~217 nm and a strong negative band at ~197 nm, characteristic of PPII-like conformations.[16, 17] The 0.2 M NaCl or KCl solution spectra are essentially identical to that in pure water. In 1.0 M NaCl or KCl, the positive band slightly decreases in amplitude while the

trough becomes less negative, indicating only a slight destabilization of the PPII-like conformation.[17] The PPII-like features slightly further decrease in 2.0 M salt solutions; the NaCl and KCl CD spectra remain identical. These results are consistent with Lizuka et al [18] and Wada's [19] experimental investigations.

We calculated the salt induced fractional α-helical concentration, f_α, by using a two-state model (eq 5.1) by utilizing the reported θ_{223} value for the pure α-helix of PGA ($[\theta]_\alpha$ = -35400 deg.cm^2.dmol^{-1} [20]) and the Fig. 5.1 measured θ_{223} value for PGA in pure water where unfolded conformations dominate [13] ($[\theta]_{unfold}$ = 3250 deg.cm^2.dmol^{-1}). The calculated fractional α-helical concentration increases in 1 M and 2 M salts are 0.02 ± 0.01 and 0.04 ± 0.01, respectively. This clearly indicates the negligible α-helical concentration change.

$$f_\alpha = \frac{[\theta]_{223} - [\theta]_{unfold}}{[\theta]_\alpha - [\theta]_{unfold}} \qquad (5.1)$$

The CD spectra measured at 30 ^{o}C and 50 ^{o}C (See Fig. C1-2 in Appendix C) also indicate that similar high NaCl or KCl concentrations do not significantly alter the PGA conformational equilibrium.

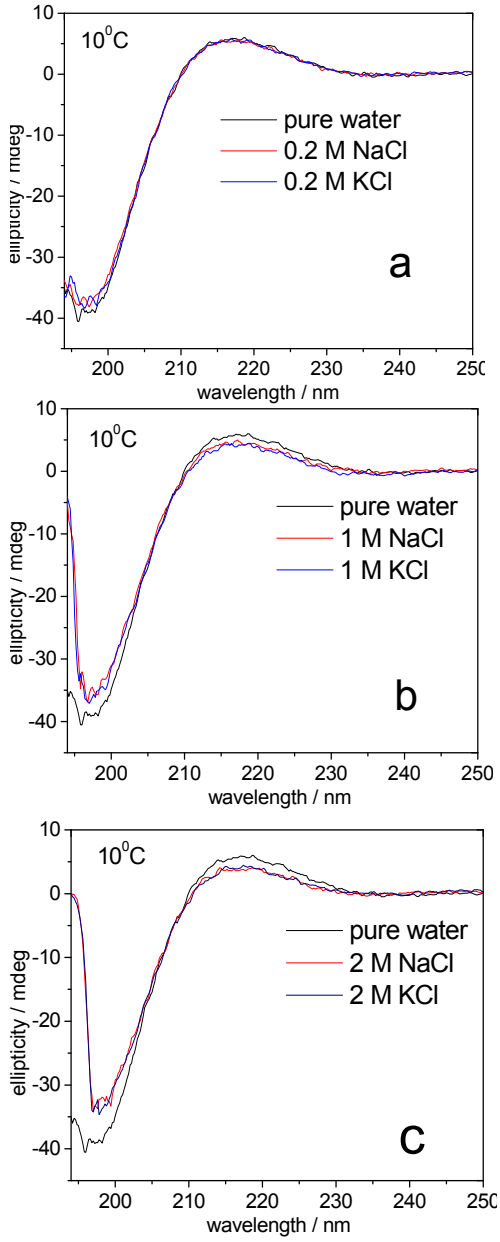

Figure 5.1: CD spectra of 1 mg/ml PGA in pure water and in a) 0.2 M, b) 1.0 M and c) 2 M NaCl and KCl at pH 8.3 at 10 °C.

5.3.2 UVRR results

The UVRR of PGA in pure water at pH 8.3 (Fig. 5.2a) show an AmI band at ~1667 cm^{-1} (mainly CO s), an AmII band at ~1568 cm^{-1} (mainly out of phase combination of CN s and NH b), and

(C)C_α-H bending bands at ~1395 cm^{-1}. The AmIII region which mainly involves in phase combination of CN s and NH b occurs between ~1200 cm^{-1} and ~1340 cm^{-1}. The AmIII region contains an $AmIII_2$ band doublet at ~1298 cm^{-1} and ~1317 cm^{-1}, and an $AmIII_3$ band doublet at ~1247 cm^{-1} and ~1269 cm^{-1}. The $AmIII_3$ band at ~1247 cm^{-1} derives from a PPII-like conformation, while the $AmIII_3$ band at ~1269 cm^{-1} derives from a 2.5_1-helix conformation. [13]

In 2 M NaCl and KCl, the C_α-H intensity slightly decreases compared to pure water, indicating a small α-helix content increase.[21] Also, the $AmIII_3$ region intensity slightly decreases.[1, 22] Surprisingly, the relative intensity of the PPII to 2.5_1-helix bands does not change, even though the 2.5_1-helix conformation is stabilized by electrostatic repulsion between side chains. [13, 14] The intensity in the AmI region increases dramatically because of a surprising increase in the Raman cross section of the underlying ~1660 cm^{-1} water O-H bending band due to the presence of a $Cl^- \rightarrow$ water charge transfer band.[23-25]

To calculate the magnitude of the salt induced α-helical conformation concentration increase, we subtracted the UVRR of PGA in pure water [where it exists in a PPII-like and 2.5_1-helix conformation (referred to as unfolded conformations in ***Section 5.3.1***) equilibrium. [13]], from that of PGA in 2 M NaCl and KCl such that the C_α-H band intensity at ~1395 cm^{-1} was minimized in the UVRR difference spectrum. The resulting PGA pure water UVRR intensities subtracted are directly proportional to the concentration of the PPII-like and 2.5_1-helix conformations at each temperature. From the difference spectra of the 2 M NaCl solution, we calculated a fractional α-helical concentration increase of 0.08 ± 0.03 (where the standard deviation between temperatures is ± 0.03.). The fractional α-helical concentration increase is 0.07 ± 0.03 for 2 M KCl. Thus, neither NaCl nor KCl induces much PGA α-helix formation.

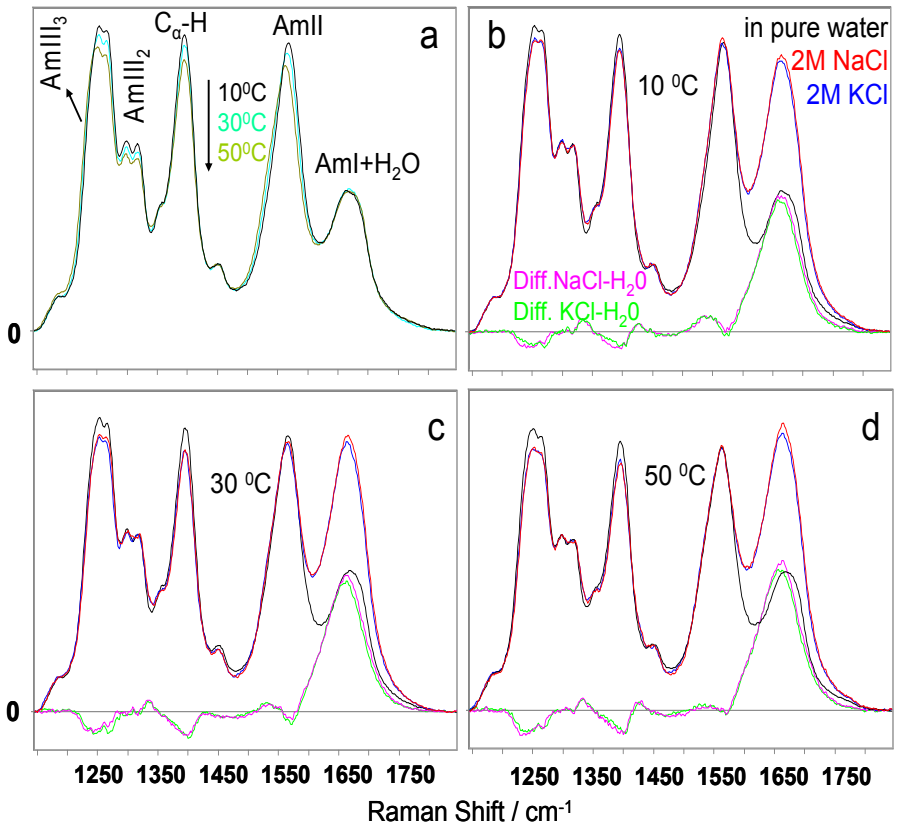

Figure 5.2: **a) Temperature dependence of 204 nm excited UVRS of 1 mg/ml PGA in pure water. UVRS of PGA in pure water and in the presence of 2 M NaCl and KCl and their difference spectra: b) at 10 ^{0}C; c) at 30 ^{0}C; d) at 50 ^{0}C; All spectra were normalized to the 1450 cm^{-1} band which shows little intensity variation.** [15]

NaCl and KCl occur in the middle of Hofmeister series, indicating that NaCl and KCl should have intermediate effects on the dehydration of PGA.[11] Collins et al.'s model of matching water affinities [4-6], that predicts that preferential ion pair formation occurs between oppositely charged ions of similar charge densities, predicts that the penultimate carboxylate would preferentially ion pair with Na^+ compared to K^+.[4] This is supported by recent experimental and theoretical studies showing that $-COO^-$ groups preferentially pair with Na^+.[26-30]

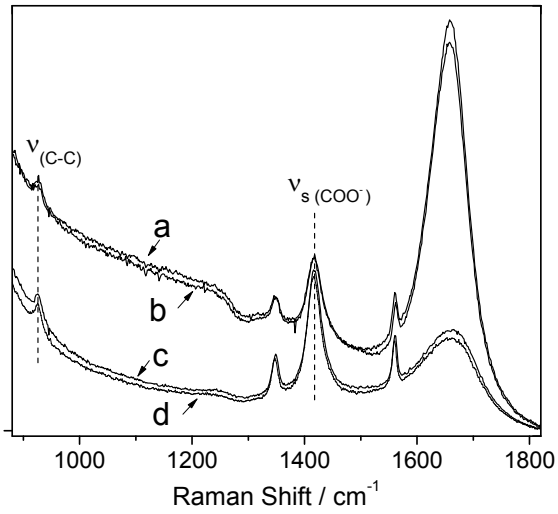

Figure 5.3: **204 nm excited UVRS of sodium acetate (NaAc) and potassium acetate (KAc) and in the presence of 4 M NaCl and 4 M KCl at 10 ^{0}C: a) 0.02 M NaAc + 4 M NaCl; b) 0.02 M KAc + 4 M KCl; c) 0.02 M KAc; d) 0.02 M NaAc.**

We measured the UVRR of Na^+ (K^+) acetate in the presence of 4 M NaCl (KCl). Previous studies indicate that ion binding to the -COO^- groups significantly shifts the carboxylate symmetric stretching band, $\nu_{s\,(COO^-)}$ and the C-C stretching band, $\nu_{(C-C)}$ to higher frequencies.[31, 32] The $\nu_{s\,(COO^-)}$ and $\nu_{(C-C)}$ band frequencies do not change (Fig. 5.3) in 4 M Na^+ and 4 M K^+, indicating that neither Na^+ nor K^+ directly binds to the COO^- groups.

Electrostatic repulsion between GLU side chains is responsible for the formation of the 2.5_1-helix conformation because it minimizes the repulsion between its splayed side chains.[13, 14] Surprisingly we observe a lack of a NaCl or KCl dependence of the PPII and 2.5_1-helix PGA conformational equilibrium. We expected that high salt concentrations would decrease the electrostatic repulsion between GLU side chains. We can estimate the electrostatic repulsion decrease induced by salt screening from eq 2:

$$\psi(l) = \psi_0 \cdot \frac{\varepsilon_w}{\varepsilon_r} \cdot e^{-l\cdot\kappa} \qquad (5.2)$$

where $\psi(l)$ is the electrostatic potential at distance l in presence of salt screening; ψ_0 is the electrostatic potential with no screening; ε_w is the dielectric constant of pure water (ε_w=83 [33]); ε_r is the dielectric constant of salt solutions (ε_r in 0.2 M, 1.0 M and 2.0 M NaCl and KCl solutions are 80, 70 and 60, respectively.[33, 34]); κ^{-1} is the Debye length which is defined by eq 3 [7]:

$$\kappa^{-1} = \sqrt{\frac{\varepsilon_r \varepsilon_0 k_B T}{2 N_A e^2 I}} \qquad (5.3)$$

where ε_0 is the permittivity of free space (ε_0= 8.854× 10^{-12} $C^2 \cdot N^{-1} \cdot m^{-2}$); k_B is the Boltzmann constant (k_B=1.380 ×10^{-23} $N \cdot m \cdot K^{-1}$); T is the absolute temperature (T=283.15 K); N_A is Avogadro's number (N_A= 6.022×10^{23} mol^{-1}); e is the elementary charge (e= 1.602×10^{-19} C); I is the ionic strength of the salt solutions. The Debye lengths, κ^{-1} in 0.2 M, 1.0 M and 2.0 M NaCl and KCl solutions are ~6.8 Å, 2.8 Å and 1.9 Å, while the distances between neighboring GLU sidechain charges are 8.3 Å and 8.4 Å for the PPII and 2.5_1-helix conformations, respectively.[13] We estimate that the GLU sidechain electrostatic repulsion should decrease by more than 50-fold for 2 M salt relative to that in pure water.

We naively expected that this change in electrostatic interactions should alter the equilibrium between the PPII and 2.5_1-helix conformations. The fact that this does not occur suggests that the ions are excluded from the region between side chains. This would also explain why the 2.5 M NaCl does not alter the PPII and 2.5_1-helix conformational equilibrium in poly-L-lysine.[35] It should be noted that our experimental results contradict the recent molecular dynamics simulation studies that indicate that Na^+ controls peptide conformations by binding to carboxylate side chain.[36, 37] Obviously, the simulations are not using appropriate force fields.[38]

5.4. CONCLUSIONS

We used circular dichroism and UV resonance Raman spectroscopy, to study the impact of screening of NaCl and KCl on the conformational equilibria of poly-L-glutamate. In contradiction to expectations, we observe a lack of impact of high concentrations of NaCl and KCl on the conformation of poly-L-glutamate. These salts appear to be excluded from the region between the side chain charges and the peptide backbone. Furthermore, we see no evidence of formation of ion pairs between Na^+ and K^+ salts and the side chain carboxylates.

5.5 ACKNOWLEDGEMENTS

We thank Prof. Jeffry Madura and Dr. Sergei V. Bykov for useful discussions. This work was supported by NIH grant 1RO1EB009089.

5.6 REFERENCES

(1) Xiong, K.; Asciutto, E. K.; Madura, J. D.; Asher, S. A. *Biochemistry* **2009**, 10818-10826.

(2) Cacace, M. G.; Landau, E. M.; Ramsden, J. J. *Quarterly Reviews of Biophysics* **1997,** 30, 241-277.

(3) Thomas, A. S.; Elcock, A. H. *Journal of the American Chemical Society* **2007,** 129, (48), 14887-14898.

(4) Collins, K. D. *Methods* **2004,** 34, (3), 300-311.

(5) Collins, K. D.; Neilson, G. W.; Enderby, J. E. *Biophysical Chemistry* **2007,** 128, (2-3), 95-104.

(6) Collins, K. D. *Biophysical Journal* **1997,** 72, (1), 65-76.

(7) Debye, P.; Huckel, E. *Phys. Z* **1923,** 24, 185-206.

(8) Shoemaker, K. R.; Kim, P. S.; York, E. J.; Stewart, J. M.; Baldwin, R. L. *Nature* **1987,** 326, 573-567.

(9) Hol, W. G. J. *Prog. Biophys. molec. Biol* **1985,** 45, 149-195.

(10) Hol, W. G. J.; Duijnen, P. T. v.; Berendsen, H. J. C. *Nature* **1978,** 273, 443-446.

(11) Collins, K. D.; Washabaugh, M. W. *QUARTERLY REVIEWS OF BIOPHYSICS* **1985,** 18, 323-422.

(12) Zhang, Y. J.; Cremer, P. S. *Current Opinion in Chemical Biology* **2006,** 10, (6), 658-663.

(13) Mikhonin, A. V.; Myshakina, N. S.; Bykov, S. V.; Asher, S. A. *Journal of the American Chemical Society* **2005,** 127, (21), 7712-7720.

(14) Krimm, S.; Mark, J. E. *Proceedings of the National Academy of Sciences of the United States of America* **1968,** 60, 1122-1129.

(15) Song, S.; Asher, S. A. *J. Am. Chem. Soc.* **1989,** 111, 4295-4305.

(16) Sreerama, N.; Woody, R. W. *Biochemistry* **1994,** 33, (33), 10022-10025.

(17) Shi, Z. S.; Chen, K.; Liu, Z. G.; Kallenbach, N. R. *Chemical Reviews* **2006,** 106, (5), 1877-1897.

(18) Iizuka, E.; Yang, J. T. *Biochemistry* **1965,** 4, 1249-1257.

(19) Wada, A. *Molecular Physics* **1960,** 3, 409-416.

(20) Yamaoka, K.; Masujima, T. *Bulletin of the Chemical Society of Japan* **1979,** 52, (5), 1286-1296.

(21) Wang, Y.; Purrello, R.; Jordan, T.; Spiro, T. G. *Journal of the American Chemical Society* **1991,** 113, (17), 6359-6368.

(22) Sharma, B.; Bykov, S. V.; Asher, S. A. *Journal of Physical Chemistry B* **2008,** 112, (37), 11762-11769.

(23) Schultz, J. W.; Hornig, D. F. *J. Phys. Chem.* **1961,** 65, 2131-2138.

(24) Wall, T. T.; Hornig, D. F. *J. Chem. Phys.* **1967,** 47, 784-792.

(25) Xiong, K.; Asher, S. A. *Journal of Physical Chemistry A* **2011,** 115, (34), 9345-9348.

(26) Aziz, E. F.; Ottosson, N.; Eisebitt, S.; Eberhardt, W.; Jagoda-Cwiklik, B.; Vacha, R.; Jungwirth, P.; Winter, B. *Journal of Physical Chemistry B* **2008,** 112, (40), 12567-12570.

(27) Jagoda-Cwiklik, B.; Vacha, R.; Lund, M.; Srebro, M.; Jungwirth, P. *Journal of Physical Chemistry B* **2007,** 111, (51), 14077-14079.

(28) Vrbka, L.; Vondrasek, J.; Jagoda-Cwiklik, B.; Vacha, R.; Jungwirth, P. *Proceedings of the National Academy of Sciences of the United States of America* **2006,** 103, (42), 15440-15444.

(29) Dzubiella, J. *Journal of the American Chemical Society* **2008,** 130, (42), 14000-14007.

(30) von Hansen, Y.; Kalcher, I.; Dzubiella, J. *Journal of Physical Chemistry B* **2010,** 114, 13815-13822.

(31) Quiles, F.; Burneau, A. *Vibrational Spectroscopy* **1998,** 16, (2), 105-117.

(32) Tackett, J. E. *Applied Spectroscopy* **1989,** 43, 483-489.

(33) Buchner, R.; Hefter, G. T.; May, P. M. *Journal of Physical Chemistry A* **1999,** 103, (1), 1-9.

(34) Lyashchenko, A.; Lileev, A. *Journal of Chemical and Engineering Data* **2010,** 55, (5), 2008-2016.

(35) Ma, L.; Ahmed, Z.; Asher, S. A. *Journal of Physical Chemistry B* **2011,** 115, (14), 4251-4258.

(36) Fedorov, M. V.; Goodman, J. M.; Schumm, S. *Journal of the American Chemical Society* **2009,** 131, (31), 10854-10856.

(37) Fedorov, M. V.; Goodman, J. M.; Schumm, S. *Chemical Communications* **2009**, (8), 896-898.

(38) Kaminski, G. A.; Friesner, R. A.; Tirado-Rives, J.; Jorgensen, W. L. *Journal of Physical Chemistry B* **2001,** 105, (28), 6474-6487.

CHAPTER 6

Direct Observations of Conformational Distributions of Intrinsically Disordered P53 Peptides Using UV Raman and Explicit Solvent Simulations

This Chapter was published in *J. Phys. Chem. A.*, **2011**, *115*, 9520–9527. The co-authors are Kan Xiong, Matthew C. Zwier, Nataliya S. Myshakina, Virginia M. Burger, Sanford A. Asher, and Lillian T. Chong.

6.0 DIRECT OBSERVATIONS OF CONFORMATIONAL DISTRIBUTIONS OF INTRINSICALLY DISORDERED P53 PEPTIDES USING UV RAMAN AND EXPLICIT SOLVENT SIMULATIONS

We report the first experimental measurements of Ramachandran Ψ-angle distributions for intrinsically disordered peptides: the N-terminal peptide fragment of tumor suppressor p53 and its P27S mutant form. To provide atomically detailed views of the conformational distributions, we performed classical, explicit-solvent molecular dynamics simulations on the microsecond timescale. Upon binding its partner protein, MDM2, wild-type p53 peptide adopts an α-helical conformation. Mutation of Pro27 to serine results in the highest affinity yet observed for MDM2-binding of the p53 peptide. Both UV resonance Raman spectroscopy (UVRR) and simulations reveal that the P27S mutation decreases the extent of PPII helical content and increases the probability for conformations that are similar to the α-helical MDM2-bound conformation. In addition, UVRR measurements were performed on peptides that were isotopically labeled at the Leu26 residue preceding the Pro27 in order to determine the conformational distributions of Leu26 in the wild-type and mutant peptides. The UVRR and simulation results are in quantitative agreement in terms of the change in the population of non-PPII conformations involving Leu26 upon mutation of Pro27 to serine. Finally, our simulations reveal that the MDM2-bound conformation of the peptide is significantly populated in both the wild-type and mutant isolated peptide ensembles in their unbound states, suggesting that MDM2 binding of the p53 peptides may involve conformational selection.

6.1 INTRODUCTION

Intrinsically disordered proteins, which lack specific tertiary structures,[1] comprise at least a third of some eukaryotic genomes.[2] Many of these proteins adopt distinct conformations only upon binding to their partner proteins, suggesting a new paradigm for protein-protein recognition. A classic example is the natively unfolded N-terminal peptide fragment of tumor suppressor protein p53 (residues 17-29), which adopts an α-helical conformation upon binding to the MDM2 oncoprotein.[3] NMR studies show that this peptide is at least partially preorganized in its unbound state for binding to MDM2.[4] In particular, mutation of Pro27 to a serine further preorganizes the peptide by increasing its α-helical content; as a result, the mutant peptide has the highest MDM2 affinity observed (K_d = 47 nM).[4] Not surprisingly, this P27S mutation results in significant conformational changes for the Leu26 peptide bond that precedes the proline.[4]

Although numerous NMR studies have provided high-resolution structural information about the N-terminal domain of p53,[4-9] a detailed view of its conformational diversity in the unbound state has been lacking. An incisive approach for determining the conformational diversity of the peptide is UV resonance Raman (UVRR) spectroscopy, which can be used to determine the distributions of backbone torsional Ψ angles.[10-14] In addition, molecular dynamics (MD) simulations can be used to characterize the conformational diversity of the peptide with atomistic detail. However, due to their large computational expense, only short simulations (≤ 150 ns) have been conducted to explore the dynamics of the unbound p53 peptide.[15-19]

In this work, we use UVRR spectroscopy and microsecond-timescale classical (*i.e.* molecular mechanics) molecular dynamics (MD) simulations to examine the p53 N-terminal peptide conformational dependence on the P27S mutation. Both UVRR measurements and MD

simulations show a decrease in the PPII content and an increase in the non-PPII content upon P27S mutation. In addition, our simulations reveal that the α-helical conformations that are characteristic of the MDM2-bound state are significantly populated in the unbound state of both the wild-type and mutant p53 peptides, suggesting that MDM2 might bind the p53 peptide through conformational selection.

6.2 EXPERIMENTAL AND COMPUTATIONAL METHODS

6.2.1 Experimental Methods

Samples. The wild-type p53 peptide fragment (residues 17-29) with the sequence Acetyl-ETFSDLWKLLPEN-NH_2 and the mutant P27S peptide with the sequence Acetyl-ETFSDLWKLLSEN-NH_2 were synthesized by CHI SCIENTIFIC (≥95% purity). Isotopically labeled peptides with perdeuterated Leu26 were synthesized by AnaSpec (≥ 95% purity). Peptide samples were prepared at 1 mg/ml concentrations (~ 0.6 mM) at pH 7. Samples of Trp and Phe (≥ 95% purity) were purchased from Sigma and prepared at ~ 0.6 mM concentrations.

CD spectra. CD spectra were measured for the wild-type and P27S mutant peptides by using a Jasco-715 spectropolarimeter with a 0.02 cm path length cuvette. We co-added ten individual spectra.

UVRR spectra. UVRR spectra were measured for both the wild-type and P27S mutant peptides using an spectrometer that was described in detail by Bykov et al.[20] Briefly, 204 nm light was utilized to enhance the peptide bond vibrations by exciting within the $\pi \rightarrow \pi^*$

electronic transitions of the peptide bonds.[21] The 204 nm UV light (2 mW average power, 100 μm diameter spot, 25-40 ns pulse width) was obtained by mixing the 3rd harmonic with the 816 nm fundamental of a 1 kHz repetition rate tunable Ti:Sapphire laser system (DM20-527 TU-L-FHG) from Photonics Industries. The 229 nm UV light (1 mW average power, 100 μm diameter spot size), which was produced by an intracavity frequency doubled Ar^+ laser (Coherent, FReD 400) was utilized to enhance the Trp aromatic ring vibrations.[22]

The sample was circulated in a free surface, temperature-controlled stream. A 165° sampling backscattering geometry was used. The collected light was dispersed by a double monochromator onto a back thinned CCD camera with a Lumogen E coating (Princeton Instruments-Spec 10 System). We utilized 5-minute accumulation times, and four accumulations were co-added. Internal standard concentrations of 0.2 M $NaClO_4$ were used for the Raman studies. Raman spectra were normalized to the peak height of the 932 cm^{-1} ClO_4^- band.

Distributions of backbone torsional Ψ angles were calculated from 204 nm excited UVRR spectra using the methodology of Mikhonin et al.[11,23,24] (see Fig. D1-3 and text in Appendix D). Prior to these calculations, Raman bands due to Trp and Phe aromatic rings (Fig. D4) were subtracted from the spectra. UVRR measurements excited by 229 nm light were performed to determine the extent of solvent exposure of the Trp residues in the wild-type and mutant peptides. The differences in solvent exposure between the wild-type and mutant peptides were calculated based on differences in the Raman cross sections of the Trp Raman bands.[22]

6.2.2 Computational Methods

MD simulations. To obtain extensive sampling of conformations of the wild-type and P27S

mutant p53 peptides, ten 1-μs simulations were performed for each peptide in explicit solvent, with each simulation starting from a different conformation. One of the ten simulations was started from the MDM2-bound conformation of the peptide; each of the remaining nine simulations was started from a different random coil conformation. Heavy-atom coordinates of the bound conformations were taken from the crystal structure of the MDM2-p53 peptide complex;[3] heavy-atom coordinates of the random coil conformations were generated using the Sosnick group's unfolded state web server (http://godzilla.uchicago.edu/cgi-bin/unfolded.cgi) [25] in conjunction with the SCWRL3.0 side-chain prediction program.[26] Consistent with the peptides synthesized for the experiments (see above), each random coil conformation was capped with acetyl and amino groups at the N terminus and C terminus, respectively. Hydrogen atoms were added using ionization states present in neutral solution. Each model was solvated in dodecahedral boxes of TIP3P water[27] (total of 3498 molecules) with a minimum solute-wall distance of 12 Å, then charge-neutralized by adding two Na^+ counterions.

MD simulations were performed using the GROMACS 4.0 software package[28] and the OPLS-AA/L force field[29] in the NPT ensemble (constant number of atoms, pressure, and temperature). The temperature was maintained at 30 ^oC using the Nose Hoover thermostat[30,31] and the pressure was maintained at 1 atm using the Parrinello-Rahman barostat[32] with time constants for coupling set to 0.5 and 4 ps, respectively. Van der Waals interactions were switched off smoothly between 8 and 9 Å; a long-range analytical dispersion correction was applied to the energy and pressure to account for the truncation of these interactions.[33] Real-space electrostatic interactions were truncated at 10 Å while the long-range components of these interactions were calculated using particle mesh Ewald (PME)[34] and periodic boundary

conditions. To enable a 2-fs time step, bonds to hydrogen were constrained to their equilibrium lengths with the LINCS algorithm.[35]

To relieve unfavorable interactions, each model was subjected to energy minimization followed by a two-stage equilibration with harmonic position restraints on all non-hydrogen atoms of the peptide. During the first stage, the energy-minimized system was equilibrated for 20 ps at constant temperature (30 ^{o}C) and volume. During the second stage, the system was equilibrated for 2 ns at constant temperature (30 ^{o}C) and pressure (1 atm). After equilibration, fully unrestrained production simulations were carried out for 1-μs at 30 ^{o}C and 1 atm. Each 1-μs simulation required a month of calendar time using 16 CPUs in parallel on two quad-core 2.66GHz Xeon nodes of a Linux cluster at the University of Pittsburgh's Center for Molecular and Materials Simulations. To avoid bias towards the starting conformation, only the latter 900 ns of each simulation was used for subsequent analysis, using conformations sampled every 100 ps. Based on the distribution of alternate conformations, the ensembles of simulations for each peptide are converged (see Ramachandran plots in Fig. D5 in Appendix D).

Kinetic clustering of peptide conformations. The conformations of the wild-type peptide ensemble were clustered based on kinetic similarity using the MSMBuilder software package.[36] In short, conformations are grouped according to geometric (and assumed kinetic) similarity into a large number of microstates, and these microstates are in turn grouped by kinetic similarity into a small number of macrostates. The matrix of transition probabilities between these macrostates is then capable of describing the long-timescale kinetics of the system, assuming that the transitions between macrostates are Markovian on some sufficiently long timescale (the Markov time of the system).[37-39] In our case, all 90,000 conformations from the unbound wild-type peptide ensemble were clustered based on backbone RMSD into 500 microstates (average

microstate radius of 1.8 Å). These 500 microstates were then grouped into four macrostates which showed Markovian behavior on timescales longer than 50 ns (see Fig. D6). The conformations from the P27S mutant peptide ensemble were then assigned to these same macrostates by geometric similarity to the microstates determined above. The resulting macrostate populations were then examined to determine the population shift induced by mutation. Populations of each macrostate for the wild-type and mutant peptides were determined by Monte Carlo sampling of the macrostate-to-macrostate transition matrices for the wild-type and mutant peptide ensembles.[38]

Calculation of NMR chemical shifts and J-coupling constants. Chemical shifts of α- and amide protons were computed for each conformation in the peptide ensemble using the SHIFTX program,[40] then averaged for comparison to the experimentally measured values. J-coupling constants between α and amide protons ($^3J_{\alpha N}$) were computed for each conformation in the peptide ensemble, then averaged for comparison to the experimentally measured values. These constants were computed using a version of the Karplus equation that has been used for the analysis of peptides: $^3J_{\alpha N} = A \cos^2(\theta - 60^o) + B \cos(\theta - 60^o) + C$ where with A = 6.51, B = -1.76, C = 1.60,[41] and θ is the dihedral angle between the protons that are separated by three bonds. In this case, the dihedral angle is the backbone torsional angle Φ.

Normal mode calculations. Normal mode calculations of various peptides in the gas phase were carried out using the Gaussian'03 Suite of programs.[42] We optimized the geometry and calculated the vibrational frequencies of the peptides using density functional theory (DFT)[43-45] with the B3LYP functional[46-48] and 6-311+G** basis set. (The same level of theory and basis set was used in a previous study to calculate the dependence of the AmII′p band on

peptide conformation.[49]) Normal mode composition analysis was done by calculating the potentional energy distribution[34] by using the GAR2PED Gaussian output processing utility written by J.M.L. Martin and C. Van Alsenoy.[50]

6.3 RESULTS AND DISCUSSION

6.3.1 Temperature dependence of peptide conformations

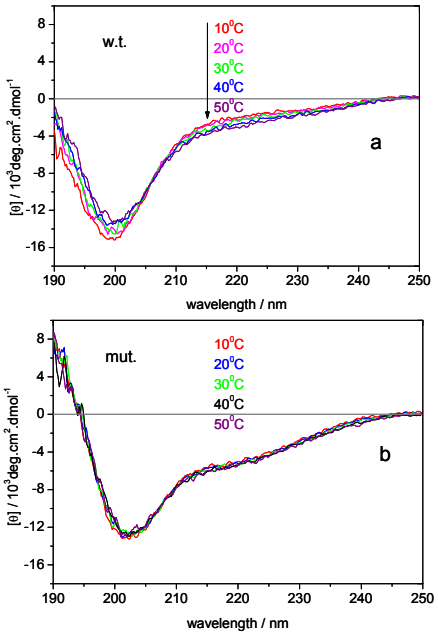

Figure 6.1: Temperature dependence of the CD spectra of a) the p53 wild-type peptide, and b) the mutant peptide.

To examine the temperature dependence of secondary structure in the wild-type and mutant p53 peptides, we performed both CD spectroscopy and UVRR measurements at temperatures ranging from 10 to 50 ^{o}C. Fig. 6.1a shows the temperature dependence of the CD spectra of the wild-type peptide. At 10 ^{o}C, the CD spectrum (red) shows a strong negative band at 200 nm with a

negative shoulder at ~220 nm. As the temperature increases, the 200 nm band slightly decreases in amplitude, while the ~220 nm band becomes slightly more negative. These CD spectra indicate that the wild-type peptide mainly adopts extended conformations.[51-53] Fig. 6.1b shows the temperature dependence of the CD spectra of the P27S mutant peptide. At 10 ^{o}C, the CD spectrum (red) shows a trough at 203 nm, and a more negative shoulder at ~220 nm than that of the wild-type peptide. This indicates an increased α-helix content in the mutant peptide, consistent with a previous study.[4] As the temperature increases, the mutant peptide CD spectrum does not change, indicating that the increased α-helix conformation does not melt below 50 ^{o}C.

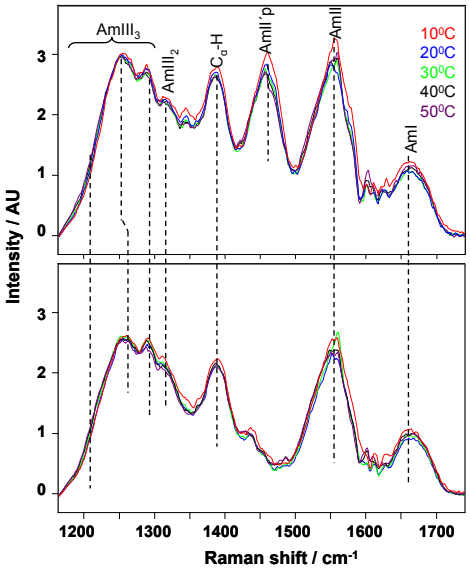

Figure 6.2: Temperature dependence of the 204 nm excited UVRR spectra of the p53 wild-type peptide (top) and the P27S mutant peptide (bottom); contributions from Trp and Phe aromatic rings (Fig. D4) have been removed.

Fig. 6.2 shows the temperature dependence of the 204 nm excited UVRR spectra of the wild-type and mutant peptides. The AmI band (~1660 cm^{-1}) arises from vibration consisting mainly of C=O stretching. The AmII band (~1550 cm^{-1}) derives from out-of-phase motion

involving C-N stretching and N-H bending. The AmII′p band (~1455 cm^{-1}) results from the C-N stretching mode of Pro27. The C_α-H bending band (~1390 cm^{-1}) derives from a C_α-H bending vibration that is resonance enhanced because of its coupling to N-H bending and C-N stretching.[10] The intensity of the C_α-H bending band will increase as the population of non-helical conformations increases.[54] The bands in the AmIII region arise from vibrations which involve in-phase contributions of C-N stretching and N-H bending. The $AmIII_3$ band frequency depends upon the Ramachandran Ψ angle due to the Ψ-angle dependent coupling between N-H bending and the (C)C_α-H bending motions.[10,23]

The $AmIII_3$ region of the wild-type peptide shows bands at ~1250 cm^{-1} and ~1290 cm^{-1}, with a shoulder at ~1200 cm^{-1}. Previous studies showed that an $AmIII_3$ band at ~1248 cm^{-1} indicates a PPII-like conformation, while $AmIII_3$ bands at ~1290 cm^{-1} and ~1200 cm^{-1} indicate different turn conformations.[23] As the temperature increases, the ~1250 cm^{-1} $AmIII_3$ band downshifts very slightly while its intensity slightly decreases; the C_α-H bending band intensity also decreases with increasing temperature. Such temperature-induced Raman spectral changes are not due to conformational changes; they result from the temperature dependence of the hydrogen bonding between water and the peptide bond amide nitrogen.[11] The lack of additional temperature-induced spectral changes indicates a temperature independent conformational distribution.

The bands in the $AmIII_3$ region of the mutant peptide (~1255 cm^{-1} and ~1290 cm^{-1}, with a shoulder at ~1200 cm^{-1}) indicate that its conformational distribution is also temperature independent. The $AmIII_3$ and the C_α-H band intensities of the mutant peptide are slightly decreased relative to that of the wild-type peptide. This Raman intensity hypochromism indicates

a greater population of α-helical conformations for the mutant peptide.[21] We calculated the non-PPII fractional increase of the mutant peptide by using the methodology of Xiong et al.[55,56] (see Appendix D). The calculated increase in the non-PPII content of the mutant peptide is 0.20 ± 0.02.

6.3.2 Conformational diversity of peptides

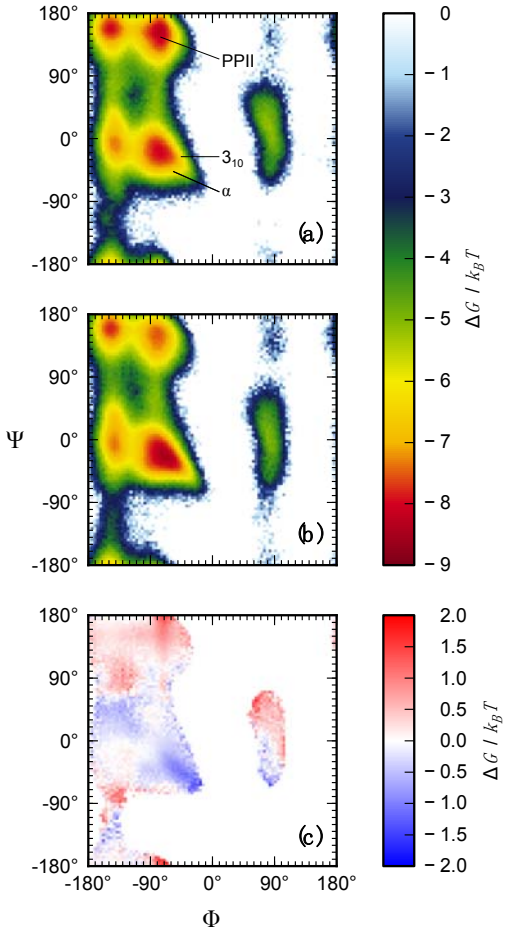

Figure 6.3: Ramachandran plots computed from explicit solvent MD simulations for a) the wild-type p53 peptide ensemble and b) the P27S mutant p53 peptide ensemble. A difference plot of b) relative to a) is presented in c).

As shown by Ramanchandran plots that were computed from our simulations (Fig. 6.3), the mutant P27S peptide ensemble has a decreased population of PPII-like conformations and an increased population of non-PPII conformations (which would include the MDM2-bound α-helical peptide conformation) relative to the wild-type peptide ensemble. Ψ-angle distributions were computed from the UVRR spectra (Fig. 6.2), allowing direct comparison of the UVRR and simulation results.

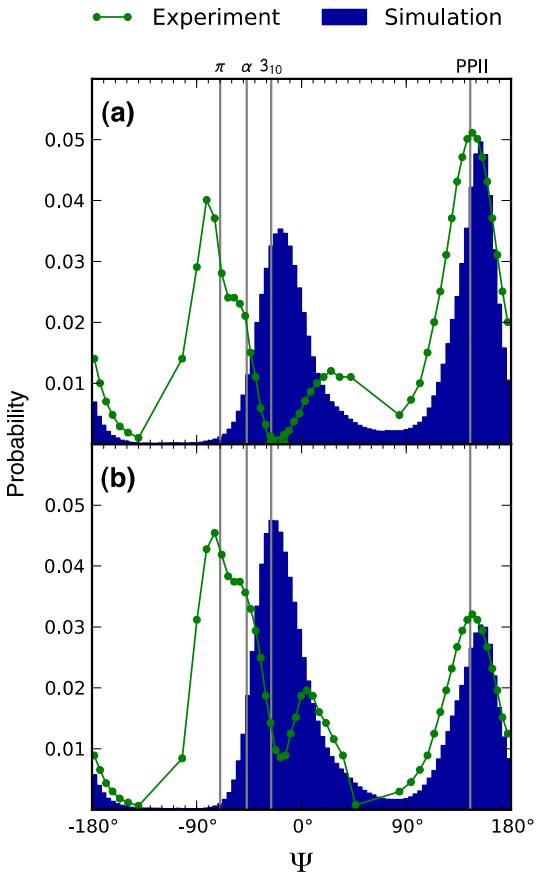

Figure 6.4: Distributions of backbone Ψ angles for the a) wild-type and b) P27S mutant peptides at 30 °C determined from explicit solvent MD simulations (blue) and UVRR spectroscopy (green).

Based on the UVRR spectra, the wild-type peptide Ψ-distribution (Fig. 6.4a) shows a broad PPII-like Ψ angle region with an average Ψ angle of ~145°. The PPII-like conformations dominate, with a negligible α-helix contribution. The probability distribution also contains Type I′ or Type III′ β turn regions with Ψ angles centered at ~30°, a γ-turn region with Ψ angles centered at ~ -60°, and a Type V β turn region with Ψ angles centered at ~ -80°. The mutant peptide Ψ-angle distribution (Fig. 6.4b) shows a decreased PPII contribution and a significantly increased α-helix-like conformation contribution. The contribution of Type I/I′ or Type II/II′ β turn regions with Ψ angles centered at ~0° significantly increases. The Type V β turn contribution also increases.

A comparison of the Ψ-angle distributions from simulations with those calculated from the UVRR spectra reveals that the relative populations of PPII and non-PPII conformations (including α-helix and 3_{10} helix conformations) in the wild-type and mutant peptide ensembles are in excellent agreement (Fig 6.4). Integration of the Ψ-angle distributions in the non-PPII region (between -140° and 84°) gives non-PPII populations of 0.38 and 0.46 for the wild-type experimental and simulation Ψ-angle distributions, respectively. Conversely, the non-PPII populations of the P27S peptide are 0.60 and 0.61 for Ψ-angle distributions from experiment and simulation, respectively. In contrast to a recent simulation study, which revealed little or no formation of 3_{10} helices for helical peptides,[57] the 3_{10} helix was the dominant non-PPII conformation in our simulations involving the p53 peptides. Given that the dominant non-PPII conformation in the UVRR experiments is the α-helix, exhibiting i+4 → i instead of the i+3 → i hydrogen bonding of a 3_{10} helix, our simulation result may be an artifact of the OPLS-AA/L force field.[29]

We also computed chemical shifts and J-coupling constants using our simulations and compared these values to those measured by NMR experiments.[4] The computed chemical shifts were within experimental error. In particular, the relative RMS deviations between computed and experimentally measured chemical shifts (in reference to the experimental value) are 0.084 and 0.069 ppm for the α- and amide protons of the wild-type peptide and 0.086 and 0.070 ppm for the α- and amide protons of the mutant P27S peptide, respectively (See Tables D1-2 in Appendix D). The J-coupling constants that were computed from our simulations are those between the C_α and amide protons ($^3J_{\alpha N}$). We were unable to compare our results for the wild-type peptide to experimental results, because the $^3J_{\alpha N}$-coupling constants for most of the residues in the wild-type p53 peptide have not been determined due to spectral overlap (Table D3). For the mutant peptide, no significant correlation ($R^2 = 0.12$) was found between the computed and experimental[4] J-couplings (Table D4). It is therefore likely that our simulations do not provide sufficient conformational sampling to reproduce the experimental J-couplings, which report on averages over timescales that may extend into the millisecond range.[58]

6.3.3 Does binding occur by conformational selection?

A potential mechanism for the binding of the p53 peptide to the MDM2 oncoprotein is conformational selection,[59] where the MDM2-bound conformation of the p53 peptide is already significantly populated in the unbound state, interconverting with alternate conformations; the presence of MDM2 then selects for the bound conformation by stabilizing this conformation over all other conformations through binding.

To explore the potential for conformational selection, we determined the population of the bound conformation in the unbound state of the p53 peptide from the kinetic clustering model described above. In the wild-type peptide ensemble, the bound state has the highest population (48 ± 15%) among the four kinetically distinct states (macrostates); as expected, this population is even greater in the mutant peptide ensemble (89 ± 6%). This supports the notion that the P27S mutation improves binding of p53 to MDM2 by allowing the unbound peptide to access its bound conformation more readily. We note that the p53 peptide may also bind MDM2 through the "fly-casting" mechanism, contacting its MDM2 partner at a distance, then folding as it reels in its MDM2 partner; this mechanism has been proposed as a general explanation of for a kinetic advantage to being intrinsically disordered vs. folded.[60] Our results do not rule out the possibility of fly casting; they simply provide support for conformational selection as a viable mechanism of MDM2-p53 binding.

6.3.4 Conformational diversity of a selected peptide residue: Leu26

As mentioned above, mutation of Pro27 to serine results in significant conformational changes in the preceding residue, Leu26.[4] The conformation of the Leu26 peptide bond can be highlighted by perdeuterating the Leu26 of the p53 wild-type and mutant peptides and then measuring UVRR spectra of the resulting isotope labeled peptides.[61,62] Fig. 6.5 shows the 204 nm excited UVRR spectra of the perdeuterated and non-deuterated Leu26 of the wild-type and mutant p53 peptides and their difference spectra. The difference spectrum (Fig. 6.5a) shows that perdeuterating the Leu residue preceding Pro27 significantly downshifts the AmII′p band as shown by the ~1445 cm^{-1} trough and the ~1472 cm^{-1} peak. This 27 cm^{-1} AmII′p downshift must

result from an AmII´p normal mode compositional change since no conformational change will occur upon isotopic substitution.

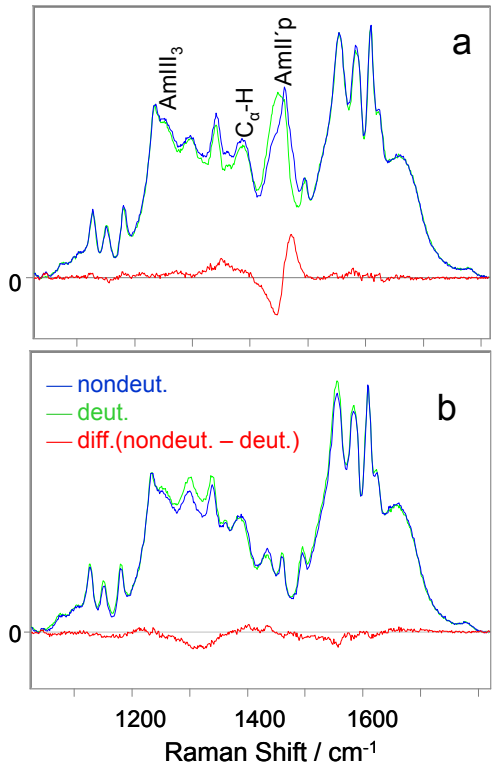

Figure 6.5. 204 nm excited UVRR spectra of Leu26 perdeuterated and non-deuterated p53 a) wild-type peptide, and b) P27S mutant peptide, and their difference spectra (red) at 30 ^{0}C. All spectra were normalized to the intensity of the AmI band.

Quantum mechanical calculations were therefore performed to calculate the normal modes of Acetyl-LP-NH_2 and its perdeuterated leucine derivative. In the non-deuterated peptide the AmII´p vibration arises mainly from C-N stretching (28%) coupled out-of-phase to Leu C_α-H in-plane bending (22%) (Table 6.1); C_α-C stretching (10%) and C=O in-plane bending (7%) contribute less. Perdeuteration of Leu26 eliminates the C_α-H bending contribution to the AmII´p normal mode and increases the C-N stretching contribution to 46%. Additionally, the

perdeuterated Leu-Pro AmII´p vibration acquires small contributions from C-N stretching (8%) and deformation (6%) of the proline ring. The C_α-C and C=O stretching contributions are preserved. These AmII´p normal mode composition changes give rise to a calculated 19 cm^{-1} downshift compared to that of the non-perdeuterated peptide. A similar calculation for Acetyl-AP-NH_2 and its perdeuterated Ala derivative shows similar normal mode composition changes (Table 6.1) that result in a 17 cm^{-1} AmII´p frequency downshift.

Table 6.1.**Calculated amide II´p frequencies and potential energy distributions for Acetyl-L-P-NH_2 and its perdeuterated lecucine isotopomer; Acetyl-A-P-NH_2 and its perdeuterated alanine isotopomer.**

	Freq. (cm^{-1})*	Potential energy distributions (>5%)
Acetyl-L-P-NH_2	1444	C-N s (28) -C_α-H inp b (22) -C_α-C s (10) -C=O inp b (7)
Acetyl-L(D)-P-NH_2	1425	C-N s (46) -C_α-C s (9) -C=O inp b (9) –C-N s (in Pro ring) (8) Pro ring def (6)
Acetyl-A-P-NH_2	1445	C-N s (31) -C_α-H inp b (18) –C_α-C s (11) -C=O inp b (7) -C=O inp b (6)
Acetyl-A(D)-P-NH_2	1428	C-N s (41) -C_α-C s (10) -C=O inp b (8) C-H inp b (Pro) (7) -C-N s (Pro ring) (7) Pro ring def (5)

***Our calculated AmII´p frequencies are about 15 cm^{-1} lower than the Fig.6.5 measured values because we did not consider the effect of hydrogen bonding or the impact of the solvent dielectric constant; we previously showed that a 25 cm^{-1} upshift in the AmII´p frequency will occur due to hydrogen bonding.[49]**

The C_α-H bending band intensity of the perdeuterated Leu26 p53 mutant peptide slightly decreases relative to that of the natural abundance mutant (Fig. 6.5b), indicating that the Leu26-Ser27 mutant peptide bond possesses a weak C_α-H bending band intensity. By using the same

methodology for calculating the non-PPII fractional increases of the mutant peptide above, we calculated the non-PPII content of this bond. The calculated non-PPII content of Leu26 is 0.72 ± 0.11.

Based on our MD simulations, the calculated non-PPII content (including α-helical conformations) of Leu26 is 0.63, which is in quantitative agreement with experiment. These results are consistent with the expectation that the Leu26-Ser27 peptide bond becomes more α-helical upon introducing the P27S mutation due to the fact that Pro is known to disrupt formation of α helices.

The P27S difference spectrum also shows a negative band centered at 1320 cm^{-1} and only small difference features between 1200 cm^{-1} and 1270 cm^{-1}. Previous studies indicate that the difference spectrum for the PPII conformation between hydrogenated (C_α-H) versus deuterated (C_α-D) of a mainly polyalanine peptide shows a strong positive band at 1248 cm^{-1} and a strong negative band at 1326 cm^{-1}. In contrast, the difference spectrum for the α-helical conformation shows only a weak positive band at 1258 cm^{-1} and a weak negative band at 1287 cm^{-1} (Fig. D4). The lack of a strong positive feature at 1248 cm^{-1} in the P27S difference spectrum indicates little, if any PPII content. The relatively flat region between 1200 cm^{-1} and 1270 cm^{-1} in Fig.6.5b might result from a broad distribution of conformations with Ψ angles around the α-helix and turn peptide bond conformation that would not show $AmIII_3$ intensities between 1200-1250 cm^{-1}. The 1320 cm^{-1} trough results from the C_α-D deuterated species bands that show up in this region.[10,63] It is important to note that the Leu26-Ser27 mutant peptide bond, even if 100% α-helix will not show the Fig. D4 difference spectrum (that derives from a long α-helical peptide with its intramolecular hydrogen bonding).

6.3.5 Solvent exposure of the Trp residue

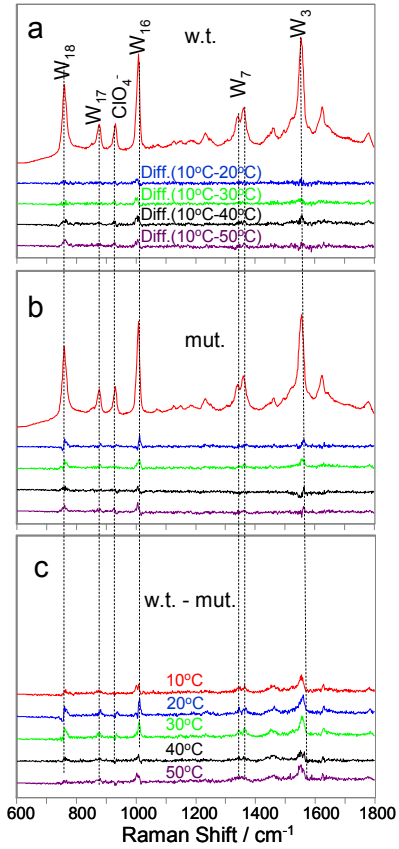

Figure 6.6. 229 nm excited UVRR spectra of the p53 wild-type and P27S mutant peptides. a) 10 °C spectra of the wild-type peptide and difference spectra between the 10 °C spectrum and that at higher temperature, b) temperature difference spectra of the mutant peptide; c) difference spectra between wild-type and mutant peptides. All spectra were normalized to the peak height of the 932 cm^{-1} ClO_4^- band.

We measured UVRR excited by 229 nm light to determine the difference in solvent exposure of the Trp residue (Trp23) in the wild-type and mutant p53 peptides. The resulting UVRR spectra (Fig. 6.6) are dominated by the in-plane Trp aromatic ring vibrations at 759 cm^{-1} (W_{18}), 876 cm^{-1} (W_{17}), 1008 cm^{-1} (W_{16}), 1341 cm^{-1} (W_7^2), 1361 cm^{-1} (W_7^1) and 1555 cm^{-1} (W_3). Previous studies showed that the 229 nm Trp band intensities increase as the Trp residue becomes less

exposed to solvent.[22] The Trp band intensities of the wild-type and mutant peptides are essentially temperature independent, indicating temperature independent solvent exposure of the Trp in both peptides. The difference spectra (Fig. 6.6c) between the wild-type and mutant peptides show that the peptides have similar Trp band intensities [wild-type average intensities were only 10 ± 6% (deviation between intensities) greater than the mutant intensities], suggesting that the Trp residue is similarly exposed to solvent in both peptides. Consistent with experiment, our simulations resulted in an insignificant difference (29 ± 64 Å²; uncertainty is one standard deviation) in the average solvent accessible surface areas of the Trp residue in the wild-type and mutant peptides.

6.4 CONCLUSIONS

To our knowledge, we have reported the first experimentally measured distributions of Ramachandran Ψ angles for intrinsically disordered peptides. These measurements were performed on an N-terminal p53 peptide and its P27S mutant form using UVRR. To provide atomically detailed views of these conformational distributions, we also performed explicit solvent MD simulations on the microsecond timescale. Based on the Ψ-angle distributions determined from both UVRR and simulations, PPII-like conformations were found to dominate the wild-type peptide ensemble and to significantly decrease in population in the mutant peptide ensemble. For each peptide, the relative populations of PPII-like conformations to non-PPII conformations from experiment and simulations are in excellent agreement. We also determined the Ψ-angle distributions for the residue preceding the proline residue in both peptides (Leu26) using isotopically labeled UVRR spectroscopy and simulations. Results from experiment and

simulation are in quantitative agreement in terms of the non-PPII content of the Leu26-Ser27 peptide bond. Even though the mutant peptide is more preorganized for MDM2 binding, no significant differences in solvent exposure of the Trp residue was found between the wild-type and mutant peptides using either 229 nm excited UVRR measurements or simulations. Finally, our simulations reveal that the MDM2-bound conformation of the peptide is significantly populated in both the wild-type and P27S mutant peptide ensembles and that this population is significantly greater in the mutant peptide ensemble. Thus, mutation of Pro27 to serine preorganizes the peptide for binding, supporting the notion that MDM2 binding of the peptide might involve conformational selection.

6.5 ACKNOWLEDGMENTS

This work was supported by NIH grant 1RO1EB009089 and NSF CAREER Award MCB-0845216. Computational resources were provided by the Center for Simulation and Modeling at the University of Pittsburgh.

6.6 REFERENCES

(1) Fink, A. L. *Curr. Opin. Struct. Biol.* **2005**, *15*, 35.

(2) Dunker, A. K.; Obradovic, Z. *Nat. Biotechol.* **2001**, *19*, 805.

(3) Kussie, P. H.; Gorina, S.; Marechal, V.; Elenbaas, B.; Moreau, J.; Levine, A. J.; Pavletich, N. P. *Science* **1996**, *274*, 948.

(4) Zondlo, S.; Lee, A.; Zondlo, N. *Biochemistry* **2006**, *45*, 11945.

(5) Botuyan, M.; Momand, J.; Chen, Y. *Fold. Des.* **1997**, *2*, 331.

(6) Lee, H.; Mok, K. H.; Muhandiram, R.; Park, K. H.; Suk, J. E.; Kim, D. H.; Chang, J.; Sung, Y. C.; Choi, K. Y.; Han, K. H. *J. Biol. Chem.* **2000**, *275*, 29426.

(7) Bell, S.; Klein, C.; Muller, L.; Hansen, S.; Buchner, J. *J. Mol. Biol.* **2002**, *322*, 917.

(8) Dawson, R.; Muller, L.; Dehner, A.; Klein, C.; Kessler, H.; Buchner, J. *J. Mol. Biol.* **2003**, *332*, 1131.

(9) Vise, P. D.; Baral, B.; Stancik, A.; Lowry, D. F.; Daughdrill, G. W. *Proteins* **2007**, *67*, 526.

(10) Asher, S. A.; Ianoul, A.; Mix, G.; Boyden, M. N.; Karnoup, A.; Diem, M.; Schweitzer-Stenner, R. *J. Am. Chem. Soc.* **2001**, *123*, 11775.

(11) Asher, S.; Mikhonin, A.; Bykov, S. *J. Am. Chem. Soc.* **2004**, *126*, 8433.

(12) Mikhonin, A. V.; Bykov, S.; Myshakina, N. S.; Asher, S. A. *J. Phys. Chem. B* **2005**, *110*, 1928.

(13) Mikhonin, A. V.; Myshakina, N. S.; Bykov, S.; Asher, S. A. *J. Am. Chem. Soc.* **2005**, *127*, 7712.

(14) Mikhonin, A. V.; Bykov, S.; Myshakina, N. S.; Asher, S. A. *J. Phys. Chem. B* **2005**, *110*, 1928.

(15) Espinoza-Fonseca, L. M.; Trujillo-Ferrara, J. G. *Biochem. Biophys. Res. Comm.* **2006**, *343*, 110.

(16) Chen, H. F.; Luo, R. *J. Am. Chem. Soc.* **2007**, *129*, 2930.

(17) Dastidar, S. G.; Lane, D. P.; Verma, C. S. *J. Am. Chem. Soc.* **2008**, *130*, 13514.

(18) Massova, I.; Kollman, P. A. *J. Am. Chem. Soc.* **1999**, *121*, 8133.

(19) Zhong, H.; Carlson, H. A. *Proteins: Struct. Funct. Bioinf.* **2005**, *58*, 222.

(20) Bykov, S.; Lednev, I.; Ianoul, A.; Mikhonin, A.; Munro, C.; Asher, S. A. *Appl. Spectrosc.* **2005**, *59*, 1541.

(21) Sharma, B.; Bykov, S. V.; Asher, S. A. *J. Phys. Chem. B* **2008**, *112*, 11762.

(22) Chi, Z. H.; Chen, X. G.; Holtz, J. S. W.; Asher, S. A. *Biochemistry* **1998**, *37*, 2854.

(23) Mikhonin, A. V.; Bykov, S. V.; Myshakina, N. S.; Asher, S. A. *J. Phys. Chem. B* **2006**, *110*, 1928.

(24) Mikhonin, A. V.; Myshakina, N. S.; Bykov, S. V.; Asher, S. A. *J. Am. Chem. Soc.* **2005**, *127*, 7712.

(25) Jha, A. K.; Colubri, A.; Freed, K. F.; Sosnick, T. R. *Proc. Natl. Acad. Sci. USA* **2005**, *102*, 13099.

(26) Canutescu, A. A.; Shelenkov, A. A.; Dunbrack, J., R.L. *Protein Sci.* **2003**, *12*, 2001.

(27) Jorgensen, W.; Chandrasekhar, J.; Madura, J.; Impey, R.; Klein, M. *J. Chem. Phys.* **1983**, *79*, 926.

(28) Hess, B.; Kutzner, C.; van der Spoel, D.; Lindahl, E. *J. Chem. Theory Comput.* **2008**, *4*, 435.

(29) Kaminski, G. A.; Friesner, R. A.; Tirado-Rives, J.; Jorgensen, W. L. *J. Phys. Chem. B* **2001**, *105*, 6474.

(30) Nose, S. J. *J. Chem. Phys.* **1984**, *81*, 511.

(31) Hoover, W. G. *Phys. Rev. A* **1985**, *31*, 1695.

(32) Parrinello, M.; Rahman, A. *J. Appl. Phys.* **1981**, *52*, 7182.

(33) Shirts, M. R.; Pitera, J. W.; Swope, W. C.; Pande, V. S. *J. Chem. Phys.* **2003**, *119*, 5740.

(34) Essmann, U.; Perera, L.; Berkowitz, M. L.; Darden, T.; Lee, H.; Pedersen, L. G. *J. Chem. Phys.* **1995**, *103*, 8577.

(35) Hess, B.; Bekker, H.; Berendsen, H.; Fraaije, J. *J. Comput. Chem.* **1997**, *18*, 1463.

(36) Bowman, G. R.; Huang, X.; Pande, V. S. *Methods* **2009**, *49*, 197.

(37) Chodera, J. D.; Swope, W. C.; Pitera, J. W.; Dill, K. A. *Multiscale Model. Simul.* **2006**, *5*, 1214.

(38) Noe, F. *J. Chem. Phys.* **2008**, *128*, 244103.

(39) Chodera, J. D.; Singhal, N.; Pande, V. S.; Dill, K. A.; Swope, W. C. *J. Chem. Phys.* **2007**, *126*, 155101.

(40) Neal, S.; Nip, A. M.; Zhang, H. Y.; Wishart, D. S. *J. Biomol. NMR* **2003**, *26*, 215.

(41) Vuister, G. W.; Wang, A. C.; Bax, A. *J. Am. Chem. Soc.* **1993**, *115*, 5334.

(42) Frisch, M. J. T., G. W.; Schlegel, H. B.; Scuseria, G. E.; Robb, M. A.; et al. Gaussian 03; Revision C.01 ed. ed.; Gaussian, Inc.: Wallingford CT., 2004.

(43) Kohn, W.; Sham, L. J. *Phys. Rev.* **1965**, *140*, A1133.

(44) Parr, R. G.; Yang, W. *Density-functional theory of atoms and molecules*; Oxford Univ. Press: Oxford, 1989.

(45) Hohenberg, P.; Kohn, W. *Phys. Rev.* **1964**, *136*, B864.

(46) Becke, A. D. *Journal of Chemical Physics* **1993**, *98*, 5648.

(47) Lee, C.; Yang, W.; Parr, R. G. *Phys. Rev. B* **1988**, *37*, 785.

(48) Miehlich, B.; Savin, A.; Stoll, H.; Preuss, H. *Chem. Phys. Lett.* **1989**, *157*, 200.

(49) Ahmed, Z.; Myshakina, N. S.; Asher, S. A. *J. Phys. Chem. B* **2009**, *113*, 11252.

(50) Martin, J. M. L.; Van Alsenoy, C. GAR2PED; University of Antwerpen: Antwerpen, 1995.

(51) Sreerama, N.; Woody, R. W. *Biochemistry* **1994**, *33*, 10022.

(52) Shi, Z.; Olson, C.; Rose, G.; Baldwin, R.; Kallenbach, N. *Proc. Natl. Acad. Sci. USA* **2002**, *99*, 9190.

(53) Shi, Z.; Chen, K.; Liu, Z.; Kallenbach, N. *Chem. Rev.* **2006**, *106*, 1877.

(54) Wang, Y.; Purrello, R.; jordan, T.; Spiro, T. G. *J. Am. Chem. Soc.* **1991**, *113*, 6359.

(55) Xiong, K.; Asciutto, E. K.; Madura, J. D.; Asher, S. A. *Biochemistry* **2009**, *48*, 10818.

(56) Xiong, K.; Asher, S. A. *Biochemistry* **2010**, *49*, 3336.

(57) Matthes, D.; de Groot, B. L. *Biophys. J.* **2009**, *97*, 599.

(58) Markwick, P. R. L.; Showalter, S. A.; Bouvignies, G.; Bruschweiler, R.; Blackledge, M. *J. Biomol. NMR* **2009**, *45*, 17.

(59) Pauling, L. *J. Am. Chem. Soc.* **1940**, *62*, 2643.

(60) Shoemaker, B. A.; Portman, J. J.; Wolynes, P. G. *Proc. Natl. Acad. Sci. USA* **2000**, *97*, 8868.

(61) Ianoul, A.; Mikhonin, A.; Lednev, I. K.; Asher, S. A. *J. Phys. Chem. A* **2002**, *106*, 3621.

(62) Mikhonin, A. V.; Asher, S. A.; Bykov, S. V.; Murza, A. *J. Phys. Chem. B* **2007**, *111*, 3280.

(63) Oboodi, M. R.; Alva, C.; Diem, M. *J. Phys. Chem.* **1984**, *88*, 501.

CHAPTER 7

Impact of Ion Binding on Poly-L-Lysine (Un)folding Energy Landscape and Kinetics

This Chapter was submitted to J. Am. Chem. Soc. The co-authors are Kan Xiong and Sanford A. Asher.

7.0 IMPACT OF ION BINDING ON POLY-L-LYSINE (UN)FOLDING ENERGY LANDSCAPE AND KINETICS

We utilize T-jump UV resonance Raman spectroscopy to study the impact of ion binding on the equilibrium energy landscape and on (un)folding kinetics of poly-L-lysine (PLL). We observe that the relaxation rates of the folded conformations (including π-helix (bulge), pure α-helix and turns) of PLL are slower than those of short alanine based peptides. The PLL pure α-helix folding time is similar to that of short alanine based peptides. We, for the first time have directly observed that turn conformations are α-helix and π-helix (bulge) unfolding intermediates. ClO_4^- binding to the lys side chain $-NH_3^+$ groups and the peptide backbone slows the α-helix unfolding rate compared to that in pure water, but little impacts the folding rate, resulting in an increased α-helix stability. ClO_4^- binding significantly increases the PLL unfolding activation barrier but little impacts the folding barrier. Thus, the PLL folding coordinate differs from the unfolding coordinate. The π-helix (bulge) unfolding and folding coordinates do not directly go through the α-helix energy well. Our results clearly demonstrate that PLL (un)folding is not a two-state process.

7.1 INTRODUCTION

The α-helix is the most common secondary structural element of proteins. Elucidating the mechanism(s) of α-helix melting and refolding is essential for understanding protein folding. Despite extensive studies over the past 50 years, the mechanism(s) by which α-helices melt and refold is still poorly understood.[1-7]

The current understanding of the α-helix (un)folding kinetics mainly derives from extensive studies of alanine based peptides. [8-20] These studies show relaxation rates in the 100 – 400 ns range depend on the peptide length,[25] the temperature, [10,15-18] the terminal capping species,[21] location on the α-helix peptide,[10,18] and the solution environment (such as pH, salts and ionic strength [22,23]).

In this work, we utilize T-jump UVRR to study the impact of $NaClO_4$ on the Gibbs free energy landscape and on the (un)folding kinetics of PLL. The equilibrium conformational transitions of PLL have been characterized by numerous techniques.[24-28] However, little is known about the accompanying conformational dynamics.

We utilize T-jump UVRR to monitor the PLL secondary structure evolution during unfolding. We for the first time have experimentally observed that turn conformations are α-helix and π-helix (bulge) unfolding intermediates. In 0.5 M $NaClO_4$ at 40 ^oC (pH 10.66), the π-helix (bulge) melts faster than the pure α-helix. ClO_4^- binding to lys side chain $-NH_3^+$ groups and the peptide bond slows α-helix unfolding but little impacts folding, resulting in an increased α-helix stability. It appears that ClO_4^- increases the PLL unfolding activation barrier but little impacts the folding barrier. This may indicate that ClO_4^- preferentially binds to PLL folded conformations, decreasing the energies of the folded conformations (the α-helix-like conformations) relative to the energies of the unfolded PPII and 2.5_1-helix conformations.

7.2 EXPERIMENTAL

Materials: Poly-L-Lysine HCl (MW_{vis} = 20900, DP_{vis} = 127, MW_{MALLS} = 11400, DP_{MALLS}= 69. DP_{vis} and DP_{MALLS} refer to the degree of polymerization measured by viscosity and multi-angle laser light scattering, respectively) was purchased from Sigma and used without further purification. $NaClO_4$ was purchased from Sigma.

T-jump UV Raman measurements: The UVRR spectrometer was described in detail by Bykov et al.[29] Briefly, 204 nm UV light (3 ns pulse width, ~1 mW average power, ~200 μm spot size) was obtained by generating the fifth anti-Stokes Raman harmonic of the third harmonic of a Nd:YAG laser (Coherent, Infinity). The peptide solution was circulated in a free surface, temperature-controlled stream. A 165^{o} sampling backscattering geometry was used. The collected light was dispersed by a double monochromator onto a back thinned CCD camera with a Lumogen E coating (Princeton Instruments-Spec 10 System). We averaged three 10-min accumulations.

To selectively heat the water solvent, we Raman-shifited the 1064 nm Nd:YAG fundamental to 1.9 μm by using a 1 m Raman shifter (Light Age Inc,; 600 psi H_2) to obtain ~1.5 mJ pulse energies at a 90 Hz repetition rate. This 1.9 μm excitation is absorbed by a water combination band, and the energy is thermalized within picoseconds by vibrational relaxation.[30]

We performed T-jump measurements from 10 to ~40 ^{o}C and from 20 to ~50 ^{o}C. The magnitudes of the T-jumps were determined by measuring the temperature sensitive water stretching bands (see Fig. E1-5 in Appendix E for details). These T-jumps were obtained by focusing the 1.9 μm laser pulses to a ~300 μm diameter spot in the flowing sample stream. To ensure that the Raman signal was obtained from the sample volume maximally heated by the IR

pulses, we adjusted the sample absorbance at 204 nm to ~40 cm^{-1} by using a 15 mg/ml peptide concentration in T-jump studies of PLL in pure water. In T-jump studies of PLL in 0.5 M $NaClO_4$, we decreased the peptide concentration to 5 mg/ml to minimize aggregation. To achieve the same 204 nm sample absorption as that of the 15 mg/ml PLL sample, we included 0.015 M NaBr that has a molar absorptivity of 5700 M^{-1} cm^{-1} at 204 nm, which is 6 times that of the peptide bond [17] (see Fig. E6 in Appendix E).

7.3 RESULTS

7.3.1 Static UVRR

Fig. 7.1a shows the temperature dependence of the 204 nm excited UVRR spectra of PLL in 0.5 M $NaClO_4$ at pH 10.65. The 10 ^oC spectrum shows an AmI band at 1650 cm^{-1} (mainly CO stretching[31]), an AmII band at 1555 cm^{-1} (mainly out of phase combination of CN stretching and NH bending[31]), and (C)C_α-H bending bands at 1392 cm^{-1}. The $AmIII_3$ bands (mainly in phase combination of CN stretching and NH bending[31]) occur between ~1200 and ~1280 cm^{-1}.

As the temperature increases, the AmI band frequency upshifts, indicating decreased hydrogen bonding of the carbonyls at higher temperatures.[32] The C_α-H band intensity significantly increases with increasing temperature, indicating α-helix melting.[33] The $AmIII_3$ band frequency downshifts and its intensity significantly increases, which also indicate α-helix melting.[34] UVRR spectra of PLL in pure water at pH 10.65 also indicate α-helix melting as the temperature increases (see Fig. E7 in Appendix E).

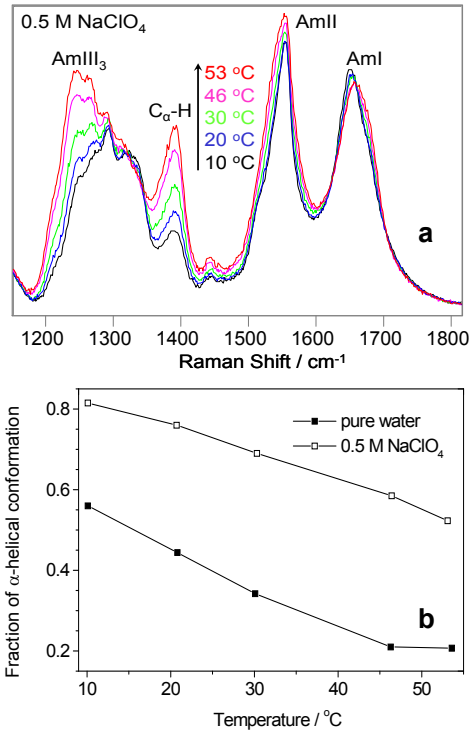

Figure 7.1: a) Temperature dependence of the 204 nm excited UVRR spectra of 1 mg/ml PLL in 0.5 M $NaClO_4$ at pH 10.65. All spectra were normalized to the 932 cm^{-1} ClO_4^- peak height. b) Calculated fractions of α-helix-like conformations of PLL in 0.5 M $NaClO_4$ and in pure water at pH 10.65.

We calculated the fractions of α-helix-like conformations of PLL at different temperatures by using the methodology of Ma et al[24]. The melting curve for PLL at pH 10.65 in pure water (Fig. 7.1b) shows a melting temperature, T_m of ~ 15 °C. Upon addition of 0.5 M $NaClO_4$, the α-helical fractions significantly increase, and T_m increases to > 50 °C.

7.3.2 Kinetic UVRR of PLL in $NaClO_4$

Fig. 7.2 shows T-jump difference UVRR spectra of PLL in 0.5 M $NaClO_4$ (pH 10.66) at

different delay times between the pump and probe laser pulses. The 28 ns difference spectra show small positive features in the $AmIII_3$ and C_α-H regions, indicating slight α-helix melting.[24] These features increase as the delay time increases.

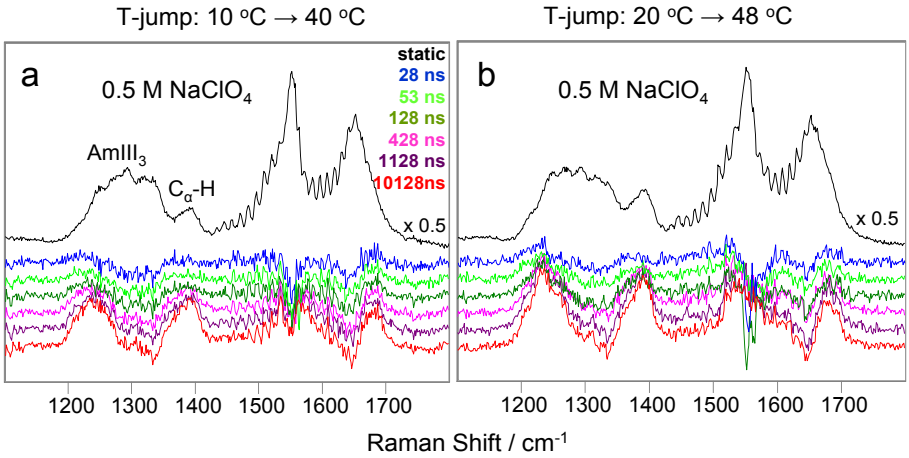

Figure 7.2 T-jump difference UVRR spectra of PLL in 0.5 M $NaClO_4$ (pH 10.66) at different delay times between the pump and probe laser pulses. These difference spectra were obtained by subtracting the static initial temperature spectrum from each of the longer delay time spectra. a) **Difference spectra for a 10 to 40 °C T-jump.** b) **Difference spectra for a 20 to 48 °C T-jump. All spectra were normalized to the 932 cm^{-1} ClO_4^- peak height before spectral subtraction. The oscillations centered at ~1550 cm^{-1} result from the rotational bands of oxygen,[35,36] and occur due to that fact that UV light is focused near the surface of the flow stream where the oxygen concentration is high.**

Transient Ψ-distributions: We calculated the delay time dependent Ramachandran Ψ probability distributions for PLL by using the methodology of Ma et al.[24] Fig. 7.3 shows Ramachandran Ψ probability distributions for PLL at 10 °C and 20 °C in 0.5 M $NaClO_4$ (pH 10.66). The static 10 °C Ψ-distribution shows dominant contributions of the π-helix (bulge) (Ψ ~ -70 °), the pure α-helix (Ψ ~ -40 °) and Type I/I′ or Type II/II′ β-turns (Ψ ~ 5 °). It also contains

contributions of the polyproline II (PPII)-like (Ψ ~ 140 °) and 2.5_1-helix (Ψ ~ 170 °) conformations.

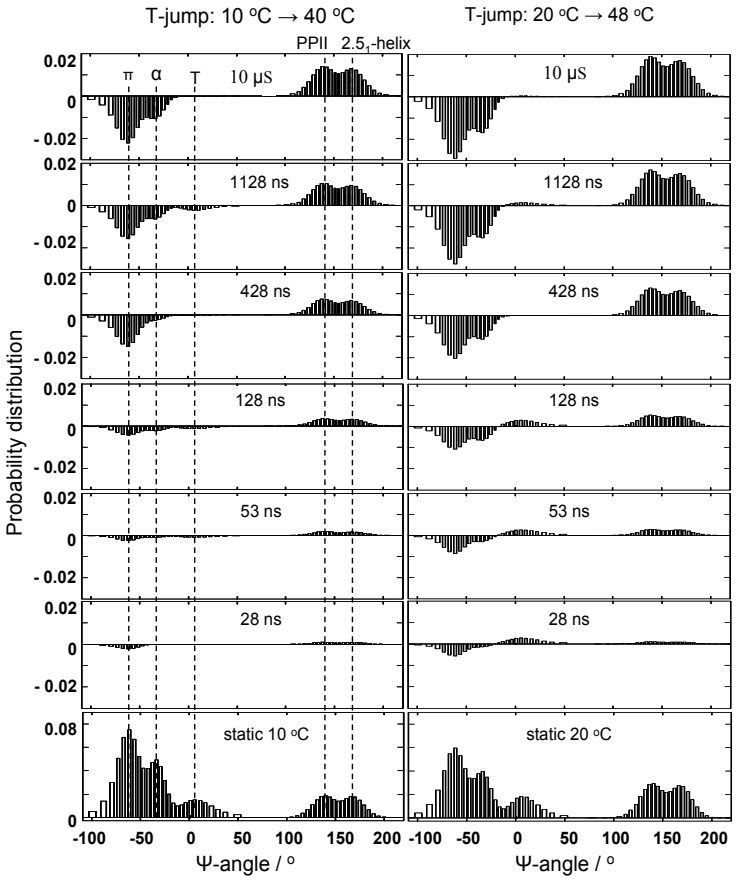

Figure 7.3: Ramanchandran Ψ probability distributions for PLL at 10 °C and 20 °C in 0.5 M $NaClO_4$ (pH 10.66). Delay time dependent difference Ramachandran Ψ probability distributions for PLL in 0.5 M $NaClO_4$ (pH 10.66). These difference Ψ distributions were obtained by subtracting the static initial temperature Ψ distribution from each of the longer delay time Ψ distributions. π: π-helix (bulge). α: pure α-helix. T: turns.

For the 10 to 40 °C T-jump, the difference distributions show that the π-helix (bulge) concentration slightly decreases at 28 ns, and further decreases at longer delay times. The pure α-helix concentration does not decrease until 53 ns. The turn concentration starts decreasing at 128

ns, then increases at 428 ns, and decreases again at 1128 ns (Fig. 7.4). The PPII and 2.5_1-helix concentrations monotonically increase as the delay time increases.

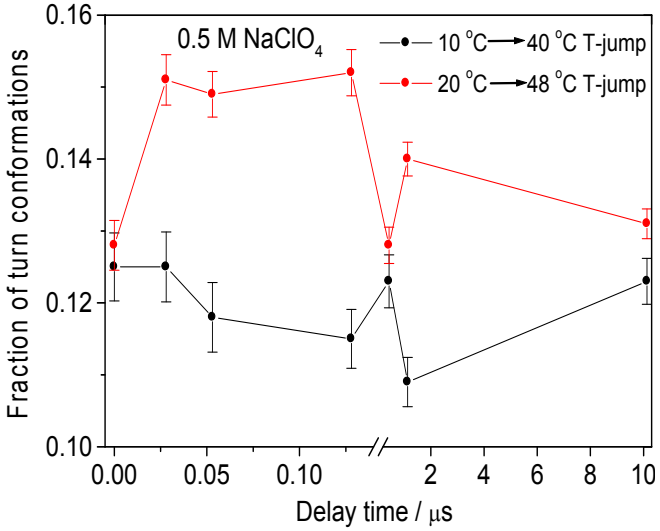

Figure 7.4: Delay time dependent fractions of turn conformations of PLL in 0.5 M $NaClO_4$ at pH 10.66.

The static 20 °C Ψ-distribution shows decreased α-helix-like concentrations and increased PPII and 2.5_1-helix concentrations, compared to those at 10 °C (Fig. 7.3). For the 20 to 48 °C T-jump, the π-helix (bulge) and pure α-helix concentrations decrease at 28 ns, and further decrease at longer delay times. The turn concentration starts increasing at 28 ns, then decreases at 428 ns, and increases again at 1128 ns (Fig. 7.4). The PPII and 2.5_1-helix concentrations monotonically increase as the delay time increases.

Relaxation rates: Fig. 7.5 shows mono-exponential fits, $\Delta f = 1 - \exp(-t/\tau)$ (where Δf is the relative change at the different delay time) to the 0.5 M $NaClO_4$ (pH 10.66) relaxation of the integrated C_α-H band intensities (that result from the extended PPII and 2.5_1-helix conformations of PLL[24]) (Fig. 7.5a), the α-helix-like (π + α + T) concentrations (Fig. 7.5b), the pure α-helix concentrations (Fig. 7.5c) and the π-helix (bulge) concentrations (Fig. 7.5d) of PLL.

The C_α-H band intensities were determined by integrating the UVRR spectral intensities from 1370 to 1410 cm^{-1} at the different delay time. The α-helix-like, the pure α-helix and the π-helix (bulge) concentrations were determined by integrating the Fig. 7.3 Ψ probabilities between $\Psi = 50^o$ and -100^o, between $\Psi = -15^o$ and -48^o and between $\Psi = -48^o$ and -100^o at the different delay time, respectively.

We find a C_α-H relaxation time for the 10 to 40 ^oC T-jump of 658 ± 71 ns, whereas for the 20 to 48 ^oC T-jump the relaxation time is 431 ± 37 ns. We also find an α-helix-like relaxation time for the 10 to 40 ^oC T-jump of 619 ± 67 ns, whereas for the 20 to 48 ^oC T-jump the relaxation time is 385 ± 22 ns. The pure α-helix relaxation time for the 10 to 40 ^oC T-jump is 1355 ± 167 ns, whereas for the 20 to 48 ^oC T-jump the relaxation time is 348 ± 38 ns. The π-helix (bulge) relaxation time for the 10 to 40 ^oC T-jump is 531 ± 96 ns, whereas for the 20 to 48 ^oC T-jump the relaxation time is 284 ± 44 ns.

Kinetic parameters: We calculated the kinetic parameters based on a two-state model for the α-helix-like conformations, the pure α-helix and the π-helix (bulge) (un)folding. Table 7.1 shows that the reciprocals of the 0.5 M $NaClO_4$ (pH 10.66) PLL pure α-helix unfolding rate constants are 2024 ± 249 ns (at 40 ^oC) and 417 ± 46 ns (at 48 ^oC), while the reciprocals of the folding rate constants are 4099 ± 505 ns (at 40 ^oC) and 2091 ± 228 ns (at 48 ^oC).

We calculated the pure α-helix un(folding) activation energies by using the Arrhenius equation: $$\ln\left(\frac{k(T_1)}{k(T_2)}\right) = -\frac{G^{\ddagger}}{R}\left(\frac{1}{T_1} - \frac{1}{T_2}\right) \qquad (7.1)$$

where k is the rate constant and $G^{\ddagger}$ is the activation energy. The calculated pure α-helix unfolding activation energy is 17.2 ± 4.2 kcal/mol, while the folding activation energy is 40.4 ± 4.2 kcal/mol.

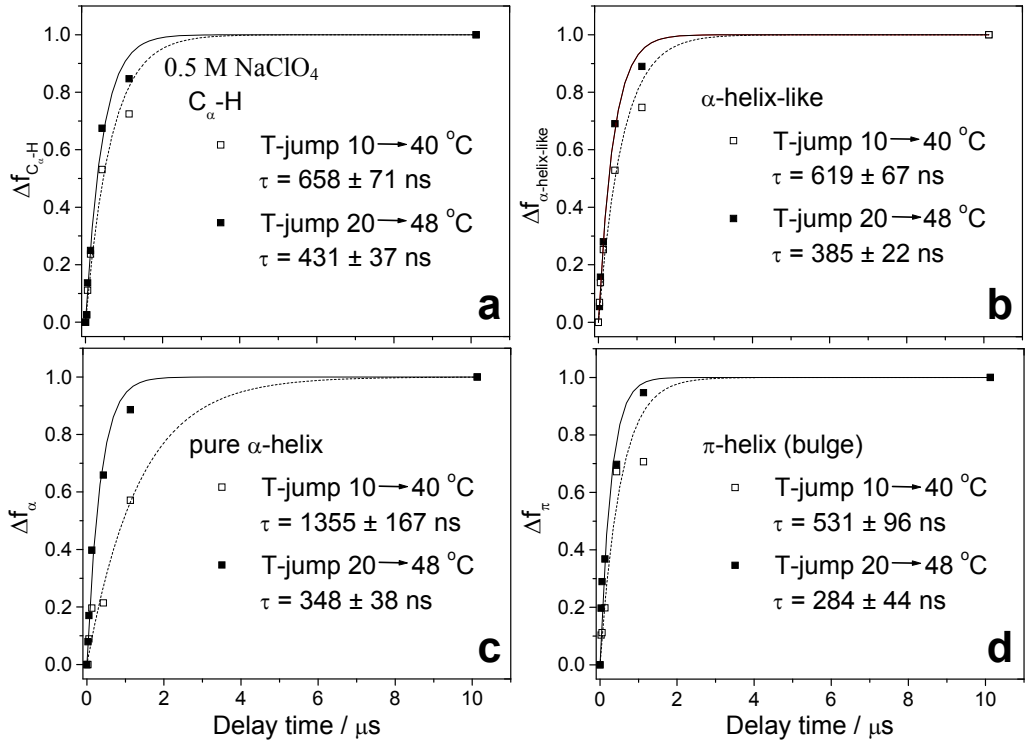

Figure 7.5. T-jump relaxation of the 0.5 M $NaClO_4$ (pH 10.66) (a) integrated C_α-H band intensities, (b) the α-helix-like concentrations, (c) the pure α-helix concentrations, and (d) the π-helix (bulge) concentrations of PLL. Plotted are the C_α-H band intensity change, $\Delta f_{C_\alpha - H}$, the α-helix-like concentration change, $\Delta f_{\alpha\text{-helix-like}}$, the pure α-helix concentration change, Δf_α and the π-helix (bulge) concentration change, Δf_π from time zero to delay time t, relative to the change from static initial temperature to static final T-jump temperature. The dashed and solid curves are mono-exponential fits for the 10 to 40 °C T-jump and the 20 to 48 °C T-jump, respectively.

Table 7.1: Kinetic parameters for the 0.5 M $NaClO_4$ (pH 10.66) PLL α-helix-like conformations, the pure α-helix, and the π-helix (bulge) (un)folding.

		Final T-jump temperature		Activation energy, $G^{\ddagger}$ / kcal/mol
		40 °C	48 °C	
α-helix like	Equilibrium constant, $K_{helical} = f_{extend}$ */$f_{helical}$	0.675 ± 0.028	1.445 ± 0.060	
	$\Delta G_{helical}{}^{\dagger} = -RT(lnK_{helical})$ / kcal/mol	0.24 ± 0.03	-0.23 ± 0.03	
	Relaxation rate, τ / ns	619 ± 67	385 ± 22	
	Folding time, $\tau_f = (k_f)^{-1}$ / ns	1037 ± 112	941 ± 54	2.5 ± 3.1
	Unfolding time, $\tau_u = (k_u)^{-1}$ / ns	1536 ± 166	651 ± 37	21.9 ± 3.1
Pure α helix	Equilibrium constant, $K_\alpha = f_{extend}/f_\alpha$	2.03 ± 0.08	5.01 ± 0.21	
	$\Delta G_\alpha{}^{\dagger} = -RT(lnK_\alpha)$ / kcal/mol	-0.44 ± 0.03	-1.03 ± 0.03	
	Relaxation rate / ns	1355 ± 167	348 ± 38	
	Folding time / ns	4099 ± 505	2091 ± 228	17.2 ± 4.2
	Unfolding time / ns	2024 ± 249	417 ± 46	40.4 ± 4.2
π helix (bulge)	Equilibrium constant, $K_\pi = f_{extend}/f_\pi$	1.47 ± 0.06	3.69 ± 0.15	
	$\Delta G_\pi{}^{\dagger} = -RT(lnK_\pi)$ / kcal/mol	-0.24 ± 0.03	-0.83 ± 0.03	
	Relaxation rate / ns	531 ± 96	284 ± 44	
	Folding time / ns	1309 ± 237	1333 ± 207	-0.5 ± 6.1
	Unfolding time / ns	893 ± 162	361 ± 56	23.2 ± 6.1

*** f_{extend} refers to the concentration of the extended PPII and 2.5_1-helix conformations. $^{\dagger}\Delta G_{helical}$ is the free energy difference between the PPII and 2.5_1-helix conformations and the α-helix-like conformations. ΔG_α is the free energy difference between the PPII and 2.5_1-helix conformations and the pure α-helix. ΔG_π is the free energy difference between the PPII and 2.5_1-helix conformations and the π-helix (bulge).**

Table 7.1 also shows the kinetic parameters for the 0.5 M $NaClO_4$ (pH 10.66) PLL α-helix-like and π-helix (bulge) (un)folding. The α-helix-like unfolding activation energy is 21.9 ± 3.1 kcal/mol, while the folding activation energy is 2.5 ± 3.1 kcal/mol. The π-helix (bulge) unfolding activation energy is 23.2 ± 6.1 kcal/mol, while the folding activation energy is -0.5 ± 6.1 kcal/mol.

7.3.3 Kinetic UVRR of PLL in pure water

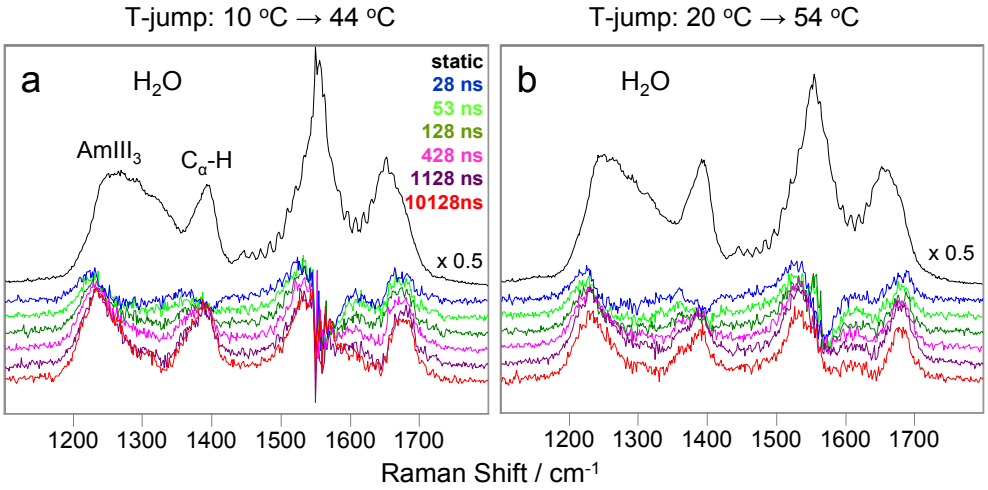

Figure 7.6: T-jump difference UVRR spectra of PLL in pure water at pH 10.66 at different delay times between the pump and probe laser pulses. These difference spectra were obtained by subtracting the static initial temperature spectrum from each of the longer delay time spectra. a) **Difference spectra for a T-jump from 10 to 44 °C. b) Difference spectra for a T-jump from 20 to 54 °C. All spectra were normalized to the ~ 3400 cm^{-1} water stretching band intensities before spectral subtraction. The oscillations centered around 1550 cm^{-1} result from the rotational bands of oxygen.[35,36]**

Fig. 7.6 shows T-jump difference UVRR spectra of PLL in pure water at pH 10.66 at different delay times between the pump and probe laser pulses. The static 10 °C and 20 °C spectra in pure water show significantly increased C_α-H band intensities relative to those in 0.5 M $NaClO_4$ (Fig. 7.2), indicating significantly decreased PLL α-helical content in pure water compared to that in 0.5 M $NaClO_4$.[33] The 28 ns difference spectra show small positive features in the $AmIII_3$ region, and slightly negative features in the C_α-H region (that result from the temperature dependence of the hydrogen bonding between water and the peptide bond amide nitrogens[37].) As the delay time increases, the positive features in the $AmIII_3$ and C_α-H region increase, indicating α-helix

melting.[34] The spectral evolution for the 20 to 54 ^{o}C T-jump is complete within 1128 ns, faster than the 10 to 44 ^{o}C T-jump.

Transient Ψ-distributions: Fig. 7.7 shows the delay time dependent Ramachandran Ψ probability distributions for PLL in pure water at pH 10.66. The static 10 ^{o}C Ψ-distribution shows contributions of the π-helix (bulge) (Ψ ~ -70 ^{o}), the pure α-helix (Ψ ~ -40 ^{o}), Type I/I′ or Type II/II′ β-turns (T1, Ψ ~ 5 ^{o}), and Type III′ β-turn or inverse γ-turn (T2, Ψ ~ 50 ^{o}). It also contains contributions of the PPII-like (Ψ ~140 ^{o}) and 2.5_1-helix (Ψ ~ 170 ^{o}) conformations. For the 10 to 44 ^{o}C T-jump, the π-helix (bulge) and pure α-helix contributions slightly decrease at 28 ns, and further decrease at longer delay times. The T1 turn contribution slightly increases at 28 ns, and then slightly decreases as the delay time increases (Fig. 7.8). The T2 turn contribution starts decreasing at 28 ns, then increases at 428 ns, and decreases again at 1128 ns (Fig. 7.8). The PPII and 2.5_1-helix contributions monotonically increase as the delay time increases.

The static 20 ^{o}C Ψ-distribution shows decreased α-helix-like concentrations and increased PPII and 2.5_1-helix concentrations, relative to those at 10 ^{o}C (Fig. 7.7). For the 20 to 54 ^{o}C T-jump, the π-helix (bulge) and pure α-helix concentrations decrease at 28 ns, and further decrease at longer delay times. The T1 concentration slightly increases at 53 ns, and starts decreasing again at 428 ns (Fig. 7.8). The T2 concentration starts increasing at 28 ns, and then starts decreasing at 128 ns (Fig. 7.8). The PPII and 2.5_1-helix concentrations increase as the delay time increases.

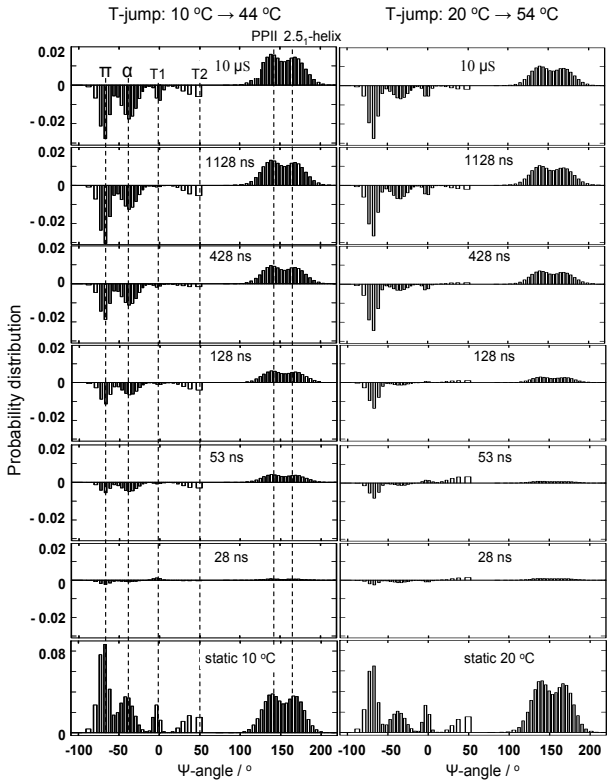

Figure 7.7: Ramanchandran Ψ probability distributions for PLL at 10 ^{o}C and 20 ^{o}C in pure water (pH 10.66). Delay time dependent difference Ramachandran Ψ probability distributions for PLL in pure water (pH 10.66). These difference Ψ distributions were obtained by subtracting the static initial temperature Ψ distribution from each of the longer delay time Ψ distributions. π: π-helix (bulge). α: pure α-helix. T1 and T2: turns.

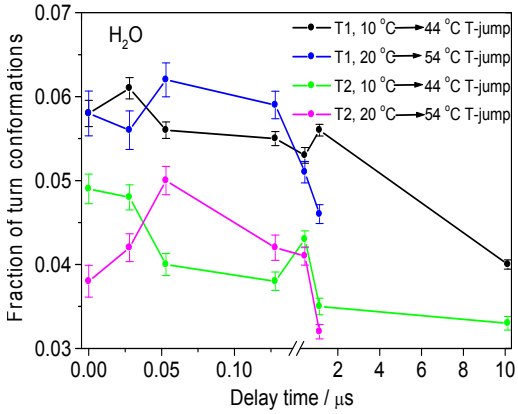

Figure 7.8: Delay time dependent fractions of T1 and T2 turn conformations of PLL in pure water (pH 10.66).

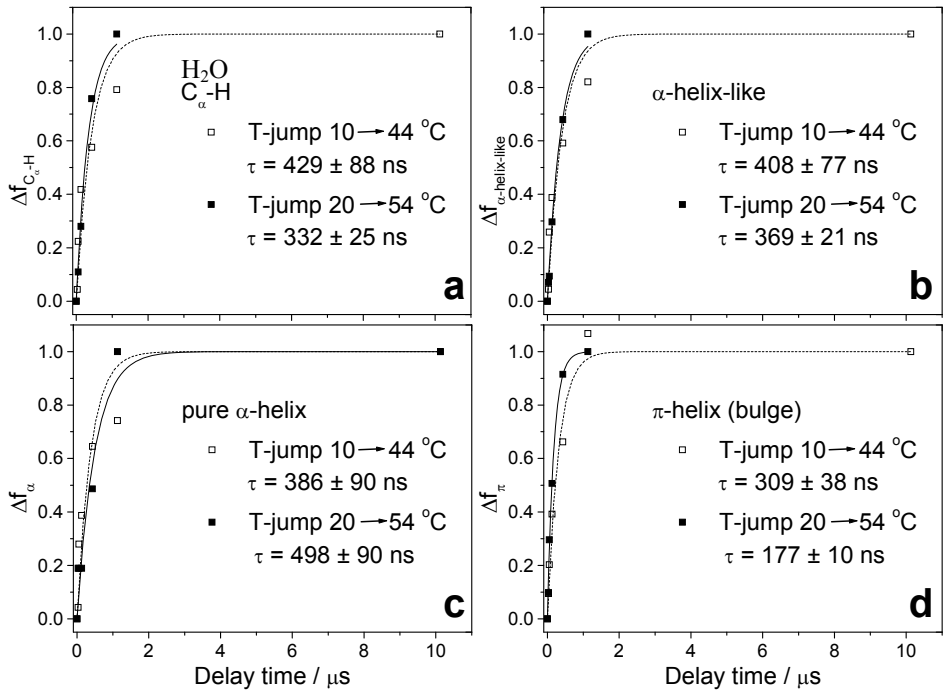

Figure 7.9: T-jump relaxation of the pure water (pH 10.66) (a) integrated C_α-H band intensities, (b) the α-helix-like concentrations, (c) the pure α-helix concentrations, and (d) the π-helix(bulge) concentrations of PLL. Plotted are the C_α-H band intensity change, $\Delta f_{C_\alpha - H}$, the α-helix-like concentration change, $\Delta f_{\alpha\text{-helix-like}}$, the pure α-helix concentration change, Δf_α and the π-helix (bulge) concentration change, Δf_π from time zero to delay time t, relative to the change from static initial temperature to static final T-jump temperature. The dashed and solid curves are mono-exponential fits for the 10 to 40 °C T-jump and the 20 to 54 °C T-jump, respectively. We calculated the C_α-H band intensities at time zero after T-jumps by using the measured static initial temperature C_α-H band intensities and the temperature dependence of the PPII and 2.5_1-helix C_α-H band intensity.[38] The conformational evolution for the 20 to 54 °C T-jump is complete within 1128 ns.

Relaxation rates: Fig. 7.9 shows mono-exponential fits, $\Delta f = 1 - \exp(-t/\tau)$ to the pure water (pH 10.66) relaxation of the integrated C_α-H band intensities (Fig. 7.9a), the α-helix-like (π + α + T1 + T2) concentrations (Fig. 7.9b), the pure α-helix concentrations (Fig. 7.9c), and the π-helix (bulge) concentrations of PLL (Fig. 7.9d).

We find a C_α-H relaxation time for the 10 to 44 ^oC T-jump of 429 ± 88 ns, whereas for the 20 to 54 ^oC T -jump the relaxation time is 332 ± 25 ns. We also find an α-helix-like relaxation time for the 10 to 44 ^oC T-jump of 408 ± 77 ns, whereas for the 20 to 54 ^oC T-jump the relaxation time is 369 ± 21 ns. The pure α-helix relaxation time for the 10 to 44 ^oC T-jump is 386 ± 90 ns, whereas for the 20 to 54 ^oC T-jump the relaxation time is 498 ± 90 ns. The π-helix (bulge) relaxation time for the 10 to 44 ^oC T-jump is 309 ± 38 ns, whereas for the 20 to 54 ^oC T-jump the relaxation time is 177 ± 10 ns.

Table 7.2: Kinetic parameters for the pure water (pH 10.66) PLL α-helix-like conformations, the pure α-helix, and the π-helix(bulge) (un)folding.

		Final T-jump temperature		Activation energy, $G^{\ddagger}$/ kcal/mol
		44 ^oC	54 ^oC	
α-helix like	Equilibrium constant, $K_{helical} = f_{extend}/f_{helical}$	1.98 ± 0.04	2.83 ± 0.07	
	$\Delta G_{helical} = -RT(\ln K_{helical})$ / kcal/mol	-0.43 ± 0.02	-0.68 ± 0.02	
	Relaxation rate, τ / ns	408 ± 77	369 ± 21	
	Folding time, $\tau = (k_f)^{-1}$ / ns	1214 ± 229	1414 ± 80	-3.1 ± 4.0
	Unfolding time, $\tau_u = (k_u)^{-1}$ / ns	614 ± 116	499 ± 28	4.2 ± 4.0
Pure α helix	Equilibrium constant, $K_\alpha = f_{extend}/f_\alpha$	6.51 ± 0.15	10.12 ± 0.26	
	$\Delta G_\alpha = -RT(\ln K_\alpha)$ / kcal/mol	-1.18 ± 0.02	-1.50 ± 0.02	
	Relaxation rate / ns	386 ± 90	498 ± 90	
	Folding time / ns	2899 ± 676	5539 ± 1001	-13.1 ± 6.0
	Unfolding time / ns	445 ± 104	547 ± 99	-4.2 ± 6.0
π helix (bulge)	Equilibrium constant, $K_\pi = f_{extend}/f_\pi$	4.12 ± 0.09	6.54 ± 0.17	
	$\Delta G_\pi = -RT(\ln K_\pi)$ / kcal/mol	-0.89 ± 0.02	-1.22 ± 0.02	
	Relaxation rate / ns	309 ± 38	177 ± 10	
	Folding time / ns	1583 ± 195	1335 ± 75	3.5 ±2.7
	Unfolding time / ns	384 ± 47	204 ± 12	12.8 ± 2.7

Kinetic parameters: Table 7.2 shows that the reciprocals of the pure water PLL pure α-helix unfolding rate constants are essentially the same of 445 ± 104 ns (at 44 ^{o}C) and 547 ± 108 ns (at 54 ^{o}C), while the reciprocals of the folding rate constant slows from 2899 ± 676 ns (at 44 ^{o}C) to 5539 ± 1090 ns (at 54 ^{o}C).

Table 7.2 also shows the kinetic parameters for the pure water PLL α-helix-like, the pure α-helix and the π-helix (bulge) (un)folding. The α-helix-like unfolding activation energy is 4.2 ± 4.0 kcal/mol, while the folding activation energy is -3.1 ± 4.0 kcal/mol. The pure α-helix unfolding activation energy is -4.2 ± 6.0 kcal/mol, while the folding activation energy is -13.1 ± 6.0 kcal/mol. This negative folding activation energy indicates a failure of two-state modeling of the PLL pure α-helix (un)folding kinetics. The π-helix (bulge) unfolding activation energy is 12.8 ± 2.7 kcal/mol, while the folding activation energy is 3.5 ± 2.7 kcal/mol.

7.4 DISCUSSION

We utilize T-jump UVRR to monitor PLL unfolding kinetics of the α-helix-like conformations (including the pure α-helix, π-helix (bulge), and turns), the pure α-helix, and the π-helix (bulge). The relaxation rate of the α-helix-like conformations of PLL in pure water is slower than that of the α-helix-like conformations of alanine based peptides due to the slower PLL unfolding that dominates the relaxation kinetics [17,18].

The PLL pure α-helix folding time is similar to that of alanine based peptides [17,18]. PLL has ≥ 69 residues, much longer than ~20-residue alanine based peptides. This result is consistent with the idea that α-helix nucleation is the rate limiting step during α-helix folding, while α-helix propagation is fast.

Turn conformations are intermediates in PLL unfolding. Previous studies proposed that turn conformations are intermediates during α-helix melting.[39-41] We observe that for the 20 to 48 ^{o}C T-jump in 0.5 M $NaClO_4$, the Type I/I′ or Type II/II′ β-turn ($\Psi \sim 5^{o}$) concentrations increase at 28 ns, as the α-helix and π-helix (bulge) concentrations decrease (Fig. 7.3). However, the PPII and 2.5_1-helix concentrations little increase at 28 ns. This indicates that Type I/I′ or Type II/II′ β-turns may be α-helix and π-helix (bulge) unfolding intermediates in the presence of ClO_4^-. Their concentrations accumulate at short delay times.

In contrast, for the 20 to 54 ^{o}C T-jump in pure water, the Type III′ β-turn or inverse γ-turn ($\Psi \sim 50^{o}$) may be intermediates because their concentrations increase at 28 and 53 ns (Fig. 7.3), as the α-helix and π-helix (bulge) concentrations decrease. Again, the PPII and 2.5_1-helix concentrations little increase at these short delay times. These results suggest that the unfolding intermediates differ between pure water and in ClO_4^- solution.

π-helix(bulge) unfolds and refolds faster than the α-helix. Previous studies of an alanine based peptide indicated that the π-bulge unfolding and folding times at 40 ^{o}C are ~12-fold faster than those of the pure α-helix (Table 7.3).

We observe for PLL that the π-helix (bulge) unfolding time at 40 ^{o}C in 0.5 M $NaClO_4$ (pH 10.66) is twice faster than that of the pure α-helix (Table 7.3). This may result from the fact the π-helix (bulge) hydrogen bonding geometry is less optimized and weaker than that of the α-helix.[42,43]

In contrast, the π-helix (bulge) and pure α-helix unfolding times at 48 ^{o}C in 0.5 M $NaClO_4$ (pH 10.66) are similar. The PLL 44 ^{o}C pure water (pH 10.66) π-helix (bulge) unfolding time is similar to that of the pure α-helix.

The PLL π-helix (bulge) folding times are always faster than those of the pure α-helix (Table 7.3).

Table 7.3: The pure α-helix and the π-helix(bulge) unfolding and folding time for an alanine peptide and PLL at different final temperatures.

	Final T-jump temperature	Unfolding time / ns		Folding time / ns	
		Pure α-helix	π-helix(bulge)	Pure α-helix	π-helix(bulge)
$A_5(A_3RA)_3A$ in pure water	40 ^oC	677 ± 230*	61 ± 18 *	3553 ± 1207 *	≥ 61 *
PLL in pure water (pH 10.66)	44 ^oC	445 ± 104	384 ± 47	2899 ± 676	1583 ± 195
PLL in 0.5 M $NaClO_4$ (pH 10.66)	40 ^oC	2024 ± 249	893 ± 162	4099 ± 505	1309 ± 237
	48 ^oC	417 ± 46	361 ± 56	2091 ± 228	1333 ± 207

*** Results of Mikhonin et al.[18]**

ClO_4^- lys side chain $-NH_3^+$ — peptide backbone binding slows α-helix (un)folding. ClO_4^- forms ion-pairs between the lys side chain $-NH_3^+$ groups and the peptide backbone [44-46] that decreases the electrostatic repulsion between side chain charges, thus, stabilizing the α-helix. Previous molecular dynamics studies indicate that the α-helix (un)folding kinetics of an alanine based peptide of sequence Ac-A$(EAAAK)_2$A-Nme is slowed by the ion binding to peptide charged groups.[23]

Table 7.4: The PLL pure α-helix folding and unfolding time.

	Pure α-helix folding time / ns	Pure α-helix unfolding time / ns
PLL in 0.5 M $NaClO_4$ (pH 10.66) at 44 ^oC	2890 ± 595 *	892 ± 183 *
PLL in pure water (pH 10.66) at 44 ^oC	2899 ± 676	445 ± 104

*** Calculated by using eq. 7.1 and Table 7.1 kinetic parameters.**

We calculated the PLL pure α-helix unfolding and folding times in 0.5 M $NaClO_4$ at 44 ^oC, by using eqn 7.1 and the Table 7.1 kinetic parameters. The calculated pure α-helix unfolding time in 0.5 M $NaClO_4$ (pH 10.66) at 44 ^oC (Table 7.4) is twice slower than that in pure water, while the folding time is the same. Thus, ClO_4^- binding to lys side chain $-NH_3^+$ groups and the

peptide backbone slows α-helix unfolding, while not impacting α-helix folding, resulting in an increased α-helix stability.

ClO_4^- binding increases (un)folding activation barriers. Table 7.5 compares the PLL (un)folding activation barriers between 0.5 M $NaClO_4$ (pH 10.66) and pure water (pH 10.66). In general, the unfolding activation barriers of PLL are much greater in the presence of ClO_4^- than in pure water. In contrast, the α-helix-like and the π-helix (bulge) folding activation barriers in 0.5 M $NaClO_4$ are identical within experimental error to those in pure water. Interestingly, the pure water pure α-helix folding activation barrier is negative, possibly indicating the opening of additional folding pathway(s) as the temperature increases.

Table 7.5: The PLL (un)folding activation energies.

		PLL in pure water (pH 10.66)	PLL in 0.5 M $NaClO_4$ (pH 10.66)
Folding activation energy / kcal/mol	α-helix-like	-3.1 ± 4.0	2.5 ± 3.1
	pure α-helix	-13.1 ± 6.0*	17.2 ± 4.2
	π-helix(bulge)	3.5 ± 2.7	-0.5 ± 6.1
Unfolding activation energy / kcal/mol	α-helix-like	4.2 ± 4.0	21.9 ± 3.1
	pure α-helix	-4.2 ± 6.0	40.4 ± 4.2
	π-helix(bulge)	12.8 ± 2.7	23.2 ± 6.1

*** The negative folding activation energy indicates a failure of a two-state modeling of the PLL pure α-helix (un)folding kinetics in pure water.**

In ClO_4^-, the pure α-helix unfolding activation barrier is a maximum and positive. These results may indicate that ClO_4^- preferentially binds to the PLL folded conformation, decreasing the energy of the folded conformation relative to the energy of the unfolded PPII and 2.5_1-helix conformations.

Ma et al observed that $NaClO_4$ slows the H/D exchange rate of the PLL unfolded conformations, and proposed that ClO_4^- binding to the backbone and the lys $-NH_3^+$ groups protects the backbone amide NH from exchange. [44] The ion-pairing between ClO_4^- and PLL is

expected to be more stable in folded conformations than in unfolded conformations, partly because of the lower dielectric constant of the folded conformations in the region between the backbone and side chains. This region of unfolded PPII-like conformations is populated by the high dielectric constant water that hydrogen bonds to the backbone and lys side chains.[47,48]

Do the PLL folding and unfolding coordinates differ? Fig. 7.10 shows the reaction coordinate for PLL pure α-helix (un)folding in 0.5 M $NaClO_4$ (pH 10.66). The calculated pure α-helix unfolding activation energy, $G^{\ddagger}_{\alpha u}$ and folding activation energy, $G^{\ddagger}_{\alpha f}$ are 40.4 ± 4.2 kcal/mol and 17.2 ± 4.2 kcal/mol, respectively (Table 7.5).

The free energy differences between the unfolded conformations and the pure α-helix are small, with ΔG_{α} of -0.44 ± 0.03 kcal/mol and -1.03 ± 0.03 kcal/mol at 40 ^{o}C and 48 ^{o}C, respectively (Table 7.1). For a true two-state system, the α-helix unfolding energetics require $G^{\ddagger}_{\alpha u} = G^{\ddagger}_{\alpha f} + \Delta G_{\alpha}$ if the same reaction coordinate were followed. Thus, the system cannot be two-state and the α-helix folding coordinate must differ from the unfolding coordinate. This is not surprising since it would be unlikely, for example, for the PPII and 2.5_1-helix to follow the identical folding pathways.

Fig. 7.11 shows the reaction coordinate for PLL π-helix (bulge) (un)folding in 0.5 M $NaClO_4$ at pH 10.66. The calculated $G^{\ddagger}_{\pi u}$ and $G^{\ddagger}_{\pi f}$ are 23.2 ± 6.1 kcal/mol and -0.5 ± 6.1 kcal/mol, respectively (Table 7.5), with ΔG_{π} of -0.24 ± 0.03 kcal/mol and -0.83 ± 0.03 kcal/mol at 40 ^{o}C and 48 ^{o}C, respectively (Table 7.1). $G^{\ddagger}_{\pi u} \neq G^{\ddagger}_{\pi f} + \Delta G_{\pi}$, thus, the π-helix (bulge) folding and unfolding coordinates also differ.

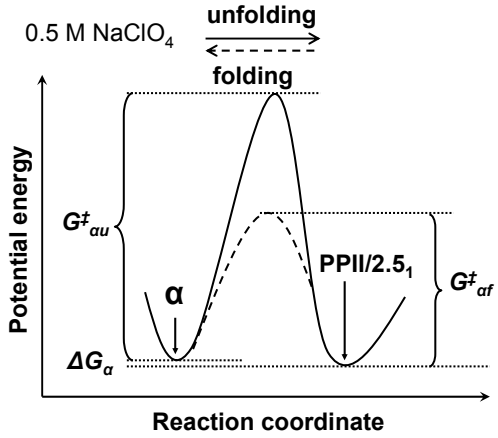

Figure 7.10: Two state reaction coordinate for the 0.5 M $NaClO_4$ PLL pure α-helix (un)folding at 40 °C and 48 °C (pH 10.66). $G^{\ddagger}_{\alpha u}$ and $G^{\ddagger}_{\alpha f}$ are the pure α-helix unfolding and folding activation energies, respectively. ΔG_{α} is the free energy difference between the unfolded PPII/ 2.5_1-helix conformations and the pure α-helix.

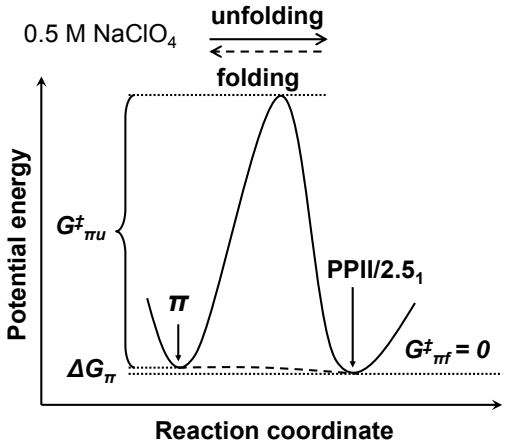

Figure 7.11: Two-state reaction coordinate for the PLL π-helix(bulge) (un)folding in 0.5 M $NaClO_4$ at 40 °C and 48 °C (pH 10.66). $G^{\ddagger}_{\pi u}$ and $G^{\ddagger}_{\pi f}$ are the π-helix (bulge) unfolding and folding activation energies, respectively. ΔG_{π} is the free energy difference between the unfolded PPII/2.5_1-helix conformations and the π-helix (bulge).

A two-state modeling of the PLL pure α-helix (un)folding kinetics in pure water (pH 10.66) gives a negative folding activation energy of -13.1 ± 6.0 kcal/mol (Table 7.5), indicating that the PLL pure α-helix (un)folding in pure water is not a two-state process.

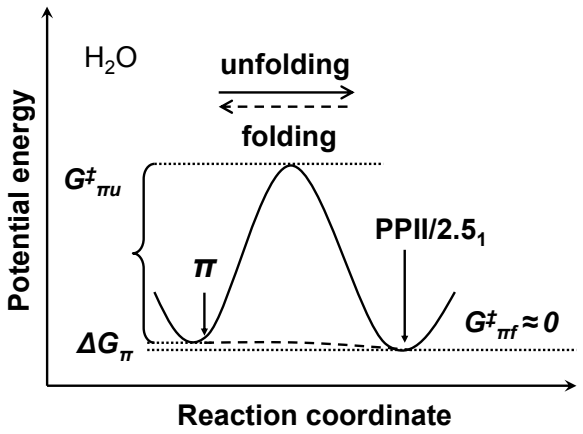

Figure 7.12: Two-state reaction coordinate for the PLL π-helix(bulge) (un)folding in pure water at 44 °C and 54 °C (pH 10.66). $G^{\ddagger}_{\pi u}$ and $G^{\ddagger}_{\pi f}$ are the π-helix (bulge) unfolding and folding activation energies, respectively. ΔG_{π} is the free energy difference between the unfolded PPII/2.5$_1$-helix conformations and the π-helix (bulge).

Fig. 7.12 shows the pure water (pH 10.66) reaction coordinate for the PLL π-helix (bulge) (un)folding. The calculated $G^{\ddagger}_{\pi u}$ and $G^{\ddagger}_{\pi f}$ are 12.8 ± 2.7 kcal/mol and 3.5 ± 2.7 kcal/mol, respectively (Table 7.5). ΔG_{π} are -0.89 ± 0.02 kcal/mol and -1.22 ± 0.02 kcal/mol at 44 °C and 54 °C, respectively (Table 7.2). $G^{\ddagger}_{\pi u} \neq G^{\ddagger}_{\pi f} + \Delta G_{\pi}$, thus, in pure water the π-helix(bulge) folding and unfolding coordinates differ.

Contribution of Ramachandran Ψ angle to α-helix and π-helix (bulge) (un)folding reaction coordinate. By using the methodology of Ma et al, [24] we calculated the Ramachandran Ψ-angle probability distributions, and by assuming Boltzmann distributions, we then calculated the projection of the Gibbs free energy landscapes for PLL in 0.5 M $NaClO_4$ along the Ramachandran Ψ-angle coordinate (Fig. 7.13). The 40 °C energy landscape (Fig. 7.13) shows an α-helix-like basin where the π-helix (bulge) free energy is lowest, and the pure α-helix and turn conformations occur at higher energies. The Gibbs free energy landscape also contains an unfolded basin consisting of PPII and 2.5$_1$-helix conformations. As the temperature increases to

48 °C, the α-helix-like basin free energies increase relative to that of the PPII and 2.5_1-helix unfolded basin.

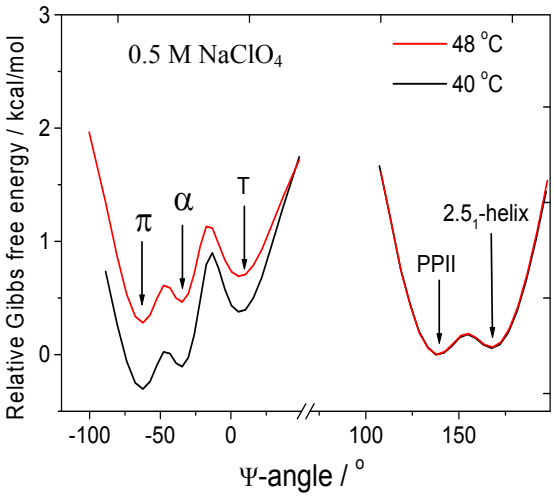

Figure 7.13: Calculated projection of the Gibbs free energy landscapes for PLL in 0.5 M $NaClO_4$ at pH 10.66, along the Ramachandran Ψ-angle coordinate. PPII is the reference state.

The π-helix (bulge) free energy minimum is determined to be 0.19 ± 0.01 kcal/mol below that of the pure α-helix. The energy barriers along the Ψ-angle coordinate between the π-helix (bulge) minimum and the pure α-helix conformation, and between the pure α-helix minimum and the π-helix (bulge) conformation are 0.33 ± 0.02 kcal/mol and 0.14 ± 0.01 kcal/mol, respectively (Fig. 7.13). This predicts that the unfolding activation barrier between the π-helix (bulge) and the PPII/2.5_1-helix conformation is ~0.3 kcal/mol more than that between the pure α-helix and the PPII/2.5_1-helix, while the folding activation barrier between the PPII/2.5_1-helix and the π-helix (bulge) folding is ~0.1 kcal/mol more than that between the PPII/2.5_1-helix and the pure α-helix, if the α-helix and π-helix (bulge) (un)folding were constrained to evolve along the Ψ angle coordinate. However, the PLL π-helix (bulge) unfolding and folding activation energies in 0.5 M $NaClO_4$ (Table 7.5) are both calculated to be many kcal/mol less than those of

pure α-helices. This indicates that the π-helix (bulge) unfolding and folding is not constrained to pass through the α-helix well and must instead involve a reaction coordinate(s) other than a pure Ψ angle reaction coordinate.

We also calculated the Gibbs free energy landscapes for PLL in pure water at pH 10.66 (Fig. 7.14). The 44 ^{o}C energy landscape shows an α-helix-like basin where the π-helix (bulge) free energy is lowest, followed by the pure α-helix and T1 and T2 turn conformations. As the temperature increases to 54 ^{o}C, the α-helix-like basin free energies increase relative to that of the PPII/2.5$_1$-helix basin.

A similar situation occurs for PLL in pure water. In pure water, the π-helix (bulge) free energy is 0.74 ± 0.02 kcal/mol below that of the pure α-helix. The energy barriers along the Ψ-angle coordinate between the π-helix (bulge) minimum and the pure α-helix conformation, and between the pure α-helix minimum and the π-helix (bulge) conformation are 1.5 ± 0.2 kcal/mol and 0.76 ± 0.17 kcal/mol, respectively (Fig. 7.14). This predicts that the unfolding activation barrier between the π-helix (bulge) and the PPII/2.5$_1$-helix is ~1.5 kcal/mol more than that between the pure α-helix and the PPII/2.5$_1$-helix, while the folding activation barrier between the PPII/2.5$_1$-helix and the π-helix (bulge) is ~0.76 kcal/mol more than that between the PPII/2.5$_1$-helix and the pure α-helix, if the α-helix and π-helix (bulge) (un)folding were constrained to evolve along the Ψ angle coordinate. However, two-state modeling indicates that the PLL π-helix (bulge) unfolding and folding activation energies in pure water are significantly greater than those of the pure α-helix (Table 7.5). This indicates that the π-helix (bulge) unfolding and folding does not go through the α-helix energy well.

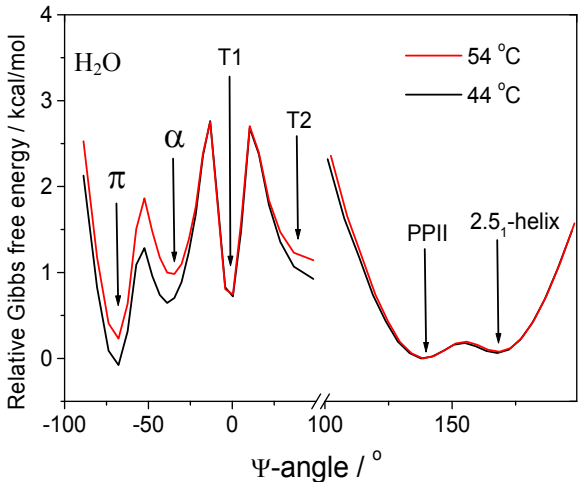

Figure 7.14: Calculated projection of the Gibbs free energy landscapes for PLL in pure water at pH 10.66, along the Ramachandran Ψ-angle coordinate. PPII is the reference state.

These results clearly demonstrate that PLL (un)folding differs dramatically from a two-state process.

PLL (un)folding reaction coordinate: Fig. 7.15 shows a multi-state reaction coordinate for the 0.5 M $NaClO_4$ PLL π-helix (bulge) and pure α-helix (un)folding. Type I/I′ or Type II/II′ β-turns are indicated to be π-helix (bulge) and α-helix unfolding intermediates. The π-helix (bulge) unfolding and folding does not dominantly go through the α-helix energy well, but involves at least an additional reaction coordinate. The π-helix (bulge) and pure α-helix folding coordinates differs from their unfolding coordinates.

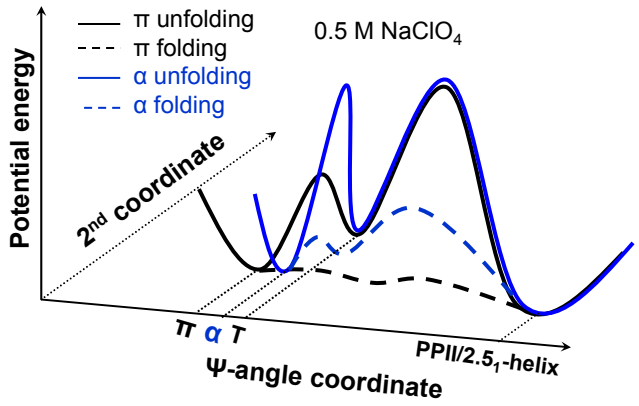

Figure 7.15: Multi-state reaction coordinate for 0.5 M $NaClO_4$ (pH 10.66) PLL π-helix (bulge) and pure α-helix unfolding and folding at 40 °C and 48 °C.

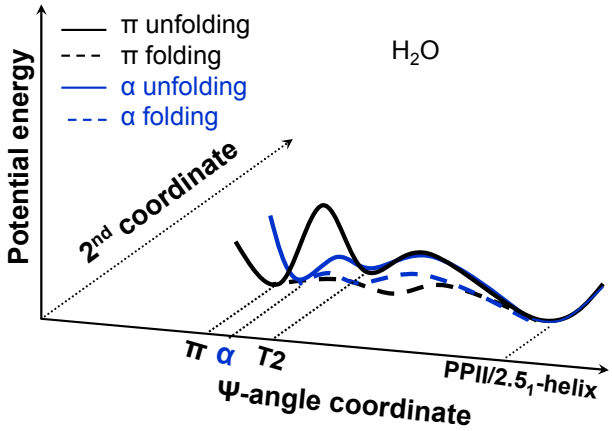

Figure 7.16: Multi-state reaction coordinate for pure water (pH 10.66) PLL π-helix (bulge) and pure α-helix unfolding and folding at 44 °C and 54 °C.

Fig. 7.16 shows a multi-state reaction coordinate for the pure water (pH 10.66) PLL π-helix (bulge) and pure α-helix (un)folding. Type III′ β-turn or inverse γ-turn (T2) are shown as π-helix (bulge) and α-helix unfolding intermediates. The π-helix (bulge) unfolding and folding does not directly go through the α-helix energy well, but involves a second reaction coordinate. The π-helix (bulge) and pure α-helix folding coordinates also differ from their unfolding coordinates.

7.5 CONCLUSIONS

We utilize T-jump UVRR to monitor the (un)folding kinetics of the pure α-helix and the π-helix(bulge). We observe that the relaxation rates of folded conformations (including the π-helix (bulge), pure α-helix and turns) of PLL are slower than those of alanine based peptides. We also, for the first time experimentally observe that turn conformations are α-helix and π-helix(bulge) unfolding intermediates. Turn conformations must have slower kinetics than the α-helix and π-helix(bulge) kinetics, resulting in relative turn concentration increases during high temperature α-helix and π-helix(bulge) unfolding.

The π-helix(bulge) melts before the α-helix in 0.5 M $NaClO_4$ (pH 10.66) at 40 ^oC. ClO_4^- binding to the lys side chain $–NH_3^+$ groups and backbone peptide bonds slows pure α-helix unfolding, but little impacts folding, resulting in an increased α-helix stability. ClO_4^- binding also increases the PLL unfolding activation barrier but little impacts the folding barrier. The PLL folding reaction coordinate differs from the unfolding coordinate. The π-helix (bulge) unfolding and folding does not directly go through the α-helix basin. Our results clearly demonstrate that PLL (un)folding is far from a two-state process.

7.6 ACKNOWLEDGEMENTS

We thank Dr. Sergei V. Bykov, David Punihaole and Jonathan Wert for useful discussions. This work was supported by NIH grant 1RO1EB009089.

7.7 REFERENCES

(1) Baldwin, R. L.; Rose, G. D. *Trends in Biochemical Sciences* **1999**, *24*, 26-33.

(2) Baldwin, R. L.; Rose, G. D. *Trends in Biochemical Sciences* **1999**, *24*, 77-83.

(3) Dobson, C. M. *Philosophical Transactions of the Royal Society of London Series B-Biological Sciences* **2001**, *356*, 133-145.

(4) Dobson, C. M.; Sali, A.; Karplus, M. *Angewandte Chemie-International Edition* **1998**, *37*, 868-893.

(5) Jahn, T. R.; Radford, S. E. *Febs Journal* **2005**, *272*, 5962-5970.

(6) Lindberg, M. O.; Oliveberg, M. *Current Opinion in Structural Biology* **2007**, *17*, 21-29.

(7) Daggett, V.; Fersht, A. *Nature Reviews Molecular Cell Biology* **2003**, *4*, 497-502.

(8) Ihalainen, J. A.; Bredenbeck, J.; Pfister, R.; Helbing, J.; Chi, L.; van Stokkum, I. H. M.; Woolley, G. A.; Hamm, P. *Proceedings of the National Academy of Sciences of the United States of America* **2007**, *104*, 5383-5388.

(9) Bredenbeck, J.; Helbing, J.; Kumita, J. R.; Woolley, G. A.; Hamm, P. *Proceedings of the National Academy of Sciences of the United States of America* **2005**, *102*, 2379-2384.

(10) Huang, C. Y.; Getahun, Z.; Zhu, Y. J.; Klemke, J. W.; DeGrado, W. F.; Gai, F. *Proceedings of the National Academy of Sciences of the United States of America* **2002**, *99*, 2788-2793.

(11) Dyer, R. B.; Gai, F.; Woodruff, W. H. *Accounts of Chemical Research* **1998**, *31*, 709-716.

(12) Balakrishnan, G.; Hu, Y.; Bender, G. M.; Getahun, Z.; DeGrado, W. F.; Spiro, T. G. *Journal of the American Chemical Society* **2007**, *129*, 12801-12808.

(13) Williams, S.; Causgrove, T. P.; Gilmanshin, R.; Fang, K. S.; Callender, R. H.; Woodruff, W. H.; Dyer, R. B. *Biochemistry* **1996**, *35*, 691-697.

(14) Thompson, P. A.; Eaton, W. A.; Hofrichter, J. *Biochemistry* **1997**, *36*, 9200-9210.

(15) Thompson, P. A.; Munoz, V.; Jas, G. S.; Henry, E. R.; Eaton, W. A.; Hofrichter, J. *Journal of Physical Chemistry B* **2000**, *104*, 378-389.

(16) Huang, C. Y.; Klemke, J. W.; Getahun, Z.; DeGrado, W. F.; Gai, F. *Journal of the American Chemical Society* **2001**, *123*, 9235-9238.

(17) Lednev, I. K.; Karnoup, A. S.; Sparrow, M. C.; Asher, S. A. *Journal of the American Chemical Society* **1999**, *121*, 8074-8086.

(18) Mikhonin, A.; Asher, S.; Bykov, S.; Murza, A. *Journal of Physical Chemistry B* **2007**, *111*, 3280-3292.

(19) Young, W. S.; Brooks, C. L. *Journal of Molecular Biology* **1996**, *259*, 560-572.

(20) Chowdhury, S.; Zhang, W.; Wu, C.; Xiong, G. M.; Duan, Y. *Biopolymers* **2003**, *68*, 63-75.

(21) Wang, T.; Zhu, Y. J.; Getahun, Z.; Du, D. G.; Huang, C. Y.; DeGrado, W. F.; Gai, F. *Journal of Physical Chemistry B* **2004**, *108*, 15301-15310.

(22) Ramajo, A. P.; Petty, S. A.; Volk, M. *Chemical Physics* **2006**, *323*, 11-20.

(23) von Hansen, Y.; Kalcher, I.; Dzubiella, J. *Journal of Physical Chemistry B* **2010**, *114*, 13815-13822.

(24) Ma, L.; Ahmed, Z.; Mikhonin, A. V.; Asher, S. A. *Journal of Physical Chemistry B* **2007**, *111*, 7675-7680.

(25) Tiffany, M. L.; Krimm, S. *Biopolymers* **1968**, *6*, 1379-&.

(26) Painter, P. C.; Koenig, J. L. *Biopolymers* **1976**, *15*, 229-240.

(27) McColl, L. H.; Blanch, E. W.; Gill, A. C.; Rhie, A. G. O.; Ritchie, M. A.; Hecht, L.; Nielsen, K.; Barron, L. D. *Journal of the American Chemical Society* **2003**, *125*, 10019-10026.

(28) Keiderling, T. A.; Silva, R. A. G. D.; Yoder, G.; Dukor, R. K. *Bioorganic & Medicinal Chemistry* **1999**, *7*, 133-141.

(29) Bykov, S.; Lednev, I.; Ianoul, A.; Mikhonin, A.; Munro, C.; Asher, S. A. *Applied Spectroscopy* **2005**, *59*, 1541-1552.

(30) Kubelka, J. *Photochemical & Photobiological Sciences* **2009**, *8*, 499-512.

(31) Mikhonin, A. V.; Ahmed, Z.; Ianoul, A.; Asher, S. A. *Journal of Physical Chemistry B* **2004**, *108*, 19020-19028.

(32) Myshakina, N. S.; Ahmed, Z.; Asher, S. A. *Journal of Physical Chemistry B* **2008**, *112*, 11873-11877.

(33) Wang, Y.; Purrello, R.; Jordan, T.; Spiro, T. G. *Journal of the American Chemical Society* **1991**, *113*, 6359-6368.

(34) Xiong, K.; Asciutto, E. K.; Madura, J. D.; Asher, S. A. *Biochemistry* **2009**, *48*, 10818-10826.

(35) Fletcher, W. H.; Rayside, J. S. *Journal of Raman Spectroscopy* **1974**, *2*, 3-14.

(36) Weber, A.; McGinnis, E. A. *Journal of Molecular Spectroscopy* **1960**, *4*, 195-200.

(37) Asher, S.; Mikhonin, A.; Bykov, S. *JOURNAL OF THE AMERICAN CHEMICAL SOCIETY* **2004**, *126*, 8433-8440.

(38) Mikhonin, A. V.; Myshakina, N. S.; Bykov, S. V.; Asher, S. A. *Journal of the American Chemical Society* **2005**, *127*, 7712-7720.

(39) Millhauser, G. L. *Biochemistry* **1995**, *34*, 10318-10318.

(40) Sundaralingam, M.; Sekharudu, Y. C. *Science* **1989**, *244*, 1333-1337.

(41) Millhauser, G. L.; Stenland, C. J.; Hanson, P.; Bolin, K. A.; vandeVen, F. J. M. *Journal of Molecular Biology* **1997**, *267*, 963-974.

(42) Lee, K. H.; Benson, D. R.; Kuczera, K. *Biochemistry* **2000**, *39*, 13737-47.

(43) Chapman, R.; Kulp, J. L., 3rd; Patgiri, A.; Kallenbach, N. R.; Bracken, C.; Arora, P. S. *Biochemistry* **2008**, *47*, 4189-95.

(44) Ma, L.; Hong, Z.; Sharma, B.; Asher, S. *J. Phys. Chem. B* **2011**, *in press*.

(45) Ebert, G.; Kuroyanagi, Y. *Polymer* **1982**, *23*, 1147-1153.

(46) Ebert, G.; Kuroyanagi, Y. *Polymer* **1982**, *23*, 1154-1158.

(47) Shi, Z.; Olson, C.; Rose, G.; Baldwin, R.; Kallenbach, N. *Proc Natl Acad Sci. USA* **2002**, *99*, 9190-9195.

(48) Shi, Z.; Chen, K.; Liu, Z.; Kallenbach, N. *CHEMICAL REVIEWS* **2006**, *106*, 1877-1897.

CHAPTER 8

UV Resonance Raman Monitors Polyglutamine Backbone and Side Chain Hydrogen Bonding and Fibrillization

This Chapter was submitted to J. Am. Chem. Soc. The co-authors are Kan Xiong, David Punihaole and Sanford A. Asher.

8.0 UV RESONANCE RAMAN MONITORS POLYGLUTAMINE BACKBONE AND SIDE CHAIN HYDROGEN BONDING AND FIBRILLIZATOIN

We utilize 198 and 204 nm excited UV resonance Raman spectroscopy (UVRR) and circular dichroism spectroscopy (CD) to monitor the backbone conformation and the GLN side chain hydrogen bonding (HB) of a short, mainly polyGLN peptide of sequence $D_2Q_{10}K_2$ (Q10). We measured the UVRR spectra of valeramide to determine the dependence of the primary amide vibrations on amide HB. We observe that non-disaggregated Q10 (NDQ10) solution (prepared by directly dissolving the original synthesized peptide in pure water) occurs in a β-sheet conformation, where the GLN side chains HB to either the backbone or other GLN side chains. At 60 ^{o}C, these solutions readily form amyloid fibrils. We used the polyGLN disaggregation protocol of Wetzel et al (*Methods Enzymol,* **2006**, *413*, 34-74) to dissolve the Q10 β-sheet aggregates. We observe that the disaggregated Q10 (DQ10) solutions adopt PPII-like and 2.5_1-helix conformations where the GLN side chains HB to water. In contrast, these samples do not form fibrils. The NDQ10 β-sheet solution structure is essentially identical to that found in the NDQ10 solid formed upon solution evaporation. The DQ10 PPII and 2.5_1-helix solution structure is essentially identical to that in the DQ10 solid. Although the NDQ10 solution readily forms fibrils when heated, the DQ10 solution does not form fibrils unless seeded by NDQ10 solution. This result demonstrates very high activation barriers between these solution conformations.

8.1 INTRODUCTION

There are at least nine neurodegenerative diseases that are caused by long CAG DNA repeats that encode for proteins with long tracts of polyGLN residues.[1,2] In these diseases, the extended polyGLN regions aggregate to form amyloid fibrils.[3-5] Previous studies suggest that polyGLN fibril structures are stabilized by both main chain and side chain HB.[6-9] However, there has been little work that investigates the role of HB in the aggregation mechanism(s) of polyGLN rich peptides and proteins.[10]

Given the central role that backbone and side chain HB can potentially play in stabilizing polyGLN aggregates, it is important to find spectral markers for tracking these HB. Backbone HB is sometimes monitored by measuring the frequencies of the backbone amide vibrations, such as the AmI vibration (mainly C=O s) and the AmIII vibration (mainly in-phase combination of CN s and NH b) and the N-H stretching vibration.[11-14] The frequency of the AmII vibration (mainly out of phase combination of CN s and NH b) also depends on backbone HB.[15]

However, a method for studying side chain HB is needed. The C=O stretching frequencies of ASN, GLN, protonated ASP and GLU side chains are sensitive to HB.[16-18] Unfortunately, the use of IR spectroscopy for monitoring side chain vibrations is challenging due to spectral congestion, and isotopic labeling is often required to unambiguously assign bands.

In this work here, we show that UVRR can selectively enhance the GLN primary amide side chain vibrations, and that these vibrations can be used to track GLN side chain HB. Here, we utilize 198 and 204 nm excited UVRR and CD to monitor the backbone conformation and the GLN side chain HB of a short, mainly polyGLN peptide Q10, of sequence $D_2Q_{10}K_2$. Previous studies of similar peptides have shown that these peptides can aggregate to form β-sheet rich

amyloid fibrils. [8,9,19-25] We observe that non-disaggregated Q10 (NDQ10) in solution occurs as β-sheets in which the GLN side chains HB to either the backbone or other GLN side chains. At 60 ^{o}C, these solutions readily form amyloid fibrils. We used the polyGLN disaggregation protocol of Wetzel et al [26] to disaggregate Q10. We observe that disaggregated Q10 (DQ10) solution adopts PPII-like and 2.5_1-helix conformations in which the GLN side chains HB to water. These samples do not form fibrils. Addition of small quantities of NDQ10 readily nucleates fibrils. This directly demonstrates that high activation barrier occurs between the monomer extended DQ10 solution conformation and the β-sheet structures that fibrillize.

8.2 EXPERIMENTAL

Materials: The short mainly polyGLN peptide of sequence $D_2Q_{10}K_2$ (Q10) (> 90% purity) was synthesized by AnaSpec Inc, by using a solid phase peptide synthesis method. Briefly, the first amino acid Fmoc-AA-OH was coupled onto the resin and the peptide was synthesized through sequential synthetic operations of Fmoc deprotection, washing, Fmoc amino acid coupling, and washing. The synthesized crude peptide was obtained after acid cleavage from the solid support resin using a TFA cocktail (where TFA is the major component).

The resulting crude peptide was then purified with preparative HPLC (using large columns and high flow rates) by using a mobile phase gradient consisting of 0.1 % (v/v) TFA in water and pure acetonitrile. The purified sample was then lyophilized.

Valeramide (97% purity) was purchased from Alfa Aesar. L-Glutamine (99% purity) was purchased from Acros. Trifluoroacetic acid (TFA, 99.5% purity) was purchased from Acros. 1,1,1,3,3,3-hexafluoro-2-propanol (HFIP, ≥ 99% purity) was purchased from Fluka.

Solutions of non-disaggregated Q10 (NDQ10) were prepared by directly dissolving the peptide in pure water at 1 mg / ml concentrations at pH 4.3. NDQ10 solid samples were prepared by evaporating the NDQ10 solution. The UVRR spectra were identical to that of the solid sample obtained from the manufacturer. We used the polyGLN disaggregation protocol of Wetzel et al [26] to dissolve the Q10 aggregates. Briefly, solutions of disaggregated Q10 (DQ10) were prepared by suspending 10 mg of Q10 in a 5 mL solution of 1:1 (v/v) TFA and HFIP [TFA alone dissolves Q10 aggregates (see Fig.F3 in Appendix F); the primary function of HFIP is to facilitate the removal of TFA. [26]]. The samples were then sonicated for 20 min [Sonication is not essential (see Fig.F3 in Appendix F)] and incubated at room temperature for ~ 2 hr. The solvents were evaporated with a gentle stream of dry N_2 gas for ~ 20 min. The peptide film was resuspended in pure water at a final concentration of ~ 1 mg/mL and the pH was adjusted to 7. The peptide solution was centrifuged at 627,000 g for 30 min at 4 ^{o}C, and the top 66% of the solution was used. DQ10 solid samples were prepared by evaporating the DQ10 solution.

CD spectra between 190 - 250 nm were measured by using a Jasco-715 spectropolarimeter with a 0.02 cm path length cuvette. Five 1-min accumulations were averaged.

The UVRR spectrometer was described in detail by Bykov et al.[27] Briefly, 204 nm UV light was obtained by generating the fifth anti-Stokes Raman harmonic of the third harmonic of a Nd:YAG laser (Coherent, Infinity). 198 nm UV light was obtained by mixing the 3rd harmonic of the 792 nm fundamental of a 1 KHz repetition rate tunable Ti:Sapphire laser (DM20-527 TU-L-FHG) from Photonics Industries.

The liquid sample was circulated in a free surface, temperature-controlled stream. A spinning cell was used for the solid samples to minimize photodegradation; the solid samples were packed into a circular groove of the cylindrical spinning disc. A 165^{o} sampling

backscattering geometry was used. The collected light was dispersed by a double monochromator onto a back thinned CCD camera with a Lumogen E coating (Princeton Instruments-Spec 10 System). We averaged four 5-min accumulations.

Electron micrographs were measured by using a Tecnai T12 microscope (FEI) operating at 120 KV. Samples were prepared on carbon coated grids and stained with 2% uranyl acetate. Samples were magnified 30,000 X.

X ray patterns were measured by using a Bruker Smart Apex CCD diffractometer.

8.3 RESULTS

UVRR of valeramide: We examined the UVRR spectra of valeramide that we used to model the GLN side chain primary amide UVRR spectra, to determine the dependence of the primary amide vibrations on their HB to water. 198 and 204 nm excitation both occur within the $\pi \rightarrow \pi^*$ electronic transition of the primary amide group.[28] Thus, the side chain amide group vibrations are selectively enhanced.

Fig.8.1 shows the 204 nm excited UVRR spectra of valeramide in water at 22 ^{o}C and 65 ^{o}C. The 22 ^{o}C spectrum shows an AmI-like shoulder at ~ 1666 cm^{-1} (mainly CO s) and an AmII-like band at 1606 cm^{-1} (mainly NH_2 b with a small contribution from CO s). It also shows a $\delta asCH_3$ shoulder at 1458 cm^{-1} (asymmetric deformation of the CH_3 group), and a strong peak at 1420 cm^{-1} where the δCH_2 band (CH_2 b) and an AmIII-like band (mainly CN s with minor contributions from CH_2 b and NH_2 r) overlap. The ωCH_2 band occurs at 1312 cm^{-1} (CH_2 w). The rNH_2^1 and rNH_2^2 bands (mainly NH_2 r) occur at 1132 and 1082 cm^{-1}, respectively. [28-30]

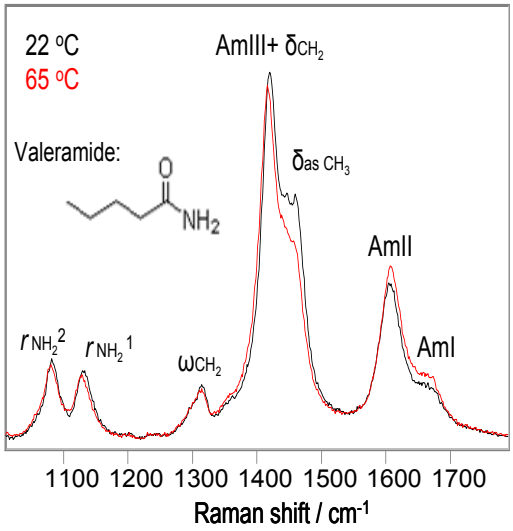

Figure 8.1: Temperature dependence of the 204 nm excited UVRR spectra of valeramide in water at 22 °C (Black) and 65 °C (Red). Water contributions were removed. The intensities were normalized to the 932 cm^{-1} ClO_4^- peak height. The ClO_4^- band is subtracted out.

As the temperature increases to 65 °C, the AmI band frequency little changes. The AmII band upshifts 2 cm^{-1}. The δasCH_3 band downshifts 2 cm^{-1} and its intensity decreases. The AmIII+δCH_2 peak downshifts 4 cm^{-1}. The ωCH_2 band does not change. The *r*NH_2^1 and *r*NH_2^2 bands both downshift 2 cm^{-1}.

In acetonitrile: The UVRR spectrum of valeramide in pure acetonitrile (Fig.8.2) changes dramatically compared to that in pure water. The AmI band upshifts 21 cm^{-1} due to the decreased HB in acetonitrile,[15] and its relative intensity dramatically increases. The AmII band upshifts 11 cm^{-1} due to the decreased HB of the -NH_2. The frequency of the δasCH_3 band shows little change. The AmIII+δCH_2 peak and ωCH_2 bands downshift 31 and 12 cm^{-1}, respectively. The rNH_2^1 and rNH_2^2 bands downshift 6 and 16 cm^{-1}, respectively.

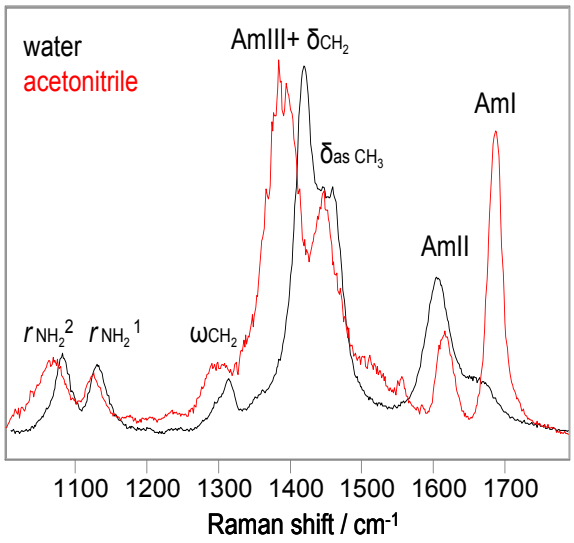

Figure 8.2: The 204 nm excited UVRR spectra of valeramide at 22 °C: Black in water; Red in pure acetonitrile. Solvent contributions were removed. The intensities were normalized to the AmIII+δCH_2 peak height.

Solid state: The UVRR spectrum of valeramide powder from the manufacturer (red, Fig.8.3) differs significantly from that dissolved in water. The AmI band upshifts 10 cm^{-1}, indicative of weakened carbonyl HB,[15] and the relative intensity of the AmI band significantly increases. The AmII band downshifts 5 cm^{-1}. The AmIII+δCH_2 peak becomes asymmetric and upshifts 12 cm^{-1}. The δasCH_3 band is not evident. The frequency of ωCH_2 band changes little. The *r*NH_2^1 and *r*NH_2^2 bands upshift 10 and 8 cm^{-1}, respectively.

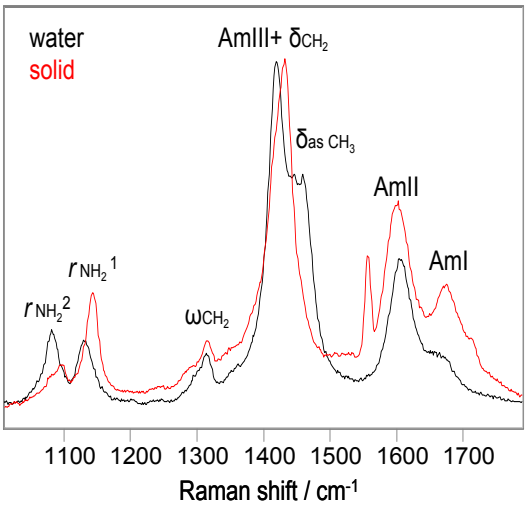

Figure 8.3: The 204 nm excited UVRR spectra of valeramide solid (Red) and in water (Black) at 22 °C. Water contributions were removed. The intensities were normalized to the AmIII+δCH$_2$ peak height.

Raman cross sections for valeramide: We calculated the Raman cross sections for valeramide in water and in acetontrile by using eq 8.1: [31]

$$\sigma_{val} = \frac{I_{val} \cdot k(\lambda_r) \cdot C_r \cdot \sigma_r}{I_r \cdot k(\lambda_{val}) \cdot C_{val}} \cdot \left[\frac{\varepsilon_{val} + \varepsilon_{ex}}{\varepsilon_r + \varepsilon_{ex}} \right] \quad (8.1)$$

where I_{val} and I_r are the relative intensities of the valeramide band and the internal standard band (which is the 932 cm^{-1} ClO_4^- band in aqueous solution or the 918 cm^{-1} C-C stretching band of acetonitrile in pure acetonitrile[32]). $k(\lambda_r)$ and $k(\lambda_{val})$ are the spectrometer efficiencies at the wavelengths of the internal standard and valeramide Raman bands. C_r and C_{val} are the concentrations of the internal standard and valeramide, respectively. σ_r is the total differential Raman cross section of the internal standard band at the excitation frequency, ν_{ex}. ε_{ex} is the sample molar absorptivity at ν_{ex}. ε_{val} and ε_r are the sample molar absorptivities at the valeramide Raman band frequency and the internal standard band frequency, respectively. The expression in

the brackets approximately corrects the Raman intensities for self-absorption in a backscattering geometry.

Table 8.1 shows the measured total differential Raman cross sections for valeramide. The 204 nm Raman cross section values of the valeramide amide bands in pure water are approximately half of those of protein backbone secondary amide bands, [33] presumably because the primary amide group electronic transition is blueshifted from that of the peptide bond secondary amides.[28]

Table 8.1: **The measured total differential Raman cross sections for valeramide (mbarn•molecule^{-1}•sr $^{-1}$) at 22 ^{o}C .**

		AmI	AmII	δasCH$_3$	AmIII+δCH$_2$	ωCH$_2$	*r*NH$_2^1$	*r*NH$_2^2$
ν_{ex} = 204 nm	in water	5.4	17	21	33	3.3	5.0	5.6
	in acetonitrile	11	3.1	13	29	3.2	1.7	4.4
ν_{ex} = 198 nm	in water	14	52	58	94	11	14	15
	in acetonitrile	41	50	35	91	10	12	16

***We did not calculate the Raman cross sections for valeramide powder because of the lack of an intensity internal standard.**

The Raman cross sections of the valeramide bands in pure acetonitrile are decreased relative to those in pure water, except for the AmI band cross section, that doubles. A similar behavior was observed for the AmI band of N-methylacetamide.[34] The increased cross section was ascribed to a larger relative CO bond excited state displacement in acetonitrile. [34] The Raman cross sections of the valeramide bands generally triple as the excitation wavelength decreases from 204 to 198 nm, except for the AmII band cross section in acetonitrile, that increases by more than 10-fold. The 198 nm Raman cross section values of the valeramide primary amide bands are similar to those of the protein backbone secondary amide bands.[33]

Table 8.2: **The measured AmI, AmII, rNH_2^1 and rNH_2^2 frequencies of valeramide.**

	AmI / cm^{-1}	AmII / cm^{-1}	rNH_2^1 / cm^{-1}	rNH_2^2 / cm^{-1}
in water at 22 ^oC	1666	1606	1132	1082
in water at 65 ^oC	1666	1608	1130	1080
in acetonitrile at 22 ^oC	1687	1617	1126	1066
powder solid at 22 ^oC	1676	1601	1142	1090

Hydrogen bonding effects on frequencies of primary amide vibrations: These UVRR studies of valeramide indicate that the AmI, AmII, rNH_2^1 and rNH_2^2 frequencies of the primary amide depend on HB. Water HB to the carbonyls downshifts the AmI band by 21 cm^{-1} (see Table 8.2), while HB to the $–NH_2$ upshifts the rNH_2^1 and rNH_2^2 bands by 16 and 24 cm^{-1}, respectively; the AmII band downshifts 16 cm^{-1} upon HB to $–NH_2$. The solid state AmI band upshifts 10 cm^{-1} relative to that in water, indicating weaker carbonyl HB in the valeramide solid than in water. The solid state AmII band downshifts 7 cm^{-1} compared to that in water, and the rNH_2^1 and rNH_2^2 bands upshift 12 and 10 cm^{-1}, respectively. This indicates stronger $–NH_2$ HB in the valeramide solid than in water.

X ray studies of butyramide solid[35] (which has one less methylene than valeramide) indicate that each carbonyl forms two HBs to the two amine H atoms of two adjacent molecules, while each $–NH_2$ forms two HBs to two carbonyls. This stronger $–NH_2$ HB may result from the fact that while the valeramide carbonyl HB geometry is more optimized in water than in the solid state, the $–NH_2$ HB is stronger in the solid state.

Q10 solution backbone conformation: We performed both CD and UVRR measurements to examine the Q10 solution backbone conformation. Previous studies of similar peptides indicate that non-disaggregated polyGLN peptides in aqueous solutions occur as β-sheets,[20,36] while freshly disaggregated polyGLN peptides adopt extended conformations.[37,38]

Fig.8.4 shows the CD spectra of Q10 solutions. The CD spectrum of the NDQ10 in pure water (dashed line) shows a trough at ~ 218 nm and a strong positive band at 197 nm, both characteristic of β-sheet.[39] The spectrum of the DQ10 in pure water (solid line) shows a very slight negative ellipticity at ~ 220 nm and a strong negative band at 200 nm, indicative of extended conformations.[40-42]

204 nm excitation occurs within the $\pi \rightarrow \pi^*$ electronic transition of the backbone secondary amides[33] and to the long wavelength side of the side chain primary amide electronic transitions.[28] Fig.8.5 shows that the 204 nm excited UVRR spectra of Q10 solutions are dominated by the backbone amide vibrations (indicated by ^{b}). The backbone amide vibrations are more enhanced by 204 nm excitation than are those of the side chain amide (indicated by ^{s}).[28]

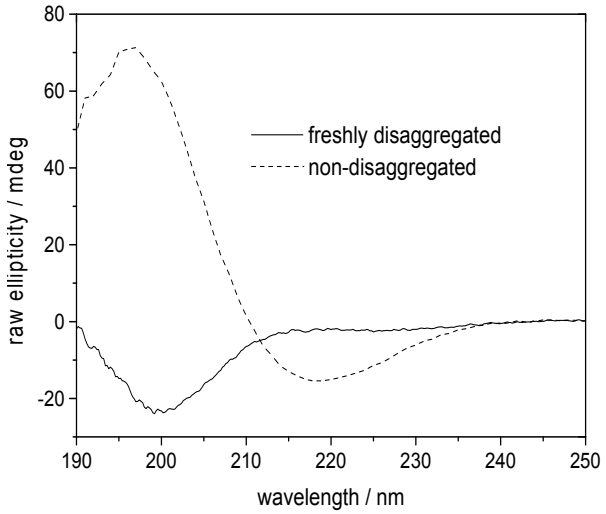

Figure 8.4. CD spectra of 1 mg/ml DQ10 (solid line) and NDQ10 (dashed line) in pure water at 22 ^{o}C. Measured by using a 0.02 cm path length cuvette.

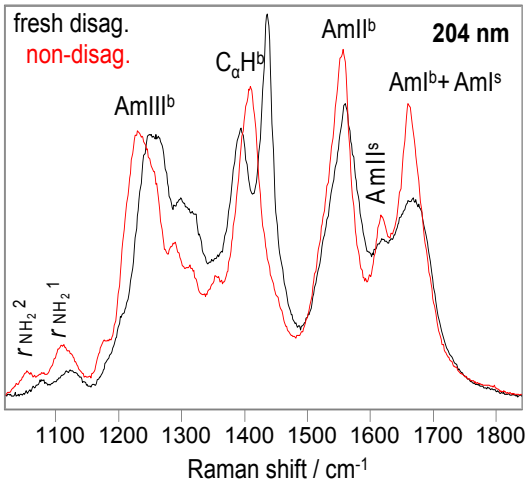

Figure 8.5. **The 204 nm excited UVRR spectra of the DQ10 (black) and NDQ10 (red) in pure water at 22 ^{o}C. ^{b} indicates backbone vibration; ^{s} indicates side chain vibration. The intensities were normalized to the AmIII^b peak height.**

The UVRR spectrum of the NDQ10 (red) shows an AmI^b band at ~ 1660 cm^{-1}, an AmII^b band at ~ 1550 cm^{-1}, the (C)C$_\alpha$-H^b bending bands at ~ 1400 cm^{-1}, and the AmIII^b region between 1180 and 1330 cm^{-1}. The AmI^b band overlaps with the GLN side chain AmI^s band; the C$_\alpha$H^b band overlaps with the side chain AmIII^s+δCH$_2$ peak.

The AmIII^b region of Q10 contains no overlapping side chain contributions. We calculated the Ramachandran Ψ probability distributions for the Q10 backbone peptide bonds from the Fig.8.5 UVRR spectra by using the methodology of Mikhonin et al [11,43,44](see Appendix F for details). The Fig.8.6 Ψ-distribution for the NDQ10 shows a dominant β-sheet contribution (Ψ ~ 138^o). It also contains contributions from Type I, Type III or Type VIII β-turn regions (Ψ ~ -40^o). The Ψ-distribution for the DQ10 shows a dominant contribution of PPII-like (Ψ ~ 145^o) and 2.5$_1$-helix conformations (Ψ ~ 170^o). It also contains contributions of Type I′ or Type III′ β-turns (Ψ ~ 30^o).

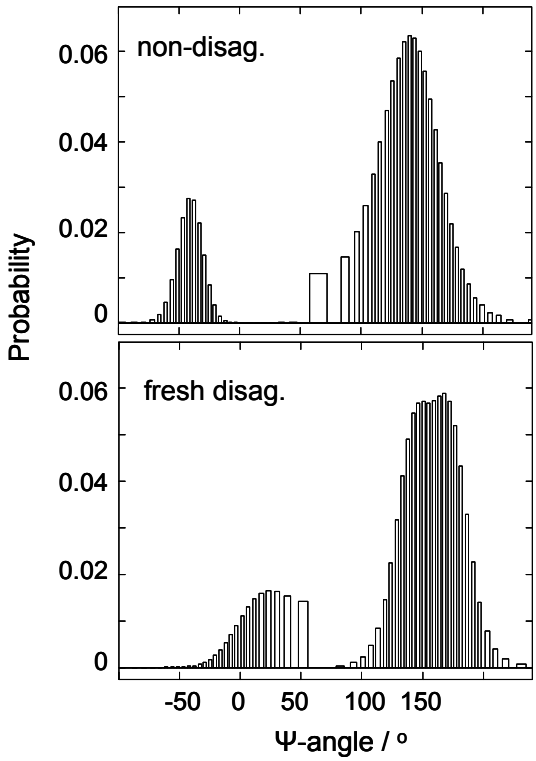

Figure 8.6. **Calculated Ψ-angle distributions for the NDQ10 and DQ10 in pure water at 22 ºC.**

Previous studies indicate that poly-L-lysine and poly-L-glutamate adopt 2.5_1-helix conformations that are stabilized by electrostatic repulsion between the charged side chains.[45-47] We surprisingly find that DQ10 adopts 2.5_1-helix conformations. The mechanism(s) by which these 2.5_1-helix conformations of Q10 are stabilized is unknown.

Q10 solution side chain hydrogen bonding: 198 nm excitation (Fig.8.7) enhances the primary amide UVRR bands significantly more than does 204 nm excitation. As a result, the difference spectrum between the 198 and 204 nm excited UVRR spectra of Q10 (Fig.8.7) is dominated by the GLN side chain primary amide bands.

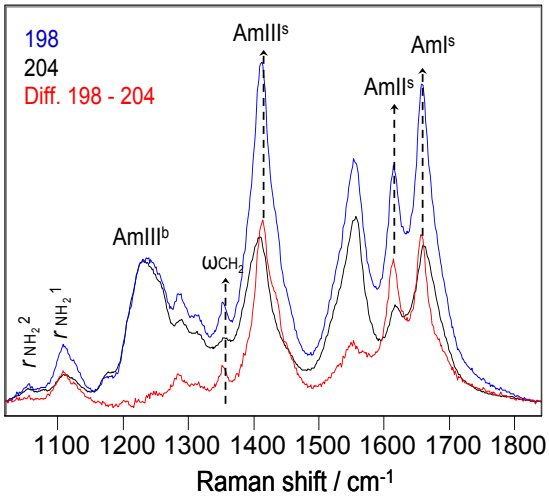

Figure 8.7. The 198 (blue) and 204 nm (black) excited UVRR spectra of the NDQ10 in pure water at 22 ^{o}C, and the difference spectrum between them (red). The intensities were normalized to the AmIII^{b} peak height before spectral subtraction.

The 198 - 204 nm difference spectrum of NDQ10 in pure water (Fig.8.8) shows an AmI^{s} band at 1657 cm^{-1} and an AmII^{s} band at 1614 cm^{-1}. It also shows an AmIII^{s} band at 1414 cm^{-1} and a ωCH_2 band at 1353 cm^{-1}. The $r NH_2^1$ and $r NH_2^2$ bands occur at 1110 and 1056 cm^{-1}, respectively.

The 198 - 204 nm difference spectrum of DQ10 in pure water (Fig.8.8, black) differs significantly from that of NDQ10. The DQ10 AmI^{s} band upshifts 26 cm^{-1}, indicating weaker HB of the GLN side chain carbonyls than that of NDQ10. The AmII^{s} frequency shows little change. The AmIII^{s} frequency upshifts 22 cm^{-1}. The DQ10 $r NH_2^1$ and $r NH_2^2$ frequencies upshift 13 and 19 cm^{-1} respectively, indicating stronger HB of the GLN side chain –NH_2 than in NDQ10.

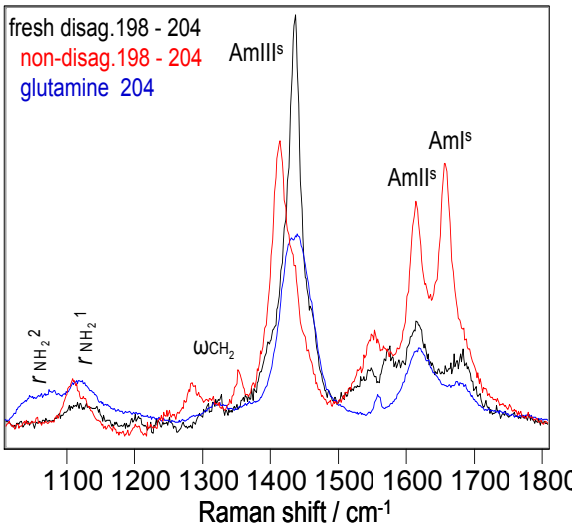

Figure 8.8. The difference spectra between the 198 and 204 nm excited UVRR spectra of the NDQ10 (red) and DQ10 (black) in pure water at 22 ^{o}C. The 204 nm excited UVRR spectrum of glutamine in pure water at pH 1.6 at 22 ^{o}C (blue).

The frequencies of the GLN primary amide vibrations of the DQ10 in pure water (Fig.8.8, black) are very similar to those of glutamine in pure water (Fig.8.8, blue), indicating that HB of the GLN side chains of DQ10 is similar to that of glutamine in pure water; i.e., the GLN side chains of DQ10 HB to water.

The DQ10 AmIII^s band significantly narrows compared to glutamine in water. This may result from the fact that the glutamine side chain has conformations in solution where the primary amide side chain interacts with the $-NH_3^+$ and –COO- groups.

Previous studies indicated that polyGLN aggregates adopt β-sheet conformations that are stabilized by both main chain and side chain HB. [6-9] We observe that the GLN side chain HB of NDQ10 differs significantly from that of DQ10. The NDQ10 AmI^s frequency downshifts 26 cm^{-1} relative to that of DQ10, and its rNH$_2{}^1$ and rNH$_2{}^2$ frequencies downshift 13 and 19 cm^{-1}

respectively. Table 8.2 shows that HB to the primary amide carbonyls significantly downshift the AmI^s frequency, while HB to the $–NH_2$ upshift the r^1NH_2 and r^2NH_2 frequencies. Thus, HB of the NDQ10 GLN side chain carbonyls is stronger than that of DQ10, while HB of its GLN side chain $–NH_2$ is weaker than that of DQ10. These results indicate that the GLN side chain carbonyls of NDQ10 do not HB to water. Instead, they HB to the backbone –NH or to GLN side chain $–NH_2$. Presumable, this conformation results in weaker $–NH_2$ HB.

Q10 solids: We measured the 204 nm excited UVRR spectra of Q10 solids formed by evaporation of the NDQ10 and DQ10 solutions. The UVRR spectrum of the NDQ10 solid (Fig 8.9, black) is very similar to that of NDQ10 in solution (Fig 8.9, red), indicating that the backbone conformations and the GLN side chain HB of NDQ10 solid and solution are essentially identical, and mainly β-sheet. The NDQ10 solid shows a powder X ray pattern (Fig 8.10) very similar to that of Perutz et al.[19] The 4.75-Å reflection (Fig 8.10) is characteristic of β-sheet structures [19].

The $AmIII^b$ region of the solvent evaporated DQ10 solid (Fig 8.9, blue) is similar to that of DQ10 solution (Fig 8.9, green), indicating that their Q10 backbone conformations are similar. The solid state $AmII^b$ band downshifts 7 cm^{-1} compared to that of solution, indicating weakened HB of the solid state backbone –NH[15]; while the solid state AmI^b and AmI^s bands upshift 5 cm^{-1} relative to that of solution, indicating weakened HB to the solid backbone carbonyls and the GLN side chain carbonyls.[15]

These results indicate the Q10 solution and solid state conformations are essentially identical.

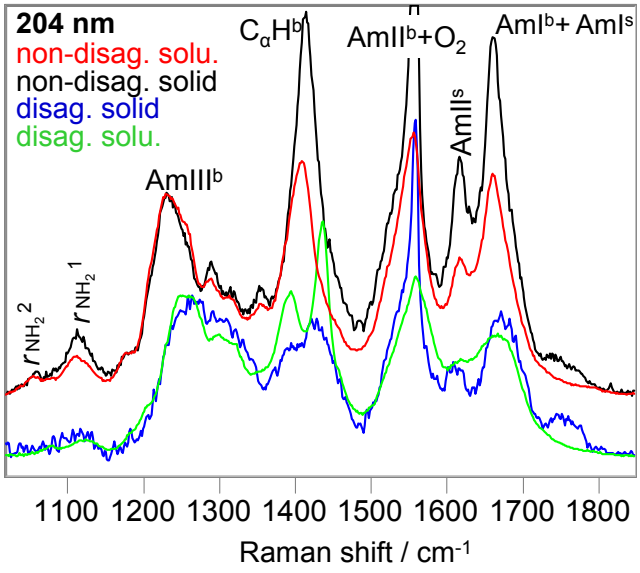

Figure 8.9. The 204 nm excited UVRR spectra of the NDQ10 solid (black) and solution (red), DQ10 solid (blue) and solution (green) at 22 °C. [b] indicates backbone vibration; [s] indicates side chain vibration. The intensities were normalized to the AmIII[b] peak height.

This suggests that the solution state activation barriers between extended PPII and 2.5_1-helix conformations and the β-sheet aggregate conformations is very high; these structures are not in a equilibrium in solution or during solution evaporation. We are presently utilizing X ray crystallography to determine the Q10 structure in the DQ10 and NDQ10 solids.

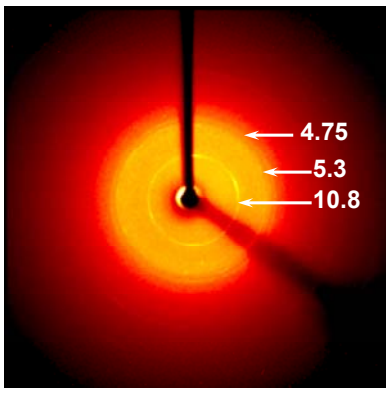

Figure 8.10. Powder x ray diffraction of NDQ10 solid. The sample was prepared by slowly evaporating NDQ10 solution on a glass slide over ~ 2 days.

8.4 DISCUSSION

Q10 Structure: CD and UVRR studies indicate that NDQ10 in pure water adopts a predominantly β-sheet structure, consistent with previous studies.[20,36] UVRR also observes turn conformations in NDQ10. The fractions of β-sheet and turn conformations are 0.84 and 0.16, respectively. This ratio suggests that NDQ10 in pure water occurs as β-hairpins in which two residues are in the turn region and eleven residues form a β-sheet (Fig.8.11).

We observe that DQ10 in pure water adopts predominantly PPII-like and 2.5_1-helix conformations (Fig.8.11), consistent with some previous studies.[37,38] Others studies, however, report random coil structures.[48-52]

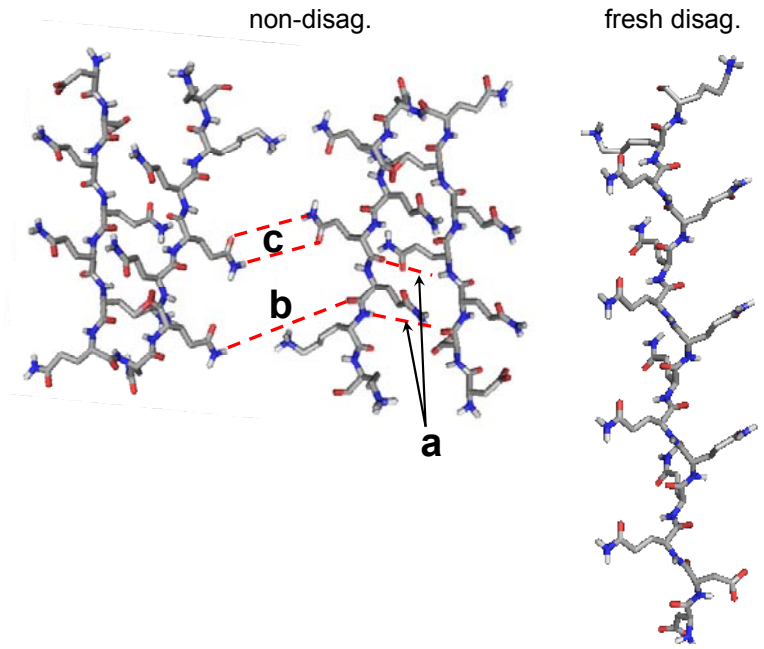

Figure 8.11: Proposed structures of NDQ10 and DQ10. NDQ10 occurs as β-sheets in which the GLN side chains HB to the backbone or other GLN side chains. DQ10 adopts PPII and 2.5_1-helix conformations in which the GLN side chains HB to water. Main chain – main chain HB a, main chain – side chain HB b, side chain – side chain HB c.

198 and 204 nm excited UVRR indicate that the GLN side chains of NDQ10 HB to the backbone or other GLN side chains, while the GLN side chains of DQ10 HB to water.

Disaggregated Q10 does not self nucleate fibrils: We observe that NDQ10 in pure water forms amyloid fibrils after incubation at 60 ^{o} C for ~ 2 days (Fig 8.12). In contrast, DQ10 does not form fibrils even after incubation for > 2 weeks at 60 ^{o} C. However, upon seeding with 1% NDQ10 solution, the DQ10 solution readily forms fibrils at 60 ^{o}C. Thus, NDQ10 appears to contain small aggregates that serve as nuclei for fibrillation. Thus, it appears that the activation barrier for DQ10 to form β-sheet aggregates that evolve to NDQ10 fibrils is quite high. Our work suggest that DQ10 solutions therefore do not self nucleate fibrils, consistent with previous studies of similar peptides.[20,50,53]

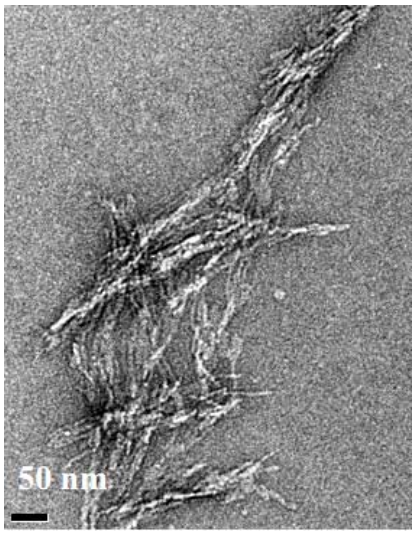

Figure 8.12. **Electron micrograph of NDQ10 fibrils in pure water after incubation at 60 ^{o} C for ~ 2 days.**

8.5 CONCLUSIONS

We utilize UVRR and CD to monitor the backbone conformation and the GLN side chain HB of

a short mainly polyGLN peptide Q10, of sequence $D_2Q_{10}K_2$. We measured UVRR spectra of valeramide to determine the dependence of primary amide vibrations on the primary amide HB. We observe that NDQ10 occurs in a β-sheet-like structure in which the GLN side chains HB to the backbone or other GLN side chains.

These solutions readily form amyloid fibrils. In contrast, DQ10 solutions adopt PPII-like and 2.5_1-helix conformations in which the GLN side chains HB to water. These samples do not form fibrils upon heating within two weeks. The NDQ10 and DQ10 solution structures are essentially identical to their solid state structures. Although the NDQ10 solution readily forms fibrils when heated, the DQ10 solution does not form fibrils unless nuclei from the NDQ10 solution are added. This indicates very high activation barriers occur between these solution conformations.

8.6 ACKNOWLEDGEMENTS

We thank Dr. Sergei V. Bykov for useful discussions. We also thank Lu Ma for help with instrumentation. This work was supported by NIH grant 1RO1EB009089.

8.7 REFERNCES

(1) Zoghbi, H. Y.; Cummings, C. J. *Human Molecular Genetics* **2000**, *9*, 909.

(2) Ross, C. A.; Poirier, M. A. *Nature Reviews Molecular Cell Biology* **2005**, *6*, 891.

(3) Wetzel, R.; Bhattacharyya, A. M.; Thakur, A. K. *Proceedings of the National Academy of Sciences of the United States of America* **2005**, *102*, 15400.

(4) Wetzel, R.; Chen, S. M.; Ferrone, F. A. *Proceedings of the National Academy of Sciences of the United States of America* **2002**, *99*, 11884.

(5) Wetzel, R.; Slepko, N.; Bhattacharyya, A. M.; Jackson, G. R.; Steffan, J. S.; Marsh, J. L.; Thompson, L. M. *Proceedings of the National Academy of Sciences of the United States of America* **2006**, *103*, 14367.

(6) Rossetti, G.; Magistrato, A.; Pastore, A.; Persichetti, F.; Carloni, P. *Journal of Physical Chemistry B* **2008**, *112*, 16843.

(7) Smith, M. H.; Miles, T. F.; Sheehan, M.; Alfieri, K. N.; Kokona, B.; Fairman, R. *Proteins-Structure Function and Bioinformatics* **2010**, *78*, 1971.

(8) Perutz, M. F.; Johnson, T.; Suzuki, M.; Finch, J. T. *Proc. Natl. Acad. Sic. USA* **1994**, *91*, 5355.

(9) Sikorski, P.; Atkins, E. *Biomacromolecules* **2005**, *6*, 425.

(10) Nagai, Y.; Inui, T.; Popiel, H. A.; Fujikake, N.; Hasegawa, K.; Urade, Y.; Goto, Y.; Naiki, H.; Toda, T. *Nature Structural & Molecular Biology* **2007**, *14*, 332.

(11) Mikhonin, A. V.; Bykov, S. V.; Myshakina, N. S.; Asher, S. A. *Journal of Physical Chemistry B* **2006**, *110*, 1928.

(12) Manas, E. S.; Getahun, Z.; Wright, W. W.; DeGrado, W. F.; Vanderkooi, J. M. *Journal of the American Chemical Society* **2000**, *122*, 9883.

(13) Wang, Y.; Purrello, R.; jordan, T.; Spiro, T. G. *J. Am. Chem. Soc.* **1991**, *113*, 6359.

(14) Mirkin, N. G.; Krimm, S. *Journal of Physical Chemistry A* **2004**, *108*, 5438.

(15) Myshakina, N. S.; Ahmed, Z.; Asher, S. A. *Journal of Physical Chemistry B* **2008**, *112*, 11873.

(16) Barth, A. *Progress in Biophysics & Molecular Biology* **2000**, *74*, 141.

(17) Takei, K.; Takahashi, R.; Noguchi, T. *Journal of Physical Chemistry B* **2008**, *112*, 6725.

(18) Natalello, A.; Frana, A. M.; Relini, A.; Apicella, A.; Invernizzi, G.; Casari, C.; Gliozzi, A.; Doglia, S. M.; Tortora, P.; Regonesi, M. E. *Plos One* **2011**, *6*.

(19) Perutz, M. F.; Finch, J. T.; Berriman, J.; Lesk, A. *Proc. Natl. Acad. Sic. USA* **2002**, *99*, 5591.

(20) Chen, S. M.; Berthelier, V.; Hamilton, J. B.; O'Nuallain, B.; Wetzel, R. *Biochemistry* **2002**, *41*, 7391.

(21) Sharma, D.; Shinchuk, L. M.; Inouye, H.; Wetzel, R.; Kirschner, D. A. *Proteins-Structure Function and Bioinformatics* **2005**, *61*, 398.

(22) Lee, C. C.; Walters, R. H.; Murphy, R. M. *Biochemistry* **2007**, *46*, 12810.

(23) Darnell, G.; Orgel, J. P. R. O.; Pahl, R.; Meredith, S. C. *Journal of Molecular Biology* **2007**, *374*, 688.

(24) Walters, R. H.; Murphy, R. M. *J. Mol. Biol.* **2009**, *393*, 978.

(25) Kar, K.; Jayaraman, M.; Sahoo, B.; Kodali, R.; Wetzel, R. *Nature Structural & Molecular Biology* **2011**, *18*, 328.

(26) O'Nuallain, B.; Thakur, A. K.; Williams, A. D.; Bhattacharyya, A. M.; Chen, S. M.; Thiagarajan, G.; Wetzel, R. *Amyloid, Prions, and Other Protein Aggregates, Pt C* **2006**, *413*, 34.

(27) Bykov, S.; Lednev, I.; Ianoul, A.; Mikhonin, A.; Munro, C.; Asher, S. A. *Applied Spectroscopy* **2005**, *59*, 1541.

(28) Dudik, J. M.; Johnson, C. R.; Asher, S. A. *Journal of Physical Chemistry* **1985**, *89*, 3805.

(29) Kuroda, Y.; Saito, Y.; Uno, T.; Machida, K. *Bulletin of the Chemical Society of Japan* **1972**, *45*, 2371.

(30) Nandini, G.; Sathyanarayana, D. N. *Journal of Molecular Structure-Theochem* **2002**, *586*, 125.

(31) Xiong, K.; Asher, S. A. *Journal of Physical Chemistry A* **2011**, *115*, 9345.

(32) Dudik, J. M.; Johnson, C. R.; Asher, S. A. *Journal of Chemical Physics* **1985**, *82*, 1732.

(33) Sharma, B.; Bykov, S. V.; Asher, S. A. *Journal of Physical Chemistry B* **2008**, *112*, 11762.

(34) Chen, X. G.; Asher, S. A.; Schweitzerstenner, R.; Mirkin, N. G.; Krimm, S. *Journal of the American Chemical Society* **1995**, *117*, 2884.

(35) Lewis, T. C.; Tocher, D. A. *Acta Crystallographica Section E-Structure Reports Online* **2005**, *61*, O1985.

(36) Sharma, D.; Sharma, S.; Pasha, S.; Brahmachari, S. K. *Febs Letters* **1999**, *456*, 181.

(37) Chellgren, B. W.; Miller, A. F.; Creamer, T. P. *Journal of Molecular Biology* **2006**, *361*, 362.

(38) Wang, X. L.; Vitalis, A.; Wyczalkowski, M. A.; Pappu, R. V. *Proteins-Structure Function and Bioinformatics* **2006**, *63*, 297.

(39) Woody, R. W. *Theory of Circular Dichroism of Proteins*; Plenum Press: New York, 1996.

(40) Sreerama, N.; Woody, R. W. *Biochemistry* **1994**, *33*, 10022.

(41) Shi, Z.; Olson, C.; Rose, G.; Baldwin, R.; Kallenbach, N. *PROCEEDINGS OF THE NATIONAL ACADEMY OF SCIENCES OF THE UNITED STATES OF AMERICA* **2002**, *99*, 9190.

(42) Shi, Z.; Chen, K.; Liu, Z.; Kallenbach, N. *CHEMICAL REVIEWS* **2006**, *106*, 1877.

(43) Mikhonin, A. V.; Asher, S. A. *Journal of the American Chemical Society* **2006**, *128*, 13789.

(44) Asher, S. A.; Mikhonin, A. V.; Bykov, S. *Journal of the American Chemical Society* **2004**, *126*, 8433.

(45) Mikhonin, A. V.; Myshakina, N. S.; Bykov, S. V.; Asher, S. A. *Journal of the American Chemical Society* **2005**, *127*, 7712.

(46) Ma, L.; Ahmed, Z.; Asher, S. A. *Journal of Physical Chemistry B* **2011**, *115*, 4251.

(47) Xiong, K.; Ma, L.; Asher, S. A. *Biophysical Chemistry* **2011**.

(48) Chen, S. M.; Ferrone, F. A.; Wetzel, R. *Proceedings of the National Academy of Sciences of the United States of America* **2002**, *99*, 11884.

(49) Crick, S. L.; Jayaraman, M.; Frieden, C.; Wetzel, R.; Pappu, R. V. *Proceedings of the National Academy of Sciences of the United States of America* **2006**, *103*, 16764.

(50) Chen, S.; Berthelier, V.; Yang, W.; Wetzel, R. *Journal of Molecular Biology* **2001**, *311*, 173.

(51) Masino, L.; Kelly, G.; Leonard, K.; Trottier, Y.; Pastore, A. *Febs Letters* **2002**, *513*, 267.

(52) Walters, R. H.; Murphy, R. M. *Journal of Molecular Biology* **2009**, *393*, 978.

(53) Chen, S.; Wetzel, R. *Protein Science* **2001**, *10*, 887.

Chapter 9

Lowest Energy Electronic Transition in Aqueous Cl^- Salts: $Cl^- \rightarrow (H_2O)_6$ Charge Transfer Transition

This work was published in *J. Phys. Chem. A*, **2011**, *115*, 9345–9348. The coauthors are Kan Xiong and Sanford A Asher.

9.0 LOWEST ENERGY ELELECTRONIC TRANSITION IN AQUEOUS Cl^- SALTS: $Cl^- \rightarrow (H_2O)_6$ CHARGE TRANSFER TRANSITION

We use UV resonance Raman spectroscopy to probe the lowest energy allowed electronic transitions of aqueous solutions containing Cl^- salts. We show that the waters hydrating the Cl^- are involved in charge transfer transitions that transfer electron density from Cl^- to the water molecules. These charge transfer transitions cause significant change in the H-O-H bond angle in the excited state, which results in a strong enhancement of the preresonance Raman intensity of the water bending modes. Our work gives the first insight into the lowest allowed electronic transition of hydrated Cl^-.

9.1 INTRODUCTION

Water, the ubiquitous solvent, is the major constituent of living organisms. Some of water's unique properties result from its small size, its highly dipolar character and its ability to form multiple hydrogen bonds. Although water has been the subject of extensive investigations there is still little understanding of liquid water's structure,[1,2] its electronic excited states,[3] as well as how water hydrates even simple molecules and ions.[4,5] This lack of understanding of the electronic structure of liquid water is not surprising since in the condensed phase its excited states are probably extended over numerous molecules and these extended electronic excited states are highly dependent upon the local and nonlocal water structure; [6,7] even the ground state water structure is poorly understood. [8]

An understanding of water electronic excited states is important because these states enable chemical transformations. The lower energy water excited states, for example, could

enable processes such as photochemical electron transfer processes to split water into H_2 and O_2, for example.[9,10]

In the work here we probe the lowest energy allowed electronic transitions of aqueous solutions of Cl^- salts and show that the waters hydrating the Cl^- are involved in charge transfer transitions that transfer electron density from Cl^- to the water molecules. These charge transfer transitions cause significant change in the H-O-H bond angles, which results in a strong enhancement of the preresonance Raman intensity of the water bending modes. Our work gives the first insight into the lowest allowed electronic transition of hydrated Cl^-.

9.2 EXPERIMENTAL

Chemicals. NaCl was purchased from Mallinckrodt Chemicals; KCl was from J. T. Baker; LiCl was from Fisher Scientific; KF was from Aldrich Chemical Company; Acetonitrile was from Sigma-Aldrich.

Raman Apparatus. The 204 nm light was obtained by mixing the 3rd harmonic with the fundamental (816 nm wavelength) of a tunable Ti:Sapphire laser system (Photonics Industries). The 229 nm light was produced by an intracavity frequency doubling an Ar^+ laser (Coherent, FReD 400). The 355 nm light was the 3rd harmonic of a Nd:YAG laser (Coherent, Infinity). The 488 nm light was from an Ar^+ laser (Coherent, Innova 90c). All incident excitation light was s-polarized (i.e. polarized perpendicular to the scattering plane) at the sample. The sample was circulated in a free surface, temperature-controlled stream. 3% (v/v) acetonitrile was used in all Raman measurements as an internal intensity standard. A 165 ^{o} sampling backscattering geometry was used. Raman scattering light from 204 and 229 nm excitation was collected and

dispersed by a double monochromator onto a back thinned CCD camera with a Lumogen E coating (Princeton Instruments-Spec 10 System). (See Bykov et al for details. [11])

Raman scattering light from 355 or 488 nm excitation was collected and dispersed by a single monochromator onto the CCD camera. A 488 nm notch filter (Kaiser Optical Systems Inc.) was used to reject Rayleigh scattering light from 488 nm excitation. A 355 nm long-pass filter (Semrock Inc.) was used to reject Rayleigh scattering light from 355 nm excitation. A crystalline quartz polarization scrambler was used to remove any polarization bias of the monochromators.

The double-monochromator and detector efficiencies were previously measured by using a deuterium standard intensity lamp (Optronic laboratories).[11] The single-monochromator and detector efficiencies were measured by using a tungsten-halogen black body standard intensity lamp (Optronic laboratories). The light from the standard lamp were scattered off a $BaSO_4$ Lambert surface and imaged onto the entrance slit of the monochromator.

9.3 RESULTS

We probe the electronic excited states of hydrated Cl^- by measuring the preresonance Raman excitation profiles of aqueous salt solutions. Early studies showed a surprising intensity increase for the water bending band of aqueous solutions containing Cl^-, Br^-, I^-.[12-14] In contrast, little intensity increase was observed for the water O-H stretching bands. Two of these previous studies vaguely suggested that the Raman intensity increase was due to a charge transfer-like transition of Cl^- to water.[15,16]

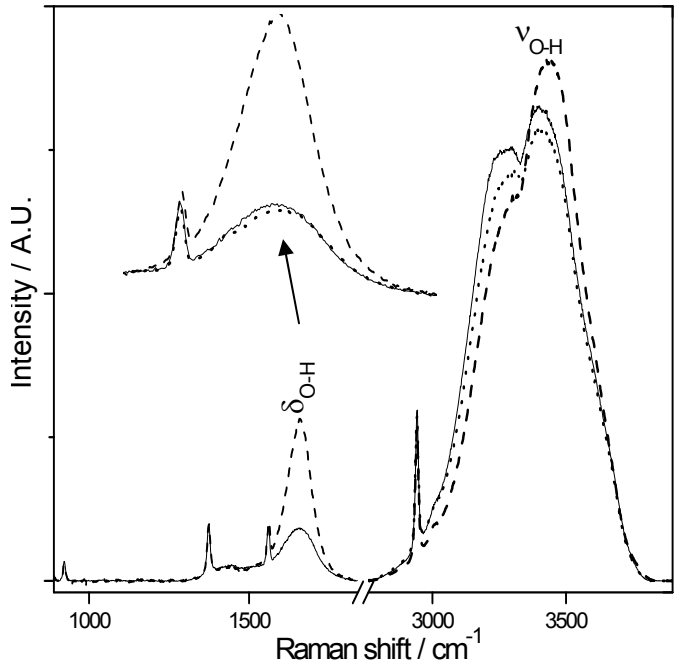

Figure 9.1: 204 nm excited UVRS of pure water (solid line) and in the presence of 2 M KCl (dashed line) or 2 M KF (dotted line) at 20 ^{o}C; δ_{H-O-H} and ν_{O-H} indicate the O-H bending band and O-H stretching band. The 918, 1373.5 and 2942.5 cm^{-1} bands result from the added 3% by volume CH_3CN which is used as an internal intensity standard. The 1550 cm^{-1} band is from atmospheric O_2.

Fig 9.1 shows the 204 nm excited UV Raman spectra (UVRS) of pure water at 20 ^{o}C. The H-O-H bending band, δ_{H-O-H} occurs at ~ 1660 cm^{-1} while the O-H stretching doublet, ν_{O-H} at ~ 3280 cm^{-1} and ~ 3400 cm^{-1} dominates the spectrum. Adding 2 M KCl significantly increases the δ_{H-O-H} band intensity and slightly narrows its band width. The higher frequency ν_{O-H} stretching band component intensity increases somewhat, while the lower frequency ν_{O-H} band component intensity decreases. The overall intensity remains essentially constant. Addition of 2 M LiCl or NaCl gives essentially identical effects as 2 M KCl (spectra not shown). In contrast, 2 M KF shows little impact on the δ_{H-O-H} and ν_{O-H} bands. Thus, cations are not impacting the

water Raman spectra, in agreement with previous Raman studies showing enhancement of water bending bands by halide ions.[14-17]

Total differential Raman Cross Sections. The Raman cross sections of the $\delta_{H\text{-}O\text{-}H}$ and $\nu_{O\text{-}H}$ bands were determined by using the 918 cm^{-1} C-C and the 2249 cm^{-1} C≡N stretching bands of acetonitrile as internal intensity standards.[18] The total differential Raman water cross sections are:

$$\sigma(\nu_{ex}) = \frac{I_w \cdot k(\lambda_{CH_3CN}) \cdot C_{CH_3CN} \cdot \sigma_{CH_3CN}(\nu_{ex})}{I_{CH_3CN} \cdot k(\lambda_w) \cdot C_w} \cdot \left[\frac{\varepsilon_w + \varepsilon_{ex}}{\varepsilon_r + \varepsilon_{ex}} \right] \qquad (9.1)$$

where I_w and I_{CH_3CN}, are the intensities of the water band and a CH_3CN band. $k(\lambda_w)$ and $k(\lambda_{CH_3CN})$ are the spectrometer efficiencies at the specific wavelengths of the water and CH_3CN Raman bands. C_{CH_3CN} and C_w are the concentrations of CH_3CN and water. $\sigma_{CH_3CN}(\nu_{ex})$ is the total differential CH_3CN Raman cross section at the excitation frequency, ν_{ex}. ε_{ex} is the Cl^- molar absorptivity at ν_{ex}. ε_w is the Cl^- molar absorptivity at the water Raman band position, ε_r is molar absorptivity due to the Cl^- at the CH_3CN band wavelength. The expression in the brackets corrects the Raman intensities for self-absorption, which only occurs for the 204 nm excitation measurement. Negligible self absorption occurs for longer wavelength excitations.

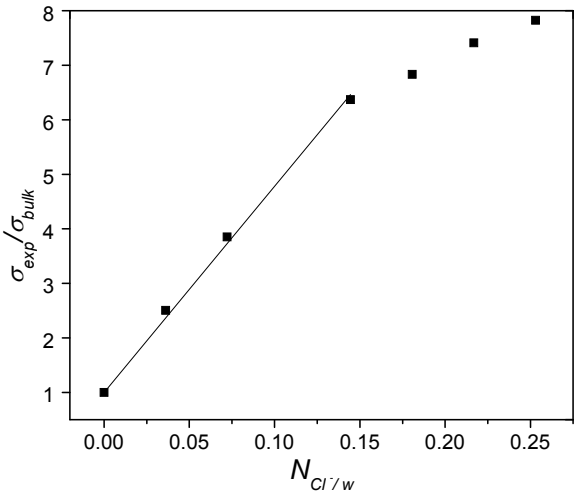

Figure 9.2: Dependence of the $\delta_{H\text{-}O\text{-}H}$ Raman cross sections (λ_{ex}=204 nm), σ_{exp} (relative to that of pure water, σ_{bulk}) on the ratio of Cl^- to water, $N_{Cl^-/w}$. The line is a linear fit to the first four data points.

$\delta_{H\text{-}O\text{-}H}$ Raman cross section dependence on Cl^- concentration. Fig 9.2 shows that the $\delta_{H\text{-}O\text{-}H}$ water band Raman cross section, σ_{exp} initially increases linearly with ratio of Cl^- ion to water molecules, $N_{Cl^-/w}$ until ~0.15 where it begins to saturate, presumably because of the depletion of bulk water to hydrate the Cl^-. We can model these data to calculate an effective water Raman cross section for the Cl^- hydrating water and for n, the number of water molecules hydrating Cl^-. This modeling assumes that the water bending mode is independently Raman scattered by bulk water molecules with a Raman cross section of σ_{bulk}, and by water molecules hydrating the Cl^- with Raman cross sections of σ_{hyd}, that are larger than that of bulk water:[12]

$$\begin{aligned}\sigma_{\exp} &= \sigma_{bulk} \cdot f_{bulk} + \sigma_{hyd} \cdot f_{hyd} \\ &= \sigma_{bulk} \cdot (1 - n \cdot N_{Cl^-/w}) + \sigma_{hyd} \cdot n \cdot N_{Cl^-/w}\end{aligned} \tag{9.2}$$

where f_{bulk} is the fraction of bulk water molecules and f_{hyd} is the fraction associated with the first hydration shell of water molecules about the Cl^-. σ_{exp} will increase linearly with $N_{Cl^-/w}$ until the

bulk water is depleted. Fig 9.2 shows water depletion when $N_{Cl^-/w}$ is >0.15 giving n~6 for the Cl^- hydration number, which is consistent with the hydration number found using other methods.[19,20]

$\delta_{H\text{-}O\text{-}H}$ Raman Excitation Profiles. Table 9.1 shows the measured total differential Raman cross sections of the *$\delta_{H\text{-}O\text{-}H}$ Raman* band, σ_A, and the $\delta_{H\text{-}O\text{-}H}$ of first hydration shell waters about the Cl^-, $\sigma_{A\,hyd}$ was calculated from eq. 9.2, as a function of excitation wavelength. σ_A increases by more than 100-fold as the excitation wavelength decreases from 488 to 204 nm. The measured σ_A of pure water is similar to values previously reported.[21] Addition of 2 M KCl increases σ_A at 204 nm 2.5 fold. Smaller increases occur at longer excitation wavelengths, further from resonance. 2 M NaCl or LiCl increases σ_A identically to 2M LiCl. 2 M KF does not affect σ_A.

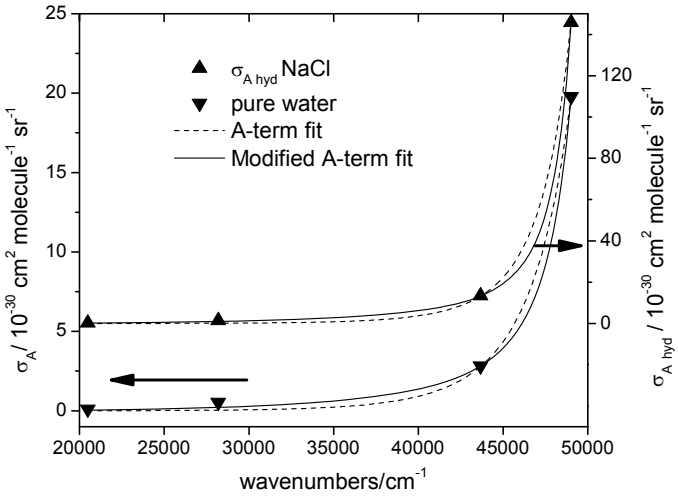

Figure 9.3: Total differential Raman cross section excitation profile of the 1660 cm^{-1} H_2O $\delta_{H\text{-}O\text{-}H}$ band. The solid line is the best fit to Eq. 9.3, while the dashed line is the best fit to a simple A-term (Eq. 9.3, K_2=0).

Fig 9.3 shows the total differential Raman cross section excitation profile of the *$\delta_{H\text{-}O\text{-}H}$* Raman band in pure water and the cross section of the first hydration shell water about the Cl^-.

The solid line is nonlinear-least-square fit of the data to a modified Albrecht A-term expression [22]:

$$\sigma_A = K_1 \cdot \nu_{ex} \cdot (\nu_{ex} - \nu_w)^3 \cdot \left[\frac{\nu_e^{\,2} + \nu_{ex}^{\,2}}{(\nu_e^{\,2} - \nu_{ex}^{\,2})^2} + K_2 \right]^2 \tag{9.3}$$

where ν_{ex} is the excitation frequency, ν_w is the Raman frequency of the water band, and ν_e is the electronic transition frequency to the pre-resonant excited electronic state. K_1 is a scaling parameter and K_2 is a constant that phenomenologically models contributions from an additional preresonant state in the far UV. The dashed line is the best fit to a simple A-term (Eq. 9.3, where $K_2 = 0$), which assumes that the pre-resonance enhancement is dominated by single electronic transition. The ν_{ex}, K_1, and K_2 values shown in Table 9.1 are obtained from nonlinear least-squares fits of eq 9.3.

The preresonance excitation profiles of the $\delta_{\text{H-O-H}}$ Raman band of pure water is well modeled by both the A-term and modified A-term expressions to yield 60,800 and 54,400 cm^{-1} for the preresonant excited state frequencies, respectively. The increase in the number of parameter enables the modified A-term modeling fit to be slightly better than the simple A-term modeling.

In contrast, for the first hydration shell waters about Cl^- for the $\delta_{\text{H-O-H}}$ Raman band we find a modeled preresonant excited state frequency of 57,600 for the A-term and 53,000 for the modified A term. Thus, the preresonance enhancing transition in the Cl^- solution occurs ~ 3,200 (A-term) or ~ 1,400 cm^{-1} (modified A-term) lower in energy than in pure water.

Table 9.1: Total differential Raman cross sections of $\delta_{H\text{-}O\text{-}H}$ Raman band, σ_A; $\delta_{H\text{-}O\text{-}H}$ of first hydration shell water about the Cl^-, $\sigma_{A\,hyd}$ (numbers underlined) and the ν_e, K_1, and K_2 parameters.

	σ_A, $\sigma_{A\,hyd}$ / 10^{-30} cm^2 molecule^{-1} sr^{-1}				A-term fit (K_2=0)		Modified A-term fit		
	204 nm	229 nm	355 nm	488 nm	$K_1\times10^{-31}$	ν_e	$K_1\times10^{-33}$	ν_e	$K_2\times10^{-8}$
water	19.8	2.82	0.54	0.11	2.84	60800	6	54400	0.772
2M LiCl	46.0	5.09	0.76	0.14					
	<u>141</u>	<u>13.3</u>	<u>1.58</u>	<u>0.26</u>	6.21	57700	16.7	53100	1
2M NaCl	47.1	5.13	0.72	0.14					
	<u>146</u>	<u>13.5</u>	<u>1.39</u>	<u>0.24</u>	6.06	57600	16.8	53000	1
2 M KCl	49.9	5.22	0.68	0.14					
	<u>159</u>	<u>13.9</u>	<u>1.19</u>	<u>0.22</u>	5.71	57300	17	52900	1
2M KF	19.2	2.86	0.54	0.11	3.07	61000	6	54400	0.786

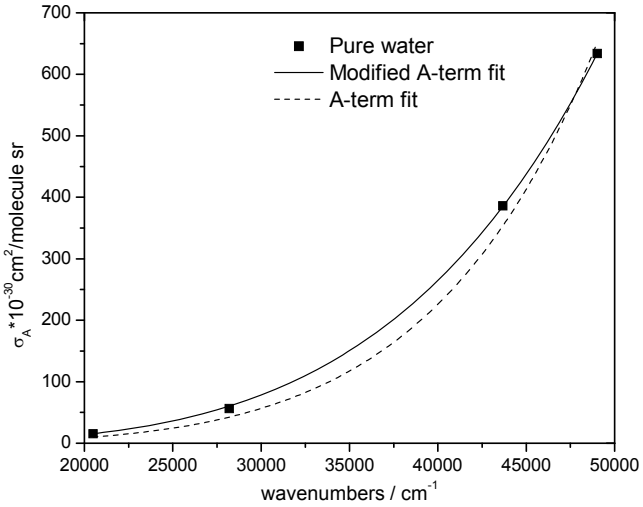

Figure 9.4: Total differential Raman cross section excitation profile of the 3400 cm^{-1} H_2O $\nu_{O\text{-}H}$ band. The solid line is the best fit to Eq. 9.3, while the dashed line is the best fit to a simple A-term (Eq. 9.3, K_2=0).

$\nu_{O\text{-}H}$ *Raman Excitation Profiles:* Table 9.2 shows the calculated total differential Raman cross sections of the $\nu_{O\text{-}H}$ vibration, σ_B. The σ_B values increase only slightly faster than ν_0^4, indicating that the preresonant excited state for $\nu_{O\text{-}H}$ is in the far UV for pure water. Adding Cl^- does not change the Raman cross sections.

Table 9.2: **Total differential Raman cross sections of $\nu_{O\text{-}H}$ Raman band, σ_B and the ν_e, K_1, and K_2 parameters.**

	σ_B / 10^{-30} cm^2 $molecule^{-1}$ sr^{-1}				A-term fit (K_2=0)		Modified A-term fit		
	204 nm	229 nm	355 nm	488 nm	$K_1\times10^{-27}$	ν_e	$K_1\times10^{-30}$	ν_e	$K_2\times10^{-9}$
water	634	368	56.3	15.5	32.9	150000	5	91000	4.62
2 M LiCl	770	484	72.4	15.6	40.4	150000	4.91	91000	5.2
2 M NaCl	725	485	67.3	15.3	46.9	150000	5	91000	5
2 M KCl	628	454	63.8	16.1	34.3	150000	5	91000	5
2 M KF	598	417	61.1	14.4	40.7	150000	4.27	91000	5

The total differential Raman cross section excitation profile of the $\nu_{O\text{-}H}$ vibration of pure water gives ν_e=150,000 $cm^{-1}$for an A-term fit or ν_e=91,000 cm^{-1} for a modified A-term fit (Fig. 9.4). As expected, addition of Cl^- does not change ν_e.

9.4 DISCUSSION

Isolated gas phase water molecules show their $2b_1 \rightarrow 3a_1$ lowest energy allowed electronic transition at 166 nm. [23] The origins of the liquid water absorption bands, as well as those of water solutions are exceptionally poorly understood. In liquid water the lowest energy allowed

electronic transition has a steeply rising edge at ~175 nm with a maximum at 147 nm. [24,25] In contrast, a strong absorption band at ~180 nm occurs in aqueous solutions of Cl^-.[26]

The fact that the bending mode in aqueous Cl^-solutions is selectively enhanced over the stretch by the 58,000 cm^{-1} absorption indicates that the hydrating water excited state shows a much larger change in their H-O-H bond angles, than in their O-H bond lengths. A LCAO consideration would suggest that the electronic transition involves transfer of electron density from the Cl^- to the LCAO σ*-like water orbitals. The LCAO picture does not clearly capture the orbital hybridization that gives rise to the normally sp^3-like OH bonding and the typical 105° bond angle. The increase in electron density from the Cl^-→water charge transfer transition removes the sp^3 hybridization. A molecular orbital picture suggests that the transition will place electron density in a σ* orbital which naively would cancel bonding of one of the O-H bonds, leaving the other O-H water bond. The net result is a very different (linear) H-O-H bond angle and a O-H bond length which is comparable to that of the ground state water. More likely we would end up with a linear excited state with similar O-H bond lengths and frequencies.

This rough picture predicts that preresonance Raman excitation in this charge transfer band would show a very large enhancement of the water bending vibration but little enhancement of the O-H stretching of the Cl^- hydrating waters.

9.5 CONCLUSIONS

We probe the electronic excited state of hydrated Cl^- by measuring the preresonance Raman excitation profiles of aqueous salt solutions. We show that the waters hydrating the Cl^- are

involved in charge transfer transitions that transfer electron density from Cl^- to the water molecules. These charge transfer transitions cause significant change in the H-O-H bond angle in the excited states, which results in a strong enhancement of the preresonance Raman intensity of the water bending modes. Our work gives the first insight into the lowest allowed electronic transition of hydrated Cl^-.

9.6 ACKNOWLEDGEMENTS

We thank David Tuschel and Sergei Bykov for helping with instrumentation setup. This work was supported by National Institutes of Health Grants IRO1EB009089.

9.7 REFERENCES

(1) Sharp, K. A.; Vanderkooi, J. M. *Acc. Chem. Res.* **2010**, *43*, 231-239.

(2) Roberts, S. T.; Ramasesha, K.; Tokmakoff, A. *Acc. Chem. Res.* **2009**, *42*, 1239-1249.

(3) Garbuio, V.; Cascella, M.; Pulci, O. *J. Phys.: Condens. Matter.* **2009**, *21*.

(4) Ben-Amotz, D.; Underwood, R. *Acc. Chem. Res.* **2008**, *41*, 957-967.

(5) Tielrooij, K. J.; Garcia-Araez, N.; Bonn, M.; Bakker, H. J. *Science* **2010**, *328*, 1006-1009.

(6) Chipman, D. M. *J. Chem. Phys.* **2006**, *124*.

(7) Couto, P. C. d.; Chipman, D. M. *J. Chem. Phys.* **2010**, *132*.

(8) Csaszar, A. G.; Czako, G.; Furtenbacher, T.; Tennyson, J.; Szalay, V.; Shirin, S. V.; Zobov, N. F.; Polyansky, O. L. *J. Chem. Phys.* **2005**, *122*, -.

(9) Engel, V.; Staemmler, V.; Wal, R. L. V.; Crim, F. F.; Sension, R. J.; Hudson, B. *J. Phys. Chem.* **1992**, *96*, 3201-3213.

(10) Elles, C. G.; Shkrob, I. A.; Crowell, R. A.; Bradforth, S. E. *J. Chem. Phys.* **2007**, *126*, -.

(11) Bykov, S.; Lednev, I.; Ianoul, A.; Mikhonin, A.; Munro, C.; Asher, S. A. *Appl. Spectrosc.* **2005**, *59*, 1541-1552.

(12) Schultz, J. W.; Hornig, D. F. *J. Phys. Chem.* **1961**, *65*, 2131-2138.

(13) Wall, T. T.; Hornig, D. F. *J. Chem. Phys.* **1967**, *47*, 784-792.

(14) R. E. Weston, J. *Spectrochim. Acta* **1962**, *18*, 1257-1277.

(15) Kanno, H.; Hlralshi, J. *J. Phys. Chem.* **1983**, *87*, 3664-3670.

(16) Abe, N.; Ito, M. *J. Raman Spec.* **1978**, *7*, 161-167.

(17) Georgiev, G. M.; Kalkanjiev, T. K.; Petrov, V. P.; Nickolov, Z. *Appl. Spectrosc.* **1984**, *38*, 593-595.

(18) Dudik, J. M.; Johnson, C. R.; Asher, S. A. *J. Chem. Phys.* **1985**, *82*, 1732-1740.

(19) Robertson, W. H.; Johnson, M. A. *Annu. Rev. Phys. Chem.* **2003**, *54*, 173-213.

(20) Narten, A. H.; Vaslow, F.; Levy, H. A. *J. Chem. Phys.* **1973**, *58*, 5017-5023.

(21) Asher, S. A.; Murtaugh, J. L. *Appl. Spectrosc.* **1988**, *42*, 83-90.

(22) Asher, S. A. *Annu. Rev. Phys. Chem.* **1988**, *39*, 537-588.

(23) M.B.Robin *Higher Excited States of Polyatomic Molecules*; Academic Press: New York, 1985; Vol. III.

(24) Verrall, R. E.; Senior, W. A. *J. Chem. Phys.* **1969**, *50*, 2746-2750.

(25) Bernas, A.; Ferradini, C.; JayGerin, J. P. *Chem. Phys.***1997**, *222*, 151-160.

(26) Scheibe, G. *Z. Phys. Chem. Abt. B* **1929**, *5*, 355-364.

APPENDIX A

MOLECULAR DYNAMIC SIMULATION DETAILS

The simulations were performed by using the AMBER 10 package [1] with a modified version of the AMBER-99 force field, ffSB99 [2]. The modified force field has improved φ/ψ dihedral parameters that can better represent residues such as glycine and alanine [2]. The force field parameters to represent ClO_4^- anions were given by Baaden et al. [3] with the atomic charges fitted to electrostatic potentials calculated at the Hartree-Fock level using a 6-31G* basis set.

The peptide was simulated in an explicit water molecule solution and in a 0.2 M $NaClO_4$ solution. The simulations in explicit water were constructed by immersing the peptide in a cubic box containing 2317 TIP3P water molecules. Three Cl^- ions were added to counterbalance the peptide charge. The 0.2 M $NaClO_4$ solution was prepared by adding the Na^+ and ClO_4^- ions coordinates to the peptide coordinates, then three Cl^- ions were also added to counterbalance the charge and finally the water molecules in a cubic box were added. The resulting ratio of ClO_4^- ions/peptide is 9.

The energies of both systems were minimized after a total of 16000 steps. After the minimization, a 50 ps NVT equilibration run at 300 K was done with the peptide fixed, in order to equilibrate the solutions. Next, the total volume and density were adjusted with another 50 ps

NPT run with the total pressure set to 1 atm. The concentration of salt after the NPT simulation was calculated resulting in 0.2 M. The production runs were carried out for both systems under NVT conditions.

We used a time step of 2 fs and trajectory data was saved every 1 ps. The simulated systems were canonical ensembles at 300 K and periodic boundary conditions were used. All bonds involving hydrogen atoms were constrained using SHAKE with a tolerance of 0.0005 Å. REMD dynamics were performed using 48 replicas at constant volume covering a range of temperatures from 270 K to 505 K. The intervals between replicas were adjusted to have a uniform acceptance ratio greater than 20%. Exchanges were attempted each 100 integration steps. Each replica was run for 10 ns, leading to a total sampling time of 480 ns.

Data collection for both cases began after 3 ns of molecular dynamics simulation in order to eliminate initial biasing.

REFERENCES

(1) Case, D. A.; Darden, T. A.; Cheatham, T. E.; Simmerling, C. L.; Wang, J.; Duke, R. E.; Luo, R.; Crowley, M.; Walker, R. C.; Zhang, W.; Merz, K. M.; Wang, B.; Hayik, S.; Roitberg, A.; Seabra, G.; Kolossvary, I.; Wong, K. F.; Paesani, F.; Vanicek, J.; Wu, X.; Brozell, S. R.; Steinbrecher, T.; Gohlke, H.; Yang, L.; Tan, C.; Mongan, J.; Hornak, V.; Cui, G.; Mathews, D. H.; Seetin, M. G.; Sagui, C.; Babin, V.; Kollman, P. A. *AMBER 10*; University of California, 2008.

(2) Hornak, V.; Abel, R.; Okur, A.; Strockbine, B.; Roitberg, A.; Simmerling, C. *Proteins: Struct, Func, Bioinform* **2006**, *65*, 712-725.

(3) Baaden, M.; Berny, F.; Madic, C.; Wipff, G. *J Phys Chem A* **2000**, *104*, 7659-7671.

APPENDIX B

B1 TFE INDUCES MORE BUT SHORTER HELICES THAN OTHER ALCOHOLS

Suppose θ_α (θ_r) is the mean residue ellipticity for the pure α-helix (melted conformation(s)) (θ_α = -26000 deg.cm^2.dmol^{-1}, θ_r = -3500 deg.cm^2.dmol^{-1} [1]); θ is the measured mean residue ellipticity of AP; $f_{\alpha Raman}$ is the UVRR calculated concentrations of α-helix-like conformations of AP. The CD α-helix fraction, $f_{\alpha CD}$ is calculated by, [1]

$$f_{\alpha CD} = \frac{\theta - \theta_r}{\theta_\alpha - \theta_r} \qquad \text{(B1)}$$

$f_{\alpha Raman}$ and $f_{\alpha CD}$ are similar in pure water, 50% methanol and 50% ethanol. A significant difference bewtween $f_{\alpha Raman}$ and $f_{\alpha CD}$ is observed in 50% TFE which is likely due to the TFE induced formation of short helices that show decreased CD signals. [2] The proportionality between $f_{\alpha Raman}$ and $f_{\alpha CD}$ is decreased in TFE (Fig B1) relative to that in ethanol and methanol, indicating that in TFE produces more but shorter helices. Given the energy cost of nucleating helix segments, [3-6] it is unlikely that the 21-residue AP adopts more than two helix segments.

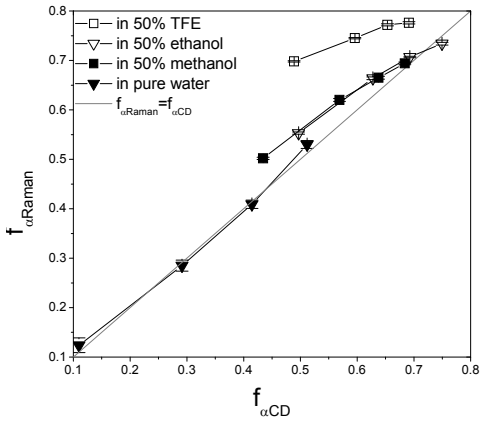

Figure B1: $f_{\alpha CD}$ vs. $f_{\alpha Raman}$ of AP.

B2: QUANTIFY THE DEPENDENCE OF THE CD MOLAR ELLIPTICITY PER PB OF AN α-HELIX, θ_n ON THE NUMBER OF PBs WITHIN THE α-HELIX, n

Suppose p_i is the probability of AP containing a single α-helix segment containing n_i α-helical PB; $\bar{n}$ is the statistical average number of helical PBs ; N = 20, is the total number of AP PB. Thus,

$$\theta = \sum_i \{\theta_{n_i} \cdot \frac{n_i}{N} + \frac{N - n_i}{N} \cdot \theta_r\} \cdot p_i \quad \text{(B2)}$$

Substituting the empirical equation proposed by Chen et al, [7] $\theta_n = \theta_\infty \cdot (1 - \frac{k}{n})$ into eq. B3:

$$\begin{aligned} \theta &= \sum_i \{\theta_\infty \cdot (\frac{n_i}{N} - \frac{k}{N}) + \frac{N - n_i}{N} \cdot \theta_r\} \cdot p_i \\ &= \frac{\theta_\infty}{N} \cdot \sum_i n_i \cdot p_i - \frac{\theta_\infty \cdot k}{N} \cdot \sum_i p_i + \theta_r \cdot \sum_i p_i - \frac{\theta_r}{N} \cdot \sum_i n_i \cdot p_i \\ &= \frac{\theta_\infty}{N} \cdot \bar{n} - \frac{\theta_\infty \cdot k}{N} + \theta_r - \frac{\theta_r}{N} \cdot \bar{n} \end{aligned} \quad \text{(B4)}$$

As the Raman intensity is more linear, [2,8] the UVRR calculated concentrations of α-helix-like conformations, $f_{\alpha Raman}$ more accurately monitors the fractions of α-helical PB. Thus,

$$f_{\alpha Raman} = \frac{\bar{n}}{N} \quad \text{(B5)}$$

substituting eq.B5 into eq.B4, thus,

$$\theta = (\theta_\infty - \theta_r) \cdot f_{\alpha Raman} + (\theta_r - \frac{k}{N} \cdot \theta_\infty) \quad \text{(B6)}$$

We fit the experimental data to eq. B6 to obtain values of θ_n and n:

$$\theta_n = -34530 \cdot (1 - \frac{1.6}{n}) \ \ \deg \cdot cm^2 \cdot dmol^{-1} \quad \text{(B7)}$$

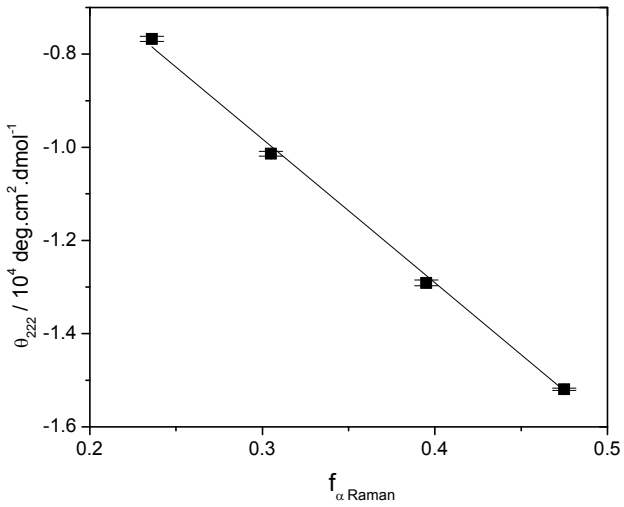

Figure B 2: **Linear fit of previously measured θ_{222} and $f_{\alpha Raman}$ of AP in pure water.**[9]

B3 PREDICTING CD ELLIPTICITY FROM RAMAN CALCULATED CONCENTRATION OF A-HELIX-LIKE CONFORMATIONS

Case 1: AP contains a single α-helix segment:

$$\theta = (\theta_\infty - \theta_r) \cdot f_{\alpha Raman} + (\theta_r - \frac{k}{N} \cdot \theta_\infty) \quad \text{(B4)}$$

Case 2: AP contains two helix segments: p_i is the probability of AP containing one helix segments of n_{i1} PBs and the second helix segment of n_{i2} PBs; $\overline{n_1}$ and $\bar{n}_2$ are the average number of helical PBs in the first and second helix segments ($\bar{n}_1 + \bar{n}_2 = N \cdot f_{\alpha Raman}$). Thus,

$$\theta = \sum_i \{\theta_{n_{i1}} \cdot \frac{n_{i1}}{N} + \theta_{n_{i2}} \cdot \frac{n_{i2}}{N} + \frac{N - n_{i1} - n_{i2}}{N} \cdot \theta_r\} \cdot p_i$$

$$= \sum_i \{\theta_\infty \cdot (\frac{n_{i1}}{N} - \frac{\mathrm{k}}{N}) + \theta_\infty \cdot (\frac{n_{i2}}{N} - \frac{\mathrm{k}}{N}) + \frac{N - n_{i1} - n_{i2}}{N} \cdot \theta_r\} \cdot p_i$$

$$= \frac{\theta_\infty}{N} \sum_i (n_{i1} + n_{i2}) \cdot p_i - \frac{k}{N} \cdot 2 \cdot \sum_i p_i + \theta_r \cdot \sum_i p_i - \frac{\theta_r}{N} \cdot \sum_i (n_{i1} + n_{i2}) \cdot p_i$$

$$= \frac{\theta_\infty}{N} \sum_i (n_i) \cdot p_i - \frac{k}{N} \cdot 2 \cdot \sum_i p_i + \theta_r \cdot \sum_i p_i - \frac{\theta_r}{N} \cdot \sum_i (n_i) \cdot p_i$$

$$= \frac{\theta_\infty}{N} \cdot (\bar{n}_1 + \bar{n}_2) - \frac{k}{N} \cdot 2 + \theta_r - \frac{\theta_r}{N} \cdot (\bar{n}_1 + \bar{n}_2)$$

$$= \theta_\infty \cdot f_{\alpha Raman} - \frac{k}{N} \cdot 2 + \theta_r - \theta_r \cdot f_{\alpha Raman}$$

$$\therefore \theta = (\theta_\infty - \theta_r) \cdot f_{\alpha Raman} + (\theta_r - \frac{2\mathrm{k}}{N} \cdot \theta_\infty) \quad \text{(B8)}$$

We can then predict the observed CD ellipticity, θ from $f_{\alpha Raman}$ in pure water, 50% methanol and 50% ethanol by using eq. B4 and in 50% TFE by using eq. B8. The results are shown in Fig.4.10.

REFERENCES

(1) Lednev, I. K.; Karnoup, A. S.; Sparrow, M. C.; Asher, S. A. *J Am Chem Soc* **1999,** 121, (35), 8074-8086.

(2) Ozdemir, A.; Lednev, I. K.; Asher, S. A. *Biochemistry* **2002,** 41, (6), 1893-1896.

(3) Doig, A. J. *Biophys Chem* **2002,** 101, 281-293.

(4) Yang, J. X.; Zhao, K.; Gong, Y. X.; Vologodskii, A.; Kallenbach, N. R. *J Am Chem Soc* **1998,** 120, (41), 10646-10652.

(5) Scholtz, J. M.; Qian, H.; York, E. J.; Stewart, J. M.; Baldwin, R. L. *Biopolymers* **1991,** 31, 1463-1470.

(6). Chen, Y.-H.; Yang, J. T.; Chau, K. H. *Biochemistry* **1974,** 13, 3350-3359.

(7) Ozdemir, A.; Lednev, I. K.; Asher, S. A. *Biochemistry* **2002,** 41, (6), 1893-1896.

(8) Mikhonin, A. V.; Asher, S. A. *J Phys Chem B* **2005,** 109, (7), 3047-3052.

(9) Xiong, K.; Asciutto, E. K.; Madura, J. D.; Asher, S. A. *Biochemistry* **2009**, 10818-10826.

APPENDIX C

CD SPECTRA AT 30 ^{0}C AND 50 ^{0}C

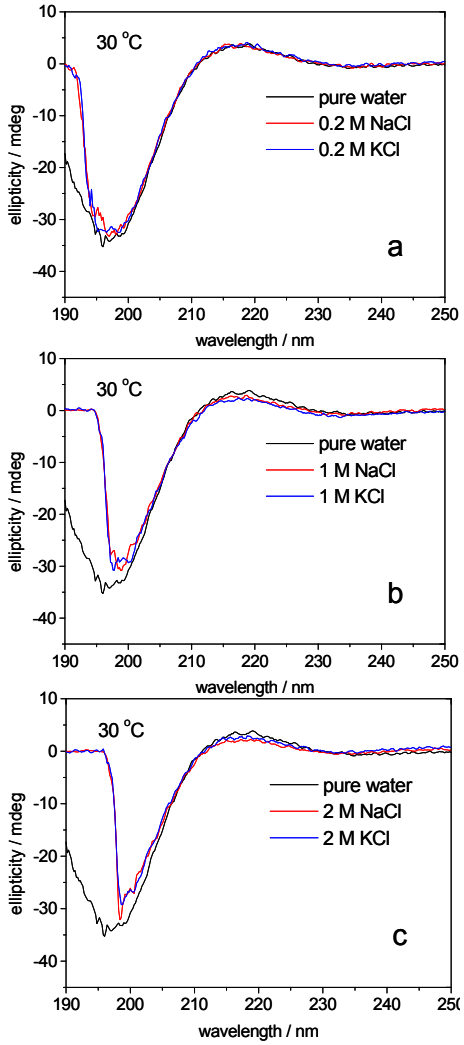

Figure C1: CD spectra of 1 mg/ml PGA in pure water and in a) 0.2 M, b) 1.0 M and c) 2 M NaCl and KCl at pH 8.3 at 30 °C. CD spectra below 200 nm at high salt concentrations are not reliable due to strong absorption of Cl^-.

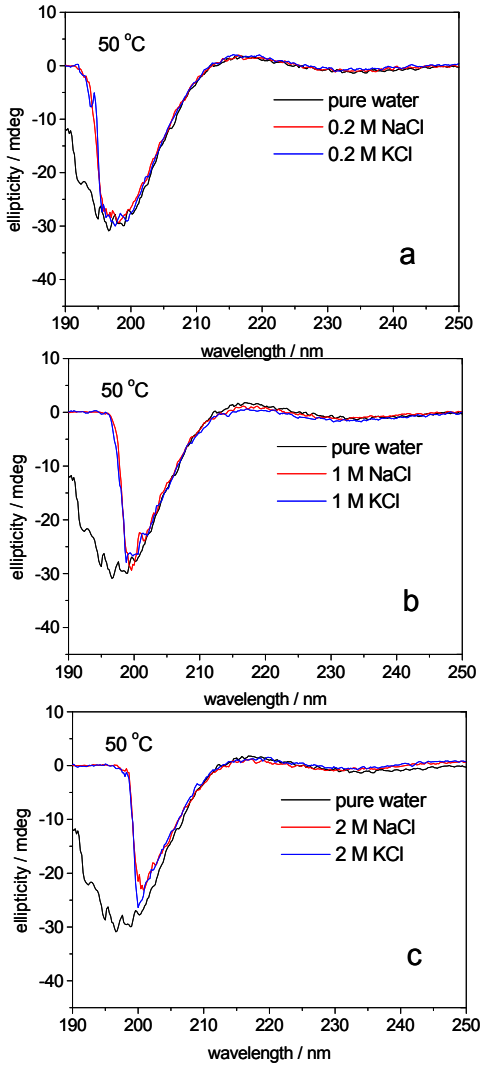

Figure C2: CD spectra of 1 mg/ml PGA in pure water and in a) 0.2 M, b) 1.0 M and c) 2 M NaCl and KCl at pH 8.3 at 50 °C. CD spectra below 200 nm at high salt concentrations are not reliable due to strong absorption of Cl^-.

APPENDIX D

D1 METHODS FOR DETERMINATION OF Ψ-ANGLE DISTRIBUTIONS FROM UVRR SPECTRA

UVRR spectrum decomposition. We used Grams Suite (Version 8.0, Thermo Fisher Scientific, Inc. Waltham, Mass., USA) to model the UVRR spectrum as the sum of Gaussian bands.[3] We constrained the $AmIII_3$ band widths to be < 50 cm^{-1}. The $AmIII_3$ region shown in Fig. D1 was fitted by four Gaussian bands. This resulted in a fitted $AmIII_3^{Ta}$ band at 1206 cm^{-1}, an $AmIII_3^{PPII}$ band at 1246 cm^{-1}, an $AmIII_3^{Tc}$ band at 1272 cm^{-1} and an $AmIII_3^{Td}$ band at 1290 cm^{-1} (Ta, Tc, and Td refer to different types of turns: Type I′ or Type III′ β turns, γ-turns, and Type V β-turns , respectively). Attempts to fit the $AmIII_3$ region by using only three Gaussian bands resulted in large residuals (Fig. D2).

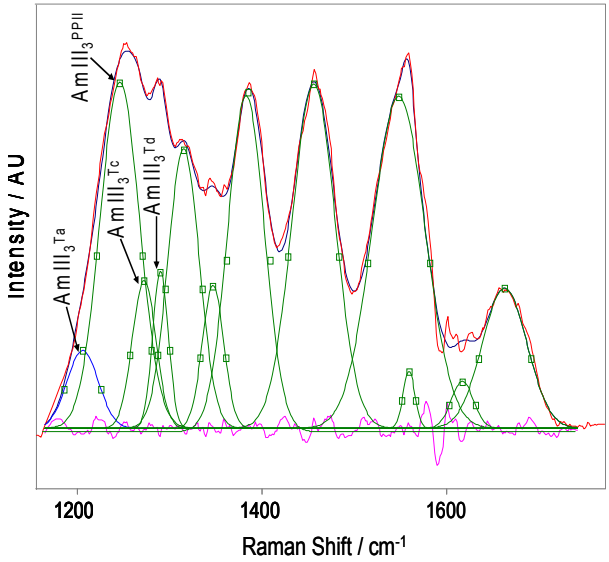

Figure D1: **Deconvolution of 204 nm UVRR spectrum of the wild-type peptide at 30 ^{0}C. Fit statistics: reduced chi-squared, $\chi^2 = 2.242$; correlation, R^2=0.9925; standard error= 57.2763.**

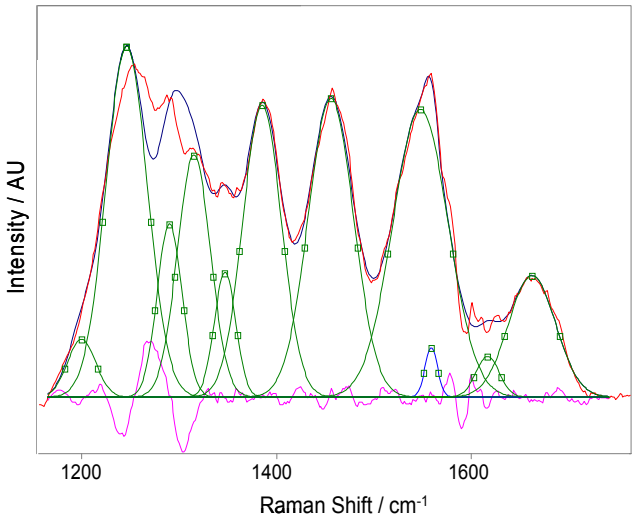

Figure D2: **Deconvolution of the $AmIII_3$ region of the wild-type peptide into the sum of 3 Gaussians. Fit statistics: reduced chi-squared, $\chi^2 = 12.172$; correlation, R^2=1.0151; standard error= 137.1674.**

$AmIII_3$ band deconvolution. We assume that the inhomogeneously broadened experimentally measured $AmIII_3$ band profile derives from different conformations and can be modeled by the sum of Lorentzian bands.[4] We deconvoluted each of the $AmIII_3$ Gaussians from

the Fig. D1 fit into the sum of Lorentzian bands with the homogeneous line widths, Γ, with different center frequencies, ve_i:

$$A(\nu) = \pi^{-1} \sum_{i=1}^{M} L_i \cdot \frac{\Gamma^2}{\Gamma^2 + (\nu - ve_i)^2} \quad \text{(D1)}$$

where L_i is the probability for a band to occur at frequency ve_i.

Quantitative correlation between the Ψ-angle and AIII$_3$ frequency. Equations have been derived correlating the Ψ-angle with the AmIII$_3$ frequency,[5-7] thus allowing us to calculate the Ψ-angle distributions.[4,6]

The Ψ-angle distribution for PPII-like conformations was calculated using the following expression derived for peptide bonds fully exposed to solvent:

$$\nu_{AmIII_3}(\Psi, t) = 1256 cm^{-1} - 54 cm^{-1} \cdot \sin(\Psi + 26^o) - 0.11 \frac{cm^{-1}}{^oC} t \quad \text{(D2)}$$

The Ψ-angle distribution for Type V β-turns (Td) was calculated by using the following expression derived for peptide bonds[8] forming two-end-on peptide bond – peptide bond hydrogen bonds:[5]

$$\nu_{AmIII_3}(\Psi) = 1244 cm^{-1} - 54 cm^{-1} \cdot \sin(\Psi + 26^o) \quad \text{(D3)}$$

The Ψ-angle distributions for Type I′ or Type III′ β turns (Ta) and γ-turns (Tc) were calculated by using the average expression derived for peptide bonds with unknown hydrogen bonding patterns in aqueous solution:[5]

$$\nu_{AmIII_3}(\Psi, t) = 1250 cm^{-1} - 54 cm^{-1} \cdot \sin(\Psi + 26^o) - 0.06 \frac{cm^{-1}}{^oC} t \quad \text{(D4)}$$

Ψ-angle distribution for the P27S mutant p53 peptide:

Calculation of non-PPII content. The wild-type p53 peptide has 12 non-proline peptide bonds contributing to Raman intensities in the AmIII, C_α-H and AmII regions (a proline peptide bond shows significantly decreased intensities in the these regions.)[9] The mutant peptide has 13 non-proline peptide bonds contributing. To normalize to the non-proline peptide bond concentration, we scaled the wild-type peptide spectrum by 13/12. To calculate the fractional increase in non-PPII conformations of the mutant p53 peptide per peptide bond, we subtracted appropriate amounts of the scaled UVRR spectrum of the wild-type peptide from the UVRR spectrum of the mutant peptide to minimize the C_α-H region intensity in the difference spectra, with the constraint that no negative features occur. Since the relative spectral intensity subtracted is directly proportional to the population of non α-helical conformations at each temperature, the difference spectra represent only α-helix-like conformations.[10,11] Based on these difference spectra, the population of non-PPII conformations for the mutant peptide was calculated to be 0.44 ± 0.02 at all temperatures.

Decomposition of the α-Helical spectrum. We modeled the $AmIII_3$ region of the calculated α-helix-like spectrum of the mutant peptide as the sum of three Gaussians (Fig. D3). By using the same methodology above, we calculated the Ψ-angle distribution for Type V β-turns by using Eqn. D.4, and for α-helix and π-bulge by using eq. D3. The Ψ-angle distribution contains contributions from α-helix-like conformations, PPII, type V β-turns, Type I′ or Type III′ β turns, γ-turns, and Type I/I′ or Type II/II′ β turns.

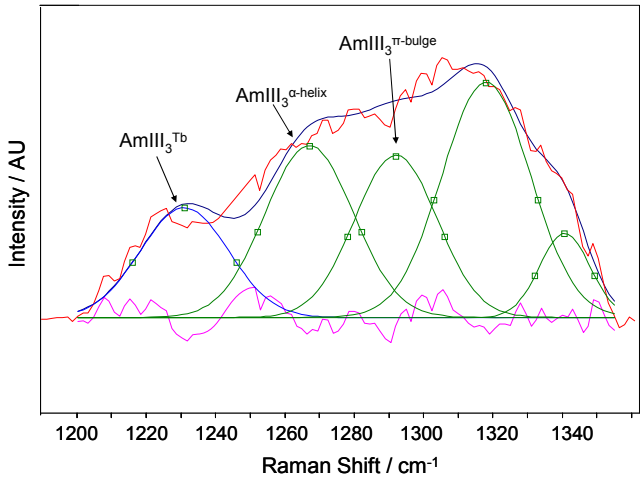

Figure D3. Deconvolution of AmIII region of calculated helical spectra of the mutant peptide into a sum of 5 Gaussian bands. Fit statistics: reduced chi-squared, χ^2 = 13.673; correlation, R^2=1.0301; standard error= 29.8235.

D2 FIGURES D4-7 AND TABLE D1-4

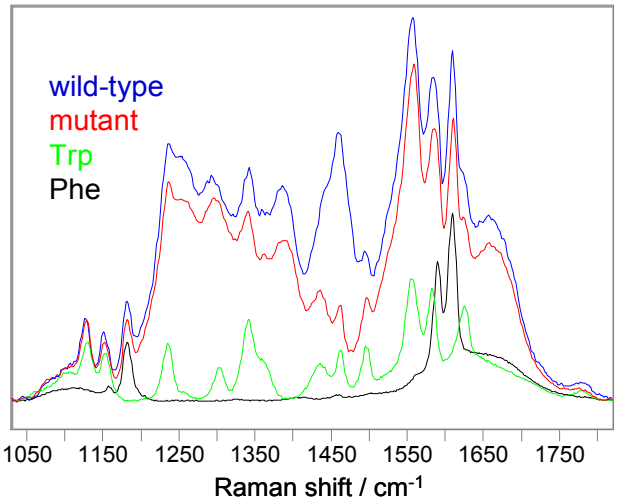

Figure D4. 204 nm excited UVRR spectra of the p53 wild-type peptide, the mutant peptide, tryptophan and phenylalanine at 30^0C.

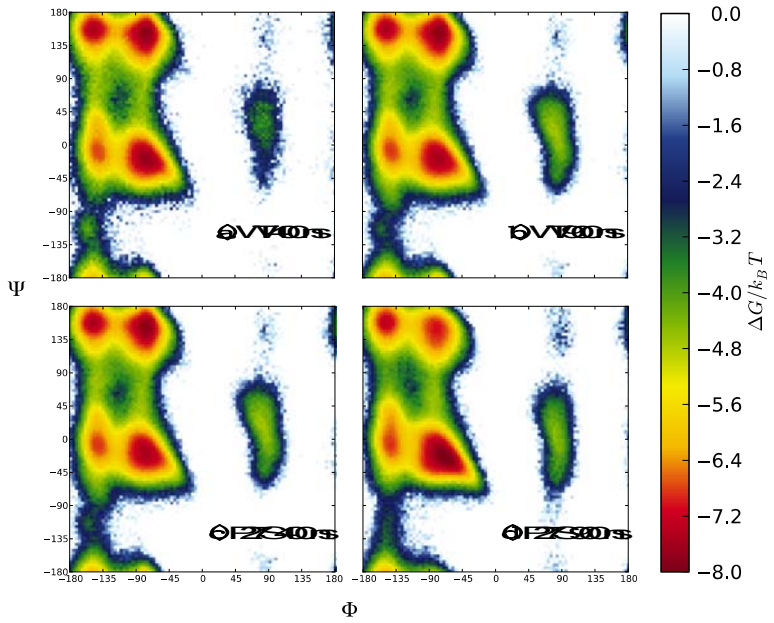

Figure D5. **Convergence of simulation ensembles by Ramachandran analysis. After discarding the initial 100 ns of each 1-μs production run started from different structures, slightly less than half (400 ns) of the remaining structures from each simulation were pooled and used to generate Ramachandran plots for the wild-type and P27S peptides; these were compared to Ramachandran plots containing the entire ensemble of structures (900 ns per initial structure). The distribution of conformations in the wild-type peptide simulation ensemble did not change appreciably when considering 400 ns of data [(a), 45,000 conformations] and when considering 900 ns of data [(b), 90,000 conformations]. Likewise, the distribution of P27S conformations did not change appreciably between 400 ns (c) and 900 ns (d) of production simulation**

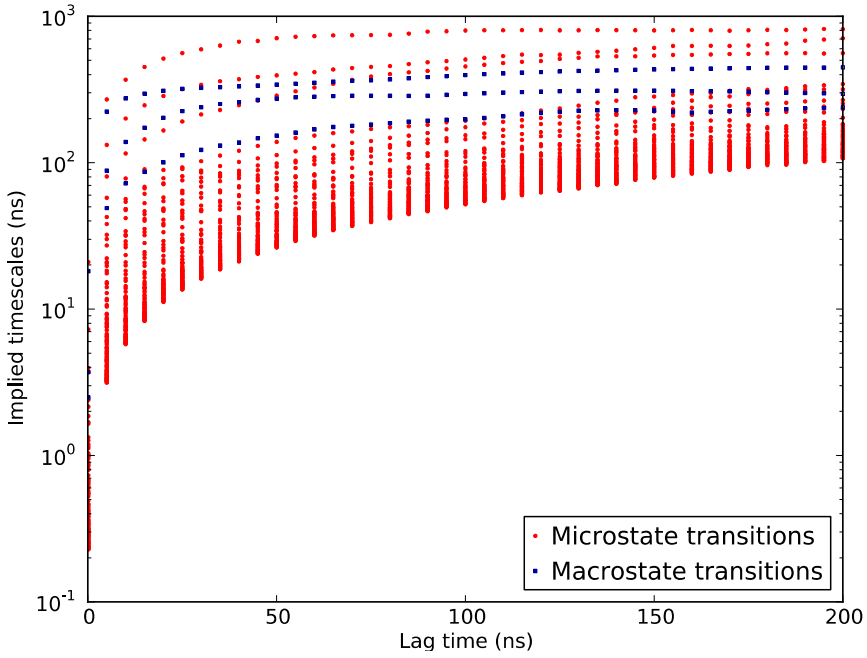

Figure D6. **Markovian behavior of the kinetic clustering of wild-type peptide configurations is demonstrated by the invariance of the "implied timescales" (related to the eigenvalues of the transition matrix) beyond a certain timescale (the Markov time of the system). Both the implied timescales of the microstate transition matrix (red circles) and those of the macrostate transition matrix (blue squares) are nearly constant after 50 ns.**

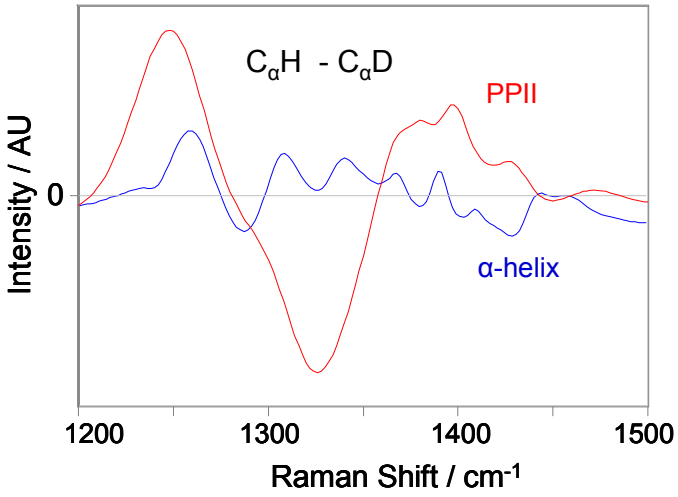

Figure D7. 204 nm UVRR difference spectra for the PPII (red) and α-helical conformations (blue) between hydrogenated (C_α-H) versus deuterated (C_α-D) of a mainly polyalanine peptide. UVRR spectra of the PPII and α-helical conformations are taken from Fig. 3A of ref.[1]

Table D1. Comparison of theoretical and experimental[2] chemical shifts for the wild-type p53 peptide.

	HN chemical shift (ppm)				HA chemical shift (ppm)			
Residue	Simulation	Experiment	RMSD	Relative RMSD	Simulation	Experiment	RMSD	Relative RMSD
Glu17	8.38	8.39	0.07	0.008	4.22	4.26	0.21	0.049
Thr18	8.38	8.22	0.50	0.061	4.04	4.28	0.49	0.115
Phe19	7.95	8.31	0.82	0.099	4.71	4.61	0.50	0.109
Ser20	8.13	8.14	0.78	0.095	4.34	4.34	0.48	0.111
Asp21	8.01	8.30	0.64	0.077	4.57	4.56	0.27	0.060
Leu22	7.95	7.97	0.56	0.071	4.26	4.11	0.32	0.079
Trp23	7.97	7.87	0.62	0.078	4.79	4.54	0.47	0.103
Lys24	7.72	7.60	0.61	0.080	4.34	4.07	0.43	0.106
Leu25	8.00	7.86	0.54	0.069	4.29	4.29	0.36	0.084
Leu26	7.60	7.98	0.56	0.070	4.40	4.63	0.36	0.077
Pro27	—	—	—	—	4.46	4.38	0.27	0.063
Glu28	8.41	8.79	0.57	0.064	4.43	4.21	0.35	0.084
Asn29	8.59	8.33	0.48	0.058	4.53	4.71	0.25	0.053
		Average:	0.56	0.069		Average:	0.37	0.084

Table D2. Comparison of theoretical and experimental[2] chemical shifts for the P27S mutant p53 peptide.

	HN chemical shift (ppm)				HA chemical shift (ppm)			
Residue	Simulation	Experiment	RMSD	Relative RMSD	Simulation	Experiment	RMSD	Relative RMSD
Glu17	8.37	8.41	0.08	0.009	4.16	4.27	0.30	0.070
Thr18	8.32	8.22	0.49	0.059	3.90	4.28	0.66	0.155
Phe19	7.87	8.33	0.87	0.104	4.70	4.58	0.41	0.089
Ser20	8.01	8.17	0.71	0.087	4.29	4.34	0.50	0.116
Asp21	8.10	8.30	0.63	0.076	4.50	4.56	0.25	0.055
Leu22	7.87	8.00	0.53	0.066	4.28	4.10	0.32	0.079
Trp23	8.17	7.95	0.58	0.073	4.59	4.46	0.44	0.099
Lys24	7.85	7.67	0.57	0.075	4.13	3.99	0.36	0.091
Leu25	7.81	7.82	0.47	0.060	4.31	4.22	0.31	0.073
Leu26	7.70	8.01	0.68	0.085	4.35	4.29	0.32	0.074
Ser27	7.81	8.06	0.62	0.077	4.38	4.34	0.35	0.081
Glu28	8.03	8.31	0.57	0.068	4.45	4.28	0.34	0.078
Asn29	8.63	8.27	0.56	0.068	4.51	4.69	0.27	0.058
		Average:	0.57	0.070		Average:	0.37	0.086

Table D3. Comparison of theoretical and experimental[2] $^3J_{\alpha N}$ coupling constants for the wild-type p53 peptide.

Residue	Simulation	Experiment	RMSD	Relative RMSD
Glu17	7.7	6.4	2.0	0.31
Thr18	6.6	7.9	2.6	0.33
Phe19	7.6	—	—	—
Ser20	7.3	5.7	2.6	0.45
Asp21	6.9	6.8	2.2	0.32
Leu22	6.5	—	—	—
Trp23	7.4	—	—	—
Lys24	7.5	—	—	—
Leu25	7.6	—	—	—
Leu26	7.3	—	—	—
Pro27	5.8	—	—	—
Glu28	7.6	5.5	2.8	0.50
Asn29	8.4	—	—	—
		Average:	2.4	0.38

Table D4. Comparison of theoretical and experimental[2] $^3J_{\alpha N}$ coupling constants for the P27S mutant p53 peptide.

Residue	Simulation	Experiment	RMSD	Relative RMSD
Glu17	7.6	6.4	2.0	0.31
Thr18	6.3	7.9	2.8	0.35
Phe19	7.5	6.4	2.2	0.35
Ser20	6.5	5.7	2.7	0.47
Asp21	6.1	—	—	—
Leu22	6.7	5.7	2.2	0.38
Trp23	6.0	5.0	2.4	0.49
Lys24	6.1	5.7	2.1	0.37
Leu25	7.5	6.1	2.1	0.35
Leu26	7.7	5.7	2.6	0.46
Ser27	7.6	6.1	2.3	0.38
Glu28	7.5	—	—	—
Asn29	8.3	7.5	1.5	0.20
		Average:	2.3	0.37

REFERENCES

(1) Mikhonin, A. V.; Asher, S. A.; Bykov, S. V.; Murza, A. *J. Phys. Chem. B* **2007**, *111*, 3280.

(2) Zondlo, S.; Lee, A.; Zondlo, N. *Biochemistry* **2006**, *45*, 11945.

(3) Ma, L.; Ahmed, Z.; Mikhonin, A. V.; Asher, S. A. *J. Phys. Chem. B* **2007**, *111*, 7675.

(4) Asher, S.; Mikhonin, A.; Bykov, S. *J. Am. Chem. Soc.* **2004**, *126*, 8433.

(5) Mikhonin, A. V.; Bykov, S. V.; Myshakina, N. S.; Asher, S. A. *J. Phys. Chem. B* **2006**, *110*, 1928.

(6) Mikhonin, A. V.; Asher, S. A. *J. Am. Chem. Soc.* **2006**, *128*, 13789.

(7) Mikhonin, A. V.; Myshakina, N. S.; Bykov, S. V.; Asher, S. A. *J. Am. Chem. Soc.* **2005**, *127*, 7712.

(8) Ding, F.; Prutzman, K. C.; Campbell, S. L.; Dokholyan, N. V. *Structure* **2006**, *14*, 5.

(9) Ahmed, Z.; Myshakina, N. S.; Asher, S. A. *J. Phys. Chem. B* **2009**, *113*, 11252.

(10) Xiong, K.; Asher, S. A. *Biochemistry* **2010**, *49*, 3336.

(11) Xiong, K.; Asciutto, E. K.; Madura, J. D.; Asher, S. A. *Biochemistry* **2009**, *48*, 10818.

APPENDIX E

E1 METHODS FOR DETERMINATION OF T-JUMPS

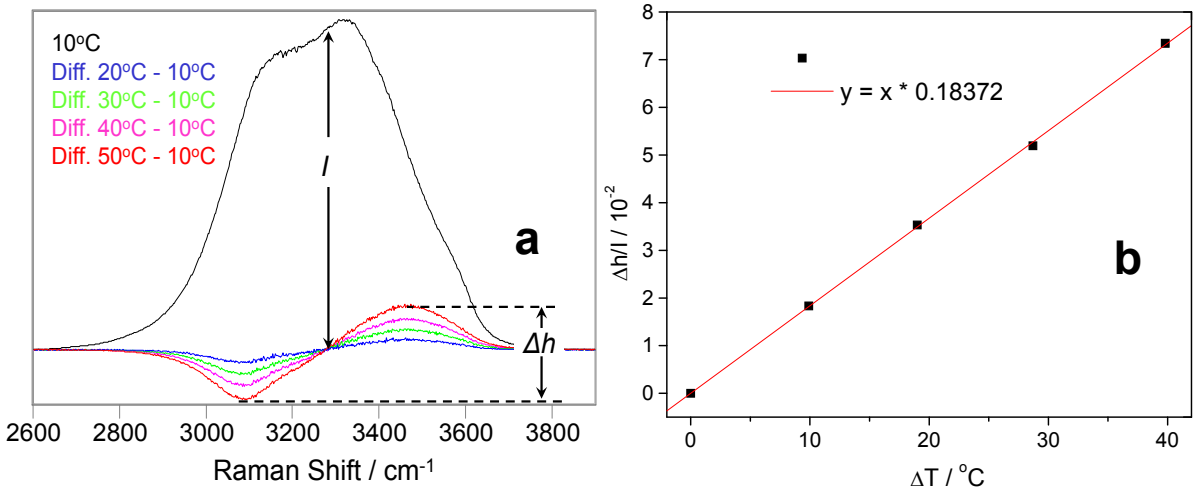

Figure E1: a) 204 nm excited water stretching bands at 10 °C and the difference spectra between higher temperatures and 10 °C. b) T-jump calibration curve which relates the magnitude of water stretching band spectral shift to the temperature change.

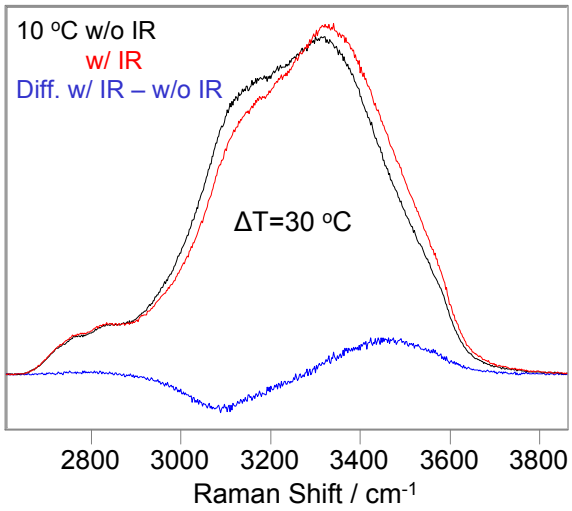

Figure E2. 204 nm excited water stretching bands of 5 mg/ml PLL in 0.5 M $NaClO_4$ (and 0.015 M NaBr) with (red) and without (black) IR pulses at 10 °C, and the difference spectrum (blue). The temperature jump is 30 °C.

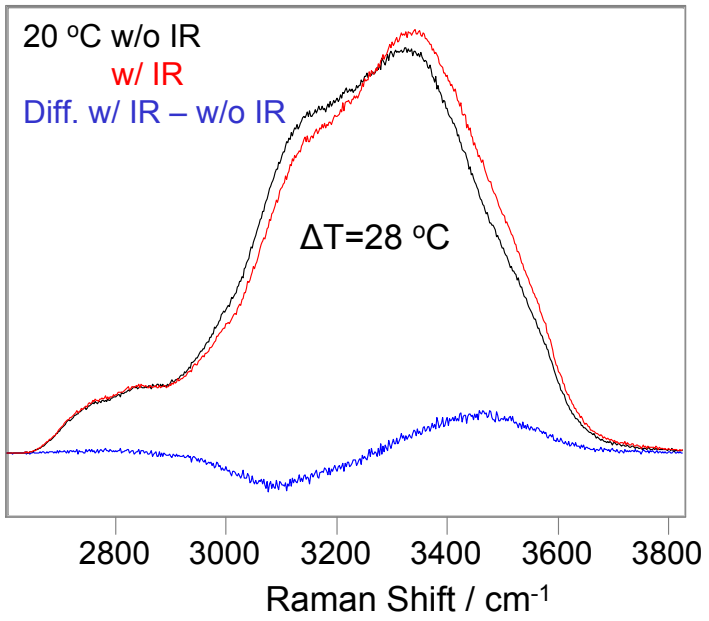

Figure E3. 204 nm excited water stretching bands of 5 mg/ml PLL in 0.5 M $NaClO_4$ (and 0.015 M NaBr) with (red) and without (black) IR pulses at 20 °C, and the difference spectrum (blue). The temperature jump is 28 °C.

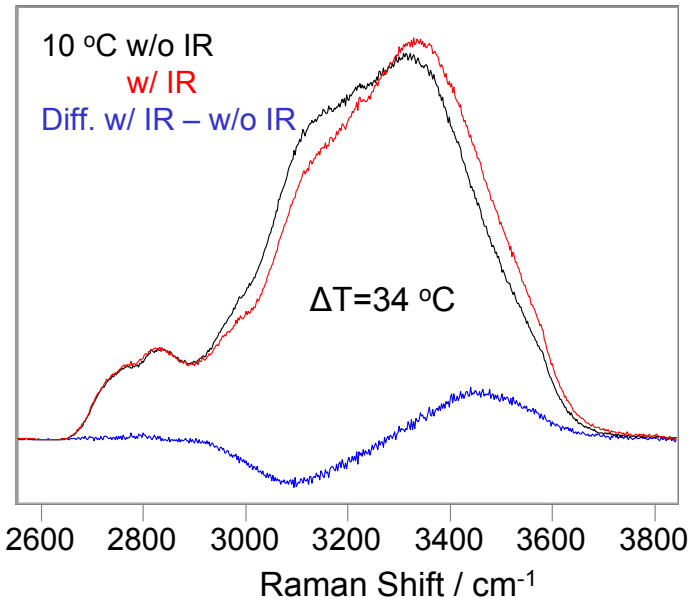

Figure E4: 204 nm excited water stretching bands of 15 mg/ml PLL in pure water with (red) and without (black) IR pulses at 10 °C, and the difference spectrum (blue). The temperature jump is 34 °C.

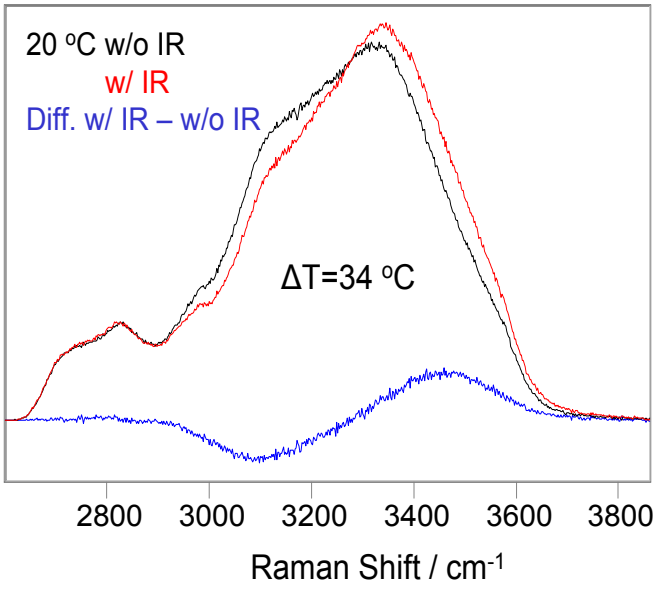

Figure E5: 204 nm excited water stretching bands of 15 mg/ml PLL in pure water with (red) and without (black) IR pulses at 20 °C, and the difference spectrum (blue). The temperature jump is 34 °C.

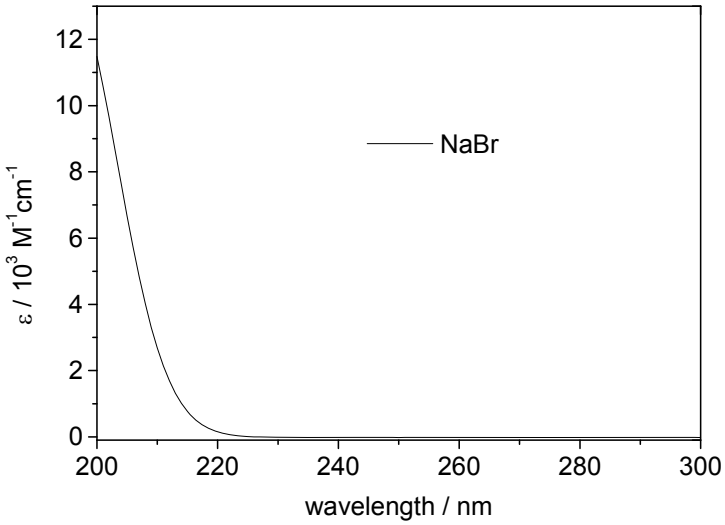

Figure E6: Molar absorptivity of NaBr in pure water.

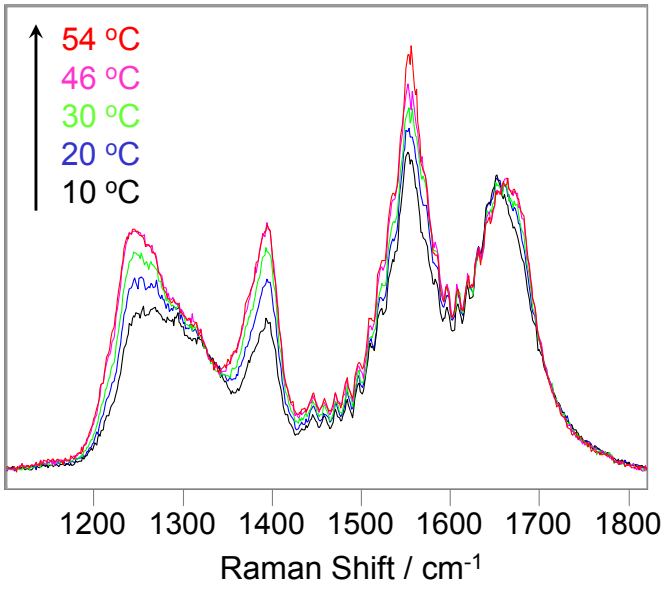

Figure E7: **Temperature dependence of 204 nm excited UVRR spectra of 1 mg/ml PLL in pure water at pH 10.65. The intensities were normalized to the isosbestic point at 1235cm^{-1}.**

APPENDIX F

F1. METHODS FOR DETERMINATION OF Ψ-ANGLE DISTRIBUTIONS FROM UVRR SPECTRA

UVRR spectrum decomposition. We used Grams Suite (Version 8.0, Thermo Fisher Scientific, Inc. Waltham, Mass., USA) to model the UVRR spectrum as the sum of Gaussians. The $AmIII^{b}$ region contains no overlapping side chain contributions. The $AmIII_3{}^{b}$ region of non-disaggregated Q10 (NDQ10) in pure water shown in Fig. F1 was fitted to two Gaussians. This resulted in a fitted $AmIII_3{}^{\beta\ b}$ band at 1231 cm^{-1} and an $AmIII_3{}^{T\ b}$ band at 1262 cm^{-1} (^{b} indicates backbone amide vibration). The $AmIII_3{}^{b}$ region of disaggregated Q10 (DQ10) in pure water shown in Fig. F2 was fitted to three Gaussians. This resulted in a fitted $AmIII_3{}^{PPII\ b}$ band at 1243 cm^{-1}, an $AmIII_3{}^{2.51\text{-}helix\ b}$ band at 1270 cm^{-1} and an $AmIII_3{}^{T'\ b}$ band at 1207 cm^{-1}. (T and T′ refer to different types of turns: Type I, Type III or Type VIII β-turn, and Type I′ or Type III′ β-turn, respectively.)

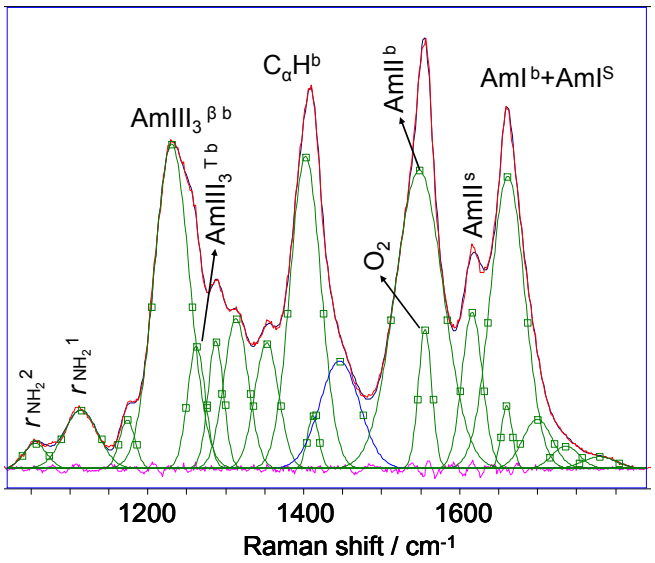

Figure F1: **Deconvolution of 204 nm UVRR spectrum of the NDQ10 in pure water at 22 ^{0}C. ^{b} indicates backbone amide bands; ^{s} indicates side chain amide bands. The AmI^{b} band overlaps the glutamine side chain AmI^{s} band; the $C_{\alpha}H^{b}$ band overlaps with the side chain AmIII^{s}+δCH_2 peak.**

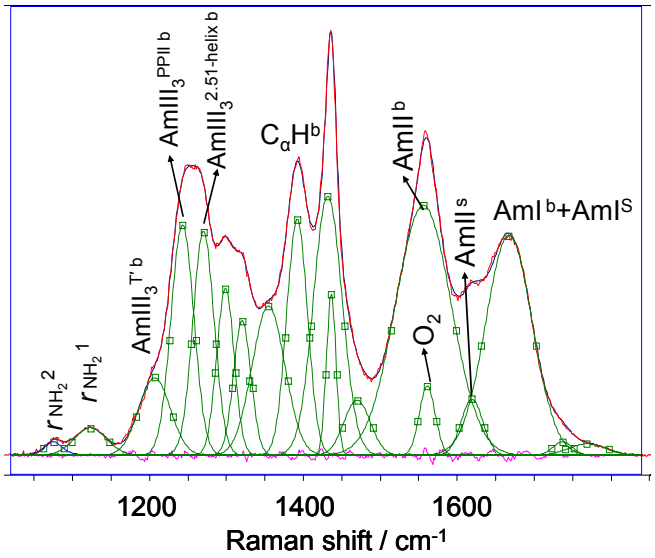

Figure F2. **Deconvolution of 204 nm UVRR spectrum of the DQ10 at 22 ^{0}C. ^{b} indicates backbone amide bands; ^{s} indicates side chain amide bands. The AmI^{b} band overlaps the glutamine side chain AmI^{s} band; the $C_{\alpha}H^{b}$ band overlaps the side chain AmIII^{s}+δCH_2 peak.**

AmIII$_3$^{b} band deconvolution. We assume that the inhomogeneously broadened experimentally measured AmIII$_3$^{b} band profile derives from different conformations and can be modeled by the sum of Lorentzian bands.[1] We deconvoluted each of the AmIII$_3$^{b} bands from the Fig. F1-2 fit into the sum of Lorentzian bands with homogeneous line widths Γ with different center frequencies ve_i:

$$A(\nu) = \pi^{-1} \sum_{i=1}^{M} L_i \cdot \frac{\Gamma^2}{\Gamma^2 + (\nu - ve_i)^2} \qquad \text{(F1)}$$

where L_i is the probability for a band to occur at frequency ve_i.

Quantitative correlation between the Ψ-angle and the AmIII$_3$ frequency. Equations exist that correlate the Ψ angle to the AmIII$_3$ frequency,[2] thus allowing the calculation of the Ψ-angle distributions.[3] The Ψ-angle distribution for PPII-like and 2.5$_1$-helix-like conformations were calculated using the following expression for peptide bonds fully exposed to water:[2]

$$\nu_{AmIII_3}(\Psi, t) = 1256 \ \ cm^{-1} - 54 \ \ cm^{-1} \cdot \sin(\Psi + 26^o) - 0.11 \frac{cm^{-1}}{^oC} t \quad \text{(F2)}$$

The Ψ-angle distribution for the β-sheet was calculated by using the following expression for peptide bonds forming two-end-on peptide bond-peptide bond hydrogen bonds:[2]

$$\nu_{AmIII_3}(\Psi) = 1244 \ \ cm^{-1} - 54 \ \ cm^{-1} \cdot \sin(\Psi + 26^o) \quad \text{(F3)}$$

The Ψ-angle distributions for Type I or Type III or Type VIII β turns and Type I′ or Type III′ β turns were calculated by using the average expression for peptide bonds with different possible hydrogen bonding patterns:[2]

$$\nu_{AmIII_3}(\Psi, t) = 1250 \ \ cm^{-1} - 54 \ \ cm^{-1} \cdot \sin(\Psi + 26^o) - 0.06 \frac{cm^{-1}}{^oC} t \quad \text{(F4)}$$

These equations correlating the $AmIII_3$ frequency with the Ψ-angle ignore the more modest Φ-angle dependencies.[4] The estimated error of this determination is suggested to be $< \pm 14^{o}$.[2]

F2 CD SPECTRA OF Q10 SOLUTIONS BY USING DIFFERENT SOLVENTS FOR DISAGGREGATION

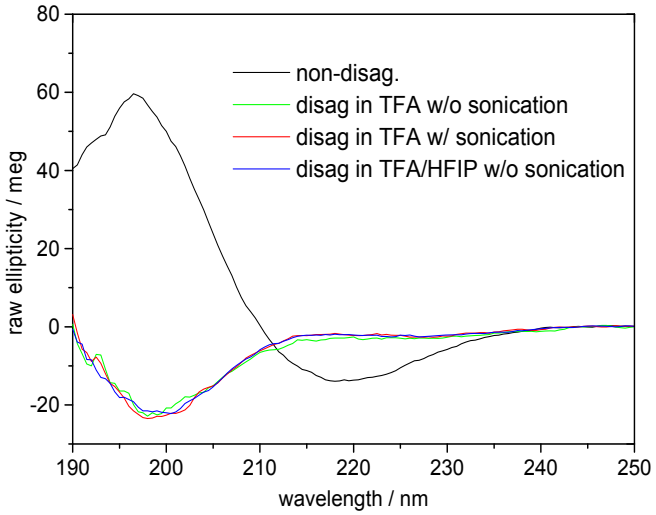

Figure F3. CD spectra of 1 mg/ml NDQ10 (black) and DQ10 in pure water at 22 °C. Disaggregation using TFA with (red), and without (green) sonication, and using 1:1 TFA/HFIP mixture without sonication (blue) give rise to essentially identical CD spectra. The peptide solutions were not centrifuged.

Fig. F3 shows the CD spectra of DQ10 solutions using different solvents for disaggregation. The CD spectrum of Q10 using TFA for disaggregation without sonication (Fig. F3, green) shows a very slight negative ellipticity at ~ 220 nm and a strong negative band at 200 nm, indicative of extended conformations.[5-7] The CD spectra of solutions without sonication are essentially identical to those with sonication (Fig. F3, red), indicating that sonication is not required. The TFA disaggregated CD spectrum is identical to the TFA/HFIP mixture disaggregated spectrum (Fig. F3, blue), indicating that TFA alone dissolves Q10 aggregates.

REFERENCES

(1) Oladepo, S. A.; Xiong, K.; Hong, Z.; Asher, S. A. *J. Phys. Chem. Lett.* **2011**, *2*, 334-344.

(2) Mikhonin, A. V.; Bykov, S. V.; Myshakina, N. S.; Asher, S. A. *J Phys Chem B* **2006**, *110*, 1928-1943.

(3) Mikhonin, A. V.; Asher, S. A. *J Am Chem Soc* **2006**, *128*, 13789-13795.

(4) Ianoul, A.; Boyden, M. N.; Asher, S. A. *J Am Chem Soc* **2001**, *123*, 7433-7434.

(5) Sreerama, N.; Woody, R. W. *Biochemistry* **1994**, *33*, 10022-10025.

(6) Shi, Z.; Chen, K.; Liu, Z.; Kallenbach, N. *Chem Rev* **2006**, *106*, 1877-1897.

(7) Shi, Z.; Olson, C.; Rose, G.; Baldwin, R.; Kallenbach, N. *Proc Natl Acad Sci USA* **2002**, *99*, 9190-9195.

10.0 CONCLUSIONS

Our work showed that UVRR is a powerful tool to study the equilibrium conformational transitions of protein and peptide, and the accompanying conformational dynamics. In addition, UVRR can probe the resonant excited state energies and geometries.

In chapter 3, we examined the impact of salts on the conformational equilibria and the folding energy landscapes of a mainly polyalanine peptide, AP of sequence $A_5(A_3RA)_3A$. We observed that $NaClO_4$ stabilizes the α-helix-like conformations of AP more than does NaCl, which stabilizes more than Na_2SO_4 at identical ionic strengths. This α-helix stabilization ordering is the reverse of the Hofmeister series of anions in their ability to disorder water hydrogen bonding. Much of the $NaClO_4$ α-helix stabilization results from ClO_4^- association with the AP terminal $-NH_3^+$ groups and arg side chains. The decreased Cl^- and SO_4^{2-} AP α-helix stabilization probably result from a decreased association with the arg and terminal $-NH_3^+$ groups. Cl^- is expected to have a smaller binding affinity and thus stabilizes α helical conformations intermediately between $NaClO_4$ and Na_2SO_4.

In chapter 4, we continued to examine the impact of alcohols on the conformational equilibria and the folding energy landscapes of AP. We observed that 2,2,2-trifluroethanol (TFE) most stabilizes the α-helical-like conformations, followed by ethanol, methanol and pure water. The π-bulge conformation is stabilized more than the α-helix, while the 3_{10}-helix is destabilized due to the alcohol increased hydrophobicity. Turns are also stabilized by alcohols. We also found that while TFE induces more α-helices, it favors multiple, shorter helix segments.

In Chapter 5, we surprisingly found that the charge screening of even 2 M concentrations of NaCl and KCl do not alter the unfolded PPII and 2.5_1-helix conformations of poly-L-

glutamate. These salts appear to be excluded from the region between the side chain charges and the peptide backbone. Furthermore, no direct ion pairing occurs between these salts and the side chain carboxylates.

In Chapter 6, we reported the first experimental measurements of Ramachandran Ψ-angle distributions for intrinsically disordered peptides: the N-terminal peptide fragment of tumor suppressor p53 and its P27S mutant form. Chong and coworkers also performed classical, explicit-solvent molecular dynamics simulations on the microsecond timescale. Both UVRR and simulations reveal that the P27S mutation decreases the extent of PPII helical content and increases the probability for conformations that are similar to the α-helical MDM2-bound conformation. In addition, UVRR measurements were performed on peptides that were isotopically labeled at the Leu26 residue preceding the Pro27 in order to determine the conformational distributions of Leu26 in the wild-type and mutant peptides. The UVRR and simulation results are in quantitative agreement in terms of the change in the population of non-PPII conformations involving Leu26 upon mutation of Pro27 to serine. Finally, our simulations revealed that the MDM2-bound conformation of the peptide is significantly populated in both the wild-type and mutant isolated peptide ensembles in their unbound states, suggesting that MDM2 binding of the p53 peptides may involve conformational selection.

In chapter 7, we utilized T-jump UVRR to study the impact of ion binding on the (un)folding kinetics of poly-L-lysine (PLL). We observe that the relaxation rates of the folded conformations (including π-helix (bulge), pure α-helix and turns) of PLL are slower than those of short alanine based peptides. However, the PLL pure α-helix relaxation rates and (un)folding times are similar to those of short alanine based peptides. Turn conformations appear to be α-helix and π-helix (bulge) unfolding intermediates. ClO_4^- binding to the lys side chain $–NH_3^+$

groups and the peptide backbone slows α-helix unfolding rate compared to that in pure water, but little impacts the folding rate, resulting in an increased α-helix stability. ClO_4^- binding also significantly increases PLL unfolding activation barriers but little impacts the folding barriers. Thus, the PLL folding coordinate differs from the unfolding coordinate. The π-helix (bulge) unfolding and folding does not go through the α-helix basin and may instead follow a different reaction coordinate(s) other than the Ψ angle. Our results clearly demonstrate that PLL (un)folding is not a two-state process.

In chapter 8, we utilized 198 and 204 nm excited UVRR and CD to monitor the backbone conformation and the GLN side chain hydrogen bonding (HB) of a short, mainly polyGLN peptide of sequence $D_2Q_{10}K_2$ (Q10). We measured the UVRR spectra of valeramide to determine the dependence of the primary amide vibrations on amide HB. We observed that non-disaggregated Q10 (NDQ10) solution (prepared by directly dissolving the original synthesized peptide in pure water) occurs in a β-sheet conformation, where the GLN side chains HB to either the backbone or other GLN side chains. At 60 ^oC, these solutions readily form amyloid fibrils. We used the polyGLN disaggregation protocol of Wetzel et al (*Methods Enzymol,* **2006**, *413*, 34-74) to dissolve the Q10 β-sheet aggregates. We observed that the disaggregated Q10 (DQ10) solutions adopt PPII-like and 2.5_1-helix conformations where the GLN side chains HB to water. In contrast, these samples do not form fibrils. The NDQ10 β-sheet solution structure is essentially identical to that found in the NDQ10 solid formed upon solution evaporation. The DQ10 PPII and 2.5_1-helix solution structure is essentially identical to that in the DQ10 solid. Although the NDQ10 solution readily forms fibrils when heated, the DQ10 solution does not form fibrils unless seeded by NDQ10 solution. This result demonstrates very high activation barriers between these solution conformations.

In chapter 9, we utilized UVRR to probe the lowest energy allowed electronic transitions of aqueous solutions containing Cl^- salts. We showed that the waters hydrating the Cl^- are involved in charge transfer transitions that transfer electron density from Cl^- to the water molecules. These charge transfer transitions cause significant change in the H-O-H bond angle in the excited states, which results in a strong enhancement of the preresonance Raman intensity of the water bending modes. Our work gave the first insight into the lowest allowed electronic transition of hydrated Cl^-.

11.0 FUTURE WORK

11.1 P53 Segment-MDM2 Binding Conformation Evolution

We utilized UV resonance Raman spectroscopy (UVRR) to determine the conformational distributions for intrinsically disordered p53 peptide (residues 17-29) and its P27S mutant form. **Asher and coworkers will continue to examine the process by which the intrinsically disordered p53 segment changes conformation during binding to MDM2. In addition, they will monitor the accompanying conformational changes that occur within the MDM2 receptor upon p53 segment binding. Their work will also examine the kinetics of the conformational changes that occur upon p53 binding.** This work is important because p53-MDM2 binding deactivates the tumor suppressing function of p53. A deep understanding of this recognition mechanism is likely to give crucial insight to enable design of p53-MDM2 binding inhibitors which could be used in cancer treatment[1-7].

Initially they will monitor the difference spectrum between the equilibrium p53 peptide/MDM2 solution compared to the sum of the spectra of the individual pure components. This difference spectrum will highlight the spectral changes that derive from conformational changes of the peptide bonds of both p53 and MDM2 upon binding. They will resolve the changes which occur to particular p53 peptide bonds by using the deuterated amino acid substituted p53 peptide segment. The remaining spectral changes will derive from the conformational alterations which occur in MDM2.

All of the studies described above detail the equilibrium conformations of the p53 peptide segment and the MDM2 protein. **They will also attempt to experimentally monitor the kinetics of recognition for the native and its P27S mutant.** The only existing kinetic data we

are aware of is a stopped flow trp fluorescence binding study[8] of p53 to MDM2 which showed a fast association constant of 9×10^7 M^{-1} sec^{-1}. This demonstrates that binding is fast, but does not give insight into the kinetics of the conformational changes which must be much slower. They will develop a fast mixer to quickly add p53 to an MDM2 solution, and monitor the conformational evolution along the length of the flow stream.

11.2 Polyglutamine Fibrillization Mechanisms

We utilized UVRR to selectively monitor the backbone and the GLN side chain hydrogen bonding (HB) of a short, mainly polyGLN peptide, Q10 of sequence $D_2Q_{10}K_2$. **Asher and coworkers will continue to monitor Q10 conformational evolution during fibrillization. They will also examine seeded Q10 fibrillization. In addition, their work will examine the dependence of Q10 fibrillization kinetics on solution environment (such as temperature and salts).** This work is important because polyGLN fibrillization is directly responsible for at least nine neurodegenerative diseases. A deep understanding of fibrillization mechanisms will enable design of polyGLN fibrillization inhibitors that could be used in treatment of neurodegenerative diseases. [9-13]

Non-disaggregated Q10 solution (NDQ10) (prepared by directly dissolving the synthesized peptide in pure water) readily forms amyloid fibrils at 60 ^oC. They will monitor NDQ10 conformational evolution at 60 ^oC.

Disaggregated Q10 solution (DQ10) (prepared by disaggregating the synthesized peptide by using the polyGLN disaggregation protocol of Wetzel et al[14]) does not form fibrils unless nuclei from the NDQ10 are added. They will monitor DQ10 conformational evolution at 60 ^oC upon seeding with the NDQ10.

They will also monitor Q10 fibrillization kinetics at different temperatures to examine the activation barriers. Electrostatic interactions between the Q10 N-terminal –2 charges and C-terminal +2 charges might assist Q10 fibrillization. They will monitor Q10 fibrillization in 2 M NaCl which significantly screens these electrostatic interactions.

RERERENCES

(1) Vassilev, L. T.; Vu, B. T.; Graves, B.; Carvajal, D.; Podlaski, F.; Filipovic, Z.; Kong, N.; Kammlott, U.; Lukacs, C.; Klein, C.; Fotouhi, N.; Liu, E. A. *Science* **2004**, *303*, 844.

(2) Wang, W.; Ei-Deiry, W. S. *Curr Op Oncol* **2008**, *20*, 90.

(3) Bell, H. S.; Ryan, K. M. *Cell Cycle* **2007**, *6*, 1995.

(4) Bowman, A. L.; Nikolovska-Coleska, Z.; Zhong, H. Z.; Wang, S. M.; Carlson, H. A. *J Am Chem Soc* **2007**, *129*, 12809.

(5) Dudkina, A. S.; Lindsley, C. W. *Curr Top Med Chem* **2007**, *7*, 952.

(6) Buolamwini, J. K.; Addo, J.; Kamath, S.; Patil, S.; Mason, D.; Ores, M. *Current Cancer Drug Targets* **2005**, *5*, 57.

(7) Chene, P. *Nat Rev Cancer* **2003**, *3*, 102.

(8) Schon, O.; Friedler, A.; Bycroft, M.; Freund, S. M. V.; Fersht, A. R. *J Mol Biol* **2002**, *323*, 491.

(9) Zoghbi, H. Y.; Cummings, C. J. *Human Mol Genet* **2000**, *9*, 909.

(10) Ross, C. A.; Poirier, M. A. *Nat Rev Mole Cell Biol* **2005**, *6*, 891.

(11) Wetzel, R.; Chen, S. M.; Ferrone, F. A. *Proc Natl Acad Sci USA* **2002**, *99*, 11884.

(12) Wetzel, R.; Bhattacharyya, A. M.; Thakur, A. K. *Proc Natl Acad Sci USA* **2005**, *102*, 15400.

(13) Wetzel, R.; Slepko, N.; Bhattacharyya, A. M.; Jackson, G. R.; Steffan, J. S.; Marsh, J. L.; Thompson, L. M. *Proc Natl Acad Sci USA* **2006**, *103*, 14367.

(14) O'Nuallain, B.; Thakur, A. K.; Williams, A. D.; Bhattacharyya, A. M.; Chen, S. M.; Thiagarajan, G.; Wetzel, R. *Amyloid, Prions, and Other Protein Aggregates, Pt C* **2006**, *413*, 34.